HORIZONTAL AXIS WIND TURBINE ROTOR BLADE: WINGLET AND TWIST AERODYNAMIC DESIGN AND OPTIMIZATION USING CFD

A THESIS SUBMITTED TO THE GRADUATE SCHOOL OF
NATURAL AND APPLIED SCIENCES OF MIDDLE EAST
TECHNICAL UNIVERSITY

BY

MONIER ALI ELFARRA

IN PARTIAL FULFILLMENT OF THE REQUIREMENTS
FOR
THE DEGREE OF DOCTOR OF PHILOSOPHY
IN
AEROSPACE ENGINEERING

JANUARY 2011

Approval of the thesis:

HORIZONTAL AXIS WIND TURBINE ROTOR BLADE: WINGLET AND TWIST AERODYNAMIC DESIGN AND OPTIMIZATION USING CFD

submitted by **MONIER ALI ELFARRA** in partial fulfillment of the requirements for the degree of **Doctor of Philosophy in Aerospace Engineering Department, Middle East Technical University** by,

Prof. Dr. Canan Özgen
Dean, Graduate School of **Natural and Applied Sciences** _______________

Prof. Dr. Ozan Tekınalp
Head of Department, **Aerospace Engineering** _______________

Prof. Dr. İbrahim Sinan Akmandor
Supervisor, **Aerospace Engineering Dept., METU** _______________

Asst. Prof. Dr. Nilay Sezer Uzol
Co-Supervisor, **Mechanical Engineering Dept., TOBB ETU** _______________

Examining Committee Members:

Prof. Dr. Ünver Kaynak
Mechanical Engineering Dept., TOBB ETU _______________

Prof. Dr. İbrahim Sinan Akmandor
Aerospace Engineering Dept., METU _______________

Assoc. Prof. Dr. Sinan Eyi
Aerospace Engineering Dept., METU _______________

Assoc. Prof. Dr. D. Funda Kurtuluş
Aerospace Engineering Dept., METU _______________

Asst. Prof. Dr. Oğuz Uzol
Aerospace Engineering Dept., METU _______________

Date: _______________

I hereby declare that all information in this document has been obtained and presented in accordance with academic rules and ethical conduct. I also declare that, as required by these rules and conduct, I have fully cited and referenced all material and results that are not original to this work.

Name, Last name : Monier Ali ElFarra

Signature :

ABSTRACT

HORIZONTAL AXIS WIND TURBINE ROTOR BLADE: WINGLET AND TWIST AERODYNAMIC DESIGN AND OPTIMIZATION USING CFD

Elfarra, Monier Ali
Ph.D., Aerospace Engineering Department
Supervisor: Prof. Dr. İbrahim Sinan Akmandor
Co-Supervisor: Asst. Prof. Dr. Nilay Sezer Uzol

January 2010, 176 Pages

The main purpose of this study is to aerodynamically design and optimize winglet, twist angle distribution and pitch angle for a wind turbine blade using CFD to produce more power. The RANS solver of Numeca Fine/Turbo was validated by two test cases, the NREL II and NREL VI blades. The results have shown a considerable agreement with measurements for both cases. Two different preconditioners have been implemented for the low Mach number flow. The results have shown the superiority of Merkle preconditioner over Hakimi one and Merkle was selected for further simulations. In addition to that, different turbulence models have been compared and the $k-\varepsilon$ Launder – Sharma has shown the best agreement with measurements. $k-\varepsilon$ Launder – Sharma was chosen for further simulations and for the design process. Before starting the design and optimization, different winglet configurations were studied. The winglets pointing towards the suction side of the blade have yielded higher power output. Genetic algorithm and artificial neural network were implemented in the design and optimization process. The optimized winglet has shown an increase in power of about 9.5 % where the optimized twist has yielded to an increase of 4%. Then the stall regulated blade has been converted into pitch regulated blade to yield more power output. The final design was produced by a combination of the optimized winglet, optimized twist and best pitch angle for every wind speed. The final design has shown an increase in power output of about 38%.

Keywords: CFD, Optimization, Winglet, Twist, Pitch

ÖZ

YATAY EKSENLİ RÜZGAR TÜRBİNİ ROTOR KANADI: SAYISAL AKIŞKANLAR DİNAMİĞİ (SAD) İLE KANATÇIK VE BÜKÜM AERODİNAMİK TASARIM VE ENİYİLEMESİ

Elfarra, Monier Ali
Doktora, Havacılık ve Uzay Mühendisliği Bölümü
Tez Yöneticisi: Prof. Dr. İbrahim Sinan Akmandor
Ortak Tez Yöneticisi: Yrd. Doç. Dr. Nilay Sezer Uzol

Ocak 2010, 176 Sayfa

Bu çalışmanın ana hedefi, daha fazla güç üretmek amacıyla, hesaplamalı akışkanlar dinamiği (SAD) yöntemleri kullanarak kanatçık, burkulma açısı dağılımı ve hücum açısı değerlerini eniyilemektir. Numeca Fine/Turbo yazılımının RANS çözücüsü, NREL II ve NREL VI test kanatları kullanılarak doğrulanmıştır. Sonuçlar, iki örnek için de, ölçümler ile yüksek derecede uyumluluk göstermiştir. Düşük Mach sayılı akış için iki farklı ön-şartlandırıcı uygulanmıştır. Sonuçlar, Merkle ön-şartlandırıcısının Hakimi'ye göre üstün olduğunu göstermiştir ve bu sebeple, daha sonraki benzeşimler için Merkle ön-şartlandırıcısı seçilmiştir. Buna ek olarak, farklı türbülans modelleri karşılaştırılmış ve $k-\varepsilon$ Launder – Sharma ölçümler ile en tutarlı sonuçları sağlamıştır. Bu sebeple, daha sonraki simülasyonlar ve tasarım süreçleri için $k-\varepsilon$ Launder – Sharma seçilmiştir. Tasarım ve eniyileme süreçlerine geçilmeden önce farklı kanatçık yapıları üzerinde çalışmalar yapılmıştır. Sonuçlar, kanadın emme tarafına doğru yönlendirilmiş kanatçıkların daha yüksek bir güç çıkışına sebep olduğunu göstermektedir. Tasarım ve eniyileme süreçlerinde genetik algoritmalar ve yapay sinir ağı yöntemleri kullanılmıştır. Eniyilenmiş kanatçıklar güç çıkışında %9.5'lik bir artış gösterirken, eniyilenmiş burkulma %4'lük bir artış göstermiştir. Ayrıca, daha fazla güç çıkışı elde etmek amacıyla, stall kontrollü olan kanatlar hücum kontrollü kanada çevrilmiştir. Bu çalışmalardan elde edilen

eniyilenmiş kanatçık tasarımı, eniyilenmiş burkulma ve eniyilenmiş hücum açısı değerlerinin bir bileşimi kullanılarak nihai tasarıma ulaşılmıştır. Bu tasarım, güç çıkışında yaklaşık %38'lik bir artış göstermektedir

Anahtar Kelimeler: SAD, Eniyilemesi, Kanatçık, Büklüme, Hatve

To my parents

Ali and Elham

ACKNOWLEDGMENT

To the one who taught me to think of people before thinking of myself, to the lawyer who spent her life defending and helping oppressed people in Palestine, to my mother **Elham Elfarra**, Rahimaha Allahu Taala (Allah may rest her soul).
To the one who taught me that justice is the most important term in life yet the only term we miss, to my father **Ali Elfarra**.

I wish to express my deepest gratitude to my supervisor Prof. Dr. Sinan Akmandor and co-supervisor Asst. Prof. Dr. Nilay Sezer Uzol for their guidance, advice, criticism, encouragements and insight throughout the research.

This study was supported by TÜBİTAK – Bilim İnsanı Destekleme.

I would like to thank Mr. Gerard Schepers in the ECN Wind Energy and Mrs. Maureen Hand and Dr. Scott Schreck in the National Renewable Energy Laboratory (NREL) for their assistance and providing experimental data for my test cases.

I would like to thank Pars Makina company team and the director Mrs. Serap Akmandor for their concern.

The help and encouragement of my friends Mustafa Kaya, Mohammed Alaqqad, Serakn Camcioğlu, Onur Turan, Ibrahim Bader, Usama Alshana, and Anas Abidi is deeply appreciated.

I am very grateful to my brother Mohammed, sisters Doaa, Dalia, Dena and Alya and their families for their ultimate moral support and concern.

Finally, I would like to express my love and thanks to my wife Ayda who spent nights and nights beside me encourage me to proceed. Also I would like to thank my son Ali Siraj for his appearance in my life 4 months before the defense and for annoying me during writing the thesis ☺.

TABLE OF CONTENTS

LIST OF TABLES

TABLES

LIST OF FIGURES

FIGURES

LIST OF SYMBOLS

Letters

c	Chord length
C_D	Drag coefficient
C_L	Lift coefficient
C_N	Normal force coefficient
C_p	Pressure coefficient
C_T	Tangential force coefficient
e	Internal energy
e_0	Total energy
$\mathbf{F}$	Invicid flux
f_{ei}	External force component
$\mathbf{F_v}$	Viscous flux
h	Enthalpy
h_0	Total enthalpy
k	Coefficient of thermal conductivity, kinetic turbulent energy
P	Power
p	Pressure
Q	Vector of conservative variables
q_j	Heat flux
r	Local blade radius
Re	Reynolds number
S_T	Source term
S_{ij}	Strain-rate tensor

t	Time
T	Temperature
u_{i}	Cartesian velocity component
V	Space volume
V_r	Relative velocity
V_z	Axial Velocity
W_f	Work performed by external forces

Greek Letters

α	Angle of attack
β	Twist angle
δ_{ij}	Kronecker delta
ε	Turbulent dissipation
θ	Local pitch angle
θ_p	Pitch angle
λ	Second coefficient of viscosity, Tip speed ratio
μ	Dynamic viscosity
ν	Kinematic viscosity
ν_T	Turbulent viscosity
ρ	Density
$\tau_{\mathrm{i}j}$	Viscous stress tensor
ϕ	Flow angle
ω	Specific turbulent dissipation rate
Ω	Angular speed

Abbreviations

ANN	Artificial Neural Network
BEM	Blade Element Momentum
CFD	Computational Fluid Dynamics
DNS	Direct Numerical Simulation
GA	Genetic Algorithm
HAWT	Horizontal Axis Wind Turbine
LE	Leading Edge
LS	Launder Sharma
LSWT	Lifting Surface Prescribed Wake
NREL	National Renewable Energy Laboratory
RANS	Reynolds Average Navier Stokes
RPM	Revolution Per Minute
SA	Spalart-Allmaras
SST	Shear Stress Transport
TE	Trailing Edge
VAWT	Vertical Axis Wind Turbine
WL	Winglet
YS	Yang Shih

CHAPTER 1

INTRODUCTION

Energy is everything. Energy exists in many different forms such as heat, kinetic, electrical, chemical … etc. Energy is not produced from nothing neither vanished but it changes from form to another. A form of energy may not be useful and needed to be transferred into a different useful one. To convert the energy from one form to another, a tool is needed. Any moving object has a kinetic energy which causes the motion of the object. Since the wind moves, so it has a kinetic energy which is very important for natural applications such as trees Vaccination and rains. However, considering industrial applications, the kinetic energy of the wind will be more useful if it can be converted into electrical energy. This is done by using wind turbines. The main purpose of the wind turbines is to convert the kinetic energy of the wind into mechanical energy by the blades and then into electrical energy by the generator.

1.1 Historical Review of Wind Energy

The wind energy was firstly used to produce mechanical energy and the system used to change the kinetic energy of the wind into mechanical energy was called windmill.

No one knows for sure when and where the first time the wind energy was used. Different speculations have been stated. Some say that they have discovered the remains of stone windmills in Egypt with an estimated age of 3000 years [1]. Others claim that the first windmill was constructed in Afghanistan in the year 644 A.D.[2]. A later description dates back to the year 945 and depicts a windmill with a vertical axis of rotation. It was used for milling grain and some of them have survived in Afghanistan up to the present time as shown in Figure (1.1).

Figure 1.1: Ancient vertical axis windmill in Afghanistan [3]

The Chinese also were using wind wheels for draining rice fields. But it is not known whether the Chinese windwheels exist before the ones in Afghanistan. The Chinese windwheels were of simple structures made of bamboo sticks and fabric sails and they also had a vertical axis of rotation, Figure (1.2).

Figure 1.2: Ancient Chinese windwheel [3]

The windmills with horizontal axis of rotation, which are the traditional windmills, were probably invented in Europe. The first reliable information dates back to the year 1180 in the Duchy of Normandy. After that windmills quickly spread all over North and Eastern Europe as far as Finland and Russia [4]. Some of these windmills, called post windmills, were found in Germany in the 13th century, Figure (1.3).

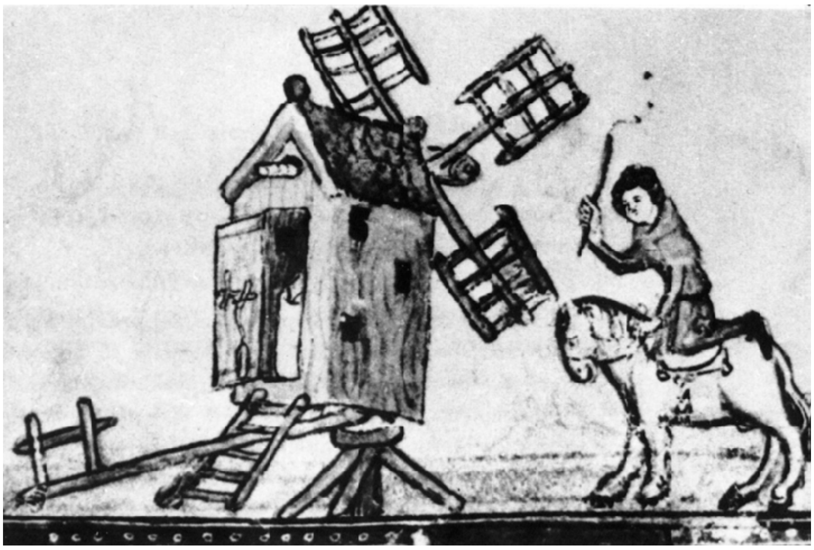

Figure 1.3: Horizontal axis post windmill in Germany [3]

For more historical information on wind energy, the reader may refer to Ref. [5,6,7,8,9,10,11]. Ref. [12] presents the history of wind turbines from ancient Persians to the mid-1950s. In addition, Ref. [13] presents a history of wind electric generation and the US research work in the period between 1970 to 1985 on different types of wind turbines. More recent comprehensive reviews of wind turbines are found in Ref. [14,15].

The historical development of windmills are documented in many publications such as in Ref. [16,17,18,19,20,21,22,23,24].

1.2 Modern Wind Turbines

The term wind turbine is the updated version of the term windmill. Wind turbine refers to the system which converts the wind energy into electrical energy. Wind turbines can be classified in two ways; first according to their aerodynamic function and secondly according to their constructional design.

The rotor aerodynamic function characterization means that whether the turbine captures the wind energy from the aerodynamic drag of the airstream acting on the rotor surface or it extracts the energy from the aerodynamic lift produced by the flow due to aerodynamically shaped blades. This classification became of less significant as almost all modern wind turbines utilize the aerodynamic lift.

The constructional design classification of wind turbines is more common. The classification is according to the position of the axis of rotation of the turbine rotor. Thus two types are produced; vertical axis wind turbines (VAWT) and horizontal axis wind turbines (HAWT).

1.2.1 Vertical Axis Wind Turbines

The oldest design of the VAWT could only be built as pure drag type rotors called Savonius rotor. The first VAWT that utilizes the aerodynamic lift was built by a French engineer called Darrieus in 1925 and it was considered as a promising concept for wind turbines. Another VAWT is the so called H-rotor. The configurations of these three VAWT types are shown in Figure (1.4):

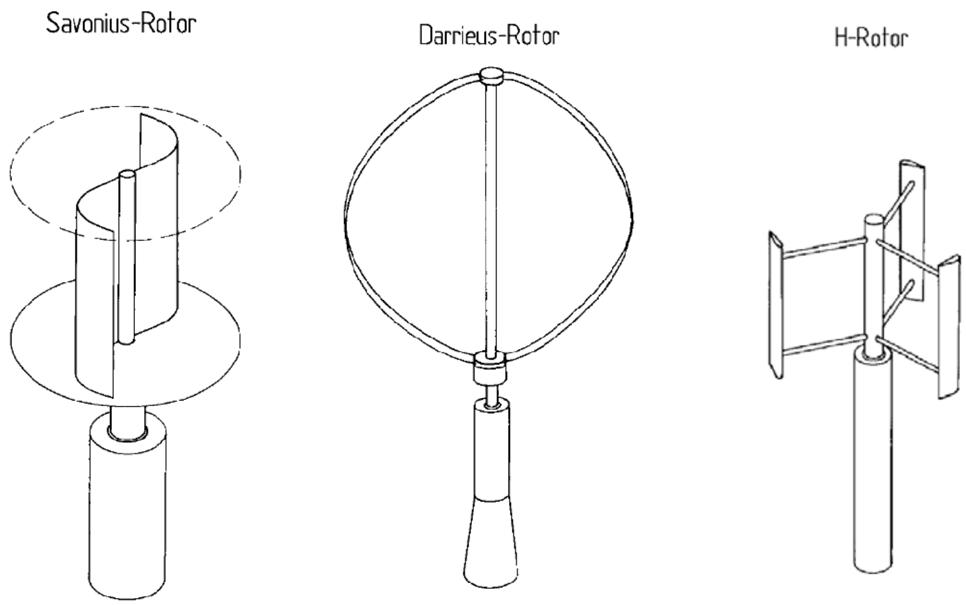

Figure 1.4: Different configurations of VAWT [reproduced from 3]

The main advantages of the VAWT:

- The possibility of housing the mechanical and electrical components at ground level. So easier maintenance and components replacement.
- No yaw system is needed

However, many disadvantages make the vertical axis wind turbines are not able to compete with the horizontal axis ones.

The disadvantages of the Savonius-Rotors are that they have a very low tip speed ratio and low power coefficients. So they are not used for electricity generation.

The Darrieus-rotor types also have low tip speed ratio so they don't have a self start ability. Also the blades are hard to manufacture and there is no power output control because they don't have pitch system.

The H-rotor with variable rotor geometry was tested to permit for a certain degree of power and speed control [25]. However, the production costs of these systems is very high.

1.2.2 Horizontal Axis Wind Turbines

The horizontal axis wind turbines are the most widely used wind turbines for generating electricity. The superiority of these turbines is based on the following advantages:

- Rotor speed and power output are controlled by bade pitch control.
- More durable in overspeed and extreme wind speed due to pitching.
- Blades can be aerodynamically optimized to achieve the highest efficiency

Figure (1.5) shows the schematic arrangement of a horizontal axis wind turbine.

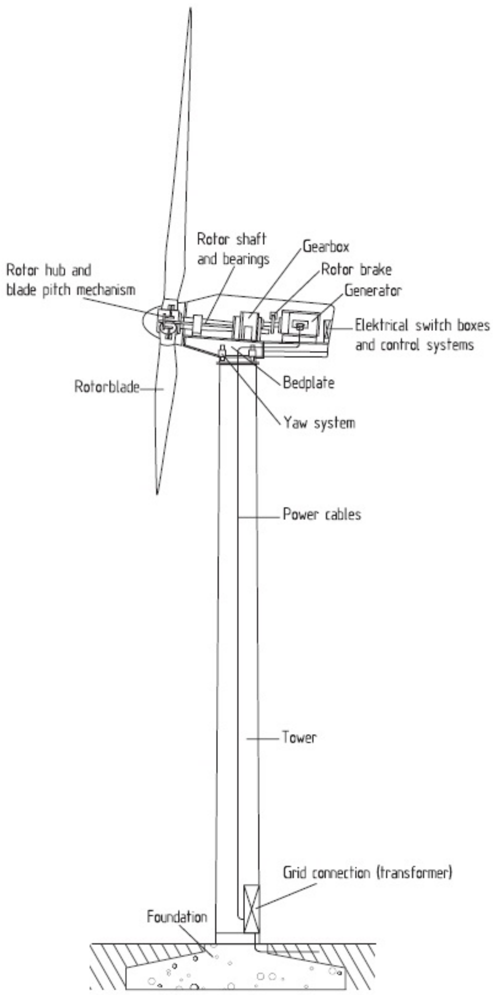

Figure 1.5: Components of a horizontal axis wind turbine [3]

The present study focuses on the horizontal axis wind turbines for the simulations.

1.3 Power Regulation Methods

The power captured by the turbine from the wind increases as the wind speed increases. At high wind speeds, the power output of the rotor may exceed the limits set by the design strength of the rotor structure. In addition to that, the power output of the rotor is limited by the maximum allowable power of the generator and if it exceeds this limit, it may result in serious problems in the generator. To avoid the continuous increase of power at high wind speeds, a power regulating system is needed. The idea is to reduce the aerodynamic forces by either influencing the aerodynamic angle of attack, reducing the projected swept area of the rotor (by yawing) or by changing the effective free-stream velocity at the rotor blades. Since the wind speed can’t be controlled, so the only way to control the effective free stream velocity is to control the rotor speed.

In the present study, influencing the angle of attack is considered for power regulation.

The most effective way of influencing the aerodynamic angle of attack is by controlling the blade pitch angle so that the angle of attack becomes smaller; hence less power is extracted from the wind. Also it is possible to change the pitch angle of the blade to a larger angle of attack up to the critical aerodynamic angle of attack, at which the air flow separates at the surface of the rotor blades, thus limiting further increase in the extracted power. These methods are called pitch regulating methods.

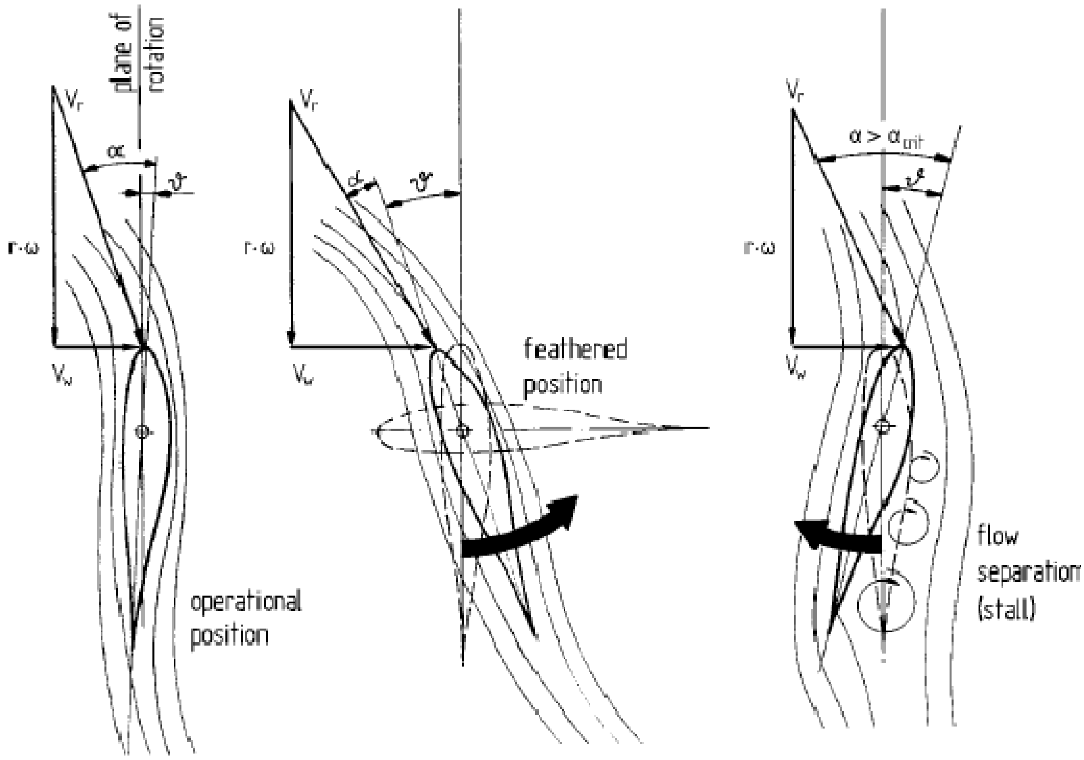

Figure 1.6: Pitch regulation towards feather or stall [3]

Another method of regulating the power is the stall regulation. Figure (1.6) shows that even without blade pitching, at high wind speeds stall occurs. So the stall regulation is based on the aerodynamic design of rotors. The blade twist is designed such that the blade stalls at certain wind speed so that the power input is limited. However, and as will be discussed later in this study, it is hard to design a stall regulated blade which maintains the same power level after certain high wind speed. A comparison in terms of power curve and axial thrust between pitch regulated and stall regulated blades is shown in Figure (1.7).

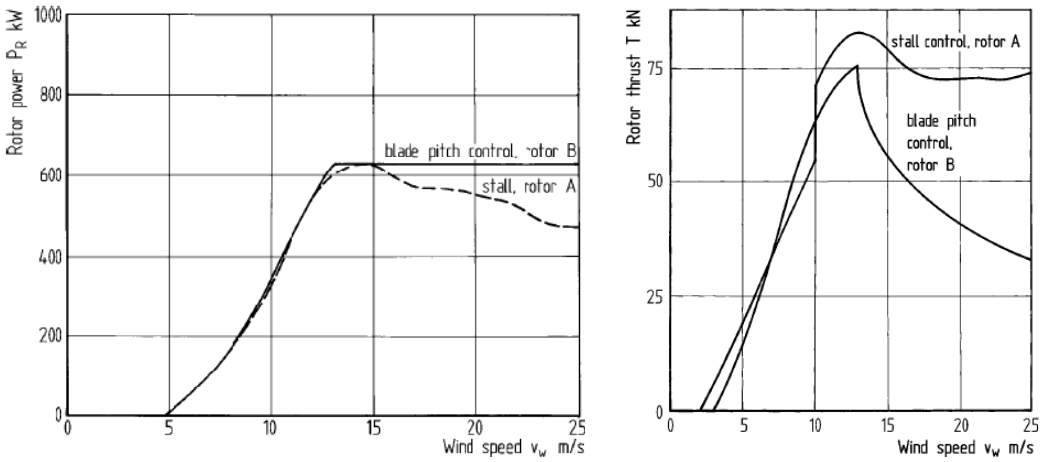

Figure 1.7: Power curve and axial thrust comparison between pitch and stall regulated rotors [26]

From Figure (1.7) it is clear that the pitch regulated blades produces more stable power for less axial thrust at high wind speeds.

In this study both stall and pitch regulated blades will be addressed and simulated.

1.4 Aerodynamics of HAWT

The aerodynamic design of wind turbine rotor blade requires finding the relationship between the actual shape of the rotor (e.g. the number of blades, twist distribution, airfoil selection,..etc) and its aerodynamic properties.

Different methods have been used in the aerodynamics design and simulation of the HAWT. Some of these methods and their advantages are listed below.

1.4.1 Blade Element Momentum Theory

Most of the rotors of the current HAWT are designed using a combination of 2-D airfoil analysis and design tools [27, 28 and 29], and combined blade element and momentum (BEM) theory [30, 31 and 32]. Many comprehensive computer codes using this methodology, such as Ref. [33], have been developed. In some of these analyses, unsteady flow effects are captured using unsteady potential flow theory and dynamic stall models [34]. Many of these BEM codes have been documented in Ref. [35], which is maintained by the National Renewable Energy Laboratory (NREL).

The BEM methods are computationally efficient and highly useful. They are the most widely used methods for design and analysis of HAWT. In Ref. [36], BEM combined with genetic algorithm was used in optimization of HAWT blade. However, these methods are incapable of accurately modeling three dimensional effects such as three-dimensional cross flows, tower shadow effects, tip relief effects, and sweep effects. These three-dimensional effects can alter the airloads, affect the fatigue life, and significantly influence the total cost of ownership of HAWT systems.

Many attempts have been done by researchers to increase the accuracy of the BEM methods in the stall and post stall regime. For example Ref. [37, 38 and 39] used advanced 2-D CFD methods combined with experiments to produce the necessary airfoil tables for the BEM methods. The 2-D stall characteristics are empirically modified so that the blade sections stall at a higher angle of attack to mimic 3-D stall. The complexity of 3-D effects makes this “stall delay” model inaccurate. A stall delay model might predict an accurate result at one span-wise station, but completely fail to predict the stall at another station. More sophisticated stall delay models are needed to reduce the time needed for computation.

1.4.2 Lifting Surface, Prescribed-Wake Code

This method is an attempt to model the 3-D aerodynamic characteristics of the rotor in a better way. The Lifting Surface Prescribed Wake code (LSWT) was developed for NREL [40].

From its name, this method combines a lifting surface representation of the rotor with a model of the rotor wake. The wake model allows the trailing edge vorticies shed by the blade close to the blade tip to roll up. The LSWT method shows an improvement over the 2-D methods. Moreover, if the wake obstacle interactions are known, this method can be used for more complex flows including tower shadow effects and non-axial flow effects. However, this method is based on invicid theory that can’t handle the flow at stall and post stall regimes. To overcome this problem, known stall normal force coefficient C_N and tangential force coefficient C_T values are used to calibrate the strength of singularity on each panel. From those coefficients, the lift and drag coefficients (C_L and C_D) as well as the angle of attack can be obtained and the tip vortex and root vortex strength can be estimated.

In fact the LSWT is used as a calibration tool for BEM codes before stall. Where after the stall it is used to convert the C_N and C_T into C_L, C_D and angle of attack.

An advanced version of the LSWT is used in CAMARD II, an aeromechanical analysis of helicopters and rotorcrafts. This version solves the potential flow. It uses a vortex lattice representation of the rotor coupled to a free wake model made of trailing and shed vorticies.

The free wake models are suitable candidates for advanced modeling. They give a more accurate and detailed description of the aerodynamic wake than BEM methods. They can be used for applications where other BEM methods can't be used [41]. The advantage of the method lies in its ability to calculate general flow cases such as yawed wake structures and dynamic inflow. However, they are more computationally expensive than BEM and prescribed wake but still more computationally efficient than CFD.

1.4.3 Computational Fluid Dynamics; Navier-Stokes Solvers

In CFD, the Navier-Stokes solver solves the governing equations of the flow directly. So it has the potential to predict the correct flow fields without a prior knowledge of the airfoil load characteristics. The main advantage of this method is its robustness. It can be used at all wind speeds and it can predict the 3-D flow characteristics accurately unlike other methods. However, the drawback of CFD is its computational time cost. Compared to other BEM methods, CFD requires much more computational power making it less suitable for design when a large number of design variables must be parametrically changed. However, with the computational power progress of the computers, it is possible to use CFD in the design making use of parallel computations on large clusters.

Full Navier-Stokes simulations of HAWT have been completed by some researchers. Using the experimental data of NREL Phase II, the accuracy of BEM, vortex lattice and Reynolds Average Navier-Stokes (RANS) were compared in Ref. [39]. The performance of the same rotor was predicted in Ref. [42] and the results show a reasonable agreement with the experiment. The RANS simulations provided greater details of flow around the blade than were available from the simpler approaches.

RANS solver was also used for prediction of aerodynamic loads on NREL Phase II and III in Ref. [43]. Unsteady flow simulation around NREL Phase VI rotor blade was completed and the CFD results showed an agreement with experimental results in Ref. [44]. Computational studies on HAWT using RANS with different turbulence models were conducted in Ref. [45, 46].

As a conclusion, the RANS approach shows its superiority over simpler methods such as BEM.

In this study, the CFD approach is used for the simulations and design.

1.5 Literature Review

The present study focuses on the effect of Winglets, twist distribution and pitch on HAWT using CFD.

1.5.1 Winglets for HAWT

The interest in the study of blade tip geometric modifications has been increased in the last few years. Many studies have been conducted in this field such as the ones by Ref. [47, 48]. Such modification is intended to improve the aerodynamic performance of turbine rotors and to make them less sensitive to wind gusts [49]. Tilting the blade tip is considered similar to the effect of winglets which decreases the induced drag of the blade by changing the downwash distribution, hence increasing the power production [50]. The idea is to add a winglet which is able to carry aerodynamic loads so that the vortex caused by the winglet spreads out the effect of the tip vortex which results in decreasing the downwash and reducing the induced drag [51].

1.5.2 Twist and Pitch for HAWT

Blade pitch and twist have been widely studied in literature. Ref. [52] showed that twisting the blades may achieve the same performances as in the case of changing the chord. An optimization model was developed to optimize the airfoil, chord and twist in Ref. [53], and the results showed high improvement in the output power.

Due to the vital role of pitch and twist in increasing the power production, they have been included in many wind turbine experiments and reports as in Ref. [54, 55, 56, 57, 58, 59].

1.5.3 Design and Optimization

There are several optimization techniques that are used in literature. These techniques are usually classified as local, global or other methods.

Local methods rely on the derivatives which only search for only one part of the design space and stop after finding a local optimum. Local methods include Adjoint, Alternating Directional Implicit (ADI) and single or multi-grid preconditioners [60].

Global methods are stochastic methods that don't stuck in local optimum. They take into account the entire design space and are not based on derivatives. They only require the objective function values.

Other methods are one-shot or inverse methods [61] that are not discussed in this thesis.

Examples of global methods are the random walk methods, simulated annealing (SA) and Genetic algorithms (GA).

Random walk method is a modification of the random search method which is the simplest approach to minimize a function. Large number of candidates are selected randomly and the objective functions of these candidates are evaluated and the minima or the maxima of these functions is called the optimum [62]. The random walk method includes a search direction [63]. So if the sample is found to better than the original point, the algorithm goes to this sample. Otherwise another direction is tried and so on. The drawback of this method is that the number of function evaluations might be too high which makes the algorithm inefficient.

Simulated annealing is based on the simulation of the annealing of solid bodies [64]. The state of the system varies randomly at a given temperature. The sample is accepted if its state results in a lower energy level. However, if its state results in higher energy level, it is only accepted with an acceptance probability defined as the Boltzmann Distribution of the temperature. The simulated annealing method had many implementations and studies in literature. It was applied to airfoil aerodynamic shape design in Ref. [65]. In Ref. [66] a new multi-objective simulated annealing algorithm was proposed.

Genetic Algorithms (GA) are search algorithms that mimic the natural behavior in terms of biological evolution in order to reach the best possible solution of a given problem [67]. An initial population of potential solutions is generated and the principle of survival of the fittest is applied. Based on their performances (level of fitness) pairs of individuals are selected from this population. Weak individuals tend to die before reproducing while stronger ones live longer. In other words, this process leads to the evolution of populations of individuals that are better suited to their environment than the original populations.

GAs are widely used in mechanical and aerodynamics applications. Ref. [68, 69] used GA in the design of turbines. Ref. [36] used GA together with the BEM theory in the design of wind turbine blade. Aerodynamic optimization using CFD is found in Ref. [70, 71, 72, 73 and 74]. Ref. [75] used the GA in multi-objective aerodynamic shape design optimization. Finally, multidisciplinary optimization of wings was investigated in Ref. [76].

In this work, the Genetic Algorithm is used as the optimization technique.

1.6 Scope of the Study

The main purpose of this study is to aerodynamically design and optimize winglet, twist angle distribution and pitch angle for a wind turbine blade using CFD to produce more power. But before that, the following issues were considered:

- Study the preconditioning effects on wind turbine CFD simulations. Since the Mach number is very low, preconditioners are needed.
- Study different low Reynolds number turbulence models on two test cases and see which one gives closer results to experiments.
- Study the effect of winglets, twist and pitch on the power performance of HAWT. The NREL Phase VI is baseline blade for this study.

1.7 Thesis Outline

The thesis consists of 6 chapters.

Chapter 1: Introduction about Wind turbines, history, regulation methods, aerodynamics and literature review.

Chapter 2: States the governing equations and numerical methods used for the simulation. It also states different turbulence models and preconditioners used in the RANS solver. Information about the boundary conditions is also mentioned

Chapter 3: Two test cases are investigated and analyzed. The NREL Phase II and NREL Phase VI. The results are compared with the experimental results for different turbulence models. This chapter is important to validate the solver used and also to choose the most suitable turbulence model for further simulations.

Chapter 4: Different winglet, twist and pitch configurations were studied on the NREL Phase VI and their effects on the power output of the turbine was investigated.

Chapter 5: The best winglet configuration was optimized for better power performance. Also the spanwise twist distribution of the blade was optimized. The stall regulated blade was converted into pitch regulated and the difference in power curves was studied. Finally a combination of winglet and twist was added to the optimum pitch regulated blade and the final design was deeply investigated.

Chapter 7: Concluding remarks are stated and recommendations for future work are addressed.

CHAPTER 2

GOVERNING EQUATIONS AND NUMERICAL METHODS

The governing equations of fluid motion are represented by the conservation of mass, momentum and energy. With the viscosity effect taken into consideration, these equations are known as Navier-Stokes equations. It is accepted that the Navier-Stokes equations describe all the properties of the continuous flow system [77].

In principle, the Navier-Stokes equations describe both laminar and turbulent flows. In engineering applications (e.g., pumps, compressors, pipe lines and wind turbines) turbulent flows are prevalent and have to be simulated [78].

Turbulence is a nonlinear process with a wide range of spatial and temporal scales. The direct simulation of the turbulent flows, called direct numerical simulation (DNS) [78], in most engineering applications is not possible. Even for the very restricted cases, the DNS is difficult and costs too much CPU time. In the context of scale modeling, the most direct approach is offered by partitioning of the flow field into a mean and fluctuating part. This process produces the Reynolds Average Navier-Stokes (RANS) equations. The RANS equations can't be solved without information about the various correlation terms that make up the stress tensor. The same is true for the energy equation (closure problem). So turbulence models are necessary to address the closure problem of turbulence modeling [79].

The Mach number being very small (less than 0.07) in wind turbines applications, the CFD simulation of such flow may have convergence difficulties. To overcome this problem, preconditioning is used.

In this chapter, the numerical methods used throughout the thesis are addressed. First the Navier-Stokes equations are presented followed by RANS equations. Then different turbulence models are discussed. In addition to that, the different preconditioning methods are stated and finally the boundary conditions used in this study are explained.

2.1 Navier-Stokes Equations

The general three-dimensional Navier-Stokes equations in an integral, conservative, vector form can be written over a space volume V bounded by a surface S as:

$$\frac{\partial}{\partial t}\int_V Q\, dV + \oint_S (\mathbf{F}\cdot\mathbf{n})\, dS - \oint_S (\mathbf{F_v}\cdot\mathbf{n})\, dS = \int_V s_T\, dV \tag{2.1}$$

where Q is the vector of conservative variables given by:

$$Q = \begin{Bmatrix} \rho \\ \rho u_1 \\ \rho u_2 \\ \rho u_3 \\ \rho e_0 \end{Bmatrix} \tag{2.2}$$

with ρ, u_{i} and e_0 are density, Cartesian velocity component, and total energy respectively.

$\mathbf{F}$ is the invicid flux and $\mathbf{F_v}$ is the viscous flux defined as:

$$F_j = \begin{Bmatrix} \rho u_j \\ \rho u_1 u_j + p\delta_{1j} \\ \rho u_2 u_j + p\delta_{2j} \\ \rho u_3 u_j + p\delta_{3j} \\ \rho h_0 u_j \end{Bmatrix}, \qquad F_{vj} = \begin{Bmatrix} 0 \\ \tau_{1j} \\ \tau_{2j} \\ \tau_{3j} \\ u_i\tau_{ij} - q_j \end{Bmatrix} \tag{2.3}$$

The index $i, j = 1, 2, 3$ refers to the component in each coordinate. p and h_0 are pressure and total enthalpy respectively.

s_T contains the source terms and it is defined as:

$$\mathrm{s_T} = \begin{Bmatrix} \rho \\ \rho f_{e1} \\ \rho f_{e2} \\ \rho f_{e3} \\ W_f \end{Bmatrix} \tag{2.4}$$

with f_{e1}, f_{e2} and f_{e3} being the components of external force. W_f is the work performed by those external forces.

$$W_f = \rho \, \mathbf{f_e} \cdot \mathbf{u} \tag{2.5}$$

The total enthalpy h_0 is related to the total energy e_0 by:

$$h_0 = e_0 + \frac{p}{\rho} \tag{2.6}$$

where the total energy e_0 is given by:

$$e_0 = e + \frac{1}{2}u_i u_i \tag{2.7}$$

thus,

$$h_0 = h + \frac{1}{2}u_i u_i \quad and \quad h = e + \frac{p}{\rho} \tag{2.8}$$

here, e is the internal energy and h is the enthalpy.

The heat flux term q_j in the energy equation of Eq. (2.3) is given from the thermal conduction of Fourier law as:

$$q_j = -K\frac{\partial T}{\partial x_j} \tag{2.9}$$

where, K is the coefficient of thermal conductivity and T is the temperature.

For Newtonian fluid, the viscous stress tensor, τ_{ij}, in Eq.(2.3) is defined by:

$$\tau_{ij} = 2\mu S_{ij} + \lambda\frac{\partial u_k}{\partial x_k}\delta_{ij} \tag{2.10}$$

where, μ is the dynamic viscosity, λ is the second coefficient of viscosity, δ_{ij} is the Kronecker delta and S_{ij} is the strain-rate tensor.

μ and λ are related through:

$$\kappa = \frac{2}{3}\mu + \lambda \tag{2.11}$$

From the Stokes' hypothesis, for incompressible and/or low Mach number flows, $\kappa = 0$. Thus Eq.(2.11) becomes:

$$\lambda = -\frac{2}{3}\mu \tag{2.12}$$

The strain-rate tensor, S_{ij}, is given by:

$$S_{ij} = \frac{1}{2}\left(\frac{\partial u_i}{\partial x_j} + \frac{\partial u_j}{\partial x_i}\right) \tag{2.13}$$

Substituting from Eq.(2.12) and Eq.(2.13) into Eq.(2.10), the viscous stress tensor can be written as:

$$\tau_{ij} = \mu\left[\left(\frac{\partial u_i}{\partial x_j} + \frac{\partial u_j}{\partial x_i}\right) - \frac{2}{3}\left(\frac{\partial u_k}{\partial x_k}\right)\delta_{ij}\right] \tag{2.14}$$

To close the Navier-Stokes equations, it is necessary to find relations between the different thermodynamic variables (ρ, p, T, e, h). Assuming perfect gas and using the perfect gas relations:

$$e = C_v T, \quad h = C_p T, \quad \gamma = \frac{C_p}{C_v}, \quad C_v = \frac{R}{\gamma - 1}, \quad C_p = \frac{\gamma R}{\gamma - 1} \tag{2.15}$$

then the pressure is obtained from the equation of state of perfect gas as:

$$p = (\gamma - 1)\rho e = (\gamma - 1)\rho\left(e_0 - \frac{1}{2}u_i u_i\right) \tag{2.16}$$

2.2 Reynolds Averaged Navier-Stokes (RANS) Equations

The RANS equations are derived by decomposing the flow variables into mean and fluctuating parts as:

$$\phi = \bar{\phi} + \phi' \tag{2.17}$$

Then the viscous conservation laws are averaged over a time interval T:

$$\bar{\phi} = \lim_{T\to\infty}\frac{1}{T}\int_t^{t+T}\phi(\mathbf{x}, t)dt \tag{2.18}$$

This time interval should be large enough with respect to the time scales of the turbulent fluctuations, but small enough with respect to all other time-dependent effects.

Making use of the following relations and correlation:

$$\bar{\bar{\phi}} = \bar{\phi}, \qquad \overline{\phi'} = 0, \qquad \overline{\phi\psi} = \bar{\phi}\bar{\psi} + \overline{\phi'\psi'} \tag{2.19}$$

Eq.(2.1) becomes:

$$\frac{\partial}{\partial t}\int_V Q\,dV + \oint_S (\mathbf{F}\cdot\mathbf{n})\,dS - \oint_S (\mathbf{F_v}\cdot\mathbf{n})\,dS = \int_V s_T\,dV \tag{2.20}$$

where,

$$Q = \begin{Bmatrix} \bar\rho \\ \bar\rho\,\bar u_1 \\ \bar\rho\,\bar u_2 \\ \bar\rho\,\bar u_3 \\ \bar\rho\,\bar e_0 + (\overline{\rho' e'} + k) \end{Bmatrix}, \quad F_j = \begin{Bmatrix} \bar\rho\,\bar u_j + \overline{\rho' u'_j} \\ \bar\rho\,\bar u_1 \bar u_j + \bar p\delta_{1j} + \overline{u_1}\,\overline{\rho' u'_j} + \overline{\rho' u'_1}\,\bar u_j \\ \bar\rho\,\bar u_2 \bar u_j + \bar p\delta_{2j} + \overline{u_2}\,\overline{\rho' u'_j} + \overline{\rho' u'_2}\,\bar u_j \\ \bar\rho\,\bar u_3 \bar u_j + \bar p\delta_{3j} + \overline{u_3}\,\overline{\rho' u'_j} + \overline{\rho' u'_3}\,\bar u_j \\ \bar\rho\,\bar h_0 \bar u_j + \bar e_0\,\overline{\rho' u'_j} + (\overline{\rho' e'} + k)\,\bar u_j \end{Bmatrix} \tag{2.21}$$

and,

$$F_{vj} = \begin{Bmatrix} 0 \\ \bar\tau_{1j} - \tau^T_{1j} \\ \bar\tau_{2j} - \tau^T_{2j} \\ \bar\tau_{3j} - \tau^T_{3j} \\ \bar u_i \bar\tau_{ij} - \bar q_j + \Theta^T_j \end{Bmatrix} \tag{2.22}$$

where the kinetic energy of turbulent fluctuations k, and the Reynolds stress tensor τ^T_{ij} are given by:

$$k = \frac{1}{2}\overline{\rho u_i' u_i'} \tag{2.23}$$

$$\tau^T_{ij} = \overline{\rho u_i' u_j'} \tag{2.24}$$

Θ^T_j consists of the turbulent heat flux tensor q^T_j and other turbulent terms evolving from density-velocity correlations and triple velocity correlations of the turbulent fluctuations. Those terms are defined as:

$$\Theta^T_j = w^T_j - q^T_j - k^T_j - E^T_j \tag{2.25}$$

$$w^T_j = -\bar u_i \tau^T_{ij} + \overline{u_i' \tau_{ij}'} \tag{2.26}$$

$$q^T_j = \overline{\rho h' u_j'} \tag{2.27}$$

$$k_j^T = \frac{1}{2}\overline{\rho u_i^{'} u_i^{'} u_j^{'}} \tag{2.28}$$

$$E_j^T = \overline{u_i}\overline{\rho u_i^{'}}\overline{u_j} \tag{2.29}$$

To solve the equations above, we need to model all the turbulent terms in the equations. Such a task is very difficult. Instead, the compressible density weighted averaged (Favre-averaged) RANS equations are very common to use in literature:

The density weighted average is defined through:

$$\tilde{\phi} = \frac{\overline{\rho\phi}}{\bar{\rho}} \tag{2.30}$$

with the decomposition:

$$\phi = \tilde{\phi} + \phi^{"} \tag{2.31}$$

and the relations:

$$\bar{\tilde{\phi}} = \tilde{\phi} \quad \text{and} \quad \overline{\rho\phi^{"}} = 0 \tag{2.32}$$

The Favre-averaged RANS equations are now obtained as:

$$\frac{\partial}{\partial t}\int_V Q\, dV + \oint_S (\mathbf{F}\cdot\mathbf{n})\, dS - \oint_S (\mathbf{F_\upsilon}\cdot\mathbf{n})\, dS = \int_V s_T\, dV \tag{2.33}$$

$$Q = \begin{Bmatrix} \bar{\rho} \\ \bar{\rho}\,\tilde{u}_1 \\ \bar{\rho}\,\tilde{u}_2 \\ \bar{\rho}\,\tilde{u}_3 \\ \bar{\rho}\,\tilde{e}_0 + k \end{Bmatrix}, \qquad F_j = \begin{Bmatrix} \bar{\rho}\,\tilde{u}_j \\ \bar{\rho}\,\tilde{u}_1\tilde{u}_j + \bar{p}\delta_{1j} \\ \bar{\rho}\,\tilde{u}_2\tilde{u}_j + \bar{p}\delta_{2j} \\ \bar{\rho}\,\tilde{u}_3\tilde{u}_j + \bar{p}\delta_{3j} \\ \bar{\rho}\,\bar{h}_0\tilde{u}_j + k\,\tilde{u}_j \end{Bmatrix} \tag{2.34}$$

$$F_{\upsilon j} = \begin{Bmatrix} 0 \\ \tilde{\tau}_{1j} - \tau_{1j}^T \\ \tilde{\tau}_{2j} - \tau_{2j}^T \\ \tilde{\tau}_{3j} - \tau_{3j}^T \\ \tilde{u}_i\,\tilde{\tau}_{ij} - \tilde{q}_j + \Theta_j^T \end{Bmatrix} \tag{2.35}$$

with,

$$k = \frac{1}{2}\overline{\rho u_i^{"} u_i^{"}} \tag{2.36}$$

$$\tau_{ij}^{T} = \overline{\rho u_i'' u_j''} \tag{2.37}$$

$$\tilde{\tau}_{ij} = (\mu + \mu_t)\left[\left(\frac{\partial \tilde{u}_i}{\partial x_j} + \frac{\partial \tilde{u}_j}{\partial x_i}\right) - \frac{2}{3}\left(\frac{\partial \tilde{u}_k}{\partial x_k}\right)\delta_{ij}\right] \tag{2.38}$$

$$q_j = -(K + K_t)\frac{\partial \tilde{T}}{\partial x_j} \tag{2.39}$$

$$\Theta_j^{T} = w_j^{T} - q_j^{T} - k_j^{T} \tag{2.40}$$

$$w_j^{T} = -\bar{u}_i \tau_{ij}^{T} + \overline{u_i'' \tau_{ij}''} \tag{2.41}$$

$$q_j^{T} = \overline{\rho h'' u_j''} \tag{2.42}$$

$$k_j^{T} = \frac{1}{2}\overline{\rho u_i'' u_i'' u_j''} \tag{2.43}$$

Due to the Reynolds averaging of the Navier-Stokes equations, many extra terms have been evolved. Those terms must be modeled in order to close the RANS system of equations. In the Section (2.3), various turbulence models are addressed and studied.

More information about the Navier-Stokes and RANS equations are available in Ref. [80, 81].

2.3 RANS Equations in Rotating Frame for the Absolute Velocity

In general, for rotating systems, the governing equations are formulated in the relative system and solved for the relative velocities. However, for some applications where far field boundary conditions are necessary, such as propellers and wind turbines, the equations are formulated in the relative system but solved for the absolute velocities. This formulation makes the far field velocities more physical as they should not be affected by the rotation of the blades. So the flow at the external boundary conditions is uniform and on the other hand, the flow around the wind turbine blade is rotating. In this case, the flow at the far field is not affected by the rotation of the blades and the velocities there are the absolute ones. Where, close to the blade, the flow is rotating and the velocities are the relative ones.

The RANS equations for the absolute velocities in the rotating frame of reference is:

$$\frac{\partial}{\partial t}\int_V Q\,dV + \oint_S (\mathbf{F}\cdot\mathbf{n})\,dS - \oint_S (\mathbf{F}_\upsilon\cdot\mathbf{n})\,dS = \int_V s_T\,dV \tag{2.44}$$

$$Q = \begin{Bmatrix} \bar{\rho} \\ \bar{\rho}\,\tilde{u}_1 \\ \bar{\rho}\,\tilde{u}_2 \\ \bar{\rho}\,\tilde{u}_3 \\ \bar{\rho}\,\tilde{e}_0 + k \end{Bmatrix}, \qquad F_j = \begin{Bmatrix} \bar{\rho}\,\widetilde{w}_j \\ \bar{\rho}\,\widetilde{w}_1\widetilde{w}_j + \bar{p}\delta_{1j} \\ \bar{\rho}\,\widetilde{w}_2\widetilde{w}_j + \bar{p}\delta_{2j} \\ \bar{\rho}\,\widetilde{w}_3\widetilde{w}_j + \bar{p}\delta_{3j} \\ \bar{\rho}\,\bar{h}_0\widetilde{w}_j + k\,\widetilde{w}_j \end{Bmatrix} \tag{2.45}$$

$$F_{\upsilon j} = \begin{Bmatrix} 0 \\ \tilde{\tau}_{1j} - \tau_{1j}^T \\ \tilde{\tau}_{2j} - \tau_{2j}^T \\ \tilde{\tau}_{3j} - \tau_{3j}^T \\ \tilde{u}_i\,\tilde{\tau}_{ij} - \tilde{q}_j + \Theta_j^T \end{Bmatrix} \tag{2.46}$$

Where w_i is the x_i component of the relative velocity and u_i is the x_i component of the absolute velocity. Thus the formulation involves both the absolute and relative velocity components.

The source term is given as:

$$\mathrm{s_T} = \begin{Bmatrix} 0 \\ -\bar{\mathrm{\rho}}(\boldsymbol{\omega}\times\mathbf{u}) \\ 0 \end{Bmatrix} \tag{2.47}$$

With ω being the angular velocity of the relative frame of reference.

2.3.1 Rotation and Velocity Triangle

For the wind turbine rotor, there should be no rotation in the far field. Only the flow close to the wind turbine is affected by the rotation of the blades. Based on the formulation of Sec. (2.3), the velocity triangle of a section of the wind turbine rotor is shown in Figure (2.1):

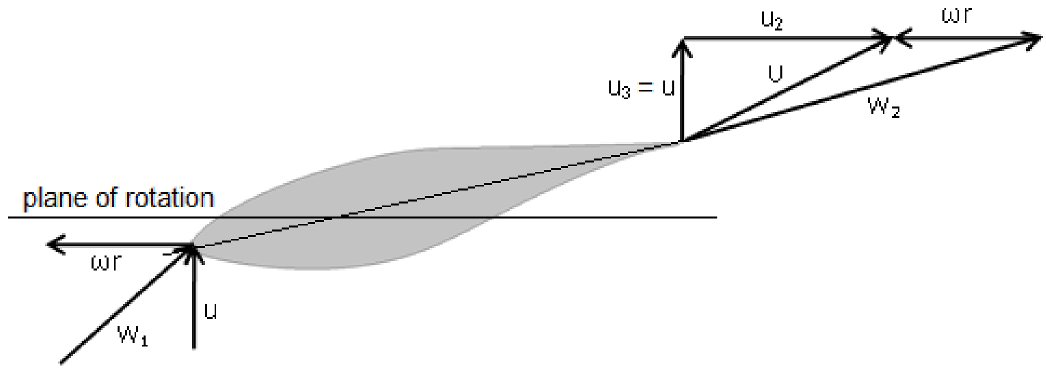

Figure 2.1: Velocity triangle for a section of the rotor blade

Where,

- u: the axial velocity (wind speed)
- U: the absolute velocity
- u_2: the azimuthal component of the absolute velocity
- u_3: the axial velocity component of the absolute velocity
- W_1: the relative velocity upstream of the blade
- W_2: the relative velocity downstream of the blade
- ωr: the rotational velocity

2.4 Turbulence Models

As stated before, it is necessary to model the turbulent terms in the RANS equation to be able to solve them. In this study, 5 different turbulence models are investigated. The turbulence models used are the Spalart-Allmaras [82, 83], the $k-\varepsilon$ Launder – Sharma [84], the $k-\varepsilon$ Yang-Shih [85], Shear Stress Transport (SST) $k-\omega$ [86] and $\overline{v^2}-f$ [87, 88]. All those models are RANS based turbulence models. Spalart-Allmaras, the $k-\varepsilon$ Launder – Sharma, the $k-\varepsilon$ Yang-Shih and the Shear Stress Transport (SST) $k-\omega$ modesl are all linear turbulent viscosity models. Whereas, v^2-f is a nonlinear turbulent viscosity model.

2.4.1 Spalart-Allmaras Model

The Spalart-Allmaras model is a one equation model. This turbulence model becomes very useful because of its robustness and ability to treat complex flows. Its main advantages over the $k-\varepsilon$ models are its robustness and lower CPU and memory usage.

The Spalart-Allmaras model is based on the resolution of additional transport equation for the turbulent viscosity. The equation contains advective, diffusive and source term. The transport equation is given by:

$$\frac{d\tilde{\nu}}{dt} = \frac{1}{\sigma}\{\boldsymbol{\nabla}\cdot[(\nu+\tilde{\nu})\boldsymbol{\nabla}\tilde{\nu}] + c_{b2}(\boldsymbol{\nabla}\tilde{\nu})^2\} + c_{b1}\tilde{S}\tilde{\nu}(1-f_{t2}) \\ - \left\{c_{w1}f_w - \frac{c_{b1}}{\kappa^2}\right\}\left\{\frac{\tilde{\nu}}{d}\right\}^2 + f_{t1}(\Delta q)^2 \tag{2.48}$$

where the eddy viscosity is defined by:

$$\nu_t = \tilde{\nu} f_{v1} \tag{2.49}$$

and,

$$f_{v1} = \frac{\chi^3}{\chi^3 + c_{v1}^3} \qquad \chi = \frac{\tilde{\nu}}{\nu} \tag{2.50}$$

$\tilde{\nu}$ is a working variable and ν is the molecular viscosity.

The different functions and constants appearing in Equations (2.43) to (2.45) are defined as below:

$$\tilde{S} = S + \frac{\tilde{\nu}}{\kappa^2 d^2} f_{v2} \qquad f_{v2} = 1 - \frac{\chi}{1+\chi f_{v1}} \tag{2.51}$$

where d is the distance to the wall, κ is the von Karman constant and S is the magnitude of the vorticity. The function f_w is defined as:

$$f_w = g\left(\frac{1+c_{w3}^6}{g^6 + c_{w3}^6}\right)^{\frac{1}{6}} \tag{2.52}$$

where,

$$g = r + c_{w2}(r^6 - r) \qquad r = \frac{\tilde{\nu}}{\tilde{S}\kappa^2 d^2} \tag{2.53}$$

The functions f_{t1} and f_{t2} are given by:

$$f_{t1} = c_{t1} g_t \exp\left[-c_{t2}\left(\frac{w_t}{\Delta q}\right)^2 (d^2 + g_t^2 d_t^2)\right], \qquad f_{t2} = c_{t3}\exp(-c_{t4}\chi^4) \tag{2.54}$$

Where:

d_t : The distance from the field point to the trip which is located on the surface

w_t : The wall vorticity at the trip

Δq : The difference between the velocities at the field point and at the trip

g_t : $g_t = \min[1.0, \Delta q / w_t \Delta x]$, with Δx being the grid spacing along the wall at the trip.

The constants used so far are:

$$\sigma = \frac{2}{3} \qquad c_{b1} = 0.1355 \qquad c_{b2} = 0.1355 \qquad \kappa = 0.41$$

$$c_{w1} = \frac{c_{b1}}{\kappa^2} + (1 + c_{b1})/\sigma = 2.5093 \qquad c_{w2} = 0.3 \qquad c_{w3} = 2.0$$

$$c_{v1} = 7.1 \qquad c_{t1} = 1.0 \qquad c_{t2} = 2.0 \qquad c_{t3} = 1.1 \qquad c_{t4} = 2.0$$

2.4.2 $k - \varepsilon$ Model

The $k - \varepsilon$ model is a two equation turbulence model. In this study, two low Reynolds number $k - \varepsilon$ models are used. These models are the $k - \varepsilon$ Launder-Sharma and the $k - \varepsilon$ Yang-Shih. The advantage of the low Reynolds number models over the standard model is that, in standard models the equations become numerically unstable when integrated to the wall. Whereas, the low Reynolds number $k - \varepsilon$ equations are directly integrated through the viscous sublayer all the way to the wall [89]. Each of the low Reynolds number $k - \varepsilon$ models is expressed by the turbulent kinetic energy equation and the turbulent dissipation rate equation as below:

$$\rho \frac{Dk}{Dt} = \frac{\partial}{\partial x_j}\left[\left(\mu + \frac{\mu_t}{\sigma_k}\right)\frac{\partial k}{\partial x_j}\right] + P_k - \rho\epsilon + L_k \tag{2.55}$$

and,

$$\rho \frac{D\epsilon}{Dt} = \frac{\partial}{\partial x_j}\left[\left(\mu + \frac{\mu_t}{\sigma_\epsilon}\right)\frac{\partial \epsilon}{\partial x_j}\right] + c_{\epsilon 1} f_1 P_k \frac{\epsilon}{k} - c_{\epsilon 2} f_2 \rho \frac{\epsilon^2}{k} + L_\epsilon \tag{2.56}$$

where P_k is the turbulent production defined as:

$$P_k = \tau_{ij} \frac{\partial u_i}{\partial x_j} \tag{2.57}$$

The turbulent viscosity μ_t is computed as:

$$\mu_t = \rho f_\mu c_\mu \frac{k^2}{\epsilon} \tag{2.58}$$

The coefficients of the $k - \varepsilon$ model are given in Table (2.1):

Table 2.1: Coefficients of the $\boldsymbol{k-\varepsilon}$ models

$\boldsymbol{k-\varepsilon}$ **model**	**Launder-Sharma**	**Yang-Shih**
c_μ	0.09	0.09
$c_{\epsilon 1}$	1.44	1.44
$c_{\epsilon 2}$	1.92	1.92
σ_k	1.0	1.0
σ_ϵ	1.3	1.3
f_μ	$e^{\left[\frac{-3.4}{(1+Re_t/50)^2}\right]}$	$1-e^{\left(Ax^a+Bx^b+Cx^c\right)^2}$
f_1	1.0	1.0
f_2	$1-0.3e^{-Re_t^2}$ $Re_t=\frac{k^2}{\nu\epsilon}$	1.0
L_k	$-2\mu\left(\frac{\partial\sqrt{k}}{\partial x_j}\right)^2$	0
L_ϵ	$-2\frac{\mu\mu_t}{\rho}\left(\frac{\partial^2 u_i}{\partial x_j^2}\right)^2$	$-\frac{\mu\mu_t}{\rho}\left(\frac{\partial^2 u_i}{\partial x_j^2}\right)^2$

The other coefficients appearing in the f_μ term of the $k-\varepsilon$ Yang-Shih are:

Table 2.2: Coefficients of the $\boldsymbol{k-\varepsilon}$ Yang-Shih model

x	$\frac{k^{0.5}y}{\nu}$
A	1.5×10^{-4}
a	1
B	5.0×10^{-7}
b	3
C	1.0×10^{-10}
c	5
d	0.5

2.4.3 Shear Stress Transport (SST) $k-\omega$ Model

The $k-\omega$ turbulence model is again a two equation model. One equation for the kinetic turbulent energy k while the second equation is for the specific turbulent dissipation rate ω. Similar to $k-\epsilon$, the $k-\omega$ model has many versions. One of the most known one is the Wilcox $k-\omega$ model [90, 91]. The Wilcox model has shown superior numerical stability to the $k-\varepsilon$ model especially in the viscous sublayer near the wall. However, the big disadvantage of the Wilcox model is that its results are extremely sensitive to the free stream value of ω in free shear layer and adverse pressure gradient boundary layer flows. Therefore, the $k-\omega$ does not seem to be an ideal model for applications in the wake region of the boundary layer. On the other hand, the $k-\varepsilon$ model behaves better in the outer portion and wake regions of the boundary layer. So a combination or blending of both of the models including the best feature of each one has been sought for. One of the results was the Shear Stress Transport (SST) $k-\omega$ model.

The two transport equations of the SST model are defined below:

$$\rho \frac{Dk}{dt} = \frac{\partial}{\partial x_j}\left[(\mu + \sigma_k \mu_t)\frac{\partial k}{\partial x_j}\right] + P_k - \beta^* \rho \omega k \tag{2.59}$$

$$\rho \frac{D\omega}{dt} = \frac{\partial}{\partial x_j}\left[(\mu + \sigma_\omega \mu_t)\frac{\partial \omega}{\partial x_j}\right] + \gamma P_k \frac{\omega}{k} - \beta \rho \omega^2 + 2(1-F_1)\rho \sigma_{\omega 2}\frac{1}{\omega}\frac{\partial k}{\partial x_j}\frac{\partial \omega}{\partial x_j} \tag{2.60}$$

where the constant $\beta^* = 0.09$. The last term on the right hand side of Eq. (2.60) is a cross diffusion term that is activated only outside the boundary layer.

F_1 is the blending function which is designed to blend the model coefficients of the original $k-\omega$ model in the boundary layer zones with the transformed $k-\epsilon$ model in free shear layer and free stream zones.

The constants appearing in Equations (2.59) and (2.60) are expressed in a ageneral compact form as:

$$\phi = F_1\phi_1 - (1-F_1)\phi_2 \tag{2.61}$$

where ϕ_1 represents the constants associated with the $k-\omega$ model (when $F_1 = 1$), and ϕ_2 represents the constants associated with the $k-\epsilon$ model (when $F_1 = 0$).

Now, γ, β, σ_k and σ_ω defined by blending the coefficients as:

- Inner model constants: $\gamma_1 = 0.5532,\ \ \beta_1 = 0.075,\ \ \sigma_{k1} = 0.5,\ \ \sigma_{\omega 1} = 0.5$
- Outer model constants: $\gamma_2 = 0.4403,\ \ \beta_2 = 0.0828,\ \ \sigma_{k2} = 1.0,\ \ \sigma_{\omega 2} = 0.856$

The blending function F_1 is defined by:

$$F_1 = \tanh\left\{min\left[max\left(\left(\frac{\sqrt{k}}{\beta^* \omega d}, \frac{500\nu}{\omega d^2}\right), \frac{4\rho\sigma_{\omega 2} k}{CD_{k\omega} d^2}\right)\right]\right\} \tag{2.62}$$

with,

$$CD_{k\omega} = max\left(2\rho\sigma_{\omega 2}\frac{1}{\omega}\frac{\partial k}{\partial x_j}\frac{\partial \omega}{\partial x_j}, 1.0e^{-20}\right) \tag{2.63}$$

and d being the distance to the nearest surface.

2.4.4 $\overline{\upsilon^2} - f$ Model

The $\upsilon^2 - f$ model is a nonlinear turbulent viscosity model. Here the turbulent stress normal to the streamlines is used instead of the turbulent kinetic energy in the definition of the turbulent viscosity. Therefore, unlike the low Reynolds number $k - \epsilon$ models, this model does not require any damping function. υ^2 represents the turbulence stress normal to streamlines and f is a redistribution function.

The model used in the thesis is derived from the one described in Ref. [92]. It is based on high Reynolds number $k - \epsilon$ model with two additional equations for the turbulent stress normal to streamlines and the redistribution function.

$$\rho\frac{Dk}{Dt} = \frac{\partial}{\partial x_j}\left[\left(\mu + \frac{\mu_t}{\sigma_k}\right)\frac{\partial k}{\partial x_j}\right] + P_k \tag{2.64}$$

$$\rho\frac{D\epsilon}{Dt} = \frac{\partial}{\partial x_j}\left[\left(\mu + \frac{\mu_t}{\sigma_\epsilon}\right)\frac{\partial \epsilon}{\partial x_j}\right] + \frac{\rho c_{\epsilon 1} P_k - \rho c_{\epsilon 2}\epsilon}{T} \tag{2.65}$$

$$\rho\frac{D\upsilon^2}{Dt} = \frac{\partial}{\partial x_j}\left[\left(\mu + \frac{\mu_t}{\sigma_\epsilon}\right)\frac{\partial \upsilon^2}{\partial x_j}\right] + kf\rho - 6\rho\upsilon^2\frac{\epsilon}{k} \tag{2.66}$$

$$L\nabla^2 f - f = \frac{(C_1 - 1)}{T} + \left[\frac{\upsilon^2}{k} - \frac{2}{3}\right] - C_2\frac{P_k}{k} - \frac{5}{T}\frac{\upsilon^2}{k} \tag{2.67}$$

The turbulent viscosity is computed as:

$$\mu_t = \rho c_\mu v^2 T \tag{2.68}$$

where the turbulent time scale T and length scale L are defined by:

$$T = min\left\{max\left[\left(\frac{k}{\epsilon}, 6\sqrt{\frac{v}{\epsilon}}\right), \frac{0.6k}{\sqrt{6}C_\mu v^2 S}\right]\right\} \tag{2.69}$$

$$L = C_L max\left\{min\left[\left(\frac{k^{3/2}}{\epsilon}, \frac{k^{3/2}}{\sqrt{6}C_\mu v^2 S}\right), C_\eta \frac{v^{3/4}}{\epsilon^{3/4}}\right]\right\} \tag{2.70}$$

where S is the magnitude of strain rate. The parameters appearing in the equations above are: $C_\mu = 0.22,\ \sigma_k = 1.0, \sigma_\epsilon = 1.3,\ C_{\epsilon 1} = 1.4\left[1 + 0.05\left(\sqrt{\frac{k}{v^2}}\right)\right]$,

$C_{\epsilon 2} = 1.9,\ C_1 = 1.4,\ C_2 = 0.3,\ C_L = 0.23,\ C_\eta = 70$

2.5 Abu-Ghannam and Shaw Transition Model

The laminar layer developed at the surface of a solid body starts as laminar and then becomes turbulent over a relatively short distance called transition region. A factor called intermittency is used to differentiate between the laminar and transition regions. The intermittency is defined as the fraction of time during which the flow over any point on a solid surface is turbulent. It should be zero in the laminar boundary layer region and one in the turbulent boundary layer region.

The location of transition could be computed from the flow solution by using empirical relations related to external parameters. In this study, the relations obtained by Abu-Ghannam and Shaw [93] are used. These relations are derived from experimental data from transition on a flat plate with pressure gradients.

According to this model, the transition starts at a momentum thickness Reynolds number defined as:

$$R_{\theta s} = 163 + \exp\left(F(\lambda_\theta) - \frac{F(\lambda_\theta)}{6.91}\tau\right) \tag{2.71}$$

Where, λ_θ is a dimensionless pressure gradient defined as:

$$\lambda_\theta = \frac{\theta^2}{\nu}\frac{dU_e}{ds} \tag{2.72}$$

Where;

- U_e : the velocity at the edge of the boundary layer
- s : the streamwise distance from the leading edge
- θ : the momentum thickness in the laminar region
- τ : the free stream turbulence level in percentage.

The function $F(\lambda_\theta)$ depends on the sign of pressure gradient:

$$F(\lambda_\theta) = 6.91 + 12.75\,\lambda_\theta + 63.64\,(\lambda_\theta)^2\ ,\quad (\lambda_\theta < 0) \tag{2.73}$$

$$F(\lambda_\theta) = 6.91 + 2.48\,\lambda_\theta - 12.27\,(\lambda_\theta)^2,\quad (\lambda_\theta > 0) \tag{2.74}$$

So Eq.(2.73) is for the adverse pressure gradient wher Eq.(2.74) is for the favorable pressure gradient.

According to relations (2.73) and (2.74), the transition is promoted in adverse pressure gradient where it is retarded in favorable pressure gradient.

2.6 Preconditioning For Low Mach Number Flows

At low Mach number values, the time marching algorithms designed for compressible flows show lack of efficiency. Two main problems are faced by the compressible flow codes at low Mach number. First, the difference in values between the convective eigenvalues (u) and the acoustic eigenvalues ($u + c$ and $u - c$) leading to a much restrictive time step for the convective waves which causes poor convergence characteristics. The second problem is round off errors mostly due to the use of the absolute pressure in the momentum equations.

This enhances the development of a low speed preconditioner in order to achieve fast convergence and more accurate solutions when the Mach number is very low. For steady state applications solved by time marching algorithm, the time derivatives of the dependent variables are multiplied by a matrix called preconditioning matrix. The aim of this matrix is to remove the stiffness of the eigenvalues, and to introduce the reduced flow variables (such as dynamic pressure and dynamic enthalpy), hence reducing the round off errors at low Mach numbers. The idea is to replace the acoustic wave speed c by a pseudo wave speed c' which is of the same order of magnitude as the fluid speed.

Two preconditioning models will be introduced here; the Hakimi preconditioning [94, 95] and the Merkle preconditioning [95, 96] and depending on the accuracy of the solution, one of them will be used for the rest of the work.

2.6.1 Hakimi Preconditioning

The Hakimi preconditioner has proved to give efficient convergence rates and accurate solutions for Mach numbers between 10^{-6} to 0.1 and Reynolds numbers from 10^{-6} to 10^{6} and aspect ratios from 1 to 2000 [95].

The preconditioned RANS equations can be written as:

$$\int_V \Gamma^{-1}\frac{\partial U}{\partial t}\, dV + \oint_S (\mathbf{F}\cdot\mathbf{n})\, dS - \oint_S (\mathbf{F_v}\cdot\mathbf{n})\, dS = \int_V s_T\, dV \tag{2.75}$$

with,

$$U = \begin{Bmatrix} p_g \\ u_1 \\ u_2 \\ u_3 \\ E_g \\ \rho k \\ \rho\epsilon \end{Bmatrix} \tag{2.76}$$

where p_g is the gauge pressure defined as:

$$p_g = p - p_{ref} \tag{2.77}$$

For perfect gas, the total gauge energy E_g is defined as:

$$E_g = c_v\left(T - T_{ref}\right) + \frac{\boldsymbol{u}^2}{2} \tag{2.78}$$

Then, the Hakimi preconditioning matrix for turbulence transport equations for compressible flow is given by:

$$
\Gamma^{-1} = \begin{pmatrix}
\frac{1}{\beta^2} & 0 & 0 & 0 & 0 & 0 & 0 & 0 & \cdots & 0 \\
\frac{(1+\alpha)u_1}{\beta^2} & \rho & 0 & 0 & 0 & 0 & 0 & 0 & \cdots & 0 \\
\frac{(1+\alpha)u_2}{\beta^2} & 0 & \rho & 0 & 0 & 0 & 0 & 0 & \cdots & 0 \\
\frac{(1+\alpha)u_3}{\beta^2} & 0 & 0 & \rho & 0 & 0 & 0 & 0 & \cdots & 0 \\
-\frac{\alpha \mathbf{u}^2 + E_g}{\beta^2} & 0 & 0 & 0 & \rho & 0 & 0 & 0 & \cdots & 0 \\
0 & 0 & 0 & 0 & 0 & \rho & 0 & 0 & \cdots & 0 \\
0 & 0 & 0 & 0 & 0 & 0 & \rho & 0 & \cdots & 0
\end{pmatrix} \tag{2.79}
$$

The preconditioning parameters α and β are defined as:

$$
\alpha = -1, \quad \beta = \sqrt{\beta^*} U_{ref} \tag{2.80}
$$

With U_{ref} is the reference velocity and β^* is a coefficient.

2.6.2 Merkle Preconditioning

Although the Hakimi preconditioner is in general sufficient and can treat any type of fluids at low Mach number, the Merkle preconditioner is used to obtain more robustness scheme that gives accurate solution at all Mach numbers and for all Reynolds numbers.

The Navier-Stokes equations can be written as:

$$
\frac{1}{\partial t} \int_V \partial Q \, dV + \oint_S (\mathbf{F} \cdot \mathbf{n}) \, dS - \oint_S (\mathbf{F_v} \cdot \mathbf{n}) \, dS = \int_V s_T \, dV \tag{2.81}
$$

with Q defined in Eq.(2.2). Now the set of independent variables is changed from the vector conservative variables Q to the vector of viscous primitive variables Q_v. This is done by splitting the unsteady term as:

$$
\int_V \frac{\partial Q}{\partial Q_v} \frac{\partial Q_v}{\partial t} \, dV + \oint_S (\mathbf{F} \cdot \mathbf{n}) \, dS - \oint_S (\mathbf{F_v} \cdot \mathbf{n}) \, dS = \int_V s_T \, dV \tag{2.82}
$$

where,

$$Q_v = \begin{Bmatrix} p \\ u_1 \\ u_2 \\ u_3 \\ T \end{Bmatrix} \tag{2.83}$$

and the Jacobian $\frac{\partial Q}{\partial Q_v}$ is given as:

$$\frac{\partial Q}{\partial Q_v} = \begin{Bmatrix} \rho_p & 0 & 0 & 0 & \rho_T \\ u_1\rho_p & \rho & 0 & 0 & u_1\rho_T \\ u_2\rho_p & 0 & \rho & 0 & u_2\rho_T \\ u_3\rho_p & 0 & 0 & \rho & u_3\rho_T \\ H\rho_p - \left(1 - \rho h_p\right) & \rho u_1 & \rho u_2 & \rho u_3 & H\rho_T + \rho h_T \end{Bmatrix} \tag{2.84}$$

The subscripts p and T denotes for the isothermal derivative with respect to the pressure and temperature respectively.

The Jacobian is replaced by the Merkle preconditioning matrix as:

$$\Gamma_v = \begin{Bmatrix} \rho'_p & 0 & 0 & 0 & \rho'_T \\ u_1\rho'_p & \rho & 0 & 0 & u_1\rho'_T \\ u_2\rho'_p & 0 & \rho & 0 & u_2\rho'_T \\ u_3\rho'_p & 0 & 0 & \rho & u_3\rho'_T \\ H\rho'_p - \left(1 - \rho h'_p\right) & \rho u_1 & \rho u_2 & \rho u_3 & H\rho'_T + \rho h'_T \end{Bmatrix} \tag{2.85}$$

The parameters $\rho'_p, \rho'_T, h'_p,$ and h'_T are the ones used to control the scaling for the dynamics of the flow. Since, $\rho'_T, h'_p,$ and h'_T have minor effects on the dynamics of the Navier-Stokes equations, the Fine/Turbo solver sets those parameters to their physical values. Hence, only the parameter ρ'_p remains in order to control the preconditioning. This parameter is expressed as:

$$\rho'_p = \frac{1}{v_p^2} - \frac{\rho_T(1 - \rho h_p)}{\rho h_p} \tag{2.86}$$

where v_p is the particle velocity calculated inside the solver.

2.7 Boundary Conditions

Two types of boundary conditions are available for the CFD simulation of wind turbine rotor blade; the solid wall boundary conditions (on the blade) and the external boundary conditions.

2.7.1 Solid Wall Boundary Conditions

The turbulent wall boundary conditions are treated as follow:

a) *Spalart-Allmaras Model:*
For the Spalart-Allmaras turbulence model, the turbulent working variable is set to zero in the solid wall:

$$\tilde{\nu} = 0 \tag{2.87}$$

b) $k - \epsilon$ *Model:*
For the $k - \epsilon$ model, the values for k and ϵ are imposed at the solid wall.

c) $k - \omega$ M*odel:*
For the $k - \omega$ model, the boundary condition on the solid wall is as follow:

$$\omega_{wall} = \frac{60\nu}{\beta_1 d^2} \tag{2.88}$$

$$k_{wall} = 0 \tag{2.89}$$

d) $\upsilon^2 - f$ *Model:*
For the $\upsilon^2 - f$ model, the boundary condition on the solid wall is as follow:

$$k_{wall} = 0 \tag{2.90}$$

$$\epsilon_{wall} = 2\nu \frac{k}{y^2} \tag{2.91}$$

$$\upsilon^2{}_{wall} = 0 \tag{2.92}$$

$$f_{wall} = 0 \tag{2.93}$$

2.7.2 External Boundary Conditions

External boundary conditions use the Riemann invariants (non-reflective boundary conditions). Detailed information about Riemann invariants are found in Ref. [97]. The boundary conditions at the far field are uniform because the velocities at the far field are not affected by the rotation of the blades. Only in blocks close to the blade, the flow is affected by the rotation. The interaction between the rotating and non-rotating blocks, is handled by the code.

The values for the static pressure, temperature and axial velocity needed to define the external boundary conditions are obtained from the experimental data. Whereas, the turbulent viscosity ν_t, the turbulent kinetic energy k and the turbulent dissipation rate ϵ are calculated as follow:

The dynamic viscosity is calculated from the Sutherland's law [98]:

$$\mu = \mu_{ref}\left(\frac{T}{T_{ref}}\right)^{3/2}\frac{T_{ref}+S}{T+S} \tag{2.94}$$

where:

- T_{ref}: Reference temperature
- μ_{ref}: Viscosity at T_{ref}.
- S: Sutherland temperature

For air as a perfect gas, the Sutherland's law coefficients are given in the table below:

Table 2.3: Sutherland's law Coefficient

Gas	$\mu_{ref}\ (kg/ms)$	$T_{ref}\ (K)$	$S\ (K)$
Air	1.716×10^{-5}	273.15	110.4

Then the kinematic viscosity is calculated from Eq.(2.95) as:

$$\nu = \mu/\rho \tag{2.95}$$

Finally, for external flows the turbulent viscosity is calculated from [65]:

$$\nu_{T\ external} = \nu_{external} \tag{2.96}$$

The turbulent kinetic energy k is calculated from the turbulent intensity T_u as follow:

$$T_u = \frac{\sqrt{\overline{\grave{u}^2}}}{U_{ref}} \tag{2.97}$$

For external flow, the turbulent intensity is reduced to 1 % [80], then:

$$k = \frac{3}{2}\left(\sqrt{\overline{\grave{u}^2}}\right)^2 \tag{2.98}$$

Using the value for k, the turbulent dissipation is calculated as:

$$\varepsilon = C_\mu \frac{\mu}{\mu_t} \frac{\rho_{ref} k^2}{\mu} \tag{2.99}$$

with $C_\mu = 0.09$.

CHAPTER 3

CFD SIMULATIONS OF TEST CASES: NRET PHASE II AND PHASE VI HAWT ROTORS

In this chapter, the results of the three-dimensional steady state Computational Fluid Dynamics (CFD) simulations of two test cases are presented. The test cases are obtained from the National Renewable Energy Laboratory (NREL). The test cases are the NREL Phase II and NREL Phase VI horizontal axis wind turbine (HAWT) rotors. Those test cases are used as a validation for the commercial CFD software Numeca Fine/Turbo solver. In addition to that, five different turbulence models are tested and the results of each model are compared with the available experimental data. This is important to choose the best turbulence model of closest solution to the experimental data which will be used throughout the rest of the thesis. The turbulence models tested are: Spalart-Allmaras, the $k-\varepsilon$ Launder – Sharma, the $k-\varepsilon$ Yang-Shih, Shear Stress Transport (SST) $k-\omega$ and $\overline{\upsilon^2}-f$. More information about those models is available in Section (2.3). Also the Spalart-Allmaras with Abu-Ghannam and Shaw transition model has been investigated for NREL II test case.

3.1 Test Case I: NREL Phase II

3.1.1 Experimental Data and Real Blade Description

The experimental data for NREL Phase II is obtained from the IEA Annex XIV database [99]. This database was built as a contribution of many European research labs and the NREL to store and document the experimental data for various tested wind turbines and make it available to researchers.

The wind turbine is a downwind three-bladed HAWT and the blades are untapered and untwisted. The S809 airfoil is used throughout the span of the blades. The S809 airfoil is a 21% thick laminar flow airfoil designed for HAWT purposes [100]. Throughout the blade span, the airfoil is pitched down by 12 degrees. The geometry and pitching of the airfoil are shown in Figure (3.1) below [101]:

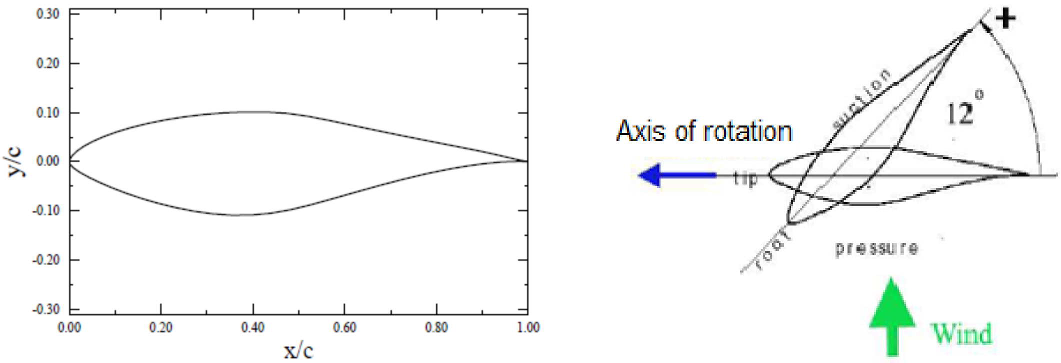

Figure 3.1: Geometry of S809 Airfoil and pitch angle

The blade description is given in the Table (3.1):

Table 3.1: NREL Phase II blade description

Number of blades	3
Rotor diameter	10.06 m
RPM	72 RPM
Cone angle	3 degrees 25’
Rotor location	Downwind
Power regulation	Stall regulated
Root extension	0.723 m
Pitch angle	12 degrees (down)
Blade profile	S809
Blade chord length	0.4572 m, constant along the span
Twist angle	0 degrees along the span
Blade thickness	At 14.4% span, t/c = 43% At 30% span, t/c = 21% Outward 30%span, t/c = 21%

The measurement of the static pressure is the most important yet most difficult task. The quality of the aerodynamic performance coefficients depends on the accuracy of the individual pressure tap measurements.

In the experiment, 28 pressure taps were installed at 4 primary spanwise sections: 30%, 47%, 63%, and 80% span. Pairs of taps at 4% chord and 36% chord were installed at different other intermediate span locations.

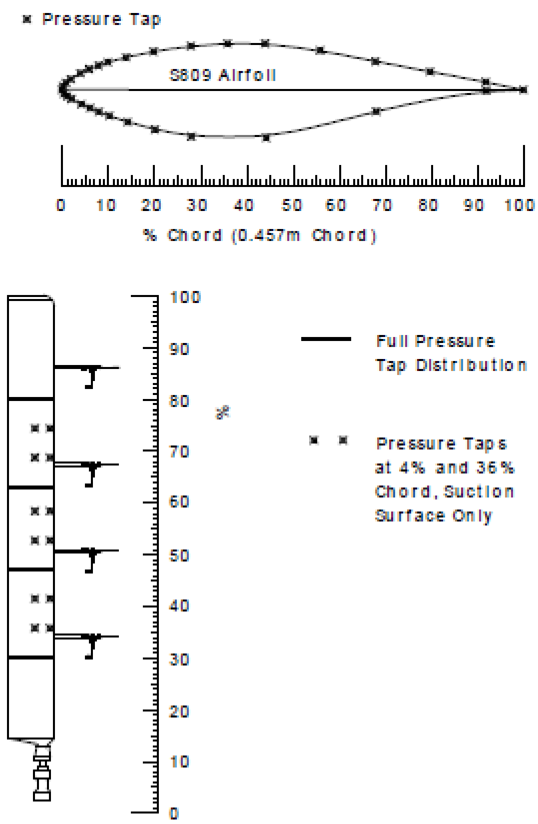

Figure 3.2: Pressure taps and probes locations of NREL II [54]

Five hole-probes were installed at 34%, 51%, 67% and 84% span to measure the static pressure and the local effective angle of attack. The pressure taps and probes locations are shown in Figure (3.2). More information about the database and the experimental setup are available in Ref. [54, 55].

3.1.2 Geometric Blade

The difference between the real blade and geometric blade is only in the trailing edge region. The real blade is of very sharp trailing edge. Meshing sharp edges is difficult and results in poor mesh quality. To overcome this problem, the trailing edge was rounded through a radius of 0.001 m. This improved the mesh quality and made it more robust.

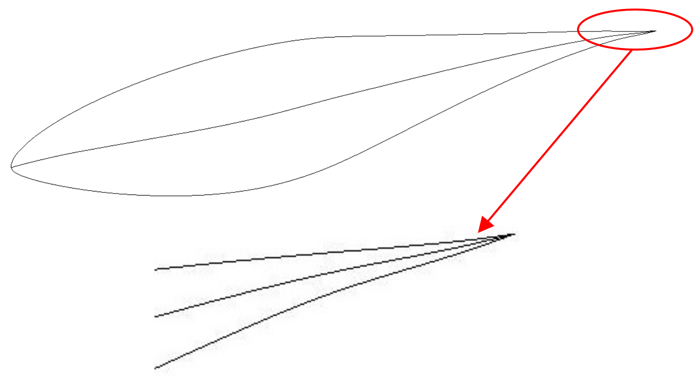

Sharp Trailing edge of the real blade section

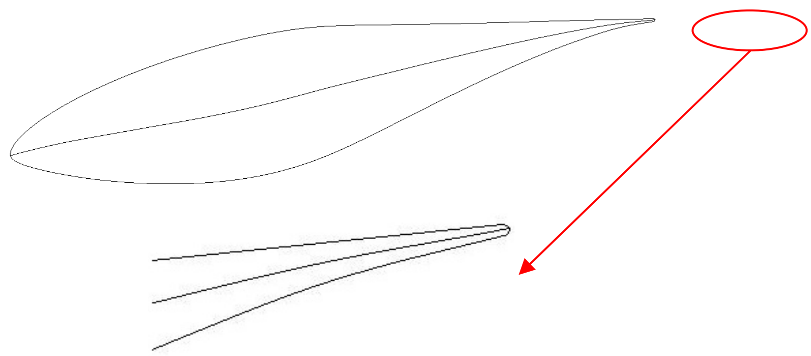

Rounded Trailing Edge of the geometric blade section

Figure 3.3: Trailing edge shape

It is believed that, such a change in the trailing edge will not have important effect on the results. Because the results are compared with experimental data. And in experiments, it is not possible to manufacture a blade of very sharp trailing edge.

The geometric blade consists of 4 sections as shown in Figure (3.4);

- Section 1: at the root of the blade
- Section 2: at 30% span where the thickness is reduced to 21%
- Section 3: at midspan
- Section 4: at the tip

It should be noted that, between section 1 and section 2, the blade thickness decreases linearly from 43% to 21%. The blade was generated using the Numeca blade generator AutoBlade.

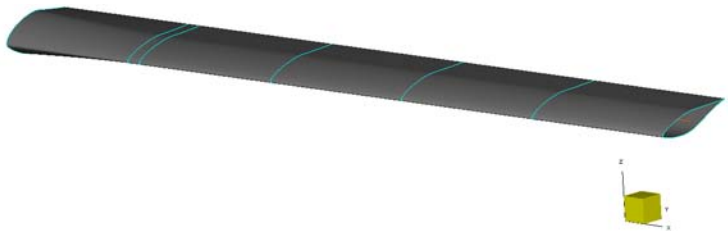

Figure 3.4: 3D NREL II blade geometry generated by AutoBlade

3.1.3 Mesh Study

The structured mesh was generated using the Numeca AutoGrid mesh generator. The mesh was generated for a single blade with imposing the periodic condition to account for the other two blades. The number of points on the entire mesh including the blade and external flow is about 2.7 million points and the number of points on one blade is 1.63 million points. The thickness of the first cell to the wall was kept at $2 \times 10^{-5} m$ so that the y^+ value falls between 1 and 9. Such range of y^+ is suitable for the tested turbulence models. The mesh quality is listed in Table (3.2) below:

Table 3.2: Mesh quality of NREL II

Field	Orthogonality (Min., Average)	Aspect Ratio (Max., Average)	Expansion Ratio (Max, Average)
Blade	(33.6, 79.0)	(20406, 545)	(2.2, 1.4)
External	(25.4, 80))	(17522, 539)	(2.5, 1.4))

From the table above, it is shown that the mesh is of high quality and robustness.

The terms mentioned in Table (3.2) are explained as below [102]:

1. *Orthogonality;* It is a measure of the minimum angle between the edges of the element.
2. *Aspect Ratio;* It is defined in Figure (3.5) below:

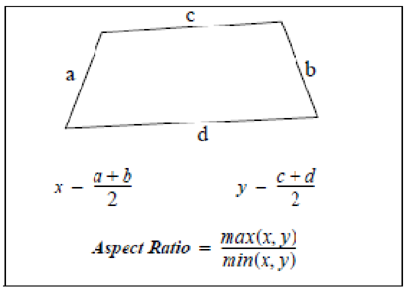

Figure 3.5: Definition of mesh aspect ratio.

3. *Expansion Ratio;* It is a measure of the size variation between two adjacent cells Figure (3.6).

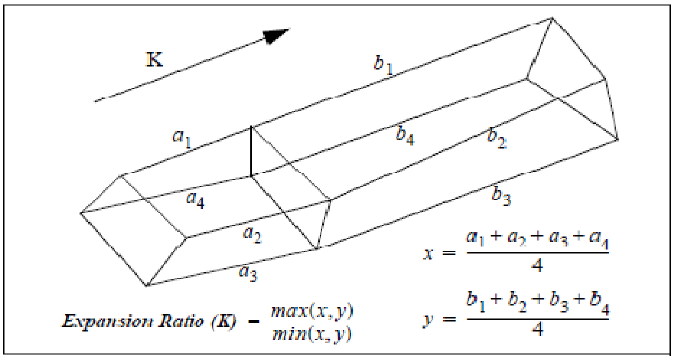

Figure 3.6: Definition of mesh expansion ratio

The 2D mesh at midspan section of the blade is shown in Figure (3.7):

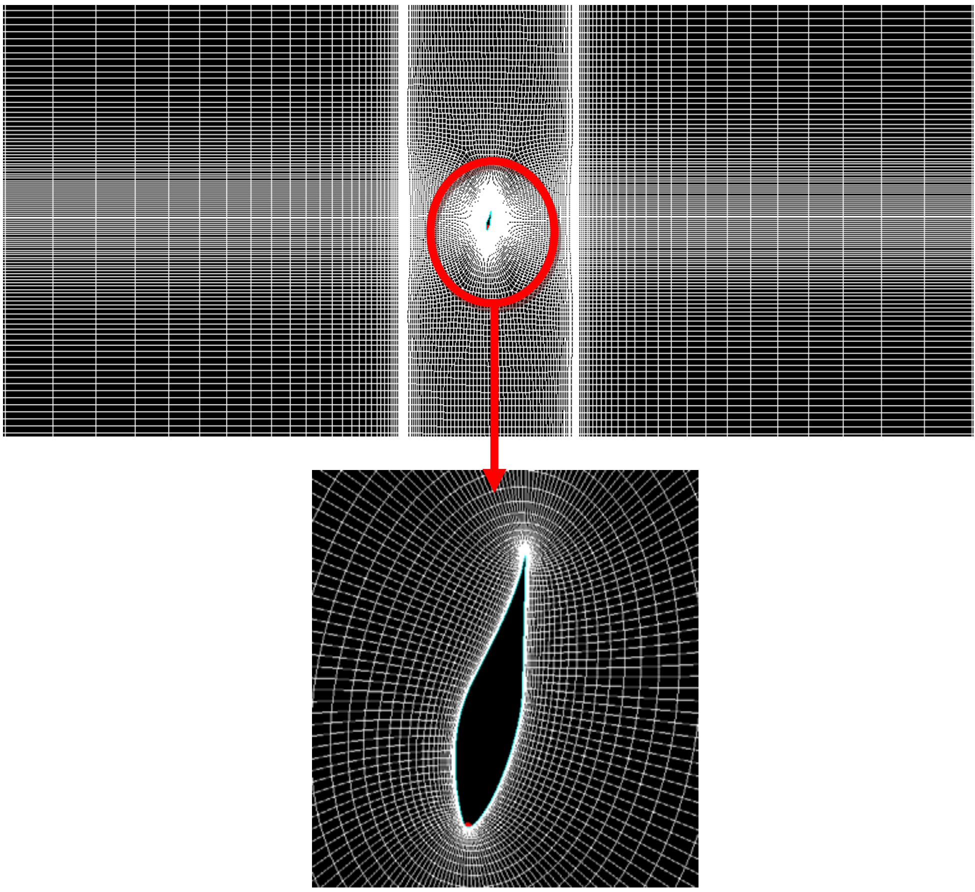

Figure 3.7: 2D mesh at blade midspan of NREL II

The mesh consists of 16 blocks which are all together stand for the mesh of the blade and the external field as shown in Figure (3.8):

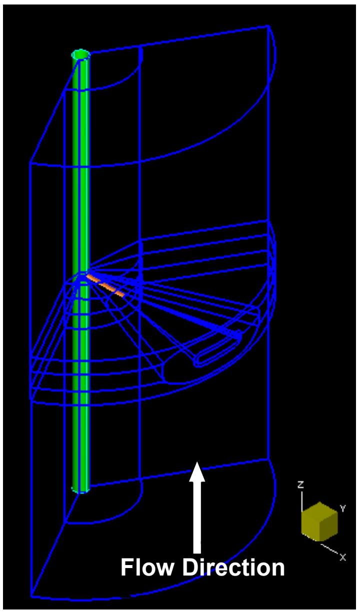

3D Mesh block structure

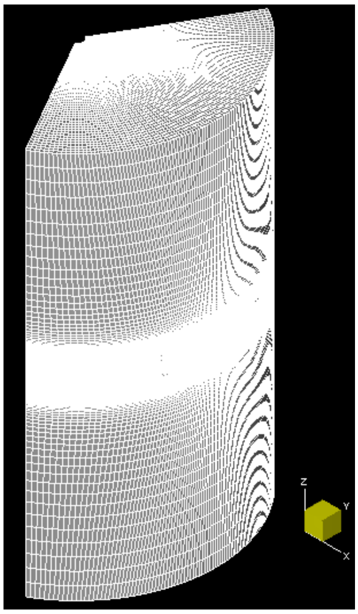

3D Mesh

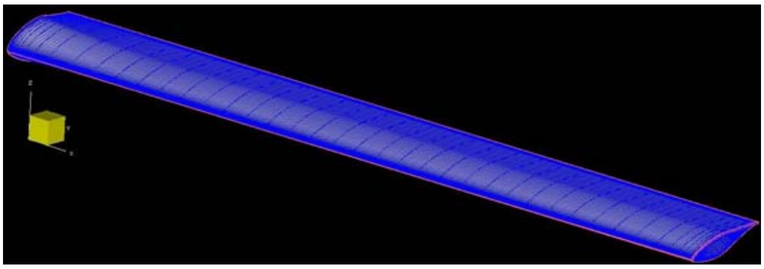

3D Blade mesh

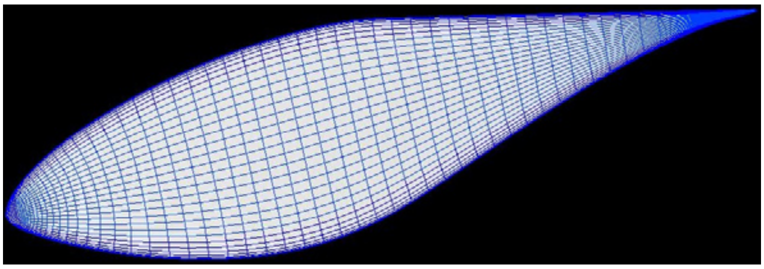

Mesh at the tip

Figure 3.8: 3D mesh for NREL II

3.1.4 Reynolds Number

To check the type of the flow if it is turbulent or laminar, the Reynolds number values have been calculated at the root and tip of the blade. The values are listed in Tables (3.3) and (3.4):

Table 3.3: Reynolds number values at the root for NREL II blade

Wind Speed (m/s)	Reynolds Number
7.2	186435
10.5	268774
12.9	327160
16.3	417522
19.2	489853

Table 3.4: Reynolds number values at the tip for NREL II blade

Wind Speed (m/s)	Reynolds Number
7.2	997105
10.5	1008911
12.9	1019312
16.3	1058294
19.2	1085255

From the results above, the lowest value for Re occurs at the root at 7m/s. This value is 186435 which corresponds to turbulent flow. So the flow at all the considered wind speeds and spanwise sections along the blade is turbulent.

3.1.5 CFD Simulation and Results

The three-dimensional steady state RANS equations are solved using the Fine/Turbo solver of Numeca International. Merkle preconditioner is imposed and 4 different turbulence models are tested. The turbulence models are; Spalart-Allmaras fully turbulent, Sparlat-Allmaras with Abo Ghannam and Shaw transition model , the $k - \varepsilon$ Launder – Sharma, the $k - \varepsilon$ Yang-Shih and $\overline{\upsilon^2} - f$.

The results in terms of power production and pressure distribution are compared with the available experimental data.

First the results of power production are compared with the experimental data. However, in the experimental data, when comparing the rotor torque derived power against the generator power, it is found that the efficiency does not match the published efficiency. To overcome this problem, a better curve fit between the mechanical and generator power is found in Ref. [103] as shown in Eq. (3.1) below:

$$P_{generator} = 0.9036 P_{mechanical} - 0.847 \tag{3.1}$$

The results are obtained at 5 different wind speeds. The comparison between the experimental and computed power for different turbulence models is shown in Figure (3.9):

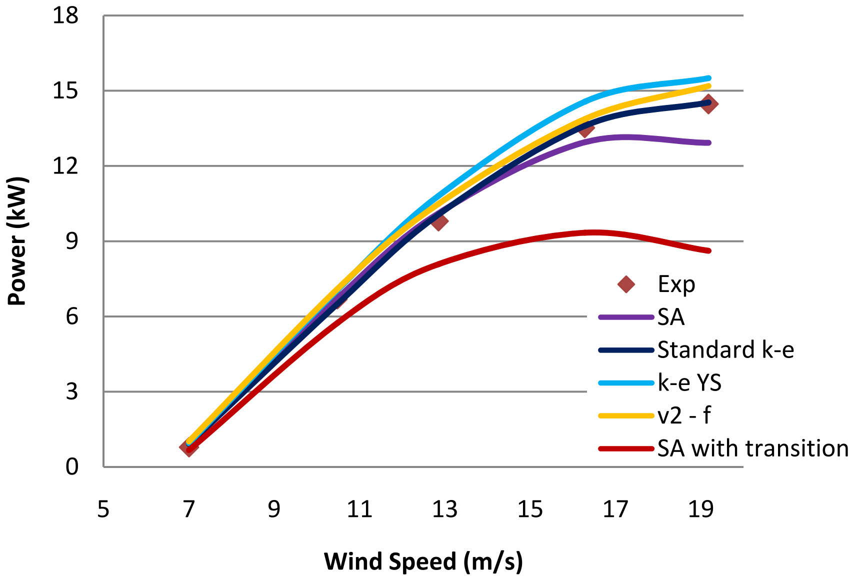

Figure 3.9: Comparison of experimental power with computed power for NREL II

All the turbulence models were found to be stable for the whole wind speed range. They have showed good convergence (more than 4 orders).

From Figure (3.9), in general, all the turbulence models show considerable agreement with the experimental data except for the Spalart-Allmaras with transition. This model shows considerable deviation from experimental results. This model is excluded from further discussions.

At pre-stall wind speeds, all the models have similar behavior in power prediction.

At moderate and stall wind speeds, Spalart-Allmaras and $k - \varepsilon$ Launder – Sharma models could predict the power more accurate. On the other hand, the $k - \varepsilon$ Yang-Shih and $\overline{v^2} - f$ overpredicted the power. Spalart-Allmaras with transition underpredicted the power.

At high wind speeds, Spalart-Allmaras underpredicted the power while $k-\varepsilon$ Yang-Shih and $\overline{v^2}-f$ overpredicted the power. On the other hand, $k-\varepsilon$ Launder – Sharma showed the best agreement with experimental data. Where, Spalart-Allmaras with transition has a poor agreement with experiment.

The power prediction results and the associated errors are listed in Table (3.3):

Table 3.5: Power prediction errors of different turbulence models for NREL II

Speed (m/s)	Exp. data	SA		$k-\varepsilon$ Launder – Sharma		$k-\varepsilon$ Yang-Sheih		V2-f	
	Power (kw)	Power (kW)	Error (%)	Power (kW)	Error (%)	Power (kW)	Error (%)	Power (kW)	Error (%)
7.217	0.79	0.95	20.79	0.92	16.46	0.95	20.79	1.02	29.44
10.48	6.69	6.73	0.51	6.50	2.85	7.05	5.40	7.10	6.11
12.85	9.80	10.11	3.17	10.06	2.68	10.80	10.26	10.49	7.06
16.28	13.52	12.95	4.22	13.60	0.61	14.56	7.71	13.87	2.58
19.18	14.47	12.93	10.65	14.54	0.45	15.50	7.14	15.19	4.97

From the above results, one may conclude that, the closest results to the experimental data were obtained by $k-\varepsilon$ Launder – Sharma turbulence model. This model could capture the correct power at pre-stall, stall and high wind speeds.

The three-dimensional gauge pressure contours on the suction side and pressure side of the blade are shown in Figures (3.10), (3.11) and (3.12) for the $k-\varepsilon$ LS turbulence model at three different wind speeds 7.2, 12.85 and 19.18 m/s.

The gauge pressure is the difference between the static pressure and the free stream pressure defined as:

$$p_{gauge} = p_{static} - p_{\infty} \tag{3.2}$$

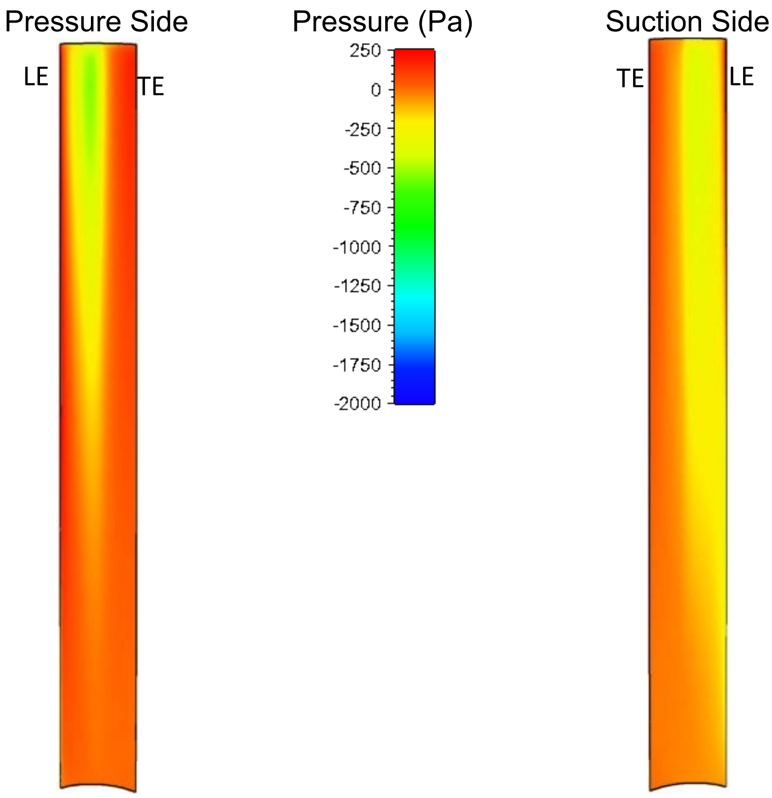

Figure 3.10: Gauge pressure contours for NREL II at 7.2 m/s

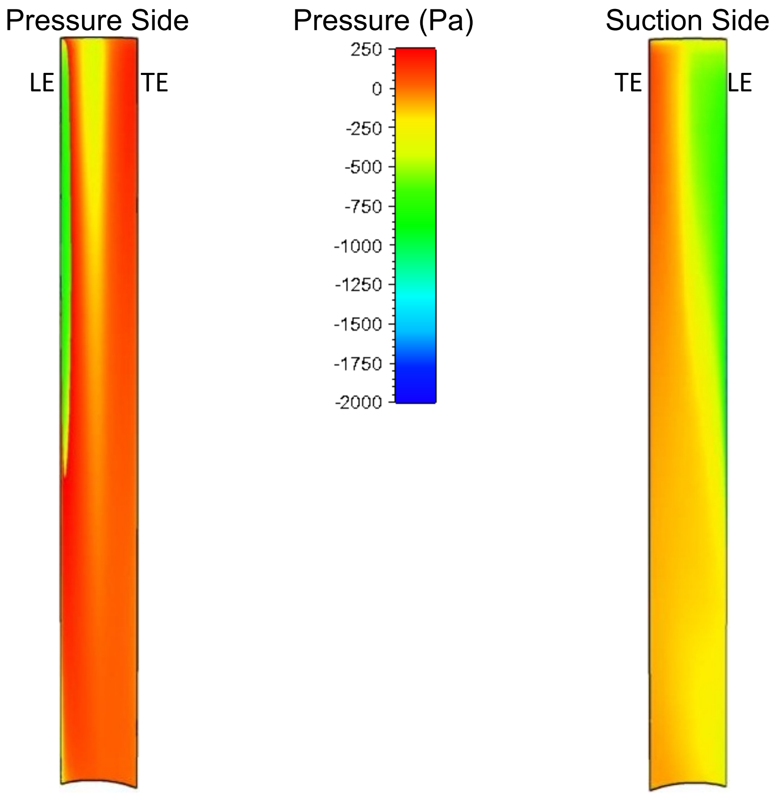

Figure 3.11: Gauge pressure contours for NREL II at 12.85 m/s

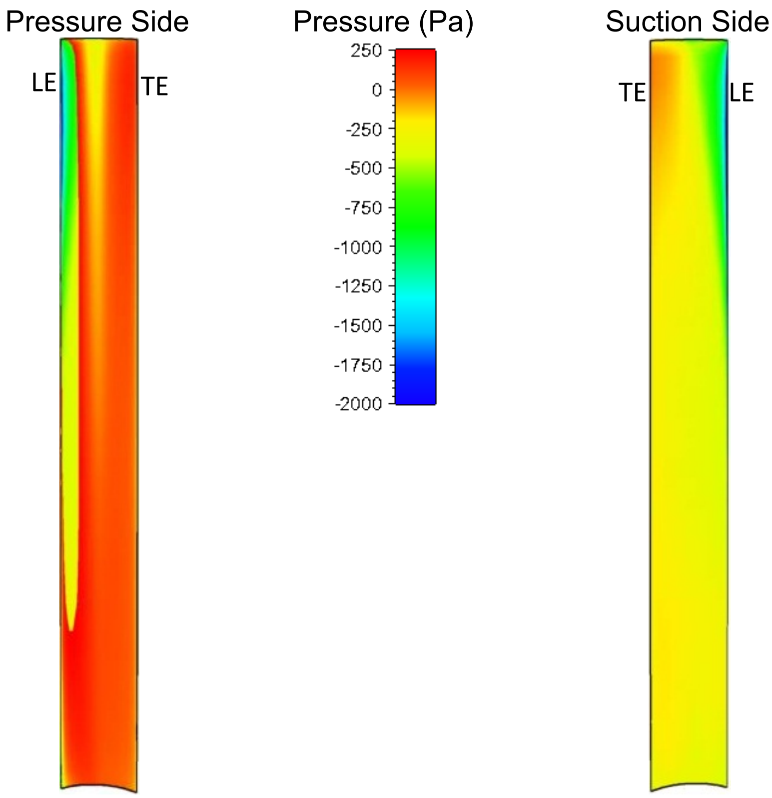

Figure 3.12: Gauge pressure contours for NREL II at 19.18 m/s

The results show considerable pressure variation in both spanwise and chordwise directions. The variation becomes more towards the tip.

The gauge pressure distribution is computed using the $k-\varepsilon$ Launder – Sharma turbulence model at four spanwise sections of the blade, 30%, 47%, 63% and 80%. In fact all other models showed similar behavior as $k-\varepsilon$ Launder – Sharma, but they are not included in the results here not to make the figures so crowded.

The results are obtained at three different wind speeds, 7m/s, 12.85 m/s and 19.18 m/s. Those wind speeds cover the pre-stall, stall and post-stall speeds.

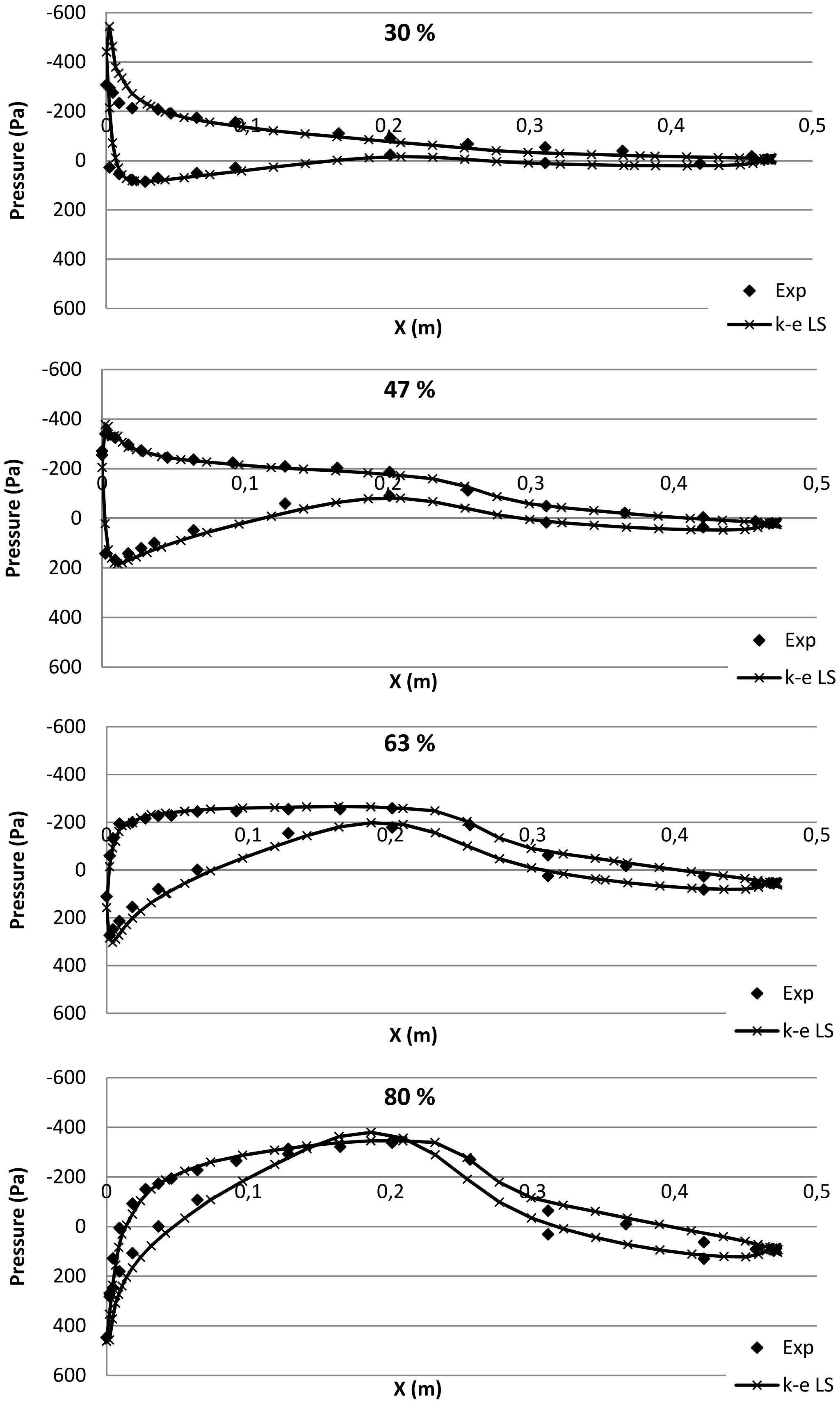

.

Figure 3.13: Pressure distribution comparison between experimental and calculated at different spanwise sections at 7.2 m/s for NREL II

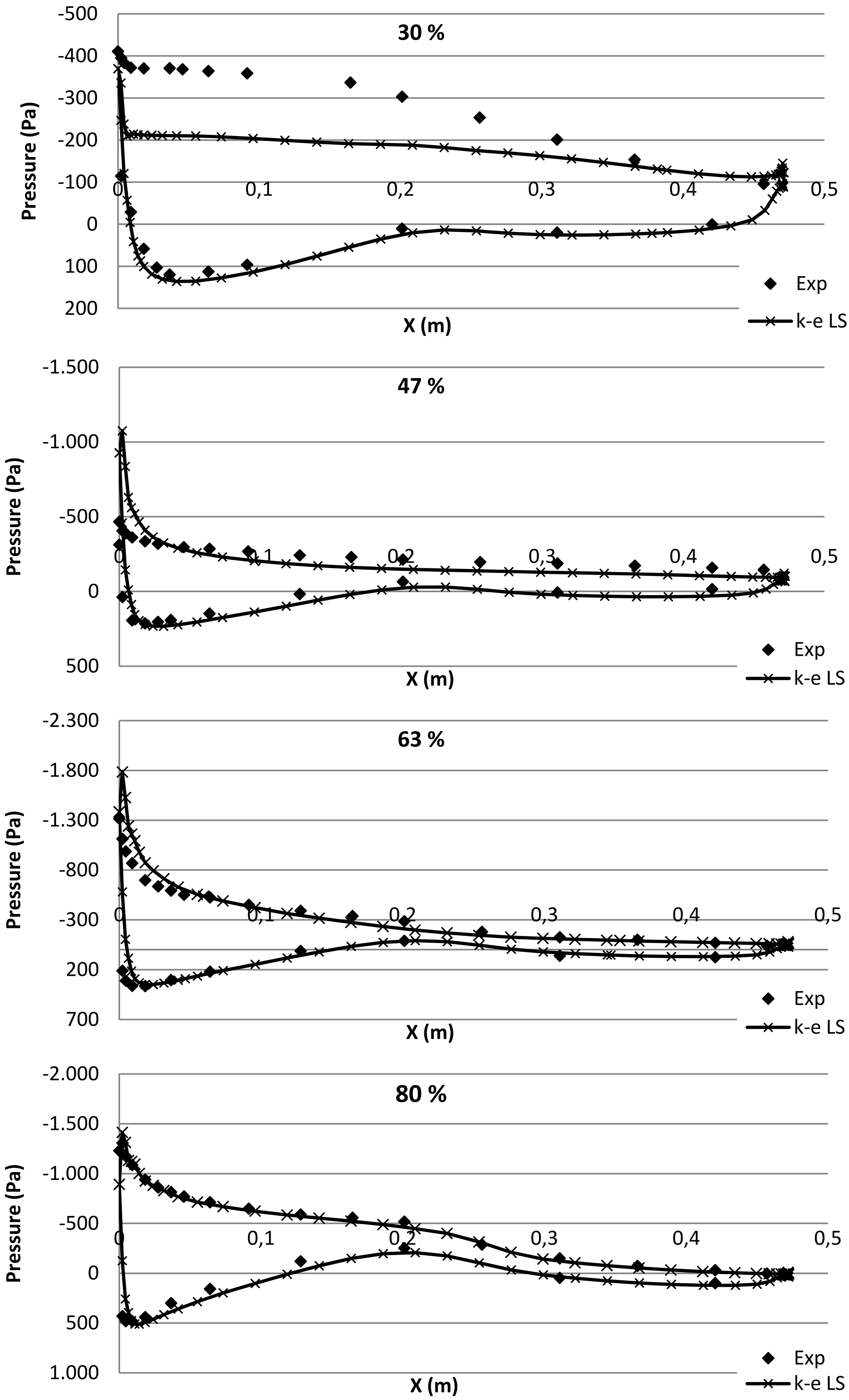

Figure 3.14: Pressure distribution comparison between experimental and calculated at different spanwise sections at 12.85 m/s for NREL II

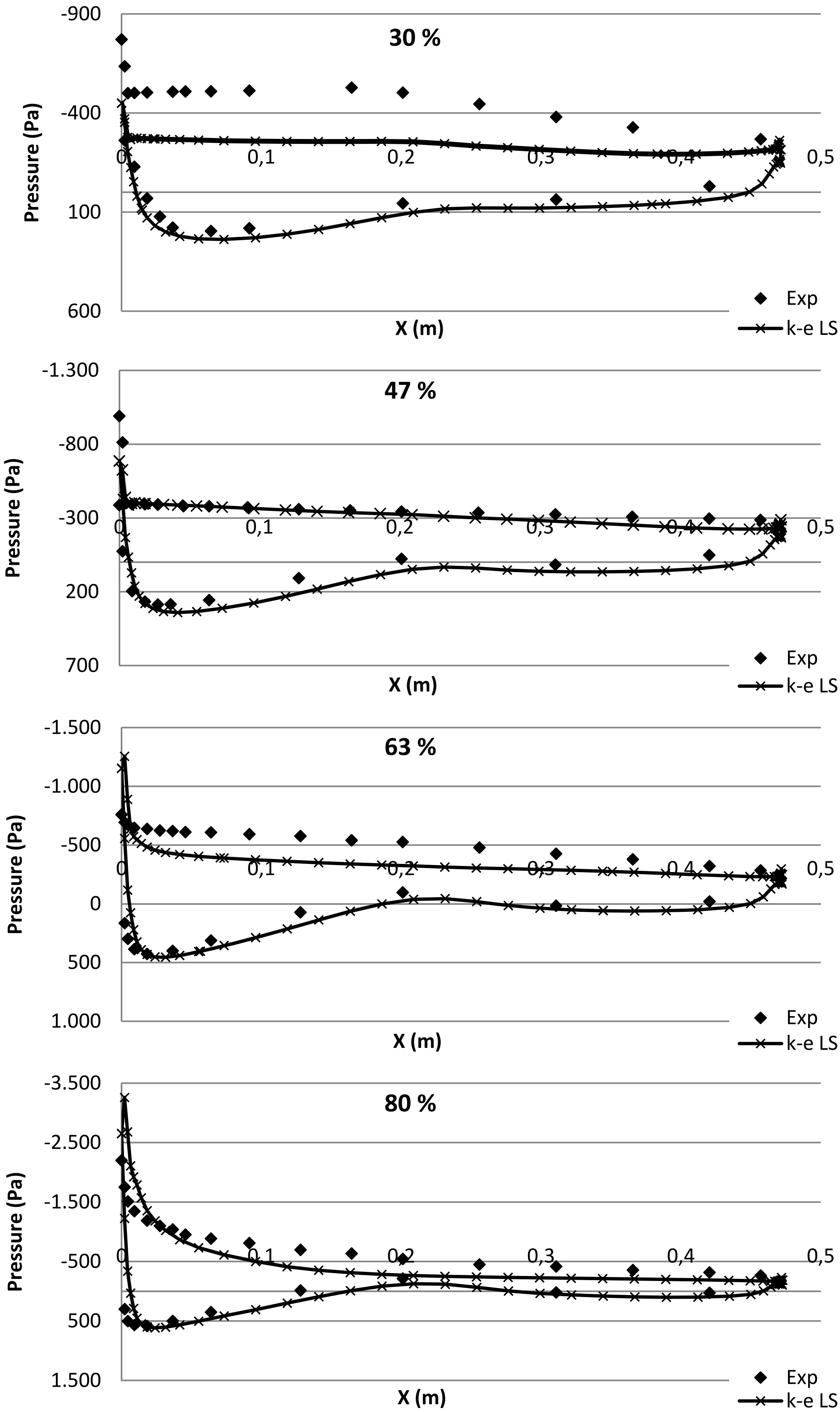

Figure 3.15: Pressure distribution comparison between experimental and calculated at different spanwise sections at 19.18 m/s for NREL II

At 7.2m/s, the computed pressure distribution at all sections of the blade is in good agreement with the experimental data as noticed from Figure (3.13). At this wind speed, the flow is completely attached and no separation occurs.

At 12.85 m/s, there is great discrepancy between the computed and experimental pressure distribution in the suction side of the inboard span of 30%. At this speed separation has occurred and the formed vorticity is stronger close to the root. So it becomes difficult for the solver with low Reynolds turbulence model to capture the separation at the suction side and that is the reason behind such discrepancy. At the other sections, it is seen from Figure (3.14) that the computed results are in good agreement with the experimental data. Same discrepancy was also noticed using different solver in Ref. [43].

At 19.18 m/s, again there is a discrepancy at the sections of 30%, 63% and 80% as shown in Figure (3.15). At this speed, the separation occurs in all the mentioned sections and the formed vorticity is stronger. Capturing the separation characteristics using solvers based on low Reynolds turbulence models is very difficult.

It should be noted that, since the aim of the thesis is to design a wind turbine blade which produces more power at low and moderate wind speeds, one should not care about the discrepancy occurring at high wind speeds.

The separation is investigated by plotting the relative velocity contours with streamlines at different spanwise blade sections. The plots were obtained for wind speeds of 7m/s, 12.85 and 19.18 m/s.

The results obtained for the relative velocity contours with streamlines supports the previous discussion.

At 7m/s, Figure (3.16) shows that no separation occurs and the pressure distribution results were in good agreement with experimental results.

At 12.85 m/s, Figure (3.17) shows that separation with two vorticies occur at 30% section. The vorticies decrease to one vortex at 47% section and then it becomes weaker at 63% section and finally it vanishes at 80%. As mentioned before the discrepancy in pressure distribution also decreases as one goes from root to tip.

At 19.18 m/s, Figure (3.18) shows that separation and formation of vorticies happen at all sections. This explains the deviation of the computed pressure distribution from the experimental results at those sections. However, as one goes towards the tip, the vorticity decreases and the also the pressure deviation decreases as well.

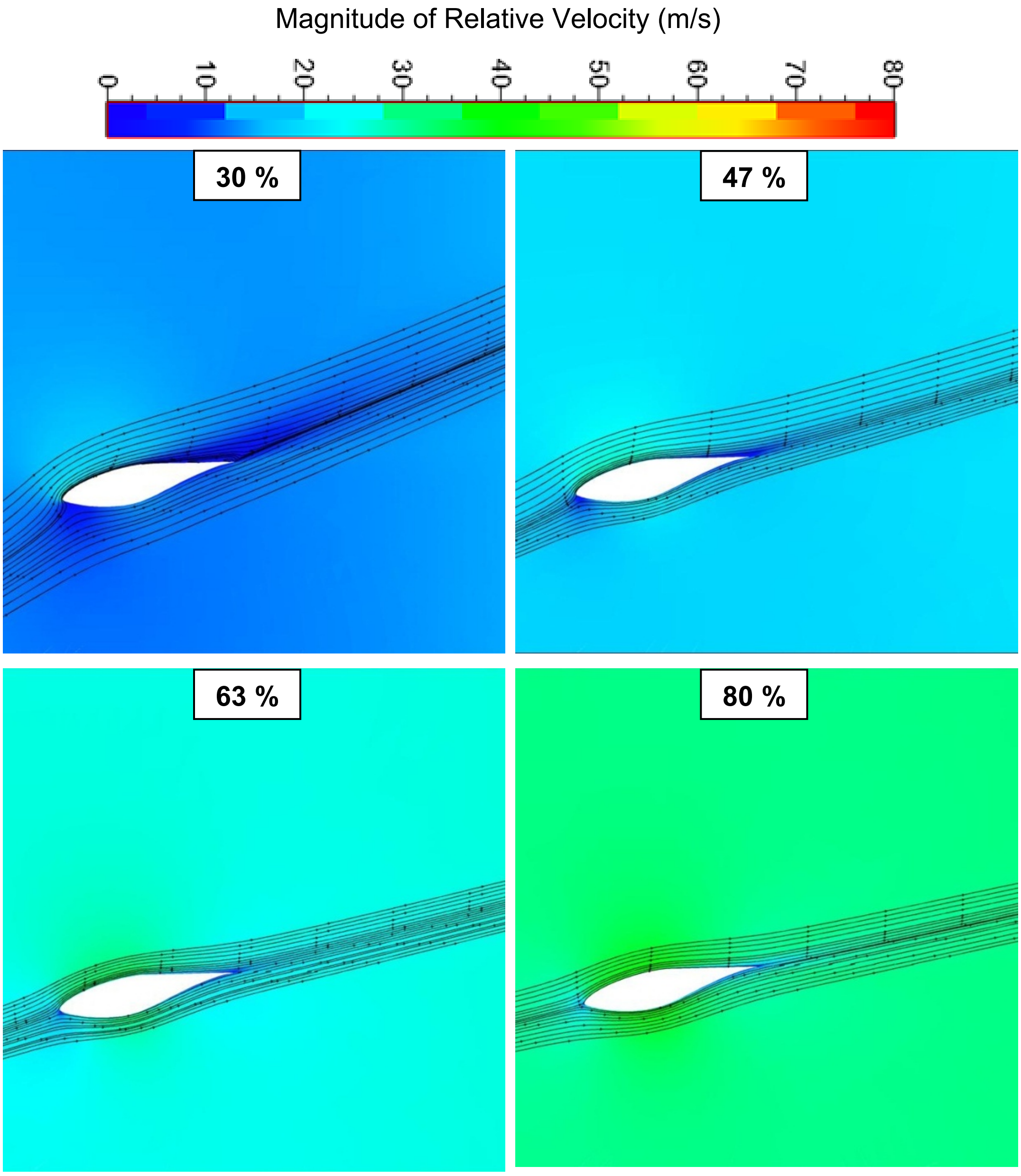

Figure 3.16: Relative velocity contours with streamlines at 7.21m/s on different sections for NREL II

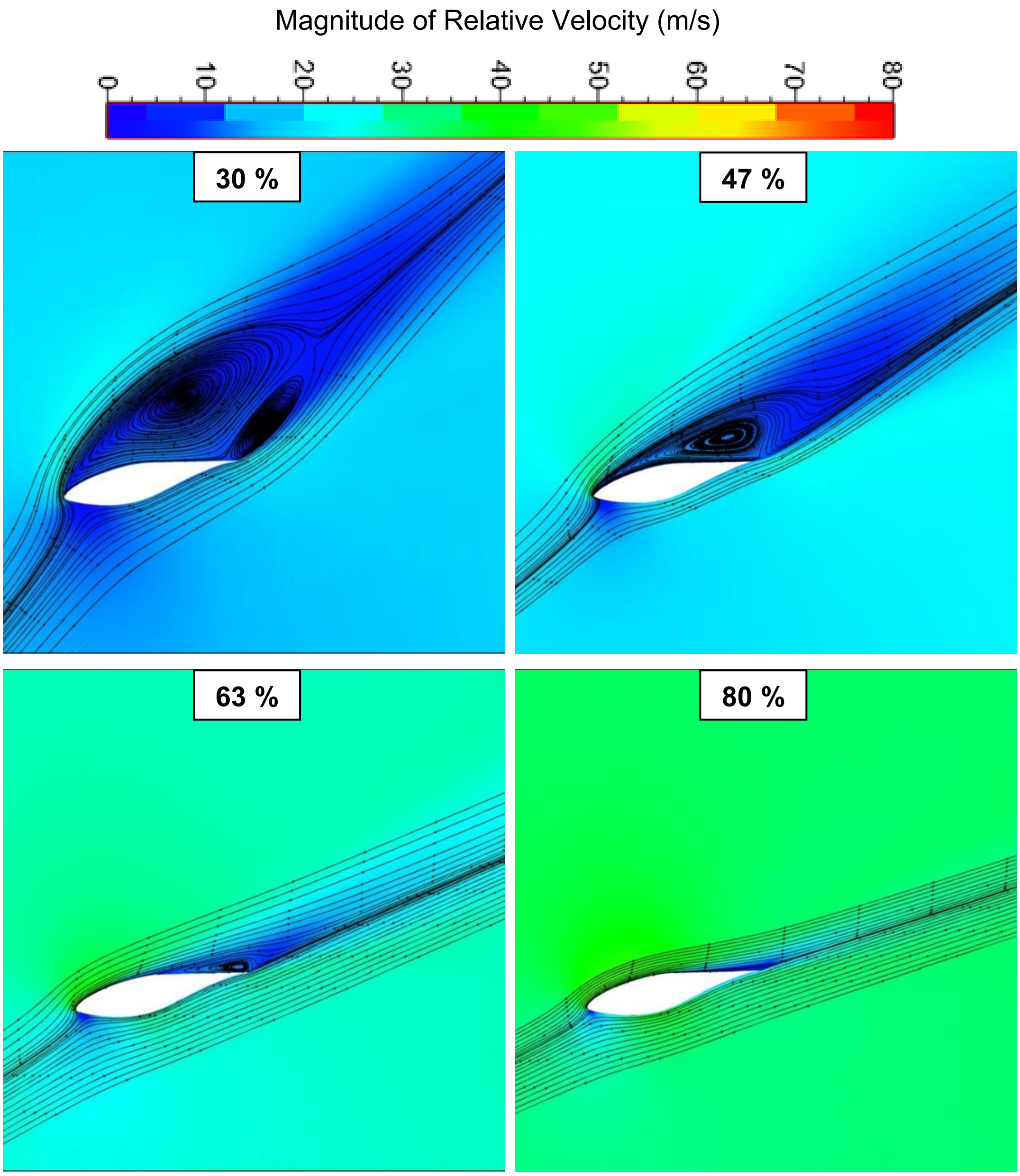

Figure 3.17: Relative velocity contours with streamlines at 12.85 m/s on different sections for NREL II

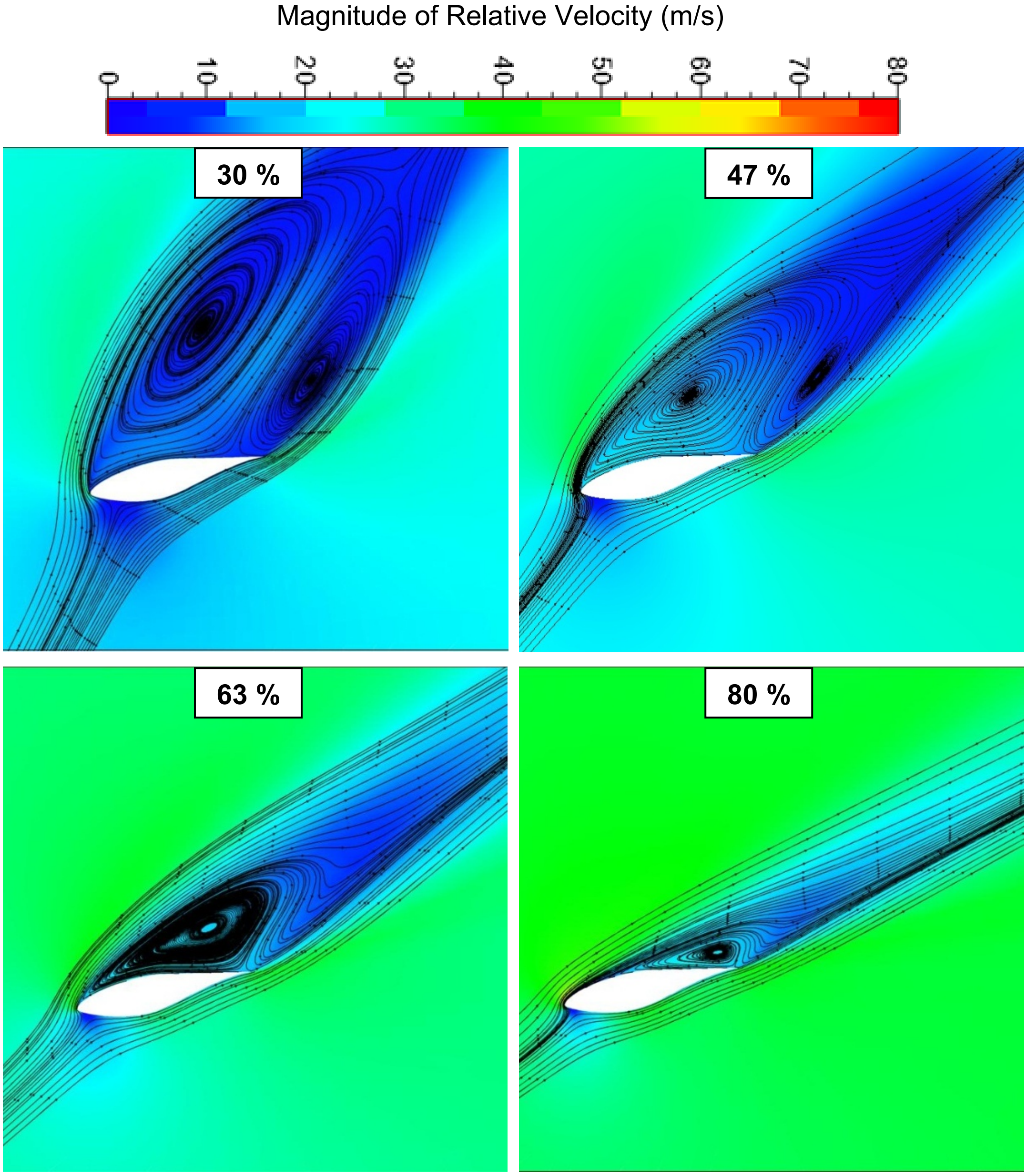

Figure 3.18: Relative velocity contours with streamlines at 19.18 m/s on different sections for NREL II

3.1.6 Results of Preconditioning

So far the Merkle preconditioner has been implemented in the computations due to the low Mach number. To see the effect of Merkle preconditioner on the convergence and accuracy of the solution, the computations without preconditioner are compared to the ones with Merkle preconditioner at two different wind speeds; 12.85 m/s and 19.18 m/s. All the computations are done using Spalart-Allmaras turbulence model.

The history of convergence for the different computations is summarized in the figures below:

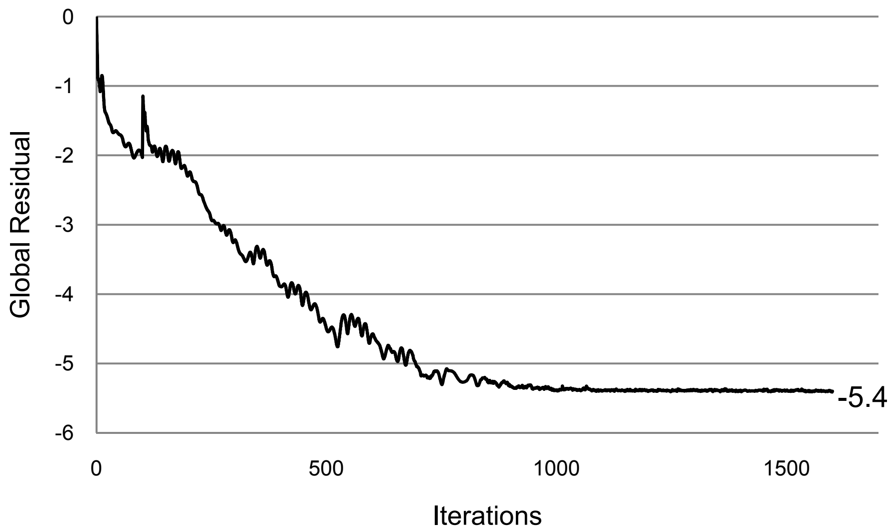

Figure 3.19: History of convergence of NREL II computation with Merkle preconditioner at 12.85 m/s

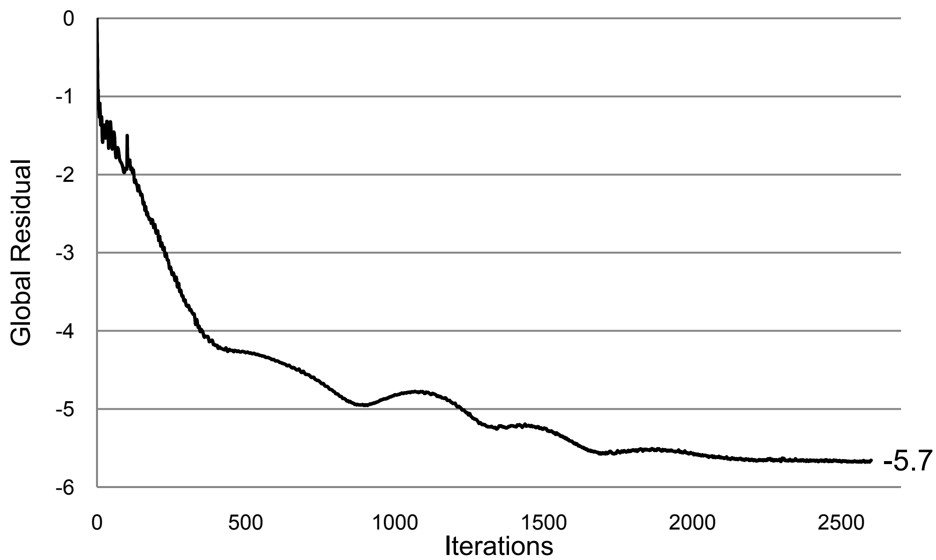

Figure 3.20: History of convergence of NREL II computation without preconditioner at 12.85 m/s

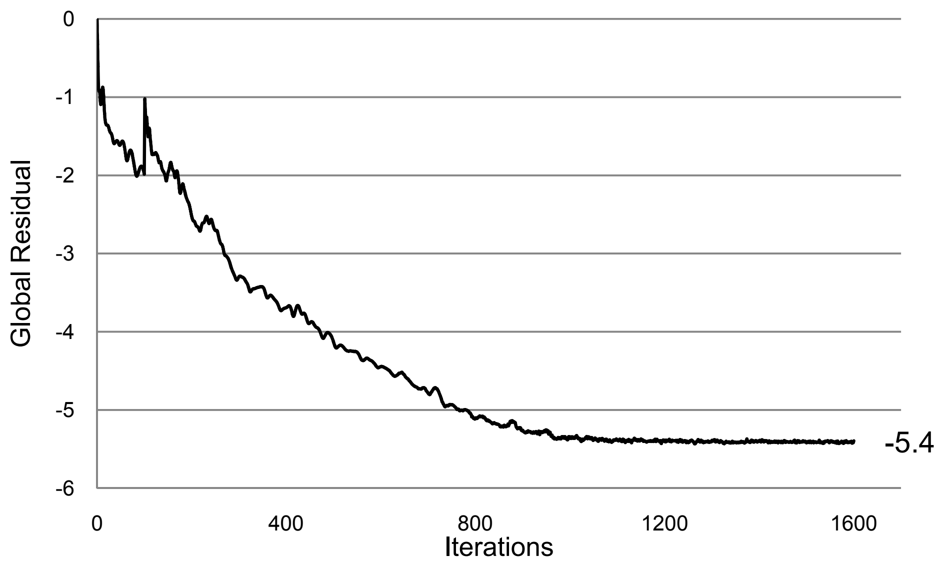

Figure 3.21: History of convergence of NREL II computation with Merkle preconditioner at 19.18 m/s

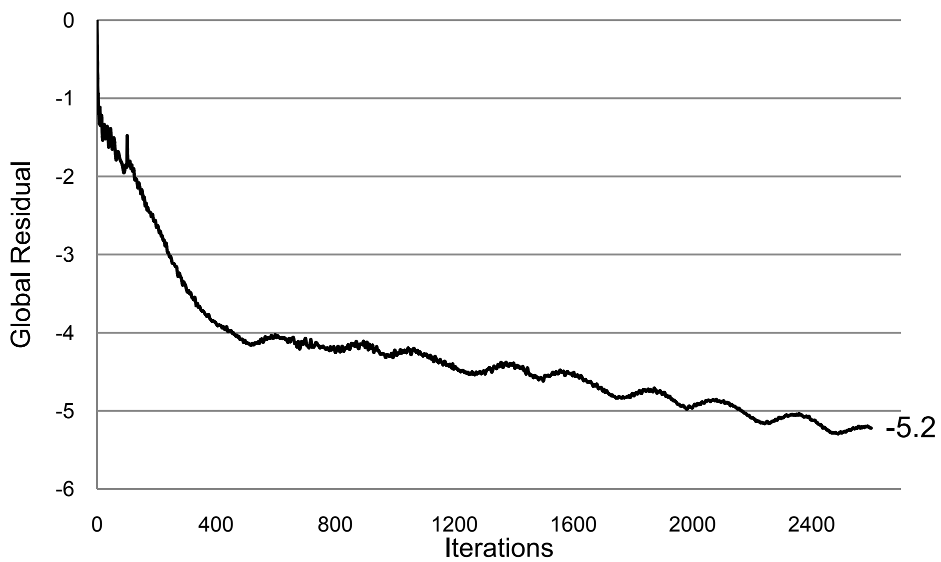

Figure 3.22: History of convergence of NREL II computation without preconditioner at 19.18 m/s

From Figure (3.19), the solution with Merkle preconditioner has converged after about 1000 iterations. On the other hand, Figure (3.20) shows that the solution without preconditioner has converged after 2000 iterations. Similar results are seen in Figures (3.21) and (3.22). So the usage of preconditioner has speeded up the convergence by about two times.

The gauge pressure distribution in the spanwise direction of the blade is given in the figures below:

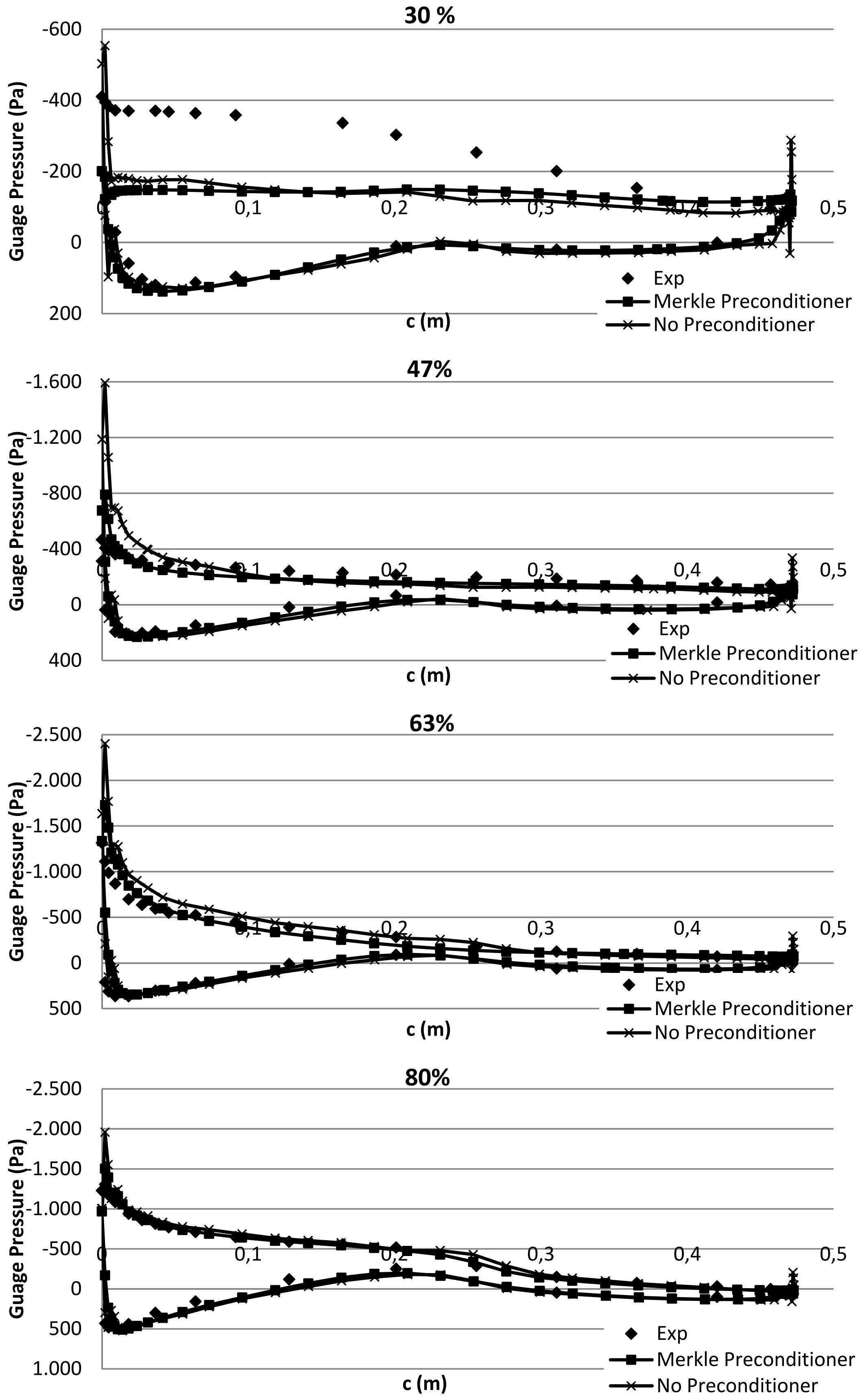

Figure 3.23: Pressure distribution comparison at 12.85 m/s for NREL II

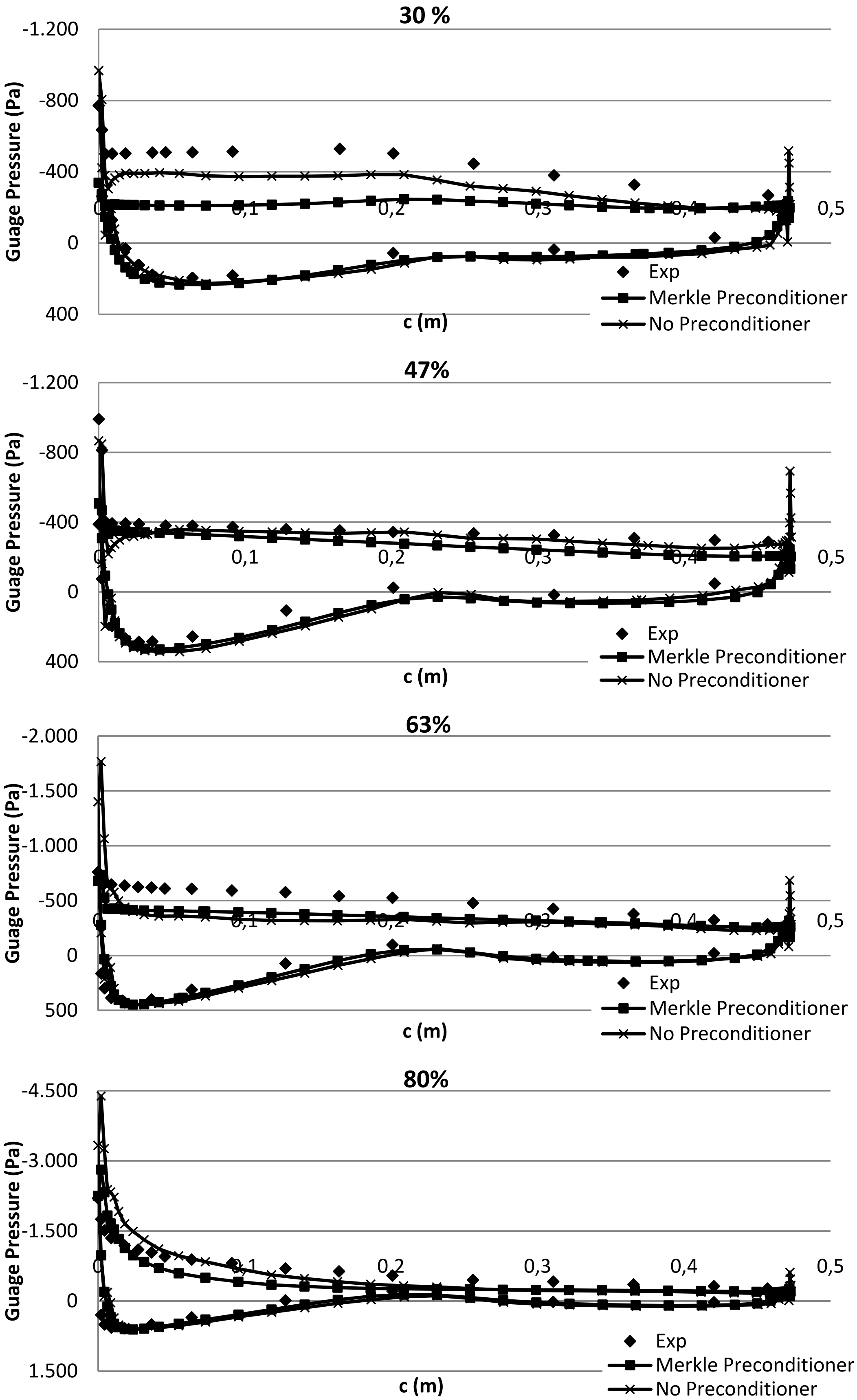

Figure 3.24: Pressure distribution comparison at 19.18 m/s for NREL II

At 12.85 m/s, Figure (3.23) shows that, at 30% span, both of the methods result in considerable deviation from experimental results. At the other spanwise locations, both of the methods show good agreement with the experimental results.

At 19.18 m/s, Figure (3.24) shows that, without preconditioning, the results are closer to the experimental data. However close the root, the results show big deviation from experiments.

3.2 Test Case 2: NREL Phase VI

3.2.1 Experimental Data and Real Blade Description

The rotor blade of NREL Phase VI is selected to be the second test case for the CFD simulation of this study. The NREL Phase VI unsteady aerodynamics experiments [56, 57] were conducted in large scale at the NASA Ames wind tunnel facilities. Among the series of tests and sequences, the blade of sequence H was selected as the baseline blade of this study. The wind turbine of this sequence is an upwind, two-bladed HAWT and the blades are tapered and twisted. Similar to NREL Phase II, the blades of this wind turbine have the S809 airfoil section from root to tip. The description of the blade is summarized in Table (3.4):

Table 3.6: NREL Phase VI blade description

Number of blades	2
Rotor diameter	10.06 m
RPM	71.63 RPM
Cone angle	0 degrees
Rotor location	Upwind
Power regulation	.Stall regulated
Blade tip pitch angle	3 degrees (down)
Blade profile	S809
Blade chord length	0.358 m – 0.728 m (linearly tapered)
Twist angle	Non-linear twist along the span
Blade thickness	t/c = 21% throughtout the span

The twist distribution along the blade is shown in Figure (3.25):

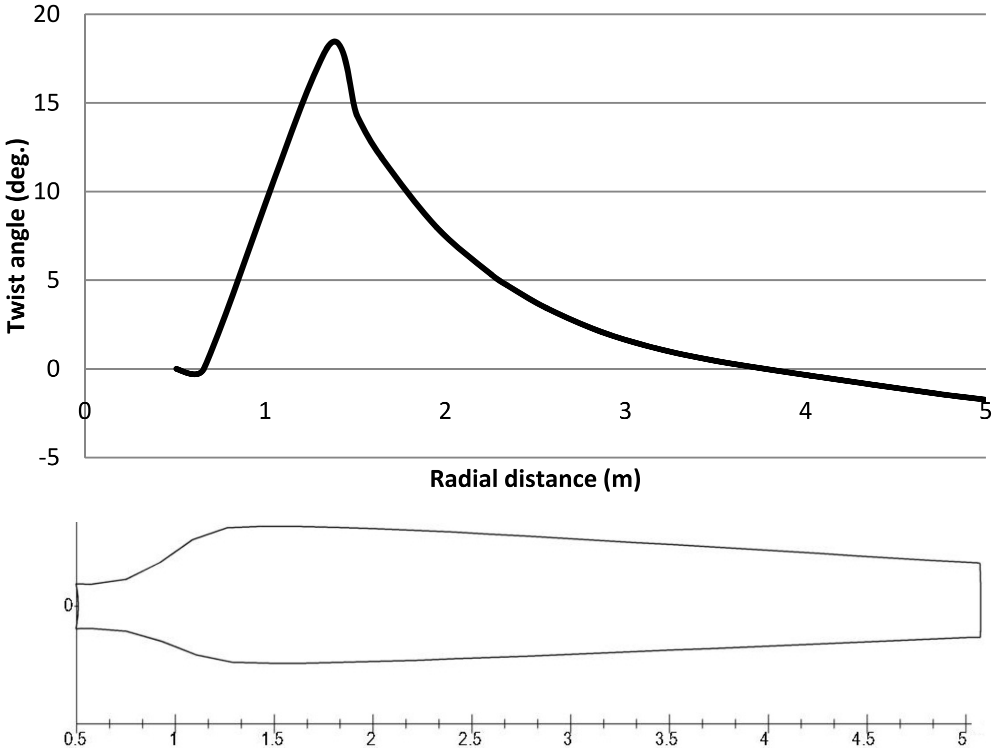

Figure 3.25: NREL VI blade twist distribution

The chord and twist variations of the blade are given in Table (3.5).

Table 3.7: Chord and twist variations along the NREL VI rotor blade [56].

Section	Radial Distance r (m)	Span Station (r/5.029 m)	Chord length (m)	Twist (degrees)
1	0	0	Hub	Hub
2	0.508	0.101	0.218	0
3	0.660	0.131	0.218	0
4	0.883	0.176	0.183	0
5	1.008	0.200	0.349	6.7
6	1.067	0.212	0.441	9.9
7	1.133	0.225	0.544	13.4
8	1.257	0.250	0.737	20.040
9	1.343	0.267	0.728	18.074
10	1.510	0.300	0.711	14.292
11	1.648	0.328	0.697	11.909
12	1.952	0.388	0.666	7.979
13	2.257	0.449	0.636	5.308
14	2.343	0.466	0.627	4.715
15	2.562	0.509	0.605	3.425
16	2.867	0.570	0.574	2.083
17	3.172	0.631	0.543	1.150
18	3.185	0.633	0.542	1.115
19	3.476	0.691	0.512	0.494
20	3.781	0.752	0.482	-0.015
21	4.023	0.800	0.457	-0.381
22	4.086	0.812	0.451	-0.475
23	4.391	0.873	0.420	-0.920
24	4.696	0.934	0.389	-1.352
25	4.780	0.950	0.381	-1.469
26	5.029	1.000	0.358	-1.775

- $r = 0\,m$: Center of the hub
- $r = 0.508\,m$: The start of the blade root, the blade section is circular
- $r = 0.883\,m$: the end of the blade root, the blade section is circular
- Between $r = 0.883\,m$ and $r = 1.257\,m$: Transition from cylindrical to S809 Airfoil
- Between $r = 1.257\,m$ and $r = 5.029\,m$: The blade sections are of S809 airfoil

The total number of sections of the blade is 26.

In the experiment, 22 pressure taps were installed at 5 primary spanwise sections: 30%, 46.6%, 63.3%, 80% and 95% span. Pairs of taps at 4% chord and 36% chord were installed at different other intermediate span locations.

5 hole probes were installed at 34%, 51%, 67%, 84% and 91% span to measure the dynamic pressure and the local effective angle of attack.

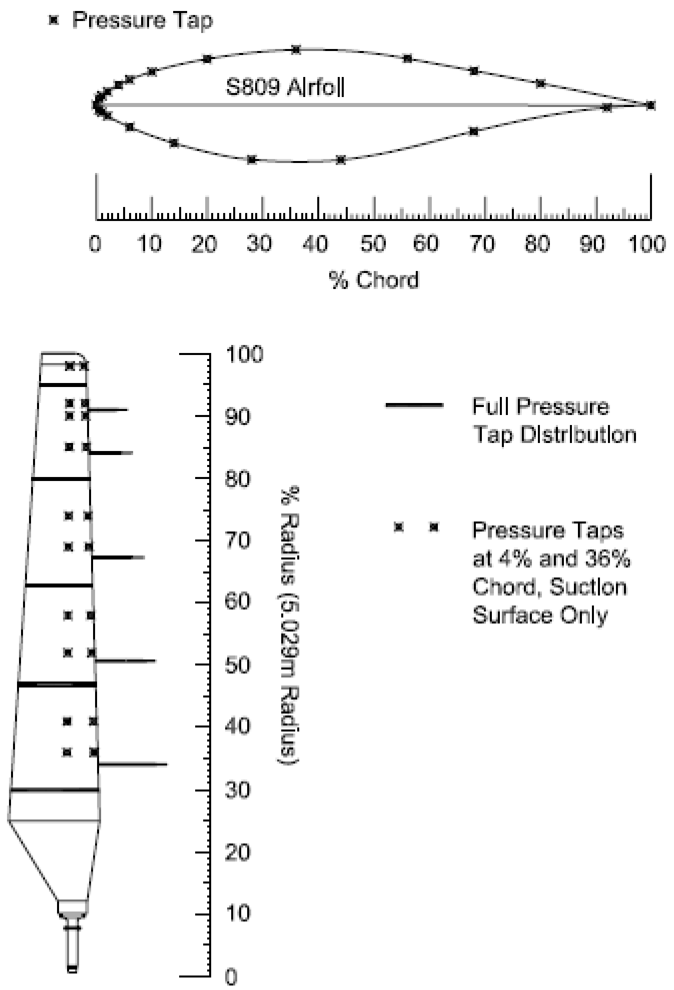

Figure 3.26: Pressure taps and probes locations of NREL VI [56]

The measured dynamic pressure was used in the calculations of pressure and force coefficients. The locations of the pressure taps and probes are shown in Figure (3.26).

3.2.2 Geometric Blade

Since the same S809 airfoil is also used in this case, the very sharp trailing edge was rounded through a radius of 0.001 m. In addition to that, the number of sections in the geometric blade has been decreased to 19 sections. The sections are stated in Table (3.6):

Table 3.8: Chord and twist variations along the NREL VI rotor geometric blade

Section	Radial Distance r (m)	Span Station (r/5.029 m)	Chord length (m)	Twist (degrees)
1	0.508	0.101	0.218	0
2	0.660	0.131	0.218	0
3	1.343	0.267	0.728	18.074
4	1.510	0.300	0.711	14.292
5	1.648	0.328	0.697	11.909
6	1.952	0.388	0.666	7.979
7	2.257	0.449	0.636	5.308
8	2.343	0.466	0.627	4.715
9	2.562	0.509	0.605	3.425
10	2.867	0.570	0.574	2.083
11	3.172	0.631	0.543	1.150
12	3.476	0.691	0.512	0.494
13	3.781	0.752	0.482	-0.015
14	4.023	0.800	0.457	-0.381
15	4.086	0.812	0.451	-0.475
16	4.391	0.873	0.420	-0.920
17	4.696	0.934	0.389	-1.352
18	4.780	0.950	0.381	-1.469
19	5.029	1.000	0.358	-1.775

The transition from cylindrical section to S809 section was done linearly in the blade generator AutoBlade of Numeca International. So the relative sections ($r = 0.883\ m$ to $r = 1.257\ m$) were removed. Also the sections at $r = 3.172\ m$ and $r = 3.185\ m$ are very close. The distance between them as a percentage of the blade length is less than 0.01% and it is not possible to have two different sections at a distance less that 0.01% in AutoBlade [104]. So the section at $r = 3.185\ m$ removed as well. The removal of the mentioned sections resulted in 19 sections for the geometric blade. For the design and optimization, it is very important to have fewer sections to save CPU time as will be discussed in Chapter 5.

Since the blade pitch angle is 3 degrees in the sequence H experiment, 3 degrees were added to the twist angle of each section.

The shape of the two-dimensional blade sections and the three-dimensional blade are shown in Figure (3.27) and (3.28):

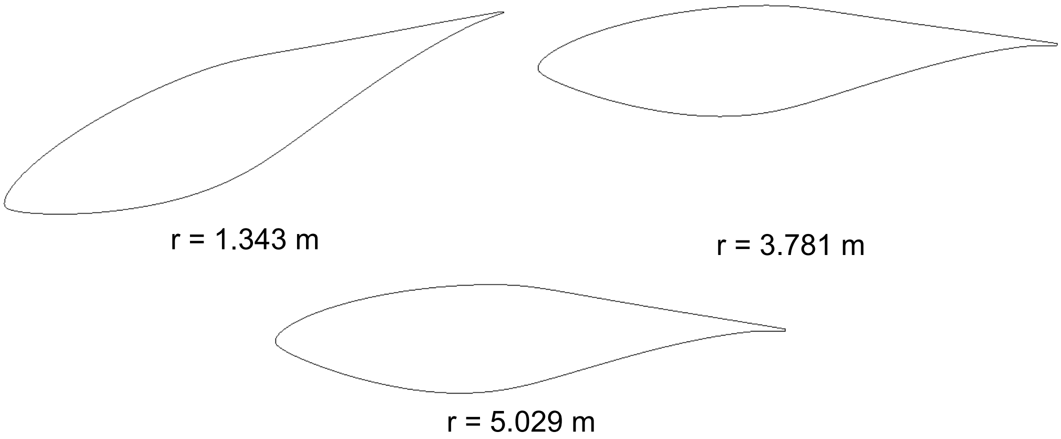

Figure 3.27: Twist and angle at different blade sections of NREL VI

Notice that the chord lengths in Figure (3.27) are not to scale.

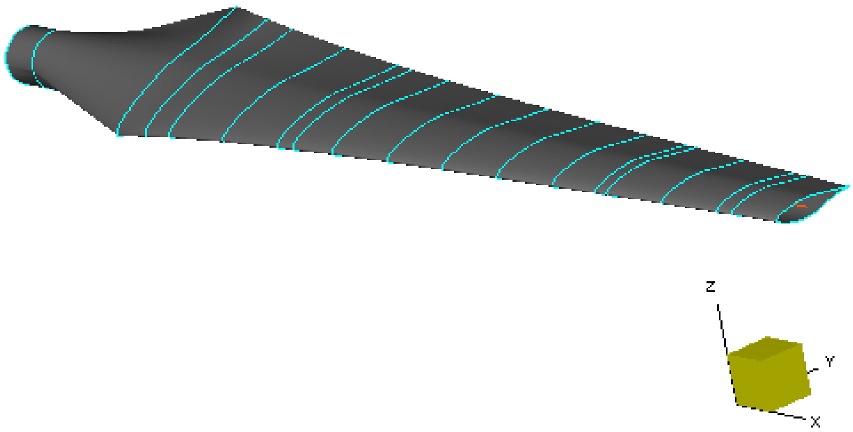

Figure 3.28: 3D NREL VI blade geometry generated by AutoBlade

3.2.3 Aerodynamic Force Coefficients

The coefficients of the aerodynamic forces acting on the blade sections are shown in Figure (3.29).

The normal and tangential forces represent the forces acting perpendicular and parallel to the airfoil chord respectively. The coefficients of these forces are computed at a certain spanwise section of the blade by integrating the pressure coefficients at that section.

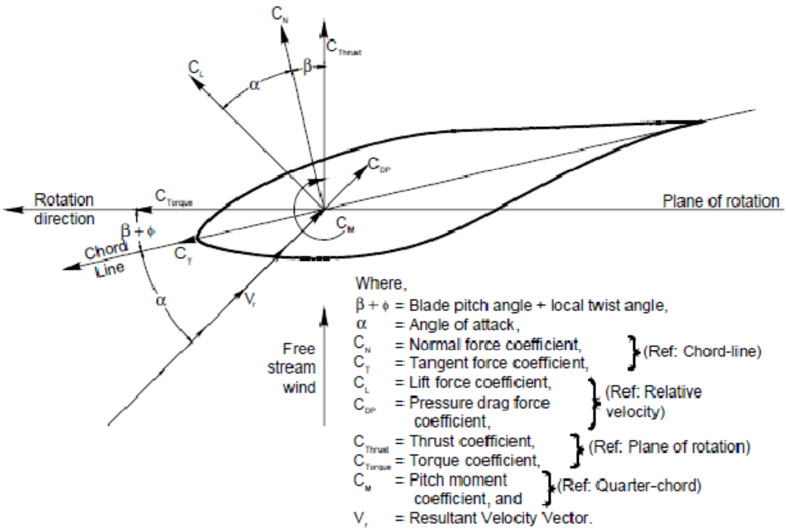

Figure 3.29: Aerodynamic force coefficients [56]

The pressure coefficient is calculated from Eq.(3.3):

$$C_p = \frac{p - p_\infty}{1/2\,\rho_\infty (U_\infty^2 + (\Omega r)^2)} \tag{3.3}$$

where,

- ρ_∞: The free stream density $[kg/m^3]$
- U_∞: The wind speed $[m/s]$
- Ω: the rotational speed $[rad/s]$
- r: the radial distance from the center of hub to the blade section $[m]$

Equations (3.4) and (3.5) give the integration procedure used to determine the normal and tangential force coefficients, C_N and C_T :

$$C_N = \sum_i \left(\frac{C_{pi} + C_{pi+1}}{2}\right)(x_{i+1} - x_i) \tag{3.4}$$

$$C_T = \sum_i \left(\frac{C_{pi} + C_{pi+1}}{2}\right)(y_{i+1} - y_i) \tag{3.5}$$

where,

- x_i: The normalized distance along the chord line
- y_i: The normalized distance orthogonal to the chord line

The values for x and y start at the trailing edge ($x = 1$), continues over the upper surface of the blade, reaches the leading edge and then continues along the lower surface and finally end at the starting point.

3.2.4 Mesh Study

The structured mesh was generated using the Numeca AutoGrid mesh generator. The mesh was generated for a single blade with imposing the periodic condition to account for the other blade. The number of points on the entire mesh including the blade and external flow is about 2.7 million points and the number of points on one blade is 1.63 million points. The thickness of the first cell to the wall was kept at $2 \times 10^{-5} m$ so that the y^{+} value falls between 1 and 9. Such range of y^{+} is suitable for the tested turbulence models. The mesh quality is shown in Table (3.7).

Table 3.9: Mesh quality for NREL VI

Field	Orthogonality (Min., Average)	Aspect Ratio (Max., Average)	Expansion Ratio (Max, Average)
Blade	(41.6, 78.5)	(21520, 565)	(2.2, 1.5)
External	(39.5, 80.0)	(33635, 525)	(2.4, 1.5)

The 2D meshes at the root and midspan are shown in Figures (3.30) and (3.31):

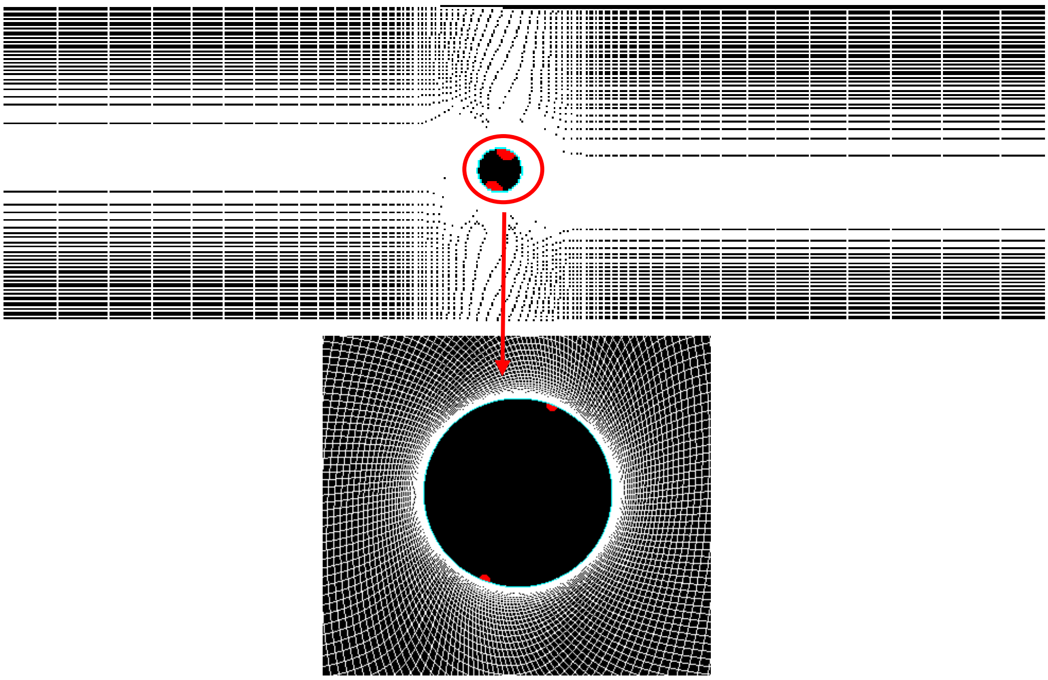

Figure 3.30: 2D mesh at the root section of the NREL VI

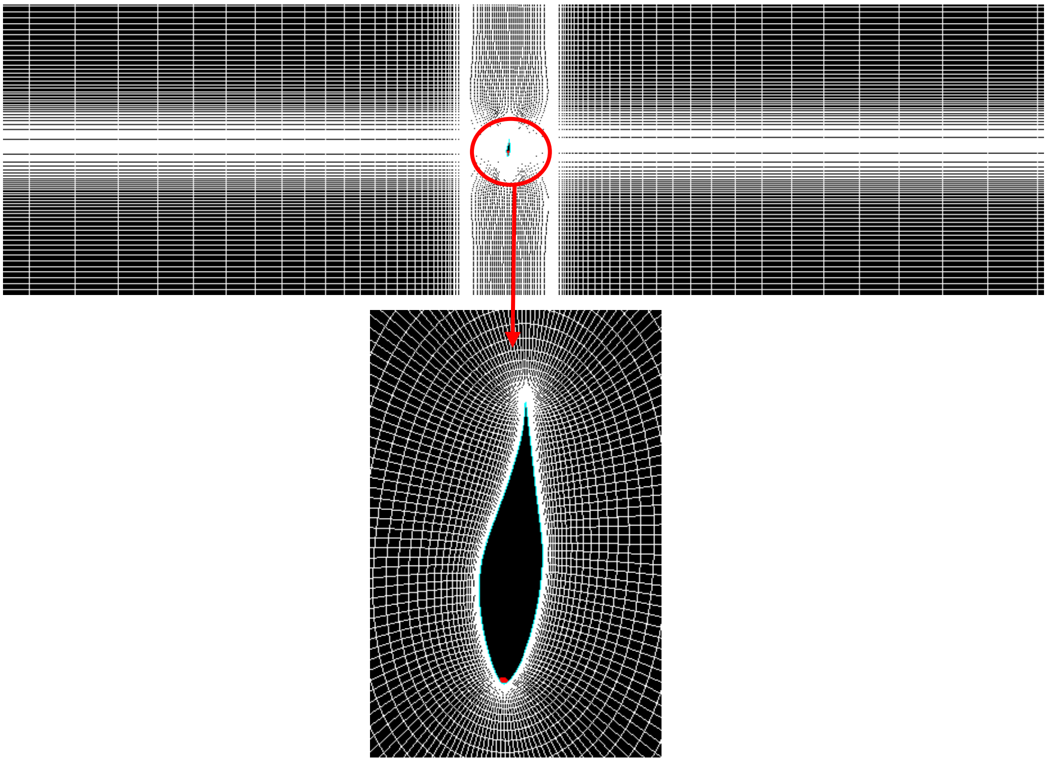

Figure 3.31: 2D mesh at the midspan section of the NREL VI

The 16 block structure of the 3D mesh and the 3D mesh are shown in Figure (3.32).

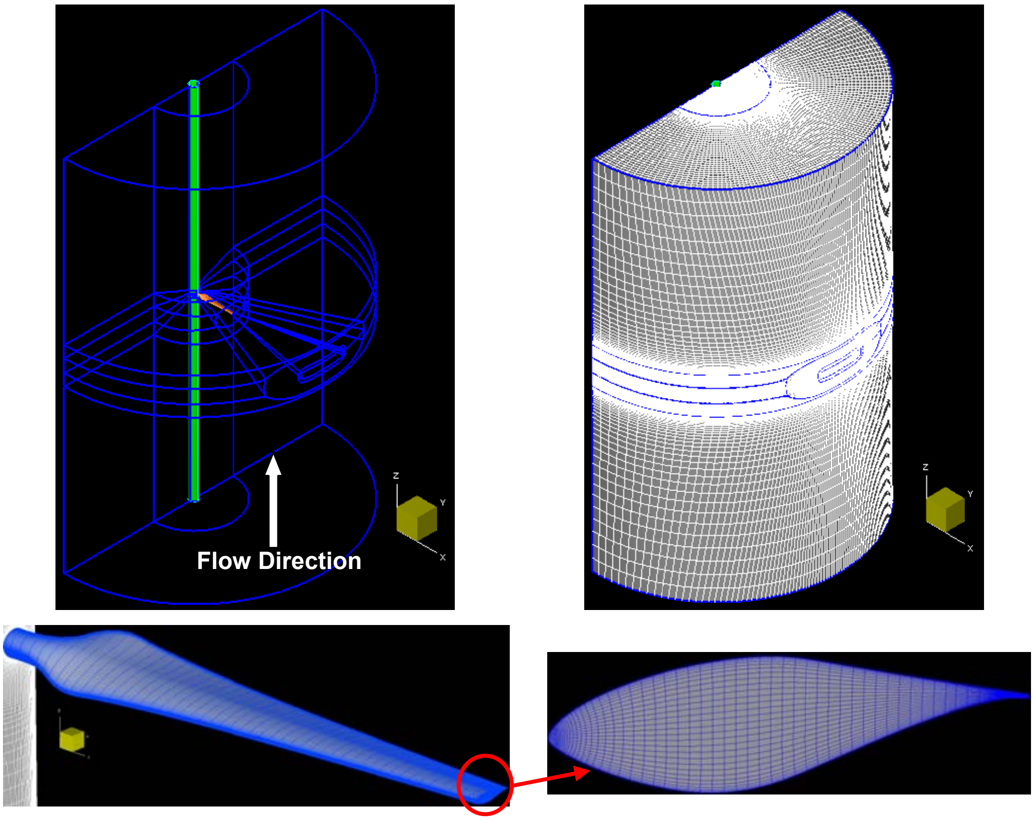

Figure 3.32: 3D mesh of the NREL VI

3.2.5 Reynolds Number

The Reynolds number values for the NREL VI blade at the root and tip for different wind speeds are listed in Tables (3.10) and (3.11):

Table 3.10: Reynolds number values at the root for NREL VI blade

Wind Speed (m/s)	Reynolds Number
5	586255
6	612152
7	641137
8	673547
9	709006
11	786933
13	864113
15	947549
17	1035345
19	1125017

Table 3.11: Reynolds number values at the tip for NREL VI blade

Wind Speed (m/s)	Reynolds Number
5	972860
6	979107
7	985066
8	993427
9	1001014
11	1019959
13	1032759
15	1049172
17	1066216
19	1085259

From the results for the Reynolds number, the flow is turbulent at all the considered wind speeds and at all the spanwise sections from root to tip.

3.2.6 CFD Simulation and Results

The three-dimensional steady state RANS equations are solved using the Fine/Turbo solver of Numeca International. Merkle preconditioner is imposed and four different turbulence models are tested. The turbulence models are; Spalart-Allmaras, the $k-\varepsilon$ Launder – Sharma, the $k-\varepsilon$ Yang-Shih and Shear Stress Transport (SST) $k-\omega$. The results in terms of power production and pressure distribution are compared with the available experimental data at 12 different wind speeds.

The comparison between the experimental and computed power for different turbulence models is shown in Figure (3.33):

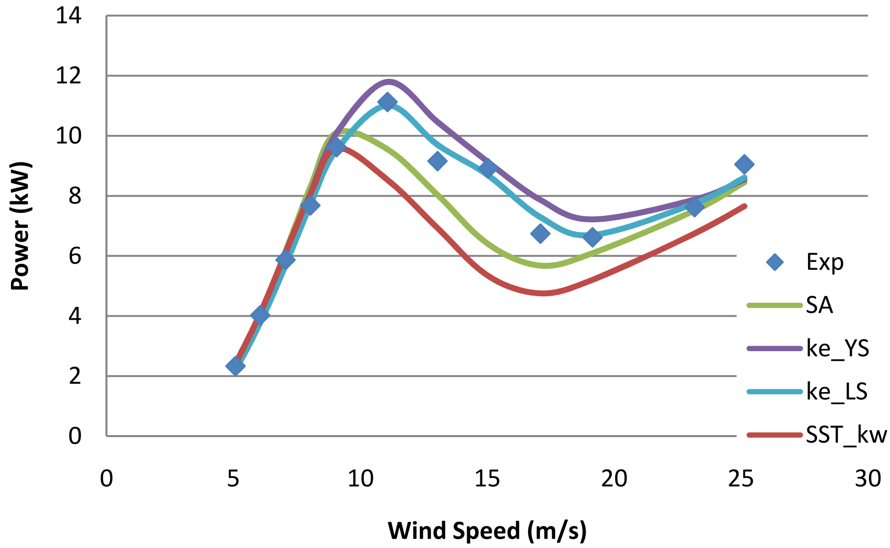

Figure 3.33: Comparison of experimental power with computed power for NREL VI

All the turbulence models are found to be stable for the whole wind speed range.

From Figure (3.33), one may notice the following: At low and moderate wind speeds (5 m/s to 9 m/s), all the models have similar behavior in power prediction.

At high wind speeds, Spalart-Allmaras and SST $k-\omega$ underpredicted the power while $k-\varepsilon$ Yang-Shih overpredicted the power. On the other hand, $k-\varepsilon$ Launder – Sharma showed the best agreement with experimental data. So the behavior of the turbulence models in predicting the power for NREL Phase VI test case is similar to their behavior for the NREL Phase II test case.

The power prediction results and the associated errors are listed in Table (3.8):

Table 3.12: Power prediction errors of different turbulence models for NREL VI

Speed (m/s)	Exp. data	SA		k-e Launder-Sharma		k-e Yang-Sheih		SST k-w	
	Power (kw)	Power (kW)	Error (%)	Power (kW)	Error (%)	Power (kW)	Error (%)	Power (kW)	Error (%)
5	2,34	2,38	1,76	2,18	6,71	2,32	0,73	2,40	2,90
6	4,03	4,09	1,60	3,78	6,17	3,97	1,46	4,09	1,65
7	5,87	6,15	4,72	5,69	3,15	5,96	1,54	6,10	3,94
8	7,68	8,30	7,99	7,72	0,45	8,07	5,04	8,06	4,96
9	9,62	10,10	4,99	9,53	0,99	10,09	4,85	9,59	0,34
11	11,12	9,55	14,15	11,00	1,08	11,80	6,03	8,53	23,28
13	9,16	8,03	12,28	9,70	5,89	10,46	14,22	6,93	24,34
15	8,92	6,39	28,30	8,68	2,69	9,12	2,29	5,34	40,16
17	6,74	5,68	15,76	7,29	8,12	7,86	16,63	4,76	29,45
19	6,62	6,09	7,99	6,70	1,12	7,22	8,98	5,21	21,38
23	7,63	7,51	1,47	7,75	1,59	7,88	3,29	6,75	11,47
25	9,05	8,45	6,58	8,61	4,85	8,54	5,59	7,66	15,39

From the above results, one may conclude that, the $k-\varepsilon$ Launder – Sharma turbulence model gives the closest results to the measurements. This model could capture the correct power at low, stall and high wind speeds. So the $k-\varepsilon$ Launder – Sharma model will be used for the coming computations.

The coming discussion shows some contrary results. According to the results of this study, the $k-\varepsilon$ Launder – Sharma gives the best results while it was expected that the SST $k-\omega$ would give better results. However, according to Ref. [105], the two-equation turbulence models are very sensitive to the grid arrangement on the normal direction. Figure (3.34) shows that the $k-\varepsilon$ (Launder – Sharma is used in the figure) is even more sensitive than SST $k-\omega$ and predicts more deviation (around 25%) of skin friction at y+ of 1.5 and the prediction becomes even worse as y+ increases. Where the SST $k-\omega$ gives a deviation of about 5% at y+ of 1.5.

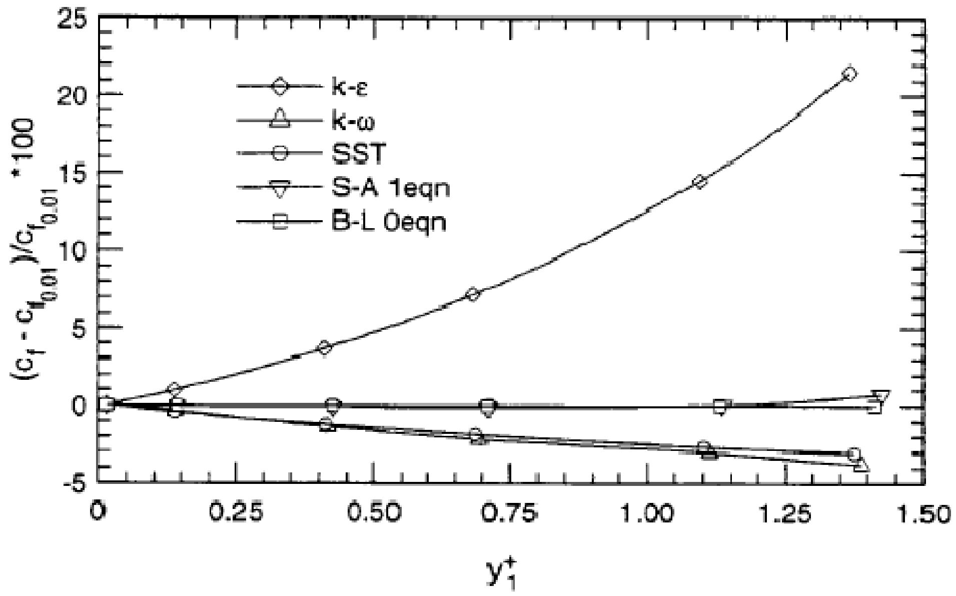

Figure 3.34: Sensitivity to the distance of the first point to the wall. [105]

In this study, the y+ value is of the order of 7. This indicates that the $k-\varepsilon$ model should give the worst results compared to SA and SST $k-\omega$. But this is not the case. In Ref. [43], NREL Phase III was investigated using different turbulence models including $k-\varepsilon$ and SST $k-\omega$ and $k-\varepsilon$ gives the best power prediction among other models. The SA model was compared with SST $k-\omega$ in Ref. [46] and it gave superior results which agree with the results in this study. To explain the contrary in the results of the different references, in Ref. [105] the results were obtained for stationery flat plate and may be for rotating turbomachinery such as wind turbines, the results would be different. But to assess this issue, more wind turbine test cases for different orders of y+ should be investigated. However, this issue is beyond the scope of this study.

The three-dimensional gauge pressure contours on the suction side and pressure side of the blade are shown in Figures (3.35), (3.36) and (3.37) for the $k-\varepsilon$ Launder – Sharma turbulence model at three different wind speeds 5, 9 and 15 m/s.

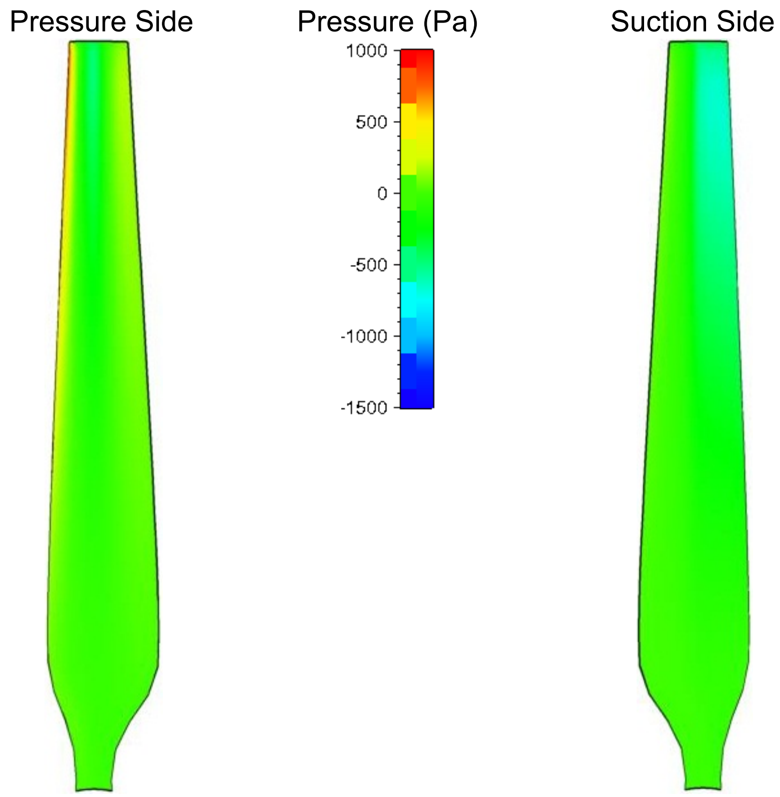

Figure 3.35: Gauge pressure contours for NREL VI at 5 m/s

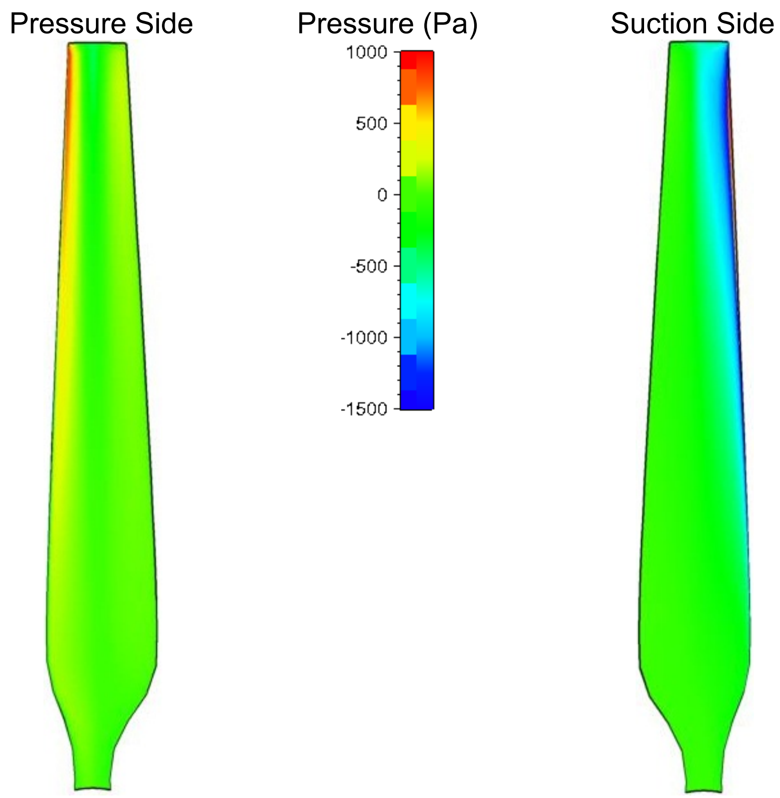

Figure 3.36: Gauge pressure contours for NREL VI at 9 m/s

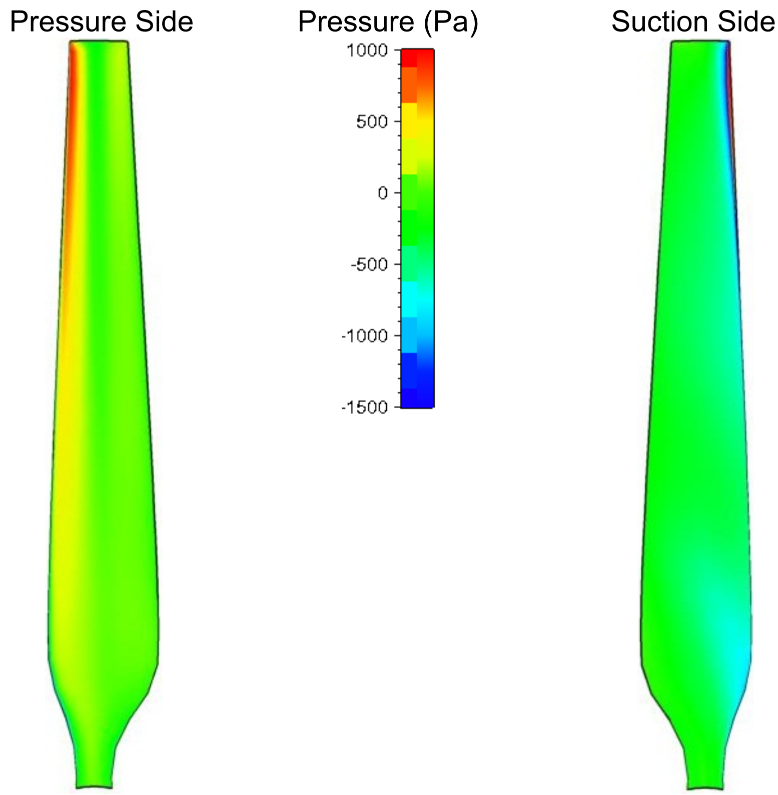

Figure 3.37: Gauge pressure contours for NREL VI at 15 m/s

The normal and tangential force coefficients at different spanwise sections of the blade are computed according to Equations (3.4) and (3.5). During operation of the wind turbine blade, the local twist and pitch angles are relatively small (in NREL Phase VI the max $\phi + \beta$ is 23 degrees). This means that the C_N is close in value to the axial thrust coefficient where, the C_T value is close to the torque coefficient and it is called the driving force coefficient, Figure (3.29).

The results of C_N and C_T for different wind speeds are plotted in Figures (3.38) and (3.39) at 30%, 47%, 63%, 80% and 95% span:

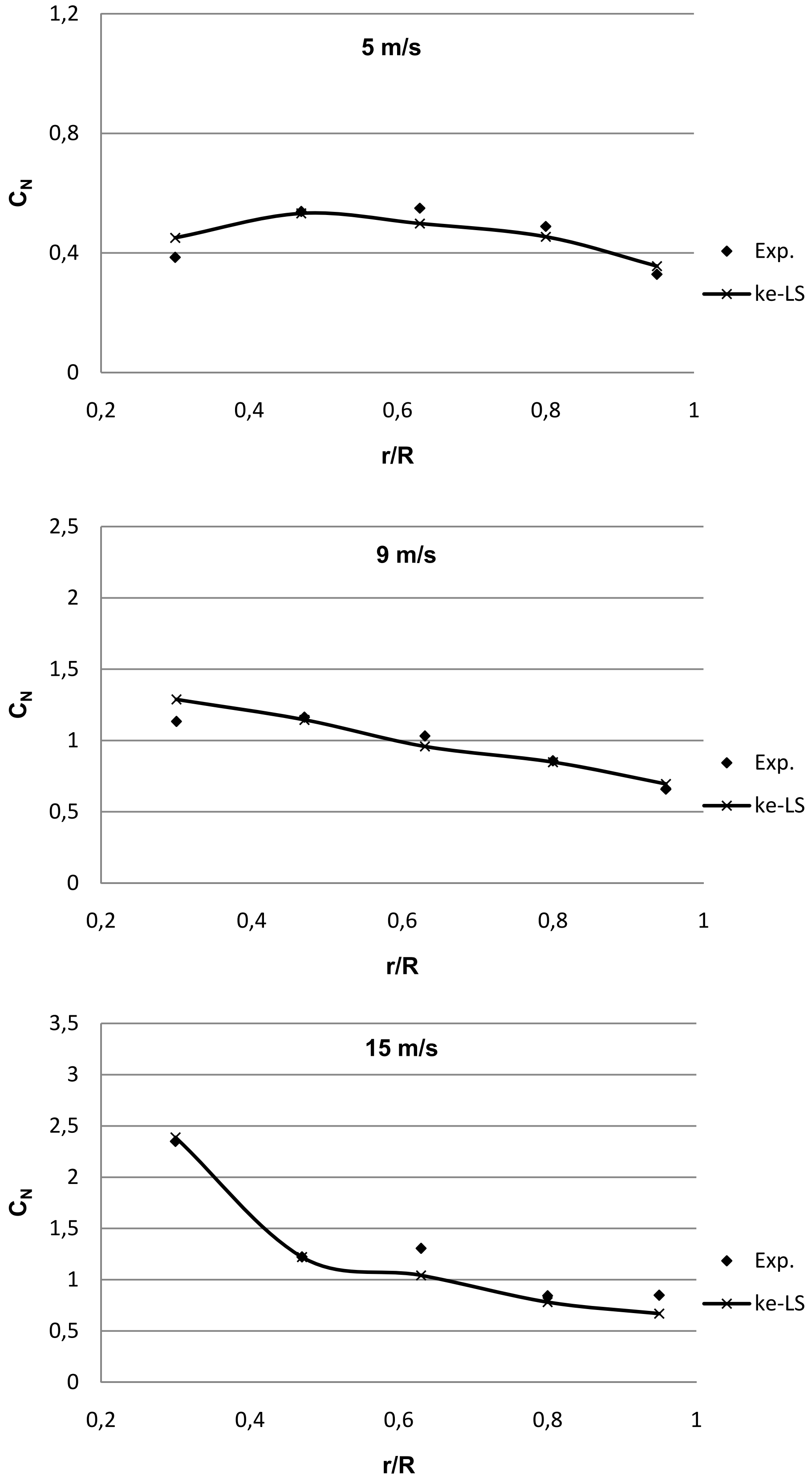

Figure 3.38: Comparison of experimental normal force coefficient with computed one at different spanwise sections

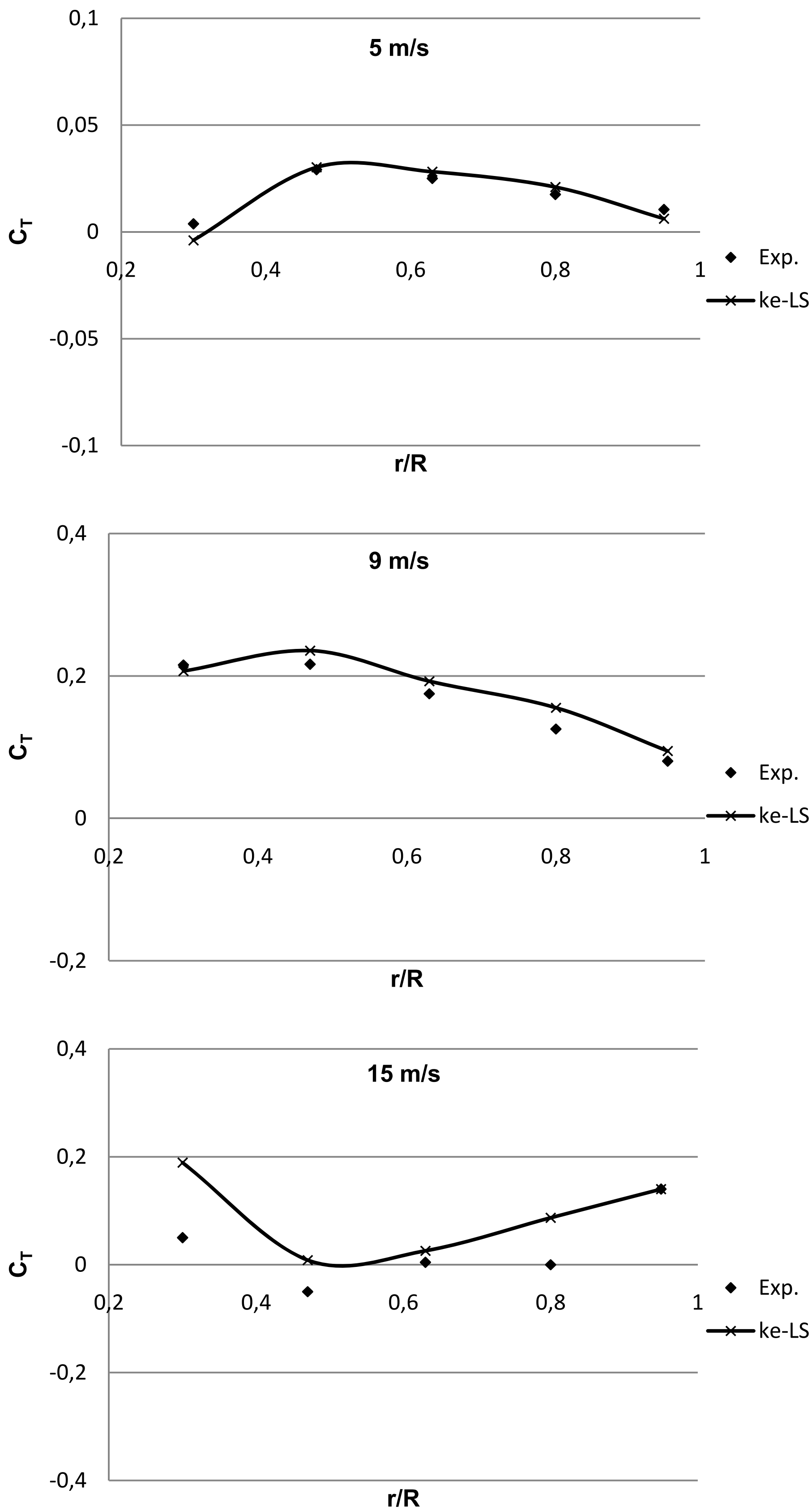

Figure 3.39: Comparison of experimental tangential force coefficient with computed one at different spanwise sections

At low wind speed, 5m/s, the lift is high compared to drag so the lift component in the tangential direction is higher than the drag component in the same direction resulting in positive C_T value meaning that the driving force acts in the direction of rotation in all the blade sections.

At higher wind speeds (9m/s) the lift continues increasing causing higher values in C_N and C_T.

Stall occurs at 11m/s and here the lift decreases while the drag suddenly increases. At wind speeds higher than stall speed (15m/s), the decrease of lift and increase in drag result in smaller C_N and smaller or even negative C_T values. Negative C_T values at some sections of the blade means that the diving force acts against the rotation in those sections.

The behavior of C_N and C_T with wind speeds is seen in Figures (3.38) and (3.39). Moreover, the figures show a considerable agreement between measured and computed C_N values. However, C_T values deviate from the experimental results. The reason behind this might be because of the difficulty of measuring the C_T values experimentally due to the sparseness of pressure taps in the leading and trailing edge regions. Also the C_T values are small compared to C_N and any small change in either lift or drag (due to experimental errors) will result in significant errors in the C_T calculations.

The pressure coefficient distribution is computed using the $k - \varepsilon$ Launder – Sharma turbulence model at five spanwise sections of the blade, 30%, 47%, 63%, 80% and 95% for three different wind speeds of 5m/s, 9m/s and 15m/s are shown in Figures (3.40), (3.41) and (3.42):

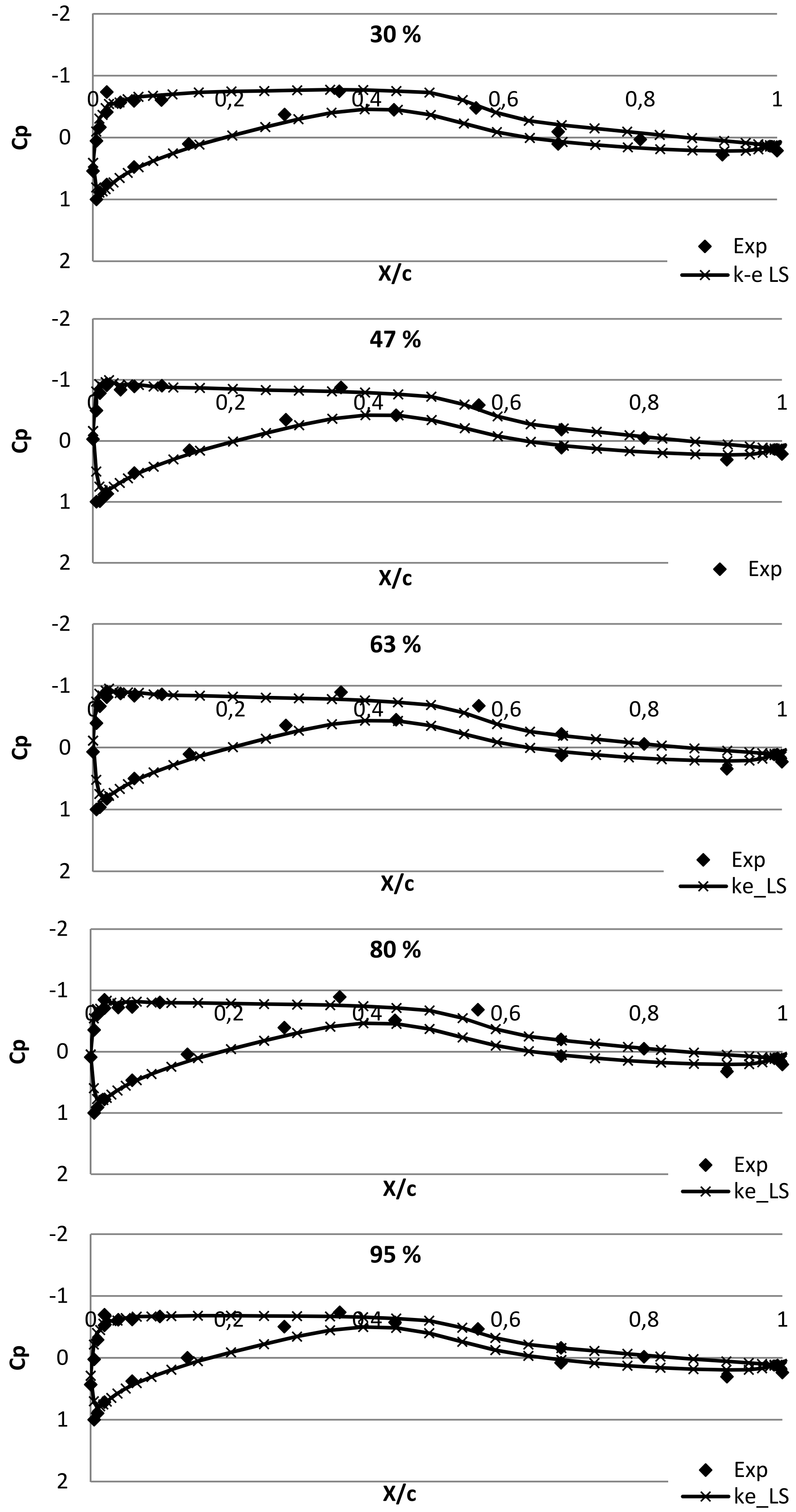

Figure 3.40: Pressure coefficient distribution comparison between experimental and calculated at different spanwise sections on NREL VI for 5 m/s

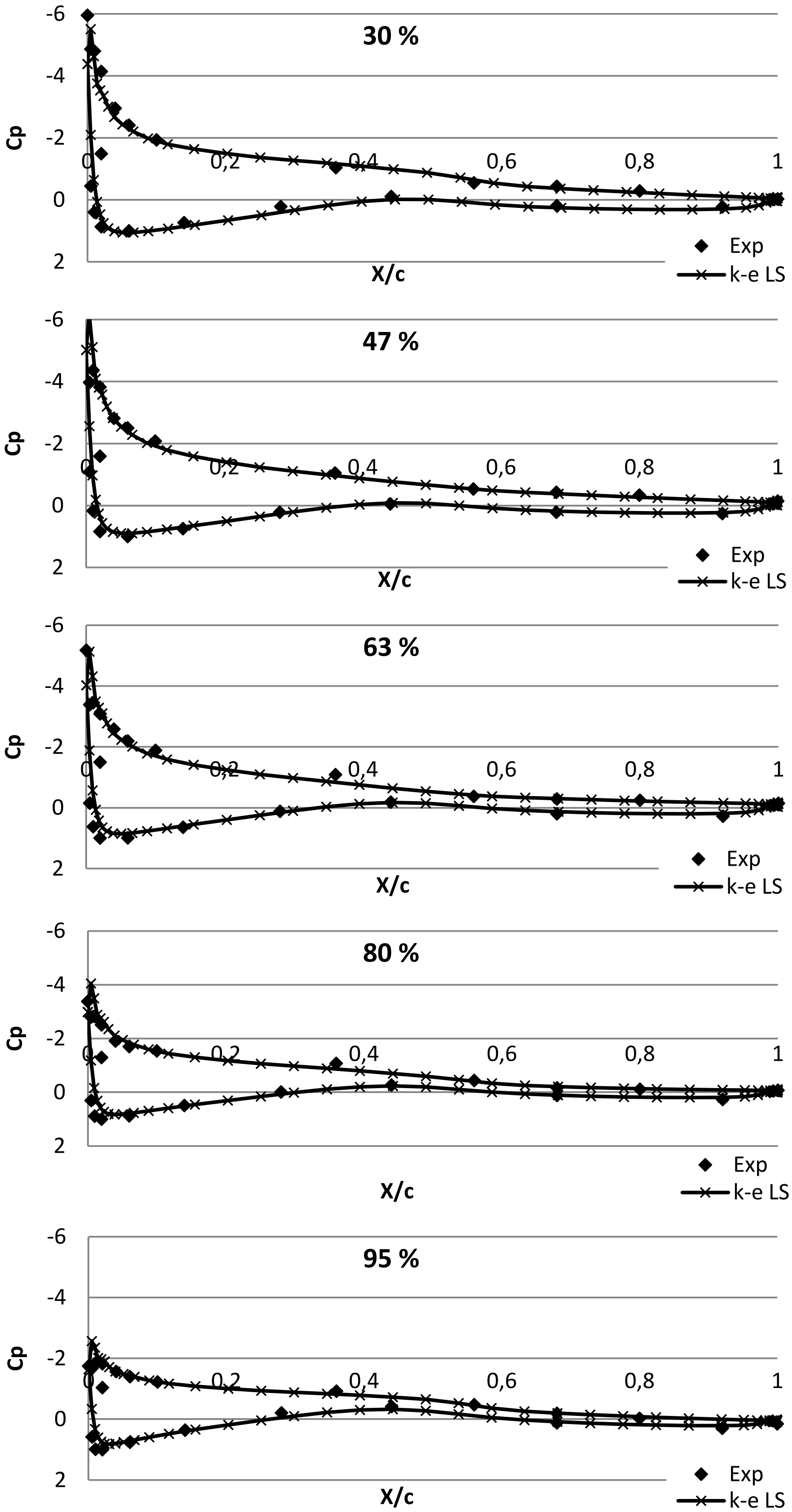

Figure 3.41: Pressure coefficient distribution comparison between experimental and calculated at different spanwise sections on NREL VI for 9 m/s

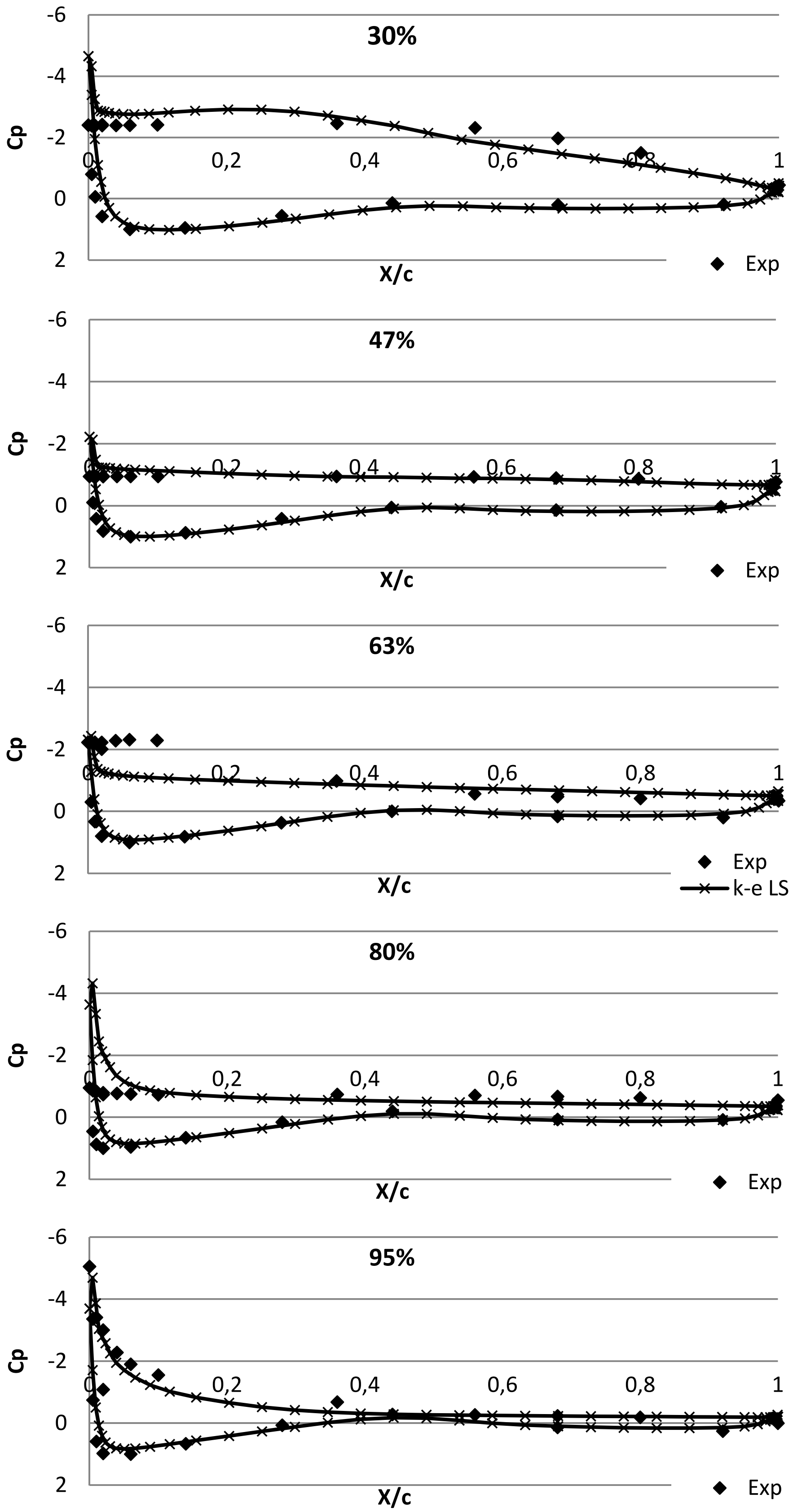

Figure 3.42: Pressure coefficient distribution comparison between experimental and calculated at different spanwise sections on NREL VI for 15 m/s

At 5 and 9 m/s, the computed pressure coefficient distribution at all sections of the blade is in good agreement with the experimental data as noticed from Figures (3.40) and (3.41).

At 15 m/s, there is a discrepancy between the computed and experimental pressure coefficient distribution in the suction side of the inboard span of 30%. Again this is due to the large separation and strong vorticies which happed at this speed and especially in this section. So it becomes difficult for the solver with low Reynolds turbulence model to capture the separation at the suction side and that is the reason behind such discrepancy. In Ref. [44], unsteady state computations using Large Eddy Simulation for turbulence modeling are conducted over the NREL Phase VI blade. The results obtained in Ref. [44] for the pressure coefficient distribution at 15m/s is of similar behavior to the results in Figure (3.40). Similar results were also obtained in Ref. [46].

The separation is investigated by plotting the relative velocity contours with streamlines at different spanwise blade sections. The plots are obtained for wind speeds of 5, 9 and 15 m/s.

At 5 m/s, Figure (3.43) shows that no separation occurs and the pressure distribution results were in good agreement with experimental results.

At 9 m/s, Figure (3.44) shows that the separation effect is small. The separation evolves from 30% section to reaches its maximum at 63% section and then decreases at 80% section and finally the separation disappears at 95% section.

At 15 m/s, Figure (3.45) shows that separation and formation of vorticies happen at all sections. This explains the deviation of the computed pressure distribution from the experimental results. And also the decrease in the C_N and C_T values.

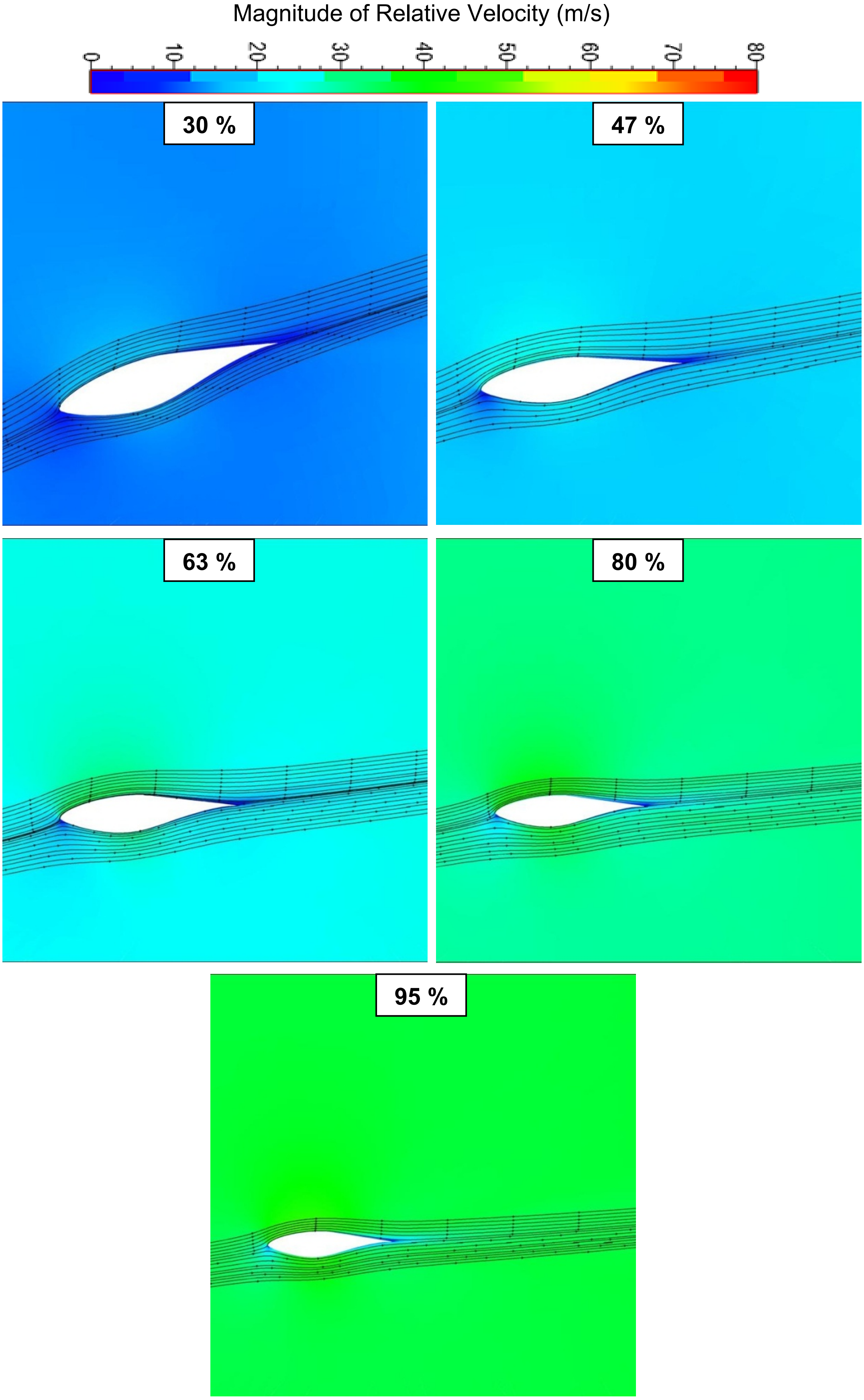

Figure 3.43: Relative velocity contours with streamlines at 5 m/s on different sections of NREL VI

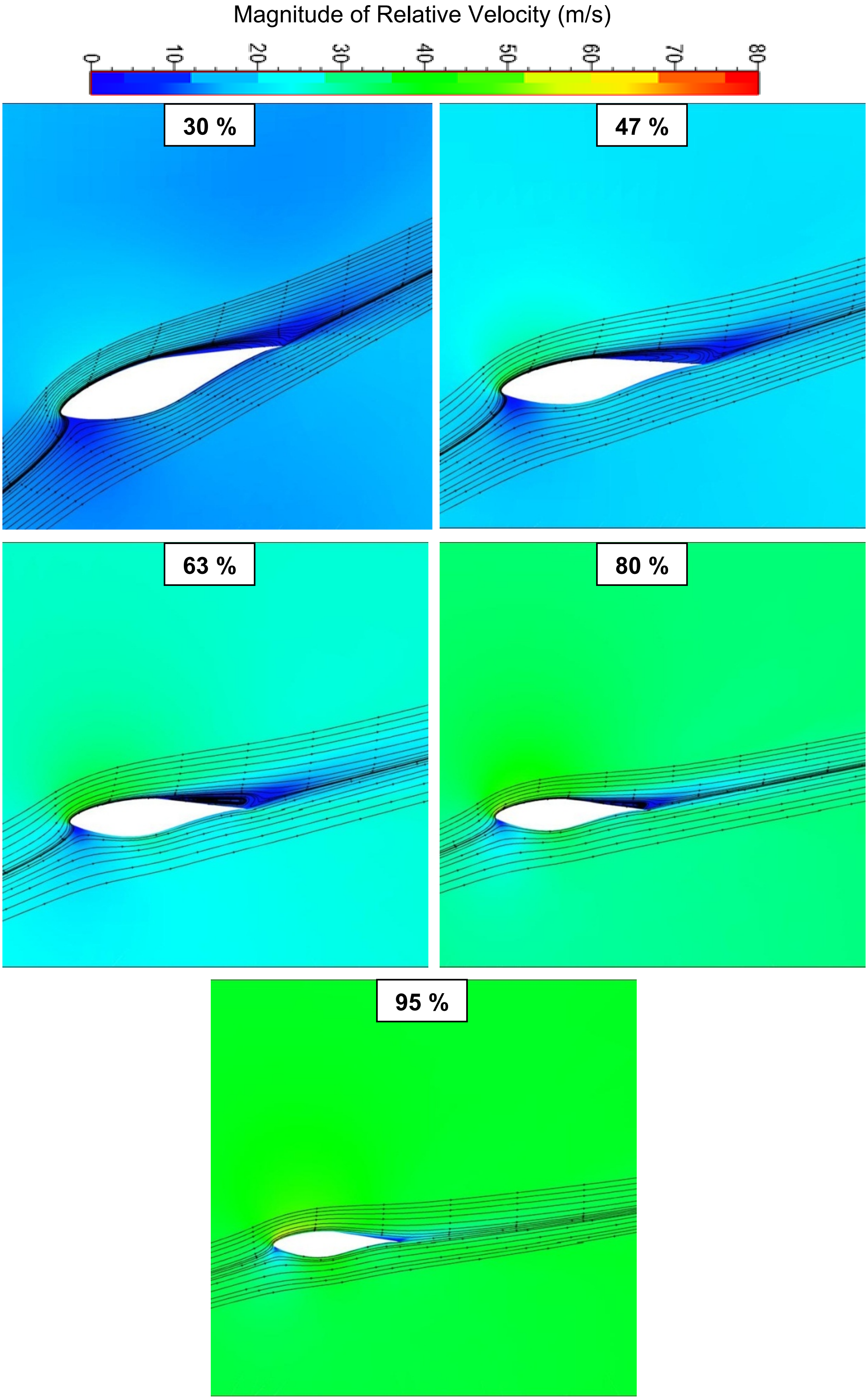

Figure 3.44: Relative velocity contours with streamlines at 9 m/s on different sections of NREL VI

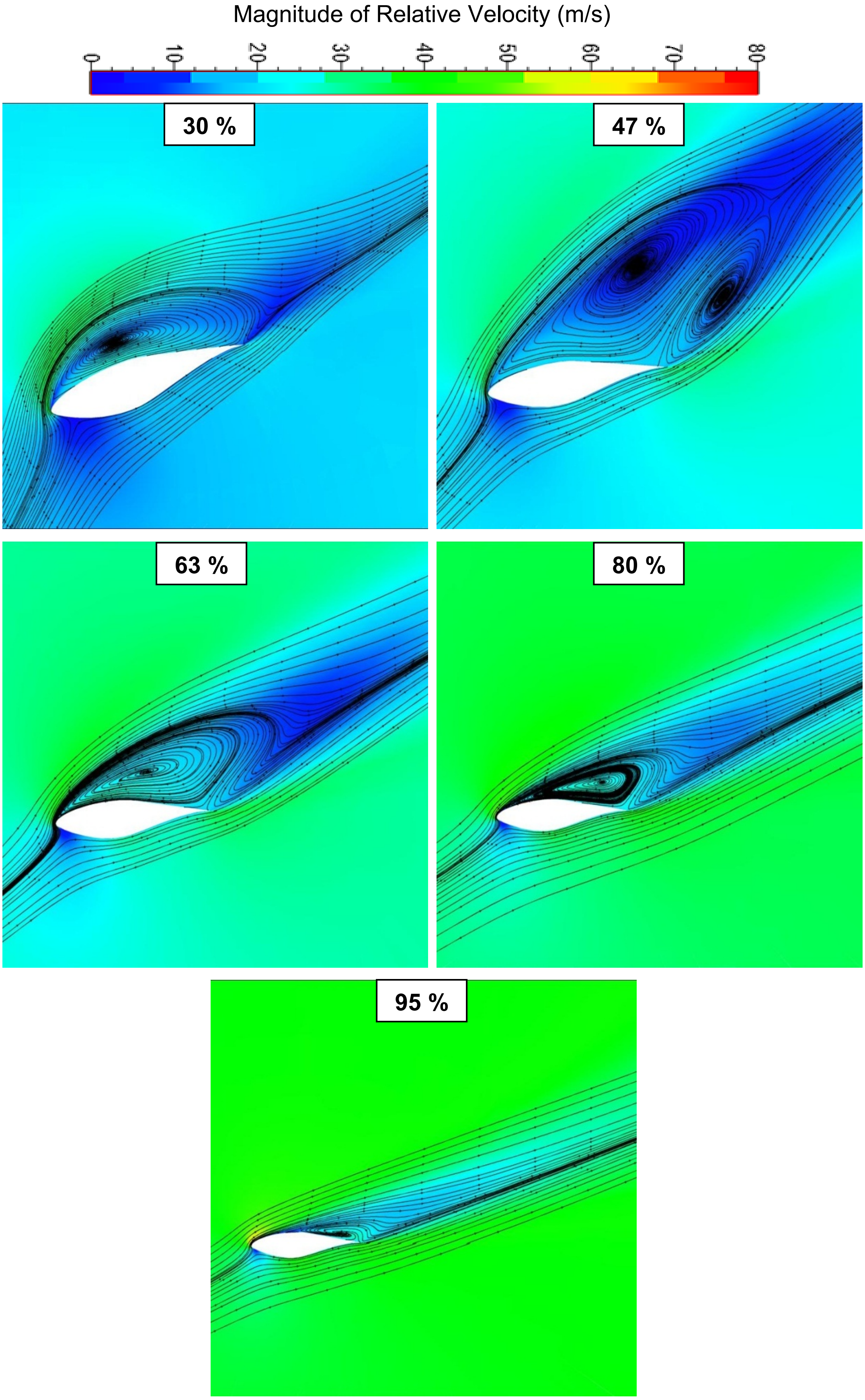

Figure 3.45: Relative velocity contours with streamlines at 15 m/s on different sections of NREL VI

3.2.7 Results of Preconditioning

So far all the results obtained in Section (3.2) are obtained using Merkle preconditioner. Here, the computations with Merkle preconditioner, Hakimi preconditioner and without any preconditioner are compared. The CFD simulations are done for the NREL Phase VI wind turbine rotor blade at wind speeds of 5m/s and 19m/s. All the computations were done using the Launder-Sharma turbulence model.

The histories of convergence for the different computations are summarized in the figures below at wind speed of 5m/s:

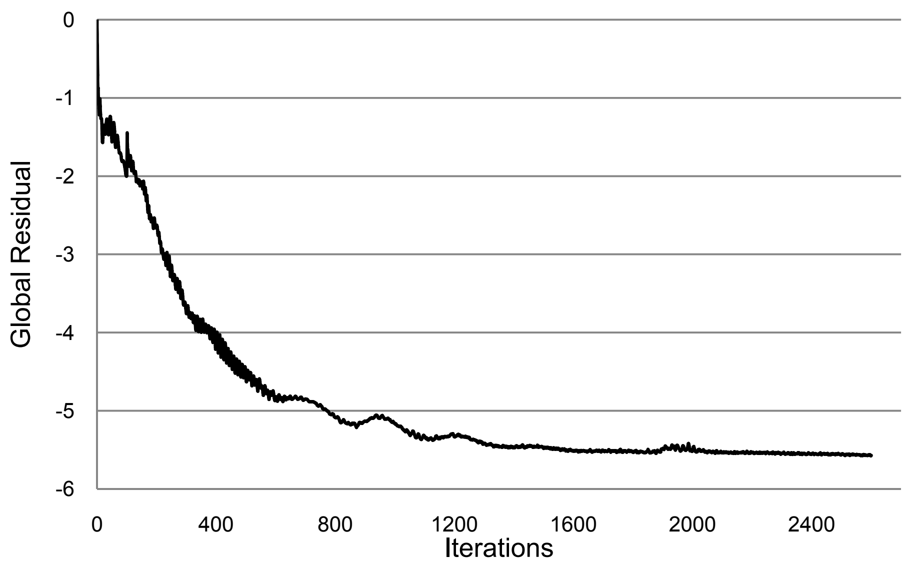

Figure 3.46: History of convergence of NREL VI computation with Merkle preconditioner at 5 m/s

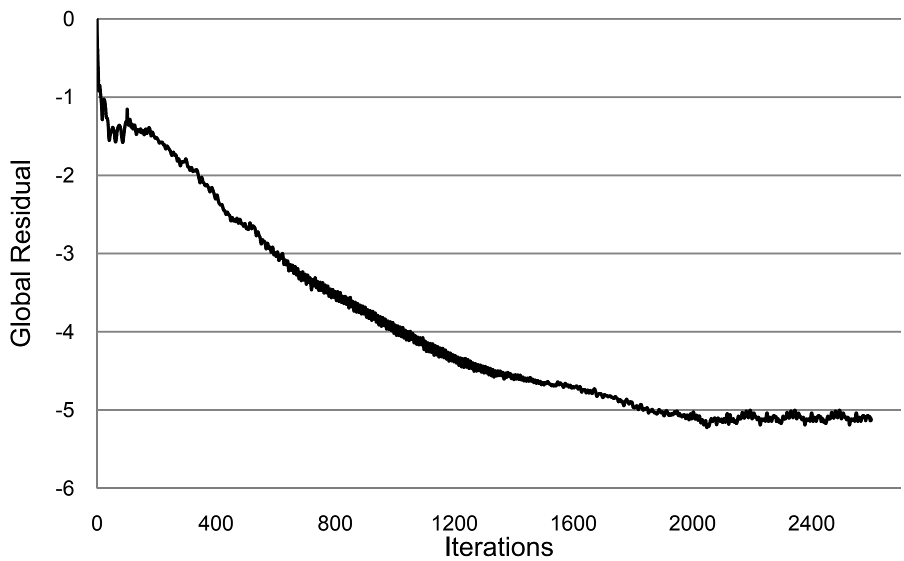

Figure 3.47: History of convergence of NREL VI computation with Hakimi preconditioner at 5 m/s

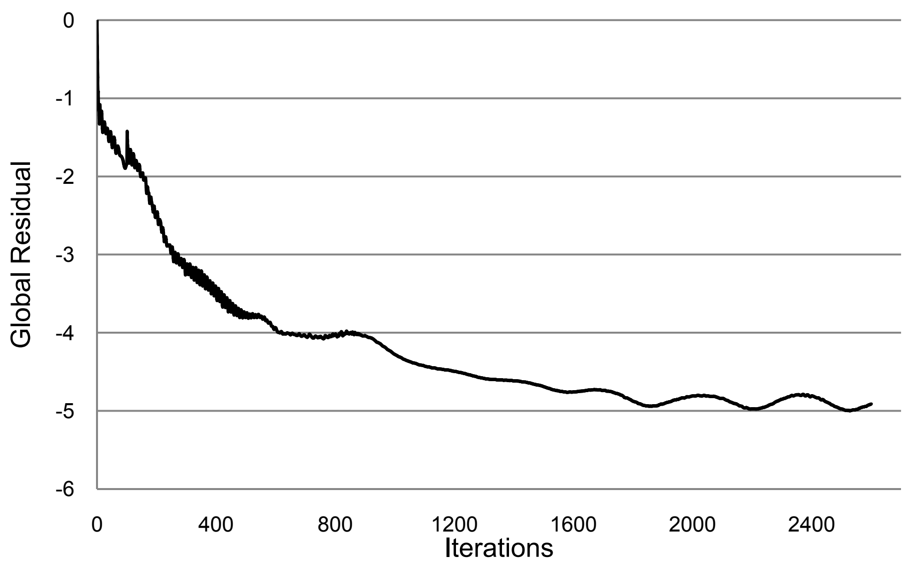

Figure 3.48: History of convergence of NREL VI computation without preconditioner at 5 m/s

From Figure (3.46), the solution with Merkle preconditioner has converged after about 1300 iterations. The convergence level of 5 orders was reached after 800 iterations. On the other hand, this level of convergence was attained after 2000 iterations in the case of Hakimi and no-preconditioner solutions.

So the usage of Merkle preconditioner has speeded up the convergence by about two times.

The results are shown in terms of pressure coefficient distribution at different spanwise sections of the blade.

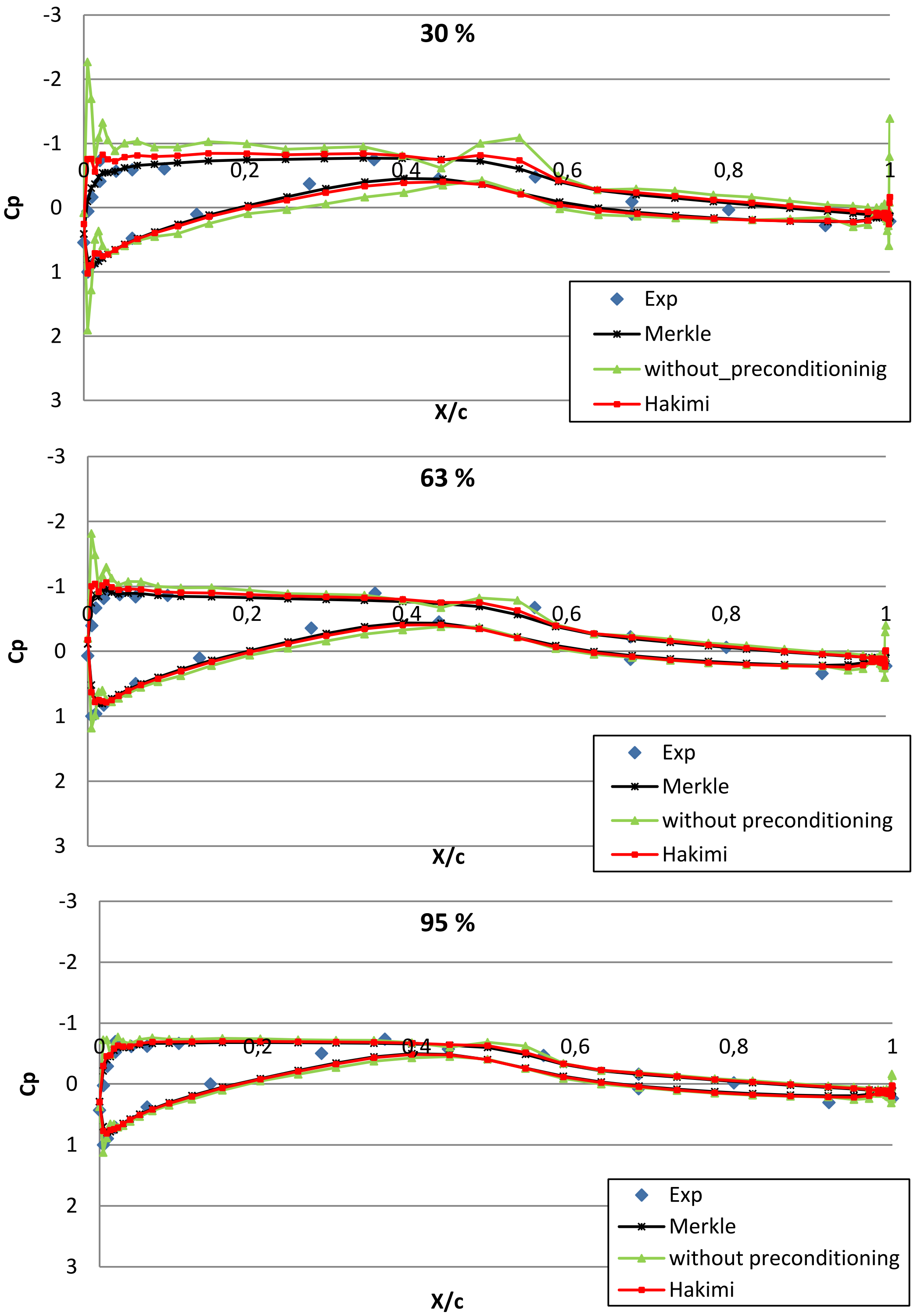

Figure 3.49: Comparison between preconditioning models at 5 m/s

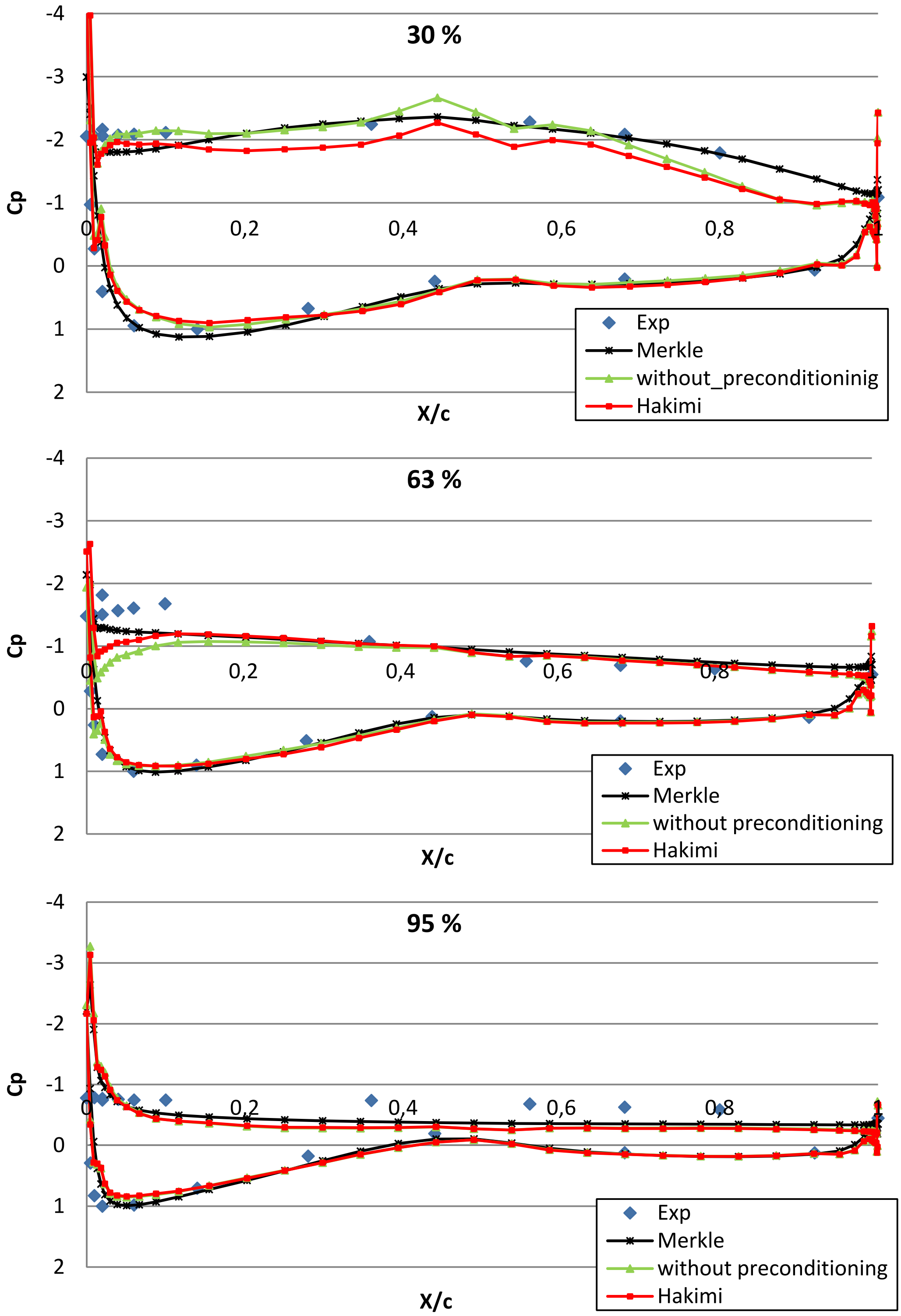

Figure 3.50: Comparison between preconditioning models at 19 m/s

From the results above, at 5m/s, it is clear that the solution without preconditioning gives bad results especially in the sections close to the root. At these sections, the speed is very low. Moving towards the tip, the speed increases and the solution without preconditioning becomes better.

The speed is calculated by adding the wind speed and the speed due to rotation as follow:

$$U = \sqrt{U_0^2 + (\Omega r)^2} \tag{3.6}$$

where U_0 is the free stream wind speed and Ω is the rotational speed (in this test, $\Omega = 72\text{ RPM} = 7.54\, rad/s$). r is the radial distance from the root to the section.

For the 5m/s case;

- At 30% span, U = 13.50 m/s $\Longrightarrow$ M = 0.039
- At 63% span, U = 26.75 m/s $\Longrightarrow$ M = 0.078
- At 95% span, U = 39.94 m/s $\Longrightarrow$ M = 0.120

In Figure (3.49), a pump is noticed at 30% span at the suction side in the case of no preconditioning. To understand the physics behind this pump, the relative velocity vectors are plotted as in Figure (3.51). From this figure, the velocity vectors are smooth at the surface showing no problem in the velocity distribution. In fact no physical conclusion could be drawn for the existing pumps.

At 19m/s, non-preconditioned solution improved even close to the root. Because the speed now is higher.

For the 19m/s case;

- At 30% span, U = 26.75 m/s $\Longrightarrow$ M = 0.078
- At 63% span, U = 32.43 m/s $\Longrightarrow$ M = 0.094
- At 95% span, U = 43.94 m/s $\Longrightarrow$ M = 0.127

Comparing the Hakimi model with the Merkle model, we see that Merkle model gives more accurate solutions in all the sections. Based on these results, it is decided to use the Merkle preconditioner throughout the work of this thesis. Note that the solution obtained by Hakimi preconditioner started convergence at β^*=300.

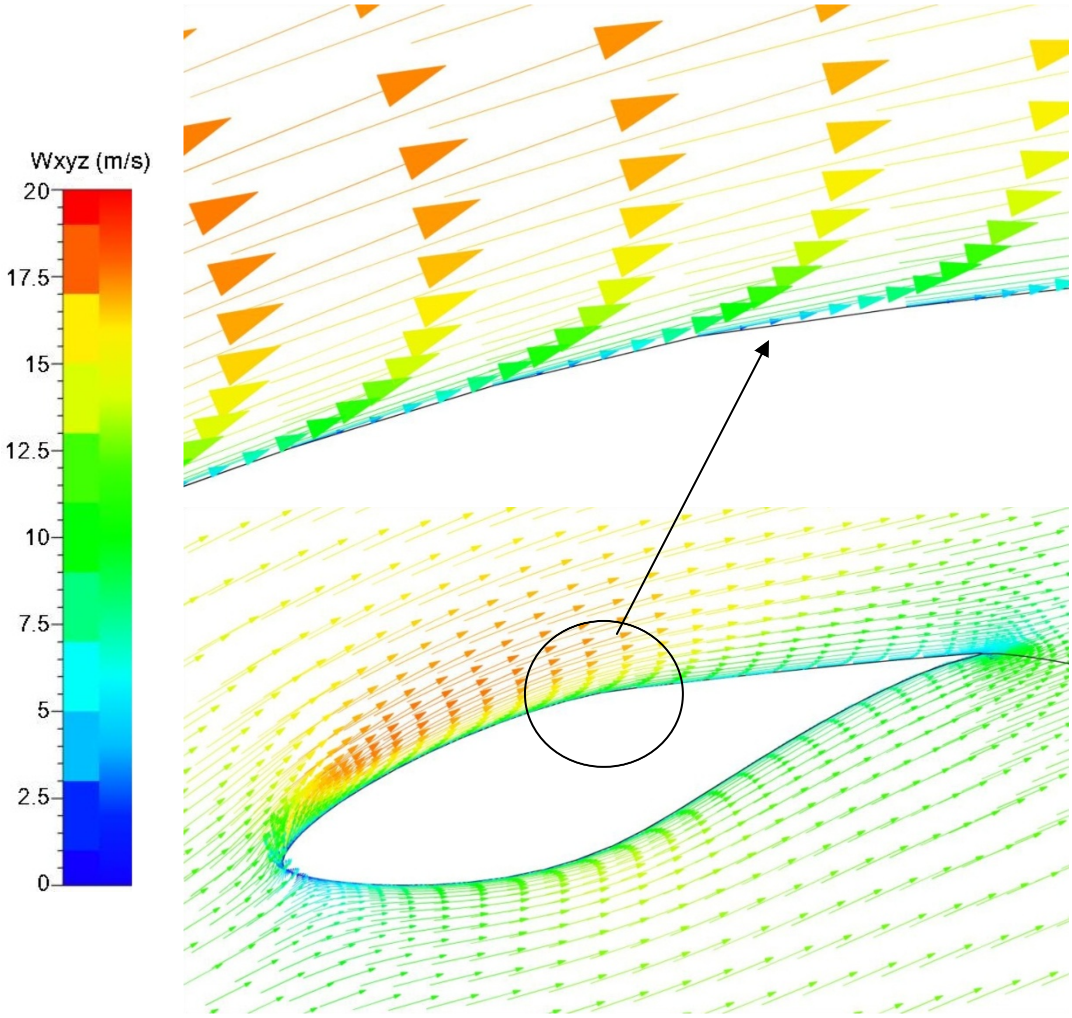

Figure 3.51: Velocity vectors at 30% span for no-preconditioning at 5m/s

CHAPTER 4

CFD SIMULATIONS FOR THE EFFECT OF WINGLETS TWIST AND PITCH

The NREL Phase VI rotor blade was selected to be the baseline blade for the coming studies. This chapter consists of two main parts; first to see the effect of adding a winglet to the blade tip on the power production of the turbine and second to see the effects of twisting the blade on the power production of the wind turbine. The study of this chapter can be considered as a pre-design process where the effective parameters will be selected to be the variable parameters in the design process of Chapter 5. The effective parameters are the ones which when changed; the power will be considerably affected. The study will be carried on for wind speeds in the range of 5 – 9 m/s. The reason behind selecting this range is that the average of wind speed usually falls within this range.

The main aim of this chapter is to study different winglet and twist configurations and decide about the best ones to be used for the design and optimization in Chapter 5. Using all possible configurations for the design will result in huge CPU time consumption and will need large computer resources for the calculations. So limiting the number of configurations and variable parameters will result in much less CPU time needs.

The chapter will start with the effect of winglets and then shift to the effect of twist. The chord change also has a great effect on the power production. However, in this study the chord will not be considered as an optimization parameter because changing the chord results in changing the structural properties of the blade, and this thesis aims at designing a more powerful wind turbine blade without changing its weight significantly.

4.1 Winglet Study

The idea is to add a winglet which is able to carry aerodynamic loads so that the vortex caused by the winglet spreads out the effect of the tip vortex which results in decreasing the downwash and reducing the induced drag [51].

To understand how the winglet reduces the drag, it is necessary first to understand the difference between the profile drag and induced drag.

The profile drag is a consequence of the viscosity of the air moving on the airfoil surface, as well as due to the pressure drag. As the wind turbine blades moves in the viscous air, part of the air sticks to while other is kept in motion. For the air to rotate with the blade, it must have taken energy from the blade. The profile drag is the cause of this transfer of energy from the blade to the air. The profile drag depends on many factors including the wetted area of the blade, the shape of the blade airfoil and the angle of attack [106, 107].

On the other hand, the induced drag is a consequence of producing lift by the blade. If there is lift, then there must be pressure difference between the sides of the blade. And the sides are distinguished as the pressure side (the side which has higher pressure) and the suction side (the side which has lower pressure). Due to this pressure difference, there is a flow around the tip from the pressure side to the suction side. This flow which is a spanwise flow is felt all along the trailing edge as the flow leaving the suction side moves inward while the flow leaving the pressure side moves outward. Once these two opposing flows meet at the trailing edge, they give rise to a swirling motion that is concentrated into the known tip vortices. The generation of vorticies requires energy and this energy is transferred from the blade to the air. This transfer of energy is induced drag.

The induced drag can be reduced by reducing the spanwise flow. The winglets provide a way to do that [108]. The idea of adding a winglet to the wind turbine blade is to produce a flow opposing the flow produced by the blade. This flow will tend to cancel or weaken the main flow of the blade and hence reduce the spanwise flow and consequently reduce the induced drag. The winglet diffuses or spreads out the influence of the tip vortex and as a result it reduces the induced drag. One should remember that, adding a winglet also results in increasing the wetted area, hence increasing the profile drag. So the designer’s aim is to obtain the most reduction in induced drag for the smallest increase in profile drag.

4.1.1 Winglet Configurations

The winglet is added by extending the blade tip by 1.5 % of the blade radius and then tilting the extra section. Based on the tilting direction, four winglet configurations have been tested to check for the best configuration for power production:

- Configuration 1: The blade tip is tilted towards the pressure side (PS)
- Configuration 2: The blade tip is tilted towards the suction side (SS)
- Configuration 3: The blade tip is tilted tangentially towards the (LE)
- Configuration 4: The blade tip is tilted tangentially towards the (TE)

For each configuration, two cant angles and two twist angles have been examined to see the effect of cant and twist angles on the power production.

The definition of the cant and twist angles of the winglet is shown in Figure (4.1):

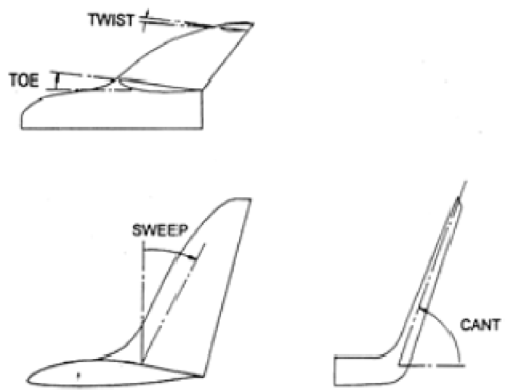

Figure 4.1: Cant and twist angle definition of winglets [50]

The produced winglets are summarized in Table (4.1):

Table 4.1: Winglets for configuration 1

Winglet	Cant angle (deg.)	Twist angle (deg.)
WL1-1	45	0
WL1-2	45	2
WL1-3	90	0
WL1-4	90	2

Where, WL1-1 refers to winglet 1 of configuration 1, WL1-2 refers to winglet 2 of configuration 1 and so on for the winglets of the other configurations. So total of 16 winglets have been tested. The different winglet configurations are shown in Figure (4.2).

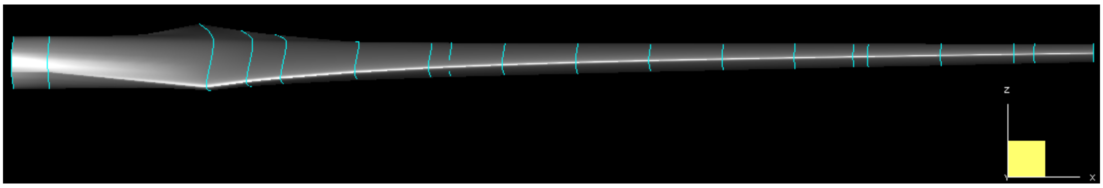

a) Original blade

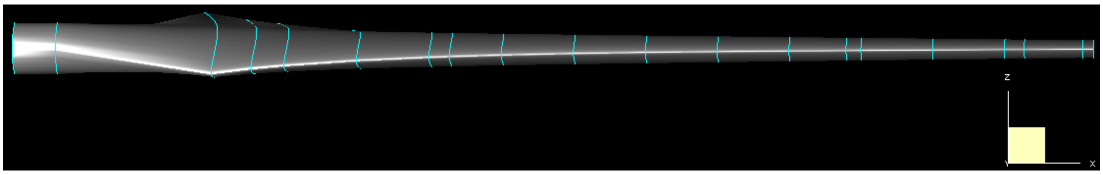

b) 1.5% extension

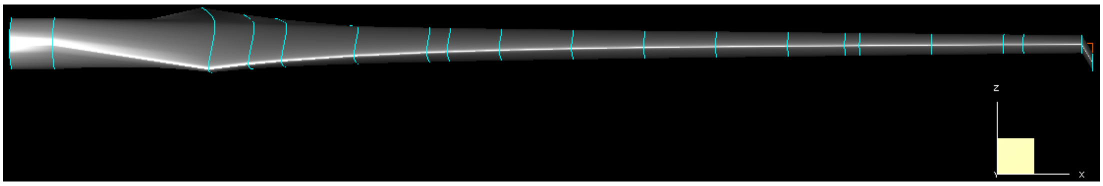

c) Tilting towards pressure side (WL 1-1)

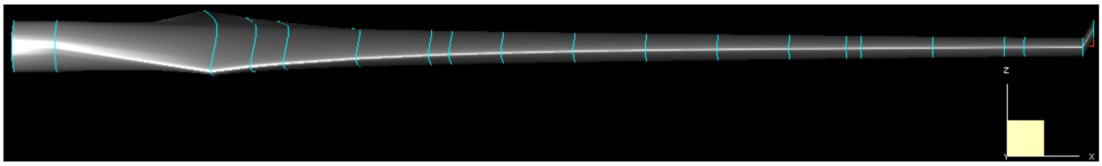

d) Tilting towards suction side (WL 2-1)

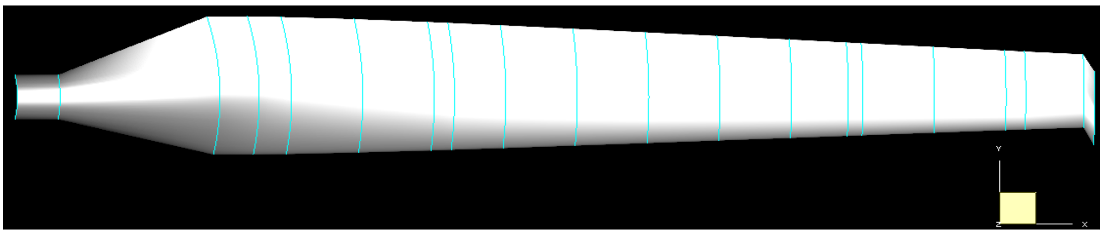

e) Tilting towards leading edge (WL 3-1)

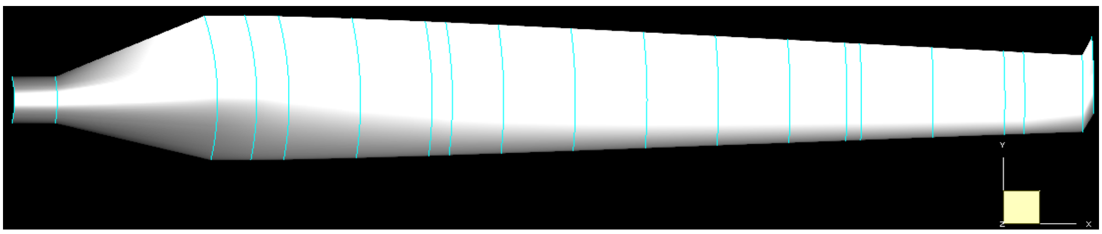

f) Tilting towards trailing edge (WL 4-1)

Figure 4.2: Different winglet configurations

4.1.2 CFD Simulations and Results

The same mesh topology used in Section (3.2) is applied here. The results were obtained by solving the RANS equations with the $k - \varepsilon$ Launder – Sharma as the turbulence model and the Merkle preconditioner. The results are obtained for the wind speed range between 5 and 9 m/s.

It is important to calculate the percentage of power increase due to the different winglet configurations. The percentage of computed power and thrust increase with respect to the original blade geometry for each configuration are listed below:

Configuration 1: Tilting towards PS

Table 4.2: Percentage of power increase for the winglets of configuration 1

Wind speed (m/s)	WL1-1		WL1-2		WL1-3		WL1-4	
	Power %	Thrust %	Power %	Thrust %	Power %	Thrust %	Power %	Thrust %
5.0	-3.15	0.73	-2.24	0.10	-0.25	0.70	-2.24	0.10
6.0	1.28	0.84	-0.50	0.56	1.92	1.13	-0.50	0.56
7.0	1.51	1.22	1.64	0.84	1.87	1.07	1.64	0.84
8.0	-0.57	0.46	0.48	0.78	1.80	0.98	0.38	0.72
9.0	1.48	0.87	0.11	0.06	1.42	1.10	0.11	0.06

Configuration 2: Tilting towards SS

Table 4.3: Percentage of power increase for the winglets of configuration 2

Wind speed (m/s)	WL2-1		WL2-2		WL2-3		WL2-4	
	Power %	Thrust %	Power %	Thrust %	Power %	Thrust %	Power %	Thrust %
5.0	4.80	3.49	3.54	2.69	2.69	3.16	3.54	3.28
6.0	5.03	3.47	4.74	3.19	5.05	3.75	5.05	3.66
7.0	4.64	3.35	3.56	2.82	3.67	3.20	3.03	2.74
8.0	4.66	3.39	4.57	3.13	4.95	3.52	4.76	3.39
9.0	4.56	3.64	3.72	2.78	2.66	2.37	3.72	2.89

Configuration 3: Tilting towards LE

Table 4.4: Percentage of power increase for the winglets of configuration 3

Wind speed (m/s)	WL3-1		WL3-2		WL3-3		WL3-4	
	Power %	Thrust %	Power %	Thrust %	Power %	Thrust %	Power %	Thrust %
5.0	-0.75	0.97	-1.82	0.24	-4.93	-1.38	-1.02	0.45
6.0	0.34	1.31	0.61	0.75	-0.50	-0.28	0.93	1.04
7.0	0.82	0.91	1.73	1.07	0.70	0.23	1.52	0.64
8.0	3.33	2.15	1.24	0.78	1.14	0.52	1.28	0.83
9.0	2.47	1.79	0.79	0.52	1.25	0.81	0.81	0.57

Configuration 4: Tilting towards TE

Table 4.5: Percentage of power increase for the winglets of configuration 4

Wind speed (m/s)	WL4-1		WL4-2		WL4-3		WL4-4	
	Power %	Thrust %	Power %	Thrust %	Power %	Thrust %	Power %	Thrust %
5.0	0.75	1.40	-1.72	0.02	-1.46	0.18	-4.25	812.90
6.0	0.82	1.59	0.75	1.03	-0.04	0.38	-1.43	1064.00
7.0	2.33	1.75	1.61	1.14	1.02	0.69	-0.50	1311.00
8.0	2.95	1.96	1.24	0.72	1.14	0.72	-0.38	1527.00
9.0	1.86	1.62	0.94	0.75	0.56	0.46	-0.50	1724.00

From the results above, it is clear that the best configuration for increasing the power production is to place the winglet towards the suction side. This result is in agreement with the results obtained in Ref. [49, 109].

Also it is clear that changing the cant and twist angles has a considerable effect on the power production. WL2-1 gives the best power results at 5 m/s while WL2-3 gives better results at 8m/s. To obtain the maximum power for a wide range of wind speeds, multipoint optimization is necessary. The multipoint optimization is explained in details in Chapter 5.

Being the best configuration, configuration 2 will be selected for further results and for the optimization in Chapter 5 as well.

Not only the power increases with a winglet but also the axial thrust. Hence, a load analysis is necessary to see the structural effects of the additional thrust.

To see the effect of the winglets on the separation and vortex formation, the relative velocity streamlines are plot for the winglets WL2-1 and compared with the original blade at different spanwise sections. However, since the stall starts after 9 m/s wind speed, the separation and vortex formation will be very clear at higher speeds. So the CFD computations are made again at wind speed 15 m/s.

The relative velocity contours with streamlines at 9 and 15 m/s are shown in Figures (4.3) and (4.4).

It is clear that the winglet has a slight effect on changing the separation and tip flow characteristics, hence pressure distributions and power levels. This is seen especially at 15m/s in sections 63% and 80%.

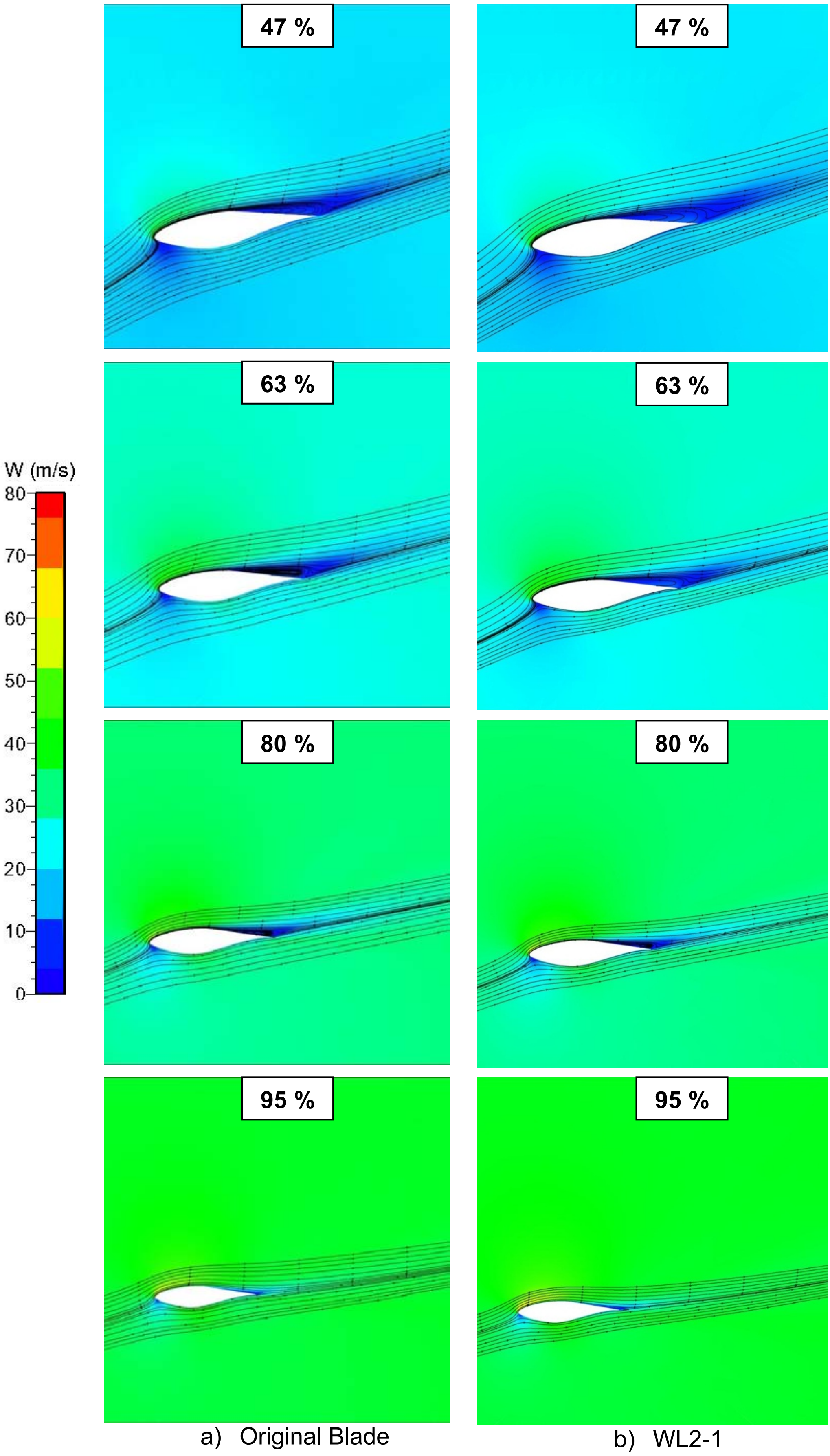

Figure 4.3: Relative velocity contours with streamlines comparison at 9m/s

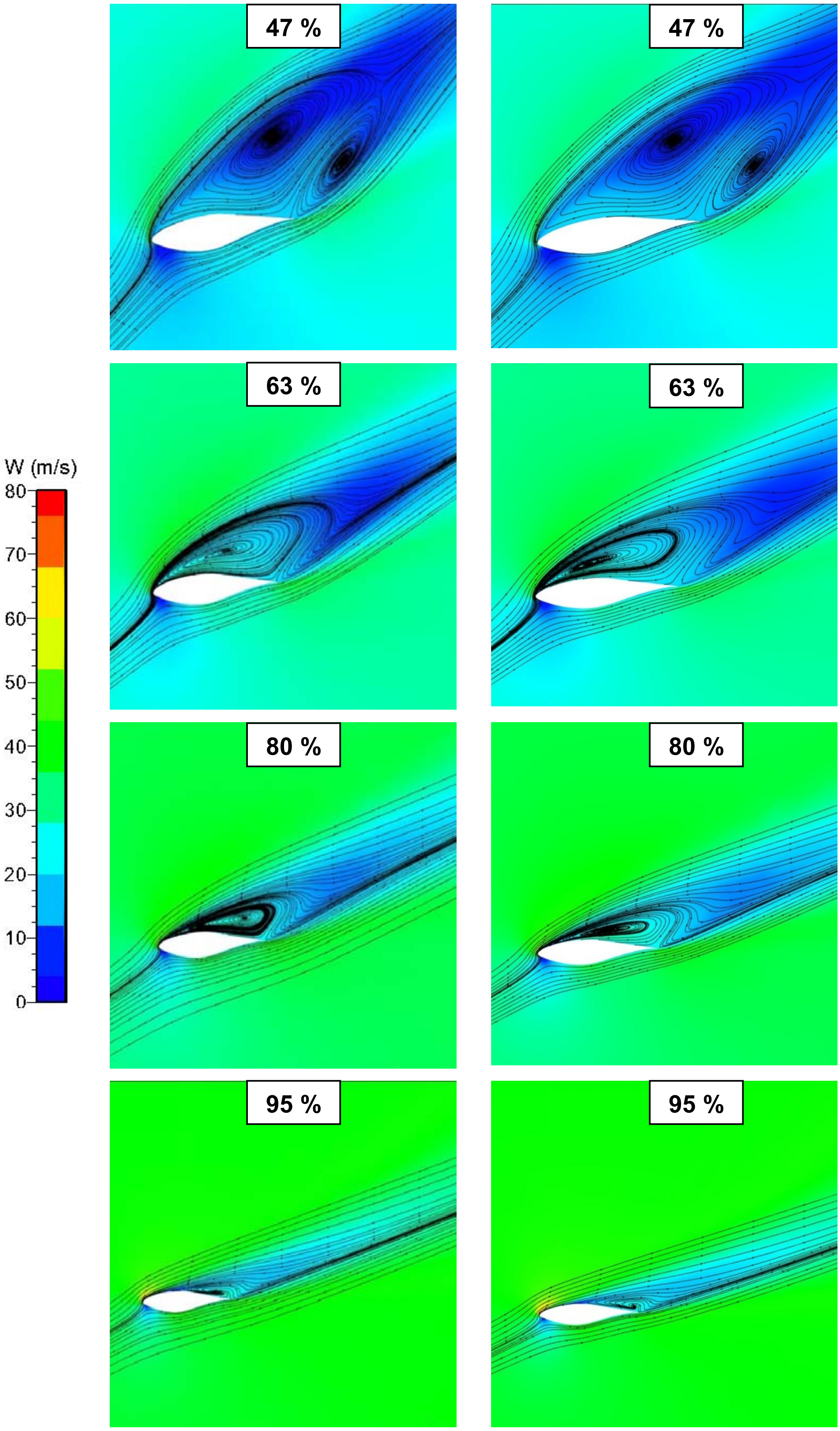

a) Original Blade b) WL2-1

Figure 4.4: Relative velocity contours with streamlines comparison on at 15 m/s

From the results obtained for the winglets, one may notice that the increase in power due to the winglets is still small. In the average of 3.5%. As mentioned before, the winglets had slight effect on the separation and vorticies. This means that, the power increase is not only due to weakening the vorticies but also due to reduction in the tip losses. An optimization of the cant and twist angels will result in more power production as stated in Chapter 5.

To better see the change in vorticity due to winglets, the magnitude of vorticity iso-surface are plotted for all the winglets of configuration 2 as well as for the original blade at 9 and 15 m/s.

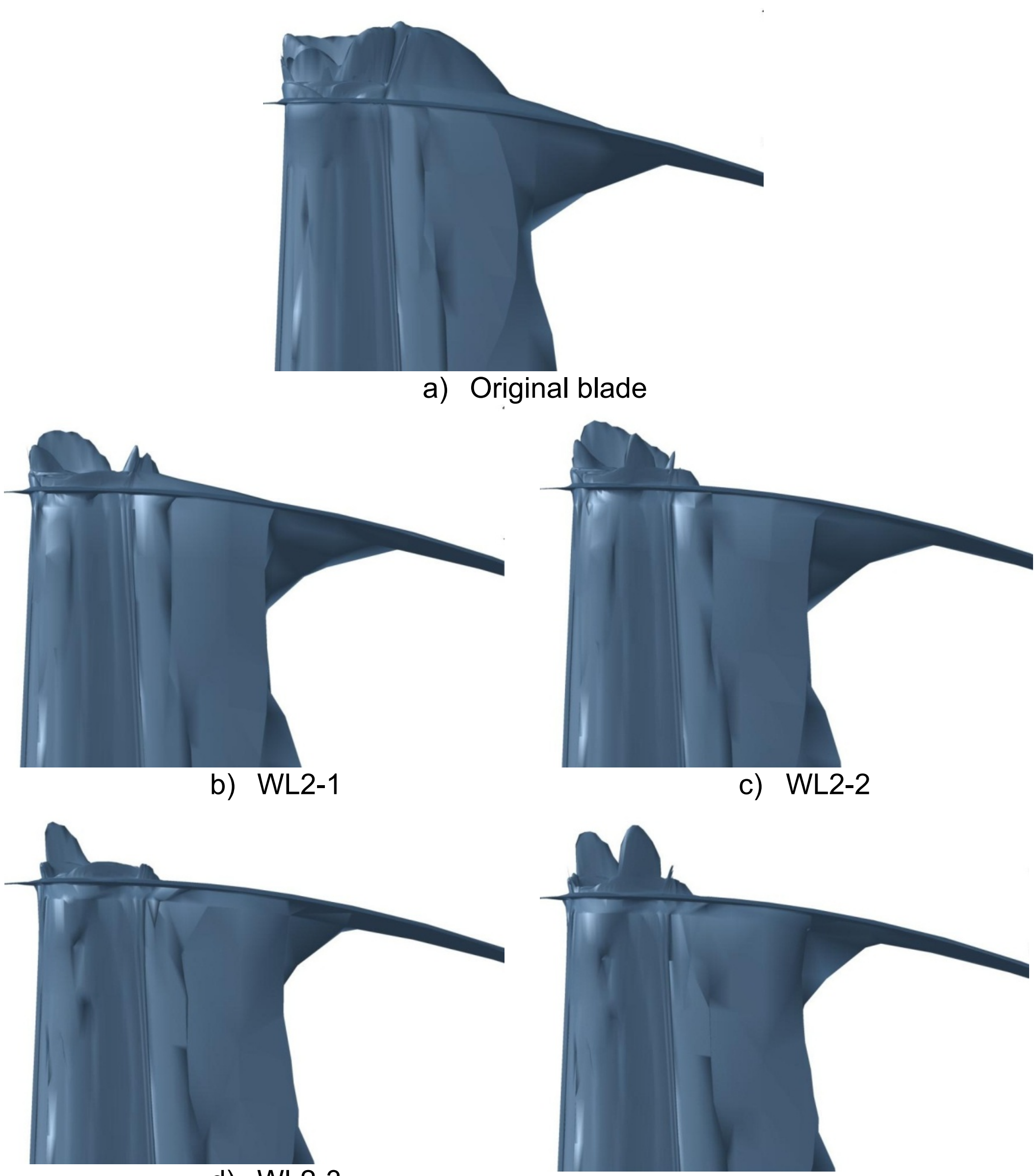

a) Original blade

b) WL2-1

c) WL2-2

d) WL2-3

e) WL2-4

Figure 4.5: Comparison of vorticity magnitude iso-surface at the blade tip region for different winglets at 9 m/s

a) Original blade

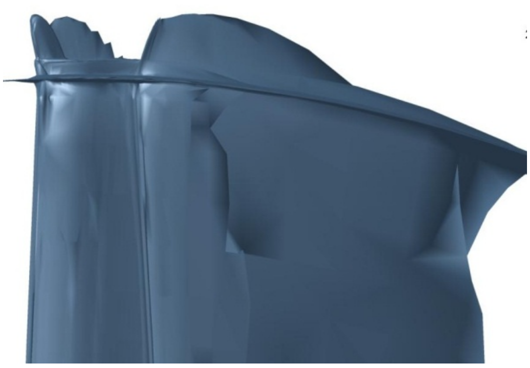

b) WL2-1

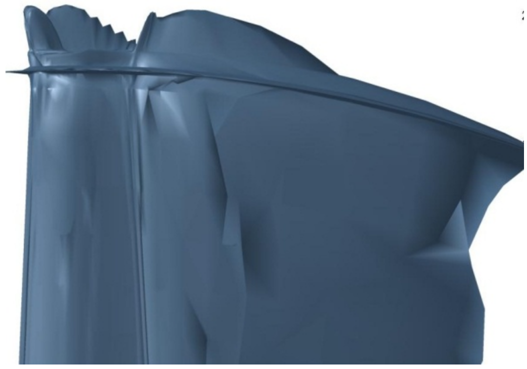

c) WL2-2

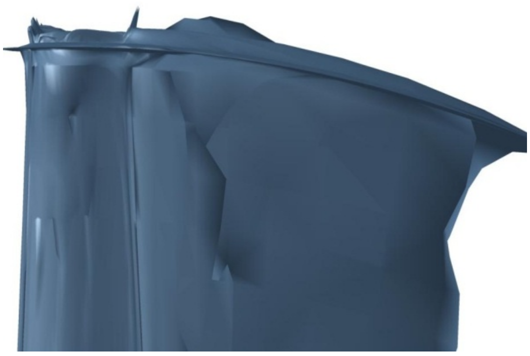

d) WL2-3

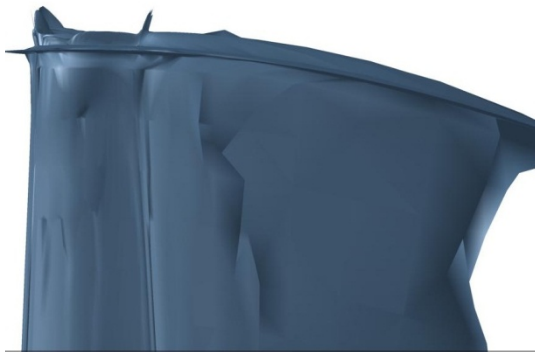

e) WL2-4

Figure 4.6: Comparison of vorticity magnitude iso-surface at the blade tip region for different winglets at 15 m/s

It is clear from the above figures that the addition of winglets changes the magnitude of vorticity. Moreover, the vorticity magnitude is different for different winglets. More and investigations about the winglets are available in Chapter 5.

4.2 Blade Pitch and Twist Study

The pitch and twist angles are very important parameters which have a considerable effect on the power production of wind turbine rotor blades. The twist angle decides on the values of the local angle of attack. Twisted blades for wind turbines have been proved to be superior to the untwisted ones due to their full utilization of the blade area to produce lift at low drag. The twist angle is defined in Figure (4.7) (reproduced from [31]):

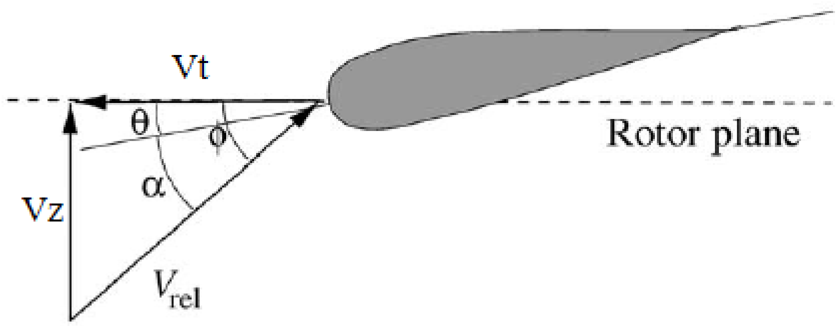

Figure 4.7: The pitch and twist angles definition

Where V_t is the tangential velocity, V_z is the axial velocity and V_{rel} is the relative velocity.

The angles appearing in Figure (4.7) are defined as follow:

- α: is the angle of attack defined as the angle between the chord line and the relative velocity.
- ϕ: is the flow angle defined as the angle between the relative velocity and the plane of rotation.
- θ: is the local pitch angle defined as the angle between the local airfoil chord line and the plane of rotation.

In fact θ is called the local pitch angle which is a combination of the pitch angle θ_p and the twist angle β:

$$\theta = \theta_p + \beta \qquad (4.1)$$

Where the pitch angle is the angle between the tip chord line and the plane of rotation. And the twist angle is measured relative to the tip chord line. The pitch angle is constant and it is added to the varying twist angle along the blade span.

In particular it is possible to use the twist to influence the flow separation and stall at a certain wind speed. For this reason, the fixed pitch rotor blades are not linearly twisted. The twist angles towards the root are greater than the angles towards the tip. This variation in twist is determined by both the stall characteristics and the starting torque [3].

The effect of different blade twist variations on the power production of the blade can be seen in Figure (4.8). It is clear that non-twisting the blade results in considerable reduction in power. The advantage of untwisted blades is the easy and low cost manufacturing. However, since the modern blades are mostly manufactured in molds and made of fiber glass, manufacturing became also easy for twisted blades. The profit of the more energy produce by twisted blades is more than the price difference of manufacturing untwisted blades.

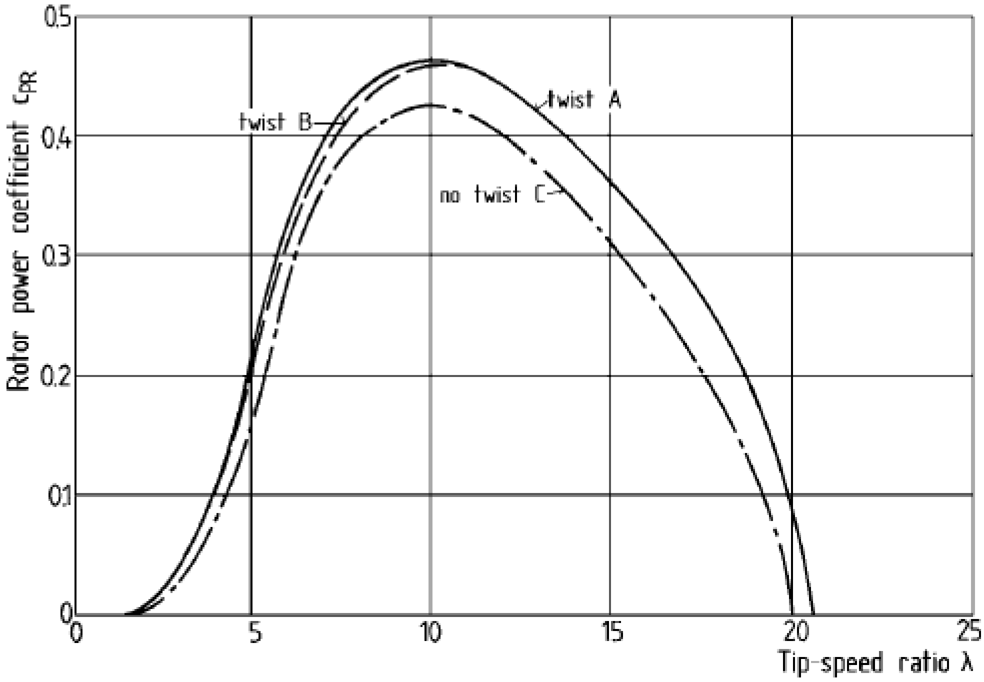

Figure 4.8: Effect of blade twist on the blade power coefficient [14]

The pitch angle effect on the power production of a wind turbine blade is shown in Figure (4.9). Similar results are given in [110].

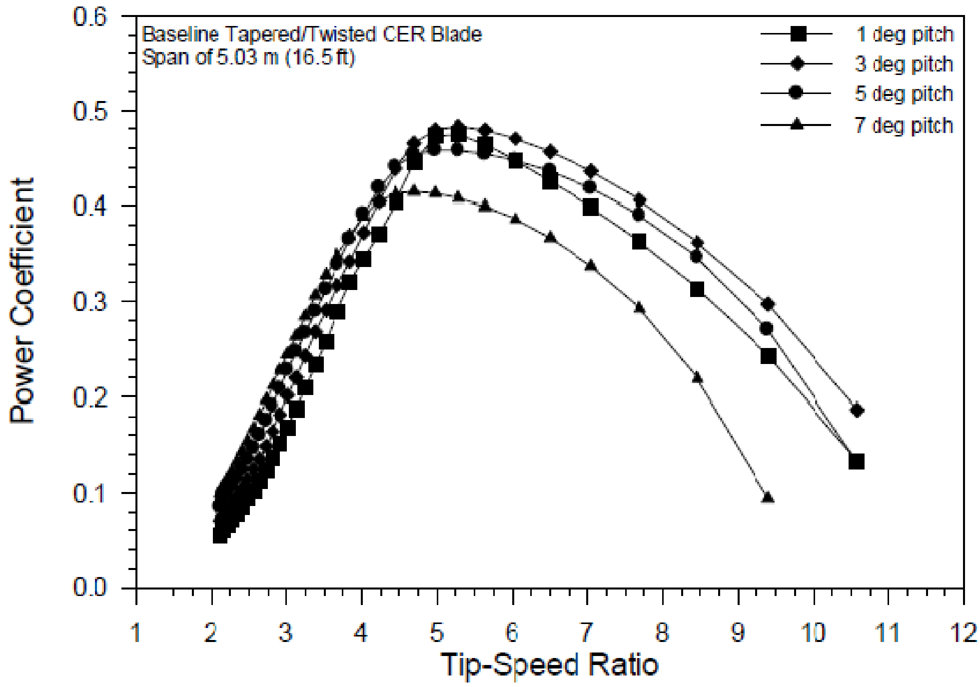

Figure 4.9: Effect of pitch angle on the blade power coefficient [57]

In this section, different pitch and twist configurations were investigated and compared to the original NREL VI blade. The analysis includes the effect of pitch and twist on the power production and the stall characteristics.

4.2.1 Pitch and Twist Configurations

The original NREL VI sequence H blade is of nonlinear twist and 3 degrees of pitch. 11 different positive and negative pitch angles have been investigated and compared to the NREL VI H. The angles are between -3 to 8 excluding the 3 degrees angle which corresponds to the original NREL VI H blade.

Positive pitch means twisting down toward wind direction. On the other hand, negative pitch means twisting up away from the wind direction.

In addition to that, another configuration related to twist is investigated. In this configuration, the twist angles of the NREL VI blade have been set to zero keeping the pitch angle of the original blade as 3 degrees. In other words, this configuration is the untwisted form of the NREL VI.

The 3D views of some blades of different pitch angles and untwisted blade are shown in Figure (4.10):

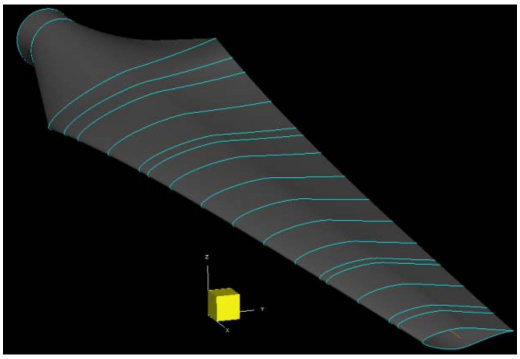
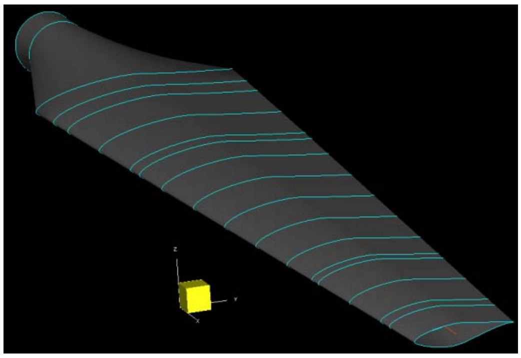

a) NREL VI

b) Untwisted blade

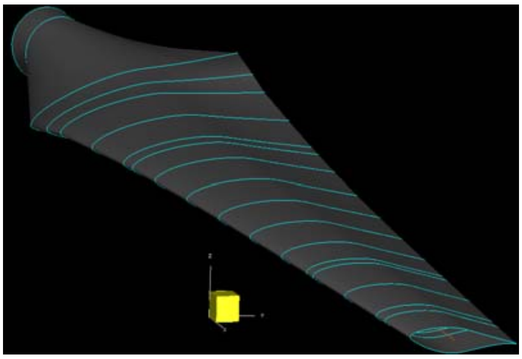
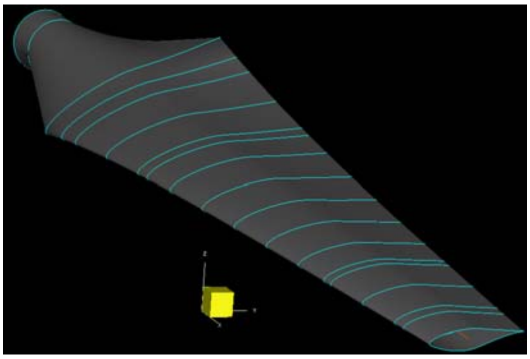

c) Pitch of -3 degree

d) Pitch of 8 degrees

Figure 4.10: 3D view of different pitch and twist configurations

4.2.2 CFD Simulations and Results

Similar to the winglet study, in the twist CFD simulation the same mesh topology used in Section (3.2) is applied. Also, the results were obtained by solving the RANS equations with the $k - \varepsilon$ Launder – Sharma as the turbulence model and using the Merkle preconditioner. The results are obtained for the wind speed range between 5 and 9 m/s.

The change of pitch and twist angles has shown a big effect on the power output. The power curves of selected different pitch angles and the untwisted blade compared to the original blade are shown in Figure (4.11):

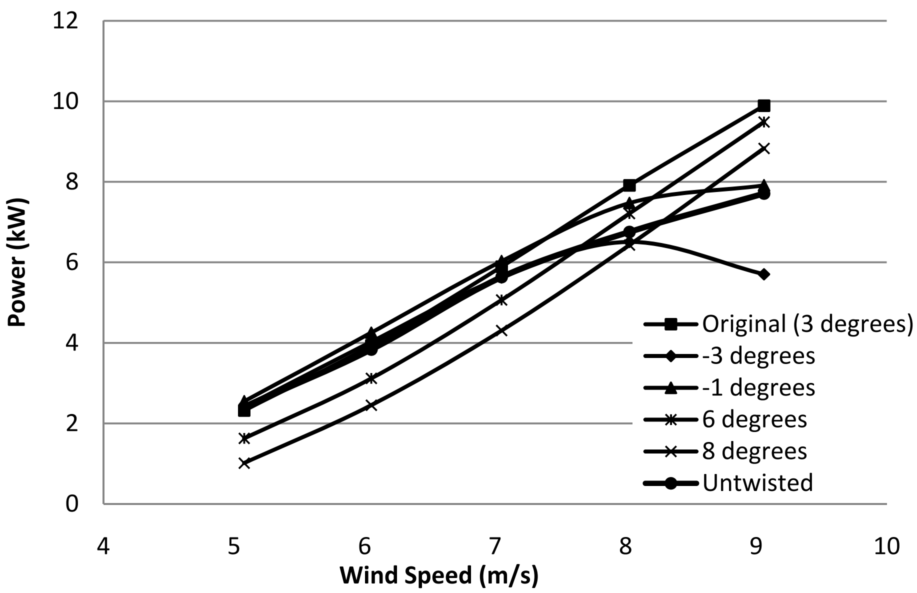

Figure 4.11: Power curves for the different pitch and twist angles

It is clear from Figure (4.11) that the blade of -3 degrees of pitch has stalled earlier than the other blades. Then the stall is delayed as the pitch angle increases. The curves corresponding to the other pitch angles are not included in the plot for sake of clarity. The untwisted blade has also shown an earlier stall.

The percentage of computed power and thrust increase with respect to the original blade geometry for each pitch angle are listed in Tables (4.6), (4.7) and (4.8):

Table 4.6: Percentage of power and thrust increase for the (-3 – 0 deg.) pitch angles

Wind speed (m/s)	-3 deg.		-2 deg.		-1 deg.		0 deg.	
	Power %	Thrust %	Power %	Thrust %	Power %	Thrust %	Power %	Thrust %
5.0	3.70	58.55	8.41	49.36	9.77	39.81	9.80	30.14
6.0	2.29	42.50	5.95	37.05	7.99	30.39	9.08	23.55
7.0	-4.50	30.56	-0.20	26.52	2.30	22.18	3.61	17.07
8.0	-17.75	20.10	-10.20	17.89	-5.58	14.95	-1.81	12.01
9.0	-42.32	11.63	-25.29	11.63	-20.01	8.10	-11.70	6.42

Table 4.7: Percentage of power and thrust increase for the (1 – 5 deg.) pitch angles

Wind speed (m/s)	1 deg.		2 deg.		4 deg.		5 deg.	
	Power %	Thrust %	Power %	Thrust %	Power %	Thrust %	Power %	Thrust %
5.0	8.89	8.09	4.61	9.92	-8.86	-10.06	-14.35	-21.20
6.0	5.99	15.95	4.40	7.79	-6.35	-8.93	-13.39	-17.79
7.0	4.19	11.74	1.83	5.87	-3.64	-7.01	-9.27	-14.02
8.0	-0.10	8.16	-0.29	3.66	-2.86	-5.94	-4.91	-11.10
9.0	-5.76	4.74	-2.56	2.14	-0.73	-4.74	-1.95	-25.56

Table 4.8: Percentage of power and thrust increase for the (6 – 8 deg.) pitch angles

Wind speed (m/s)	6 deg.		7 deg.		8 deg.		Untwisted	
	Power %	Thrust %	Power %	Thrust %	Power %	Thrust %	Power %	Thrust %
5.0	-29.80	-32.90	-45.60	-43.85	-56.28	-55.88	3,86	11,41
6.0	-20.81	-25.95	-27.40	-34.88	-37.73	-42.38	-2,64	9,29
7.0	-14.02	-21.27	-20.29	-28.44	-26.88	-35.79	-4,37	5,11
8.0	-8.86	-16.91	-14.58	-23.04	-18.72	-29.11	-14,63	2,61
9.0	-4.08	-13.36	-7.66	-18.45	-10.71	-23.08	-22,06	1,74

From the results above, there is a great change in the power for the different twist and pitch angles.

To understand the effect of the twist and pitch angles on the stall characteristics, the relative velocity contours with streamlines are plotted at different sections of the blade for pitch angles of -3 degrees and 8 degrees at 9 m/s.

From Figures (4.12) to (4.14), it is clear that the stall characteristics have been affected. In the cases of -3 degrees pitch and untwisted blade, the stall starts earlier. This is clear from the vortices formed at the suction side. Where in the case of 8 degrees pitch, the stall has been delayed. This is clear from the smooth streamlines leaving the trailing edge of the suction side.

The best pitch angle seems to be the pitch angle of the original NREL VI blade which is 3 degrees. At this angle the power is high at wide range of wind speeds. The pitch angles less than 3 degrees, they produce more power at low wind speeds but with a drastic decrease in power at moderate wind speeds. Pitch angles higher than 3 degrees, produce low power at both low and moderate wind speeds. More results for the pitch angle effect on the power production at low, mid and highe wind speeds are available in Chapter 5.

Based on the results of this chapter, one can see the effects of the winglet and the twist on the wind turbine power production. It is hard to guess the best winglet shape and the best twist distribution for the maximum power production for wide range of operating wind speeds. This task needs optimization techniques as explained in details in Chapter 5.

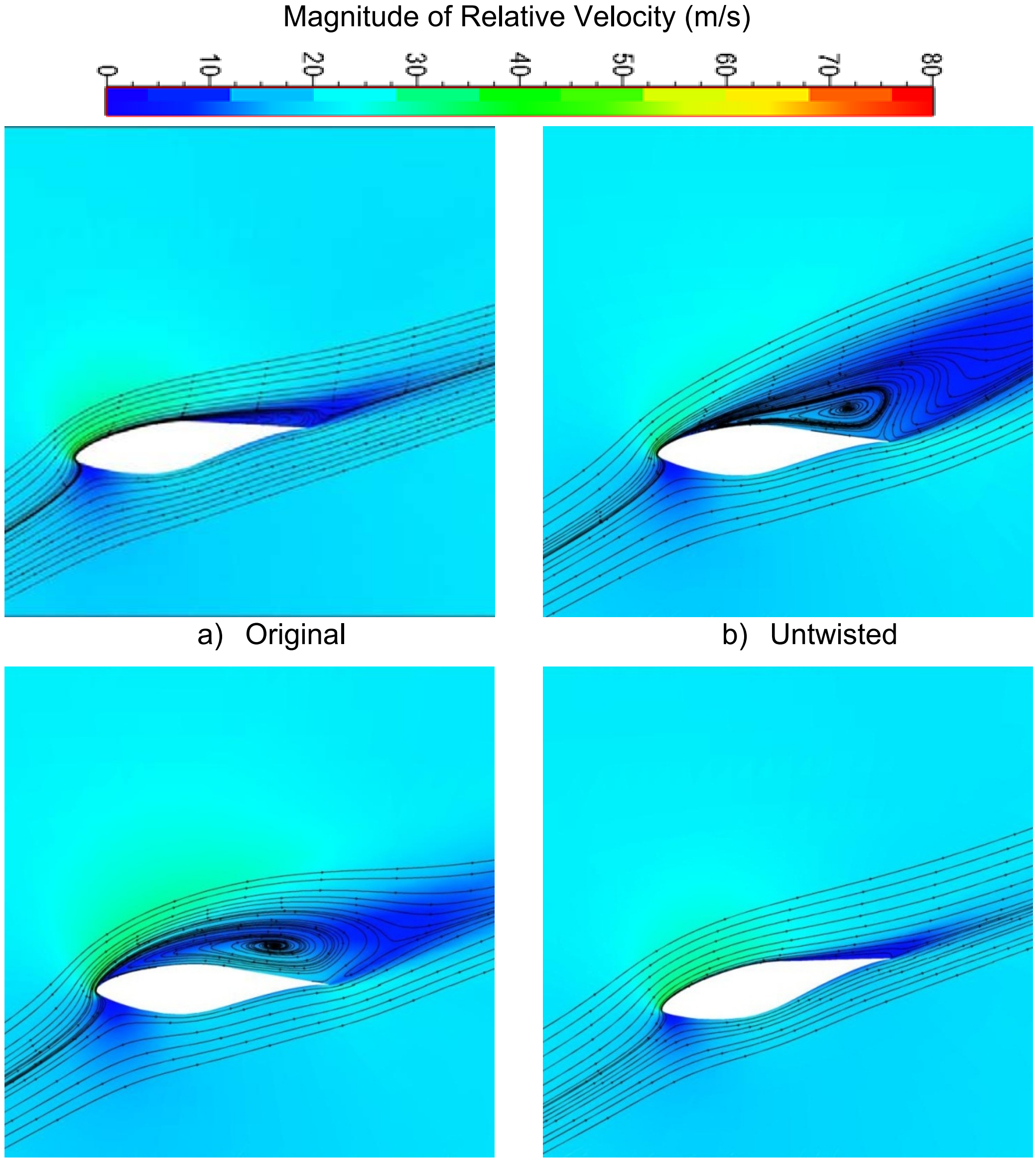

a) Original

b) Untwisted

c) Pitch of -3 degrees

d) Pitch of 8 degrees

Figure 4.12: Relative velocity contours with streamlines at 9 m/s at 47% span for different twist and pitch angles

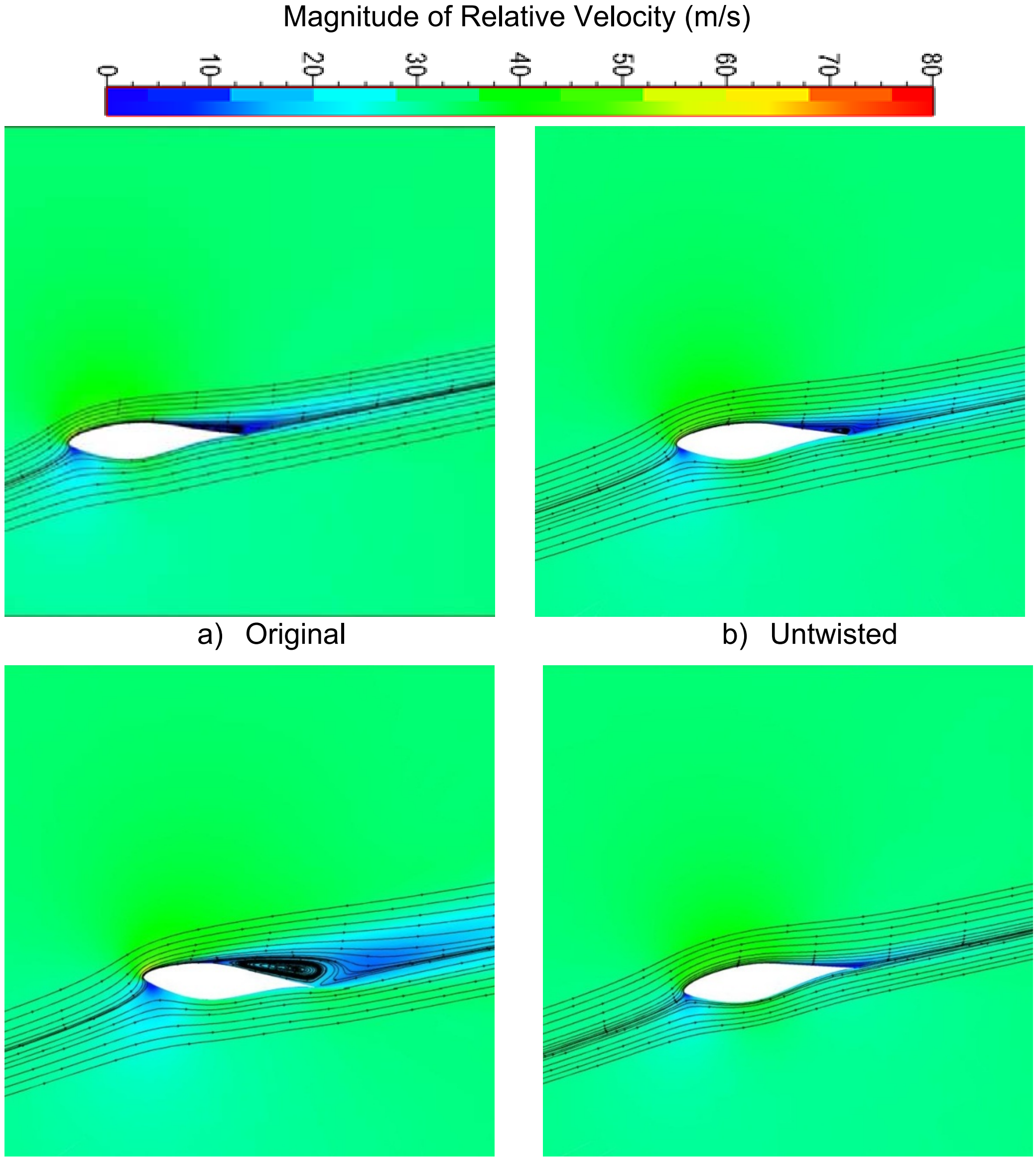

a) Original

b) Untwisted

c) Pitch of -3 degrees

d) Pitch of 8 degrees

Figure 4.13: Relative velocity contours with streamlines at 9 m/s at 80% span for different twist and pitch angles

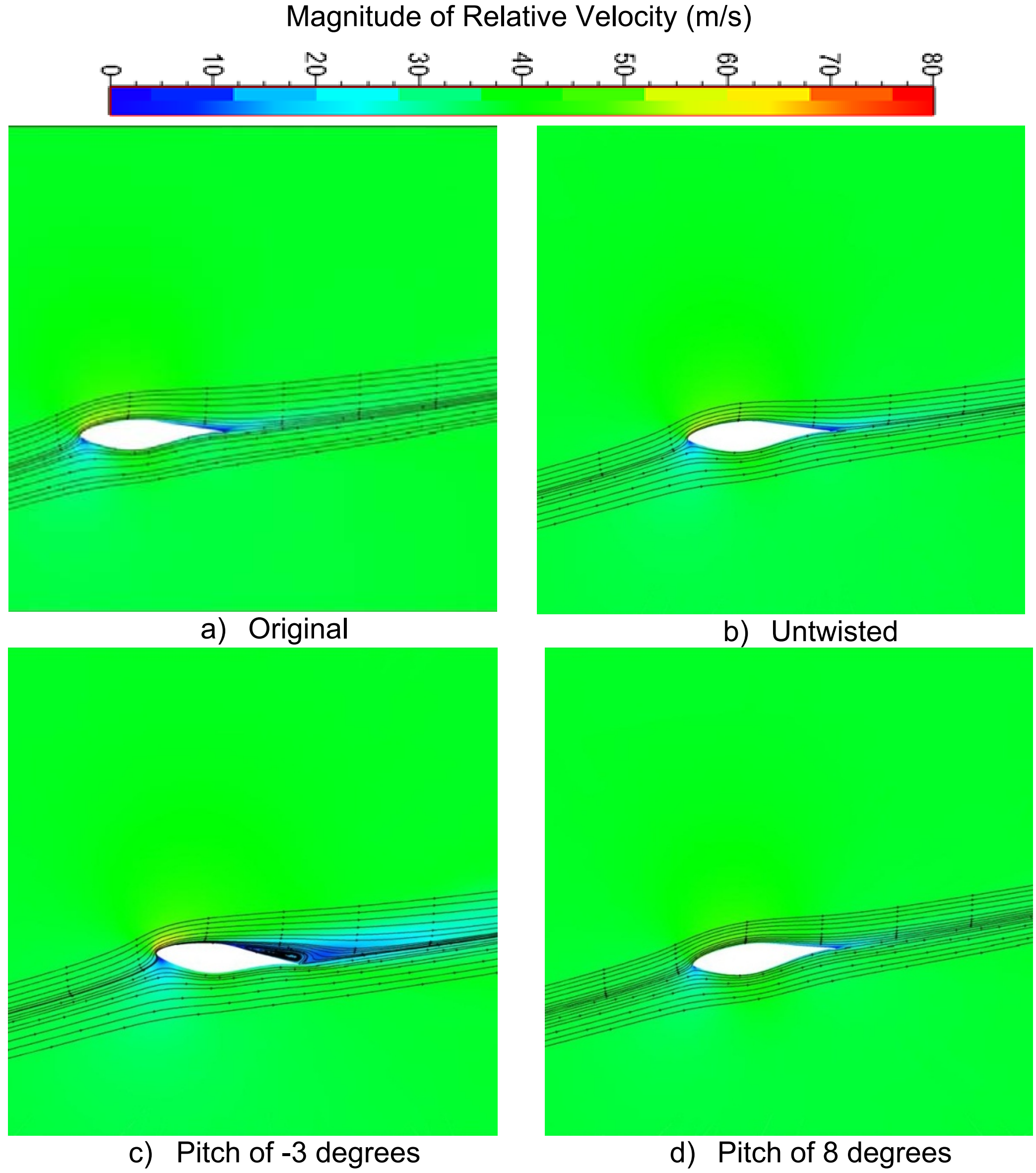

Figure 4.14: Relative velocity contours with streamlines at 9 m/s at 95% span for different twist and pitch angles

CHAPTER 5

AERODYNAMIC DESIGN AND OPTIMIZATION

Optimization of wind turbines is a multidiscipline process including optimization of aerodynamics, structure, electrics and economics. For the wind turbine blades, the aerodynamics optimization is the major concern.

The aim of this study is to optimize the wind turbine blade of NREL VI without major change in the blade structural properties and weight. The objective of optimization is to increase the torque of the blade at low and medium wind speeds. To account for wide range of operating conditions, a multipoint optimization is carried out at different wind speeds. The wind speed range is between 5 and 9 m/s.

First the optimization process and techniques are introduced. Then the winglet which was introduced in the previous chapter will be optimized and after the blade twist will be optimized separately. Finally, a CFD analysis over the final optimized geometry is carried out and the results are compared with the original NREL VI blade.

5.1 Design and Optimization – General Overview

The optimization process starts with a CFD loop which includes four processes; geometric blade generation, mesh generation of the blade, CFD simulation and post-processing. Then the CFD results will be optimized by modifying the geometrical parameters (design variables).

In the optimization, it is too expensive to perform the CFD computations for each possible geometry. Therefore, the CFD results as a function of the geometrical parameters are approximated using Artificial Neural Network (ANN) [111] and an approximate mode is resulted.

The purpose of the approximate model is to have a fast method which is able to evaluate the blade aerodynamic performance. This method requires a database containing several blade geometries and their associated aerodynamic and geometrical performances.

The samples of the database are used to construct the approximate model. Then the CFD loop is carried out only for this model and the results are stored in a new database (which includes the old database as well). Then another approximate model is constructed from the new database and CFD loop starts again and the process continues until the maximum number of the design cycles is reached. So after each design cycle, the number of samples in the database grows and the approximate model becomes more accurate.

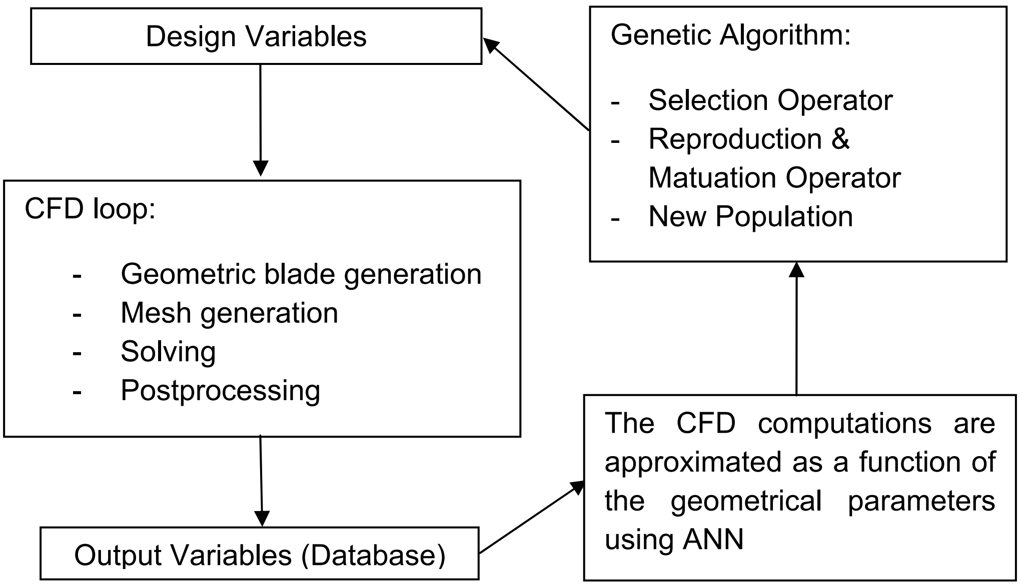

Figure 5.1: Optimization loop

5.1.1 Design Variables and Database Generation

The design variables are the geometric parameters of the blade, such as twist, chord length, airfoil profile,..etc, which change within upper and lower limits to produce different blade shapes. Those shapes are the new geometric blades used in the database. Then, meshing and CFD computations are carried out on each new blade. The new blades and their associated CFD computations are stored in the database.

It should be noted that, the number of design variables should be as low as possible to simplify the optimization process and save CPU time. On the other hand the number of design variables should be as high as possible to obtain more accurate and reliable design.

5.1.2 Objective Function

The objective function refers to the aerodynamic performance that the designer wishes to improve. In the case of wind turbines, increasing the torque and hence increasing the power is the main objective function.

However, in this study, for the several geometrical parameters or CFD results, a penalty is computed such that, the higher the penalty, the further the value from the desired result becomes. Then a pseudo-objective function is defined as the summation of these penalty terms. Thus the optimization problem is to minimize the objective function in function of geometrical parameters subject to some constraints to result in a result closest to the desired result. In other words, the general approach of the optimization problem is to transform the original constrained minimization problem into an unconstrained one by converting the constraints into penalty terms that are increasing when violating the constraints. Mathematically, the penalty Pn is defined as:

$$Pn = W\left(\frac{Q_{imp} - Q}{Q_{ref}}\right)^2 \tag{5.1}$$

Where;

- W : is a weight factor which allows to control the influence of a penalty term on the objective function, it is set by the user
- Q_{imp}: is the imposed quantity
- Q: is the computed quantity
- Q_{ref} is the a reference value

Then, the pseudo-objective function F (also called transfer function) is defined as:

$$F = \sum Pn \tag{5.2}$$

For example if the goal of optimization is to increase the torque, the penalty can be put on the torque with a desired value of 20% of increase in torque. The optimization will then result in a new blade with a torque as close to 20% increase as possible.

5.1.3 Artificial Neural Network (ANN)

The basic principle of using the ANN is to build an approximate model of the original analysis problem. In the approximate model, the CFD computations are approximated as a function of the geometrical parameters. This approximate model can be used in the optimization loop instead of the original model. In this way too much CPU cost by performing CFD computations on every possible geometry is avoided.

The ANN consists of several elementary processing units called nodes. The nodes are arranged in layers as shown in Figure (5.2) [112].

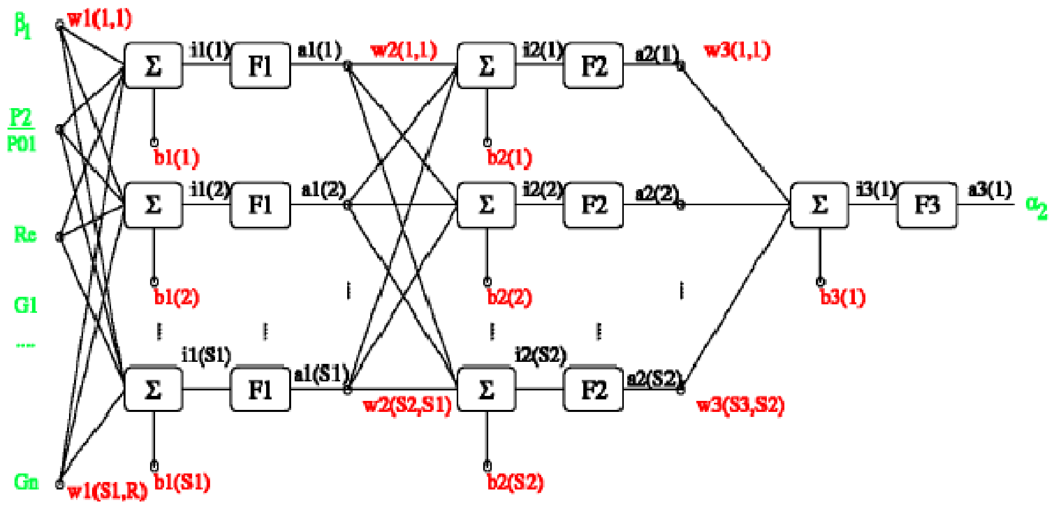

Figure 5.2: Schematic diagram of the ANN [112]

The first input layer connects all the inputs to the network. Whereas, the last output layer produces the outputs. The inputs to the ANN are the geometrical parameters of the blade shape and boundary conditions, where the outputs are the aerodynamic performance parameters. All the inputs of a layer are connected to all nodes by the weighting factor W. Each node performs the summation of the weighted inputs and bias value to form its own output. The result is then processed through the transfer sigmoidal function F. The signal is propagated in the same way up to the output layer. The output of each node of the layer is given as [113]:

$$a_n(i) = F\left[\sum_{j=1}^{S(n-1)} W_{ij}\, a_{n-1}(j) + b(i)\right] = F[i_n(i)] \quad (5.3)$$

Where:

- $a_n(i)$ is the output value of the i^{th} node of output of n^{th} layer
- $b(i)$ is the bias function

Now it is important to find the connection weight matrices and the bias vectors in order to make the actual output vector coincide with the prescribed output vector. Such connection process is called learning process. The learning process leads to the best reproduction of the geometries and CFD computations contained in the database. The algorithm tries to minimize the error that the neural network produces on the database samples. The error is defined as:

$$E^l = \frac{1}{2}\sum_{j=1}^{nout}\left(d_j^l - a_j^l\right)^2 \qquad (5.4)$$

Where;

- d_j^l is the database value of the j^{th} output of the l^{th} sample
- a_j^l is the ANN value of the j^{th} output of the l^{th} sample

In order to eliminate the error, the derivatives of the error are expressed with respect to the weight factors. This allows for the iterative calculations of the weight and bias components modifications.

5.1.4 Optimization Algorithm (Genetic Algorithm)

The choice of the optimization algorithm is mainly based on two considerations:

- Many local optima may exist in the design space and hence global optimization technique is required.
- The evaluation of the blade performance using the approximate model of ANN is very fast. Hence, the number of required function evaluations is less important than if a detailed computation was needed at each step.

Based on the above considerations, the global methods are preferred over the local ones. Among the global methods, the Genetic Algorithm is used in this study.

The generation loop of the genetic algorithm is explained in Figure (5.3):

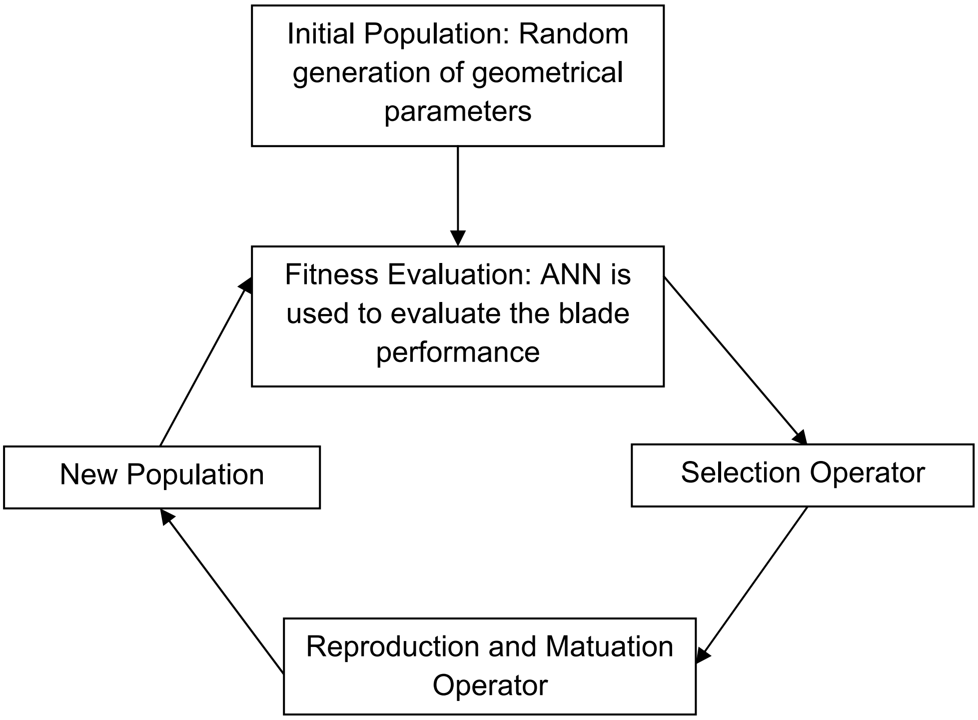

Figure 5.3: Genetic algorithm and generation loop

The terms related to the GA are explained as below:

- *Population size*: Determines the number of individuals generated during the process.
- *Number of reproduction cycles:* Determines how many times the population will be produced.
- *Truncation rate:* Determines the number of samples which are allowed to reproduce. For example if the truncation rate is 20, then only 20 best samples will be used to generate a new sample in the next generation.
- *Elitism:* Determines the number of individuals that are directly transmitted to the next generation. If the elitism is 1, this means that only the best sample is transmitted to the next generation without any modifications.

5.1.5 Illustration of the Optimization process

In this section an illustration to show how the whole optimization process is performed.

Given a flow solution variable F (objective function). Assuming that only one design variable G has been selected. Then the steps for optimization are as follow:

Step 1: Database generation

Assume that only four samples are generated in the database. The exact CFD results of the four samples are shown in Figure (5.4):

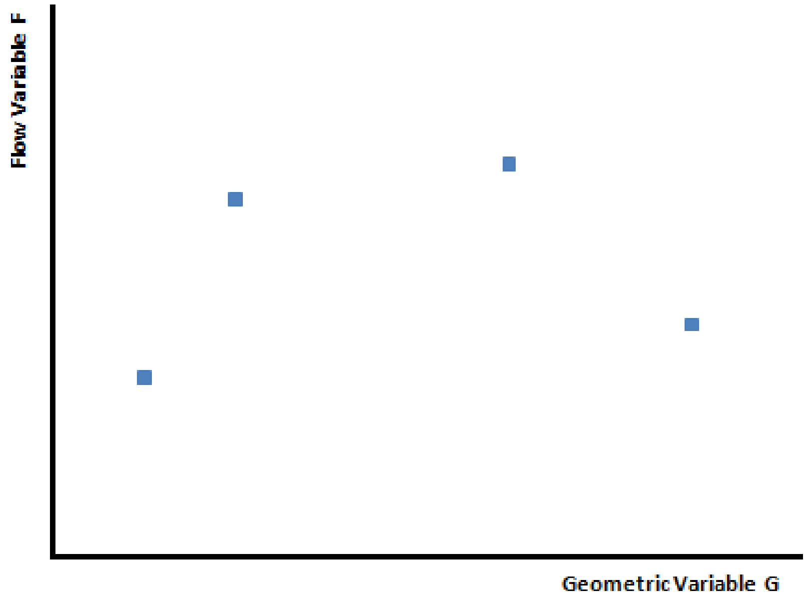

Figure 5.4: Initial database of CFD results

Step 2: Approximation of the CFD computations

The CFD computations are approximated as a function of the geometrical parameters using the ANN.

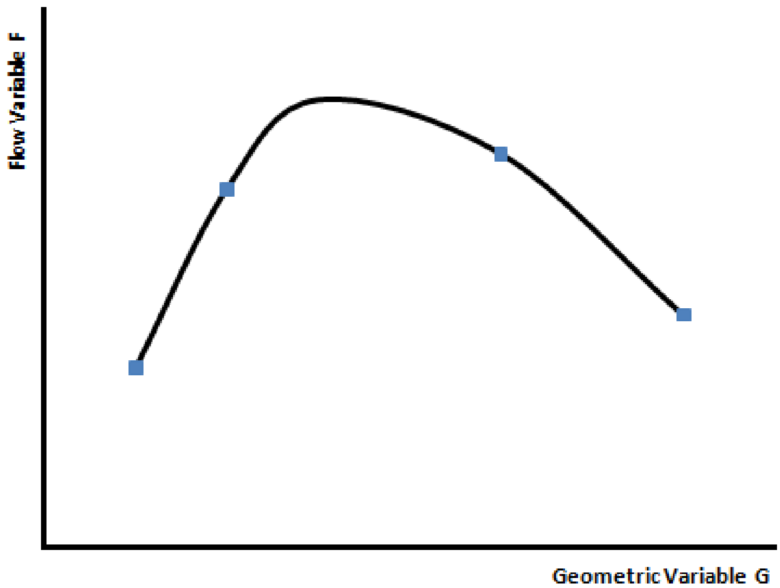

Figure 5.5: Approximate model using ANN

Step 3: Prediction of the optimum

The optimum shape corresponds to the optimum objective function is predicted by the Genetic algorithm.

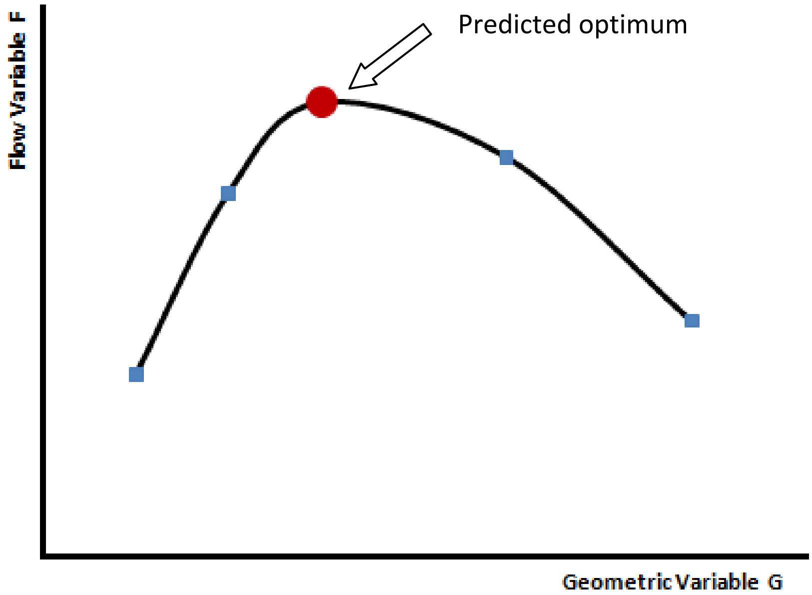

Figure 5.6: Predicted optimum by GA

Step 4: CFD computation of the predicted optimum

CFD calculations are run based on the predicted optimum. The new blade and its associated CFD computations are stored in the new database together with the initial samples. So the new database now contains five samples.

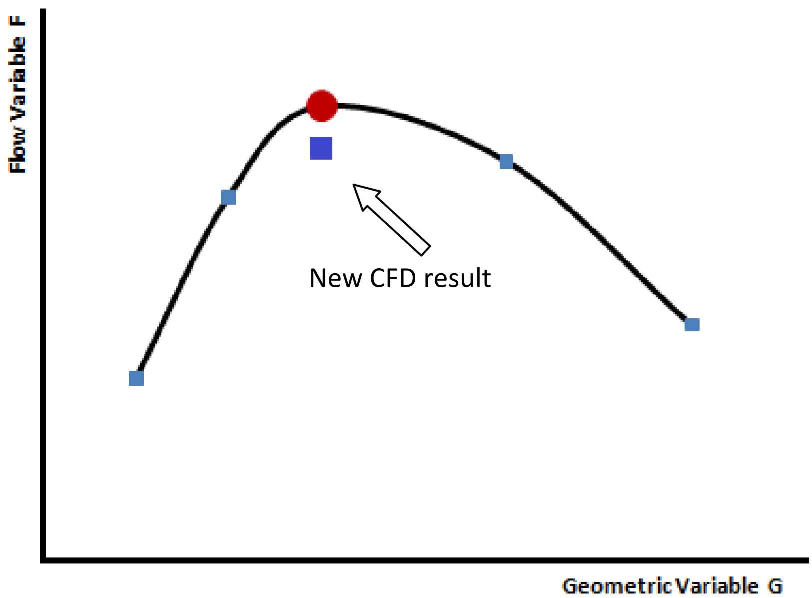

Figure 5.7: CFD calculation for the predicted optimum

Step 5: New approximation of the CFD computations

A new approximation of the new database using ANN is carried out and results in new approximate model.

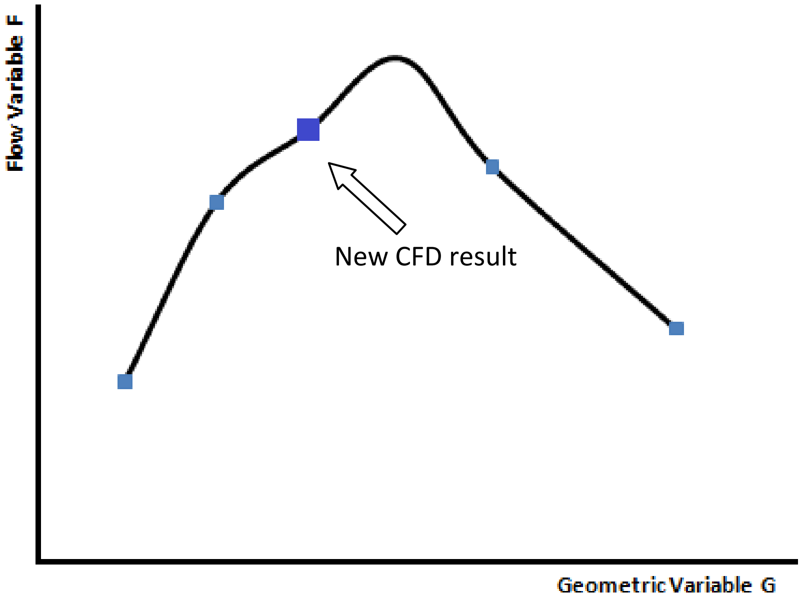

Figure 5.8: New approximate model using ANN

Step 6: Prediction of new optimum

Again the new optimum of the new database with the new ANN is predicted by the genetic algorithm.

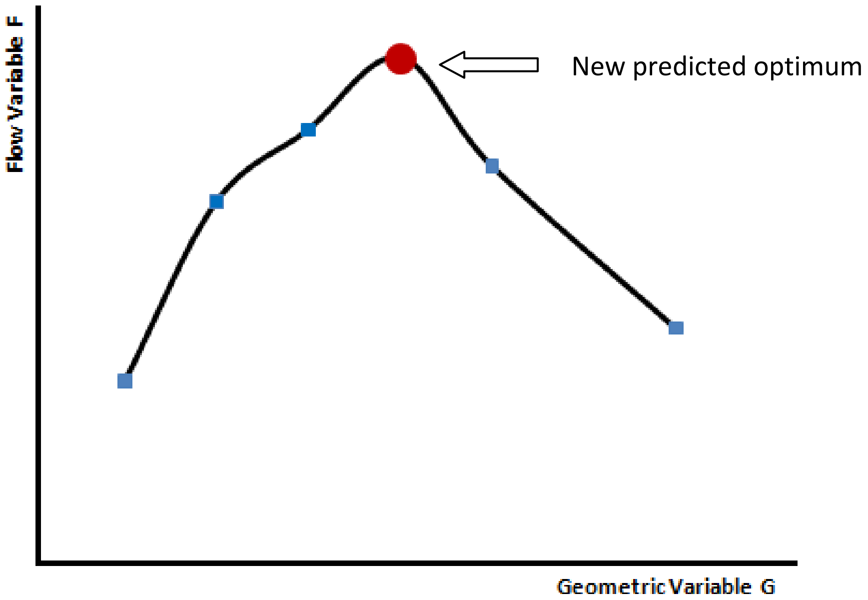

Figure 5.9: Prediction of new optimum by GA

Step 7: CFD calculation of the new predicted optimum

Again, new CFD calculations are run based on the new predicted optimum. The new blade and its associated CFD computations are stored in the new database together with the initial samples and the sample of the previous predicted optimum. So the new database now contains six samples.

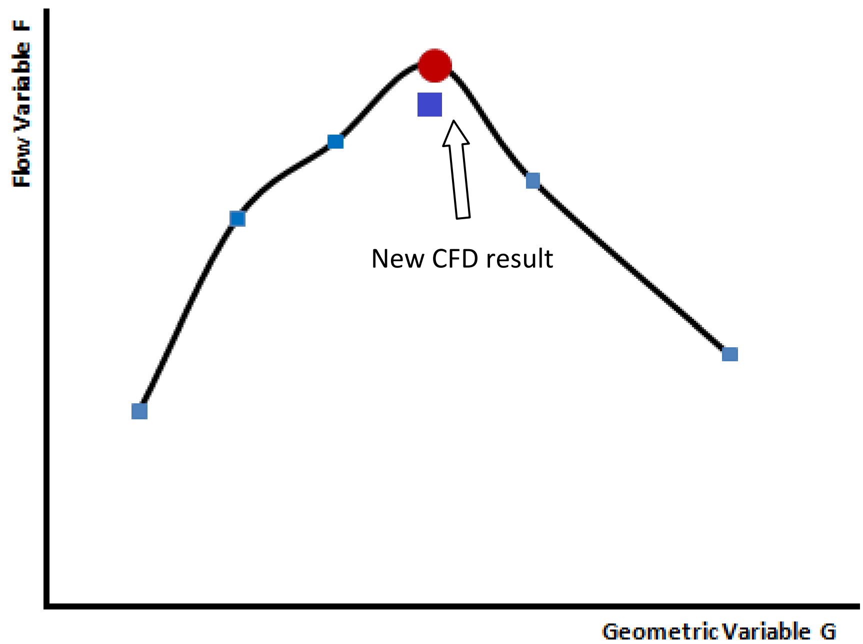

Figure 5.10: CFD computations for the new predicted optimum

The steps from 2 to 4 represent one iteration in the design process. It is also called one design cycle. The 2nd design cycle starts at step 5 and ends at step 7. The iterations continues till the number of iterations (design cycles) is reached.

5.2 Winglet Design and Optimization

The design of the winglet is based on the results obtained in Section (4.1). One configuration was used in the design process which is winglet tilted towards the suction side of the blade. That is because this configuration showed higher energy production compared to the other configurations of Section (4.1).

5.2.1 The Parametric Model

The parametric model consists of 20 sections from hub to tip. The first two sections (towards the root) are circular and the other sections are defined by the S809 airfoil. The first 19 sections correspond to the NREL VI blade, where the 20^{th} section is for the winglet.

A 2D meridional view of the wind turbine is shown in Figure (5.11):

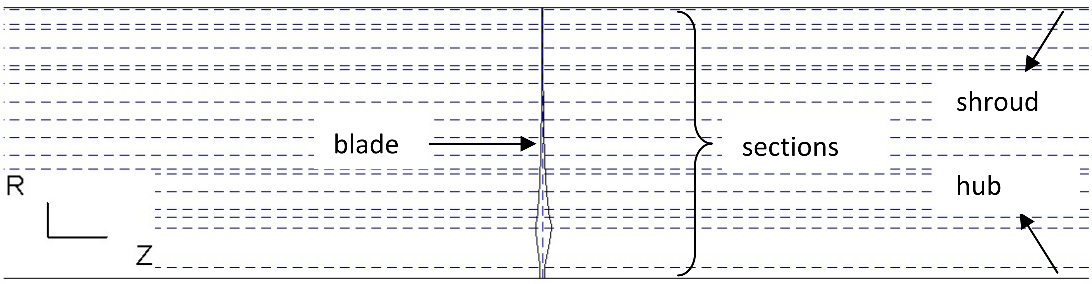

Figure 5.11: Meridional view of the wind turbine

5.2.2 Design Variables and Constraints

Only the winglet part (section 20) is optimized. The number of design variables included in the optimization is restricted to 2 parameters, the cant angle and the twist angle. All other parameters are kept constant and used as constraints.

The varying parameters are as follow:

- Cant angle: 3 angles (45, 68 and 89)
- Twist angle: 8 angles (-2,-1,…,5)

So the total number of varying parameters is 24.

It should be noted that, 0 degrees of twist of the blade with respect to the tip chord corresponds to 90 degrees of twist with respect to the wind. So in the parametric model, the twist angles are added to 90 degrees to account for position with respect to the wind.

2D view for the winglet profile at different twist angles (-2, 0, 3, and 5 degrees) is given in Figure (5.12):

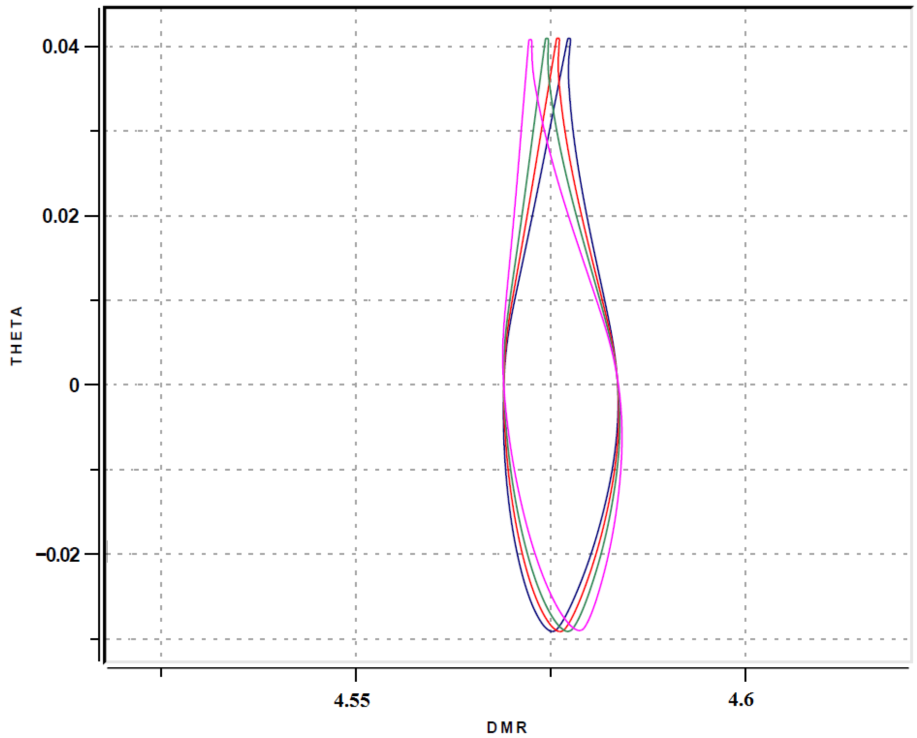

Figure 5.12: Twist variations of the winglet

In the design process, it is important to define the limits within which the design variables will change. In this case, the upper limit for cant angle is 89 degrees and lower limit is 45 degrees. While the upper limit for the twist angle is 5 degrees and lower limit is -2 degrees.

5.2.3 Database Generation

All the 24 varying parameters are considered in the design. Hence a database of 24 samples is generated which contains 24 different blade geometries and their associated aerodynamic and geometrical performances. Meshing, CFD simulations and post-processing are carried out for each sample and the results are stored for the optimization.

5.2.4 Optimization Settings and Objective Function

To guarantee wide range of operating conditions, multipoint optimization is imposed. The optimization will carry out on three different wind speeds; 5m/s, 7m/s and 9m/s. To do so, the database is generated for each operating condition resulting in 72 samples (24 samples for each operating point). The design variables and their limits as well as the meshes are the same for each operating point. However, the CFD computations are different because the boundary conditions are different for the different wind speeds.

The objective of the optimization is to increase the torque. Hence increasing the power output. The same objective is imposed for each operating point.

The genetic algorithm is imposed as the optimization method. The settings of the GA which are used in this study are as follow:

- Population size = 50
- Reproduction cycles = 50
- Truncation rate = 20
- Elitism = 1

Where the above mentioned terms were defined in Section (5.1.4).

5.2.5 Optimization Results and CPU Cost

The convergence history of the optimization procedure is shown in Figure (5.13). One may notice that the error between the neural network predictions and the CFD results decreases and both of the curves converges after 14 iterations.

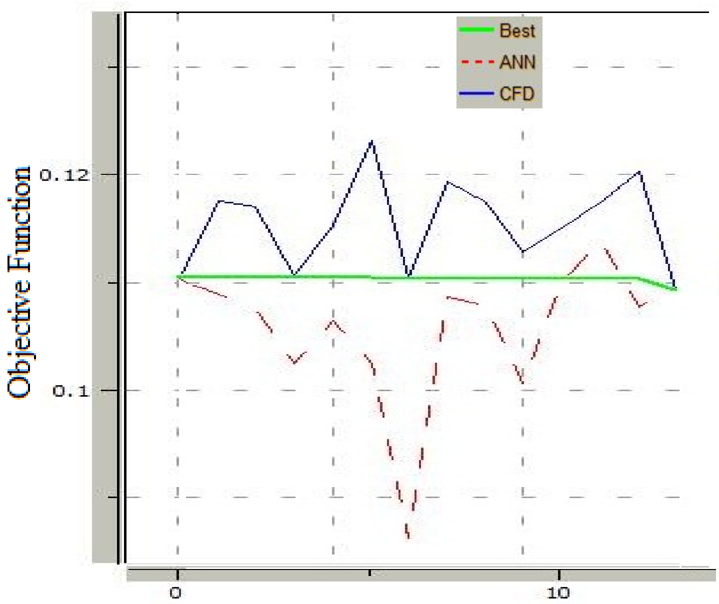

Figure 5.13: History of convergence of objective function

The cant and twist angles of the winglet of the optimized geometry converged to 84 and 2 degrees (92 degrees with respect to the wind direction) respectively to give the best shape for the maximum torque.

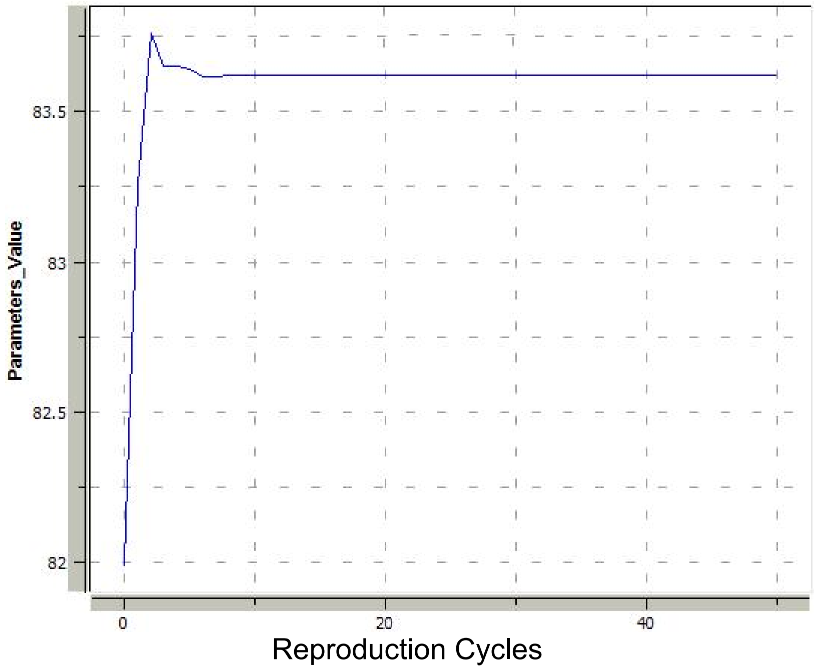

Figure 5.14: Convergence of the cant angle of the optimized winglet

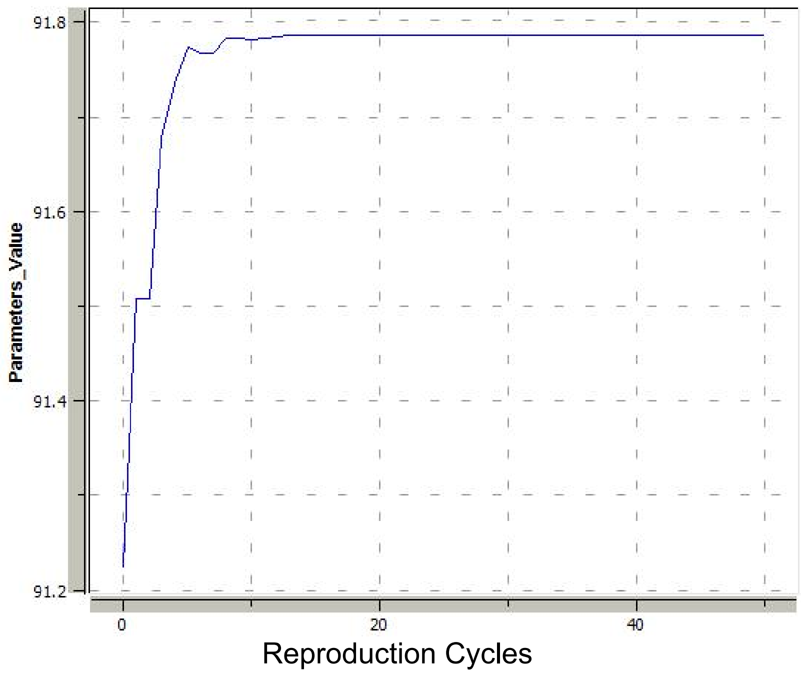

Figure 5.15: Convergence of the twist angle of the optimized winglet

The optimized winglet gave a considerable increase in torque compared with initial geometry (without winglet) as shown in Table (5.1):

Table 5.1: Optimization objectives and results

Operating Condition	Initial Torque (N.m)	Optimized Torque (N.m)	Percentage of increase (%)
5 m/s	290.3	324.4	11.7
7 m/s	755.4	823.3	9.0
9 m/s	1261.6	1363	8.0

Comparing the results in Table (5.1) with the results obtained in Table (4.3), one notices that the increase in power due to the optimization of the winglet is more than the increase due to any winglet configuration obtained in Section (4.1).

Geometrical comparisons between the initial geometry (without winglet) and the final geometry with the optimized winglet are shown as meridional view in Figure (5.16) and 2D blade profile view at the tip in Figure (5.17):

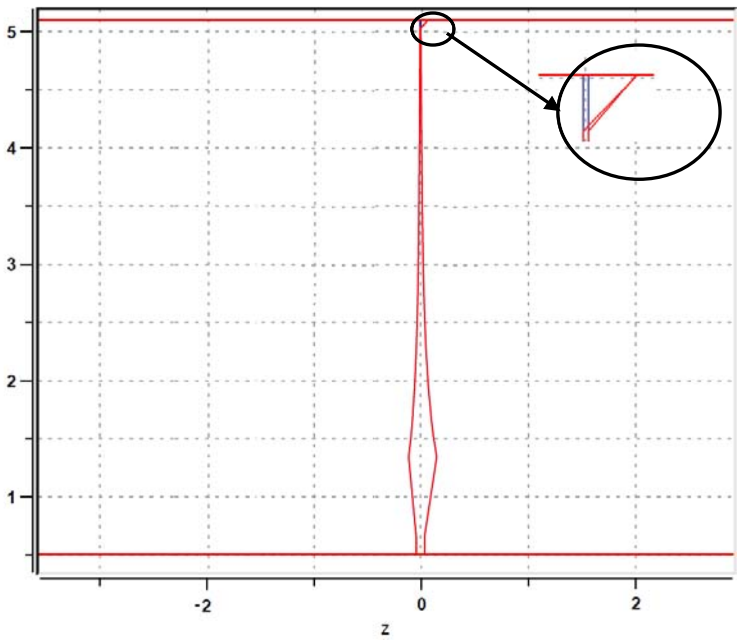

Figure 5.16: Meridional view of initial geometry and final geometry with optimized winglet

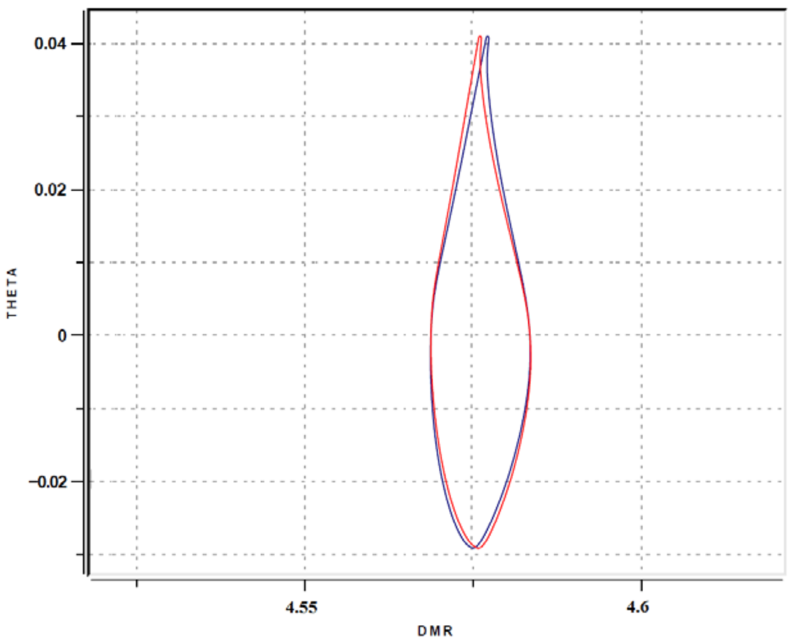

Figure 5.17: 2D blade tip profile of initial geometry and final geometry with optimized winglet

The computations were done in parallel. 4 processors were used for the computations. The operating system is Windows Vista with Intel Core 2 Quad of 2.5GHz. The CPU cost of the different processes during the design is listed in Table (5.2):

Table 5.2: CPU cost

Process	CPU time (Intel 2.5 GHz)
CFD of initial geometry for three operating conditions.	3×2 H = 6 H
Database generation: 24 samples for each operating condition.	24 × 3 × 2 H = 144 H
Optimization: 14 iterations	14 × 3 × 2.2 H = 92 H
Total	242 H per processor

5.2.6 CFD Analysis of the Final Optimized Winglet Geometry

Here is a comparison between the optimized winglet geometry and the original NREL VI blade. The computations were run for the wind speed range between 5 and 25 m/s. The power curve comparison, the percentage of power increase, the axial thrust comparison and the percentage of axial thrust increase are shown in Figures (5.18), (5.19), (5.20) and (5.21) respectively.

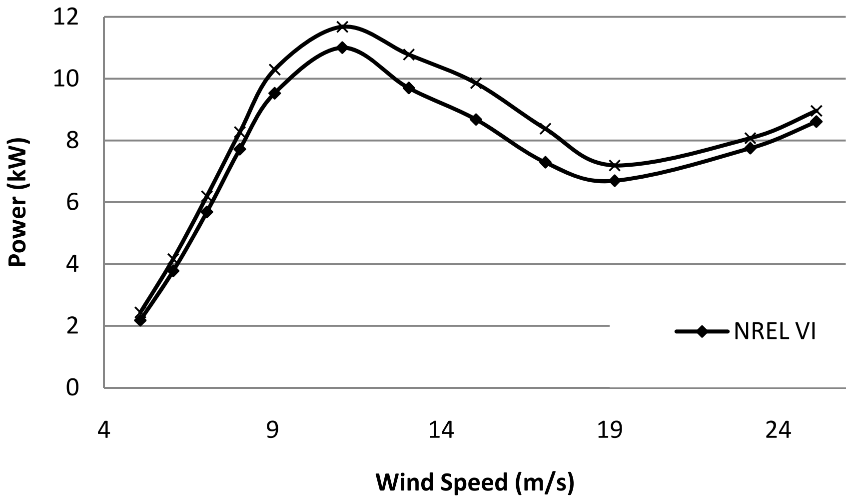

Figure 5.18: Comparison of power curve between NREL VI and optimized winglet

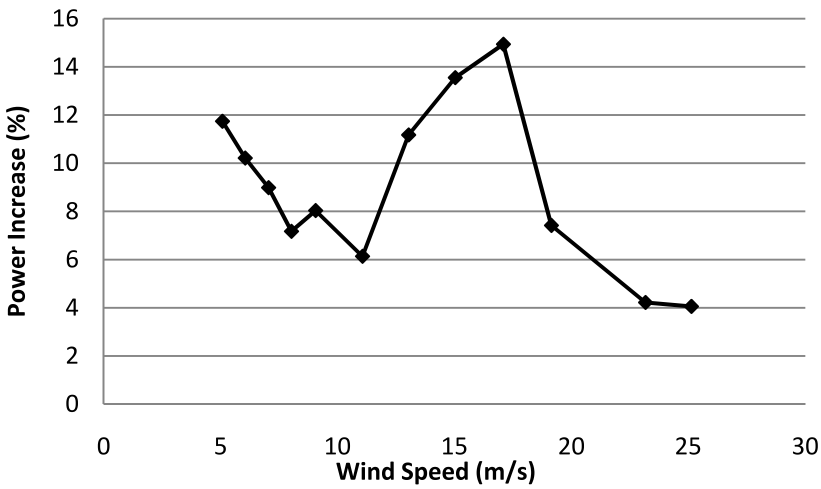

Figure 5.19: Percentage increase in power production of the optimized winglet

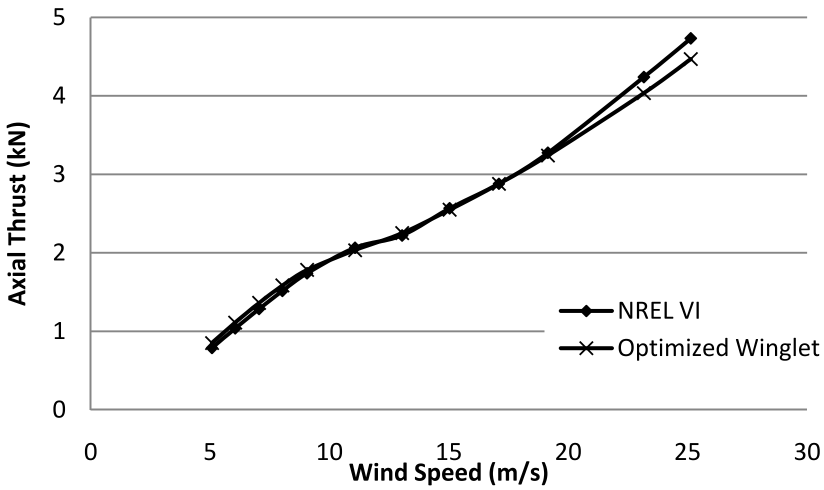

Figure 5.20: Comparison of axial thrust between NREL VI and optimized winglet

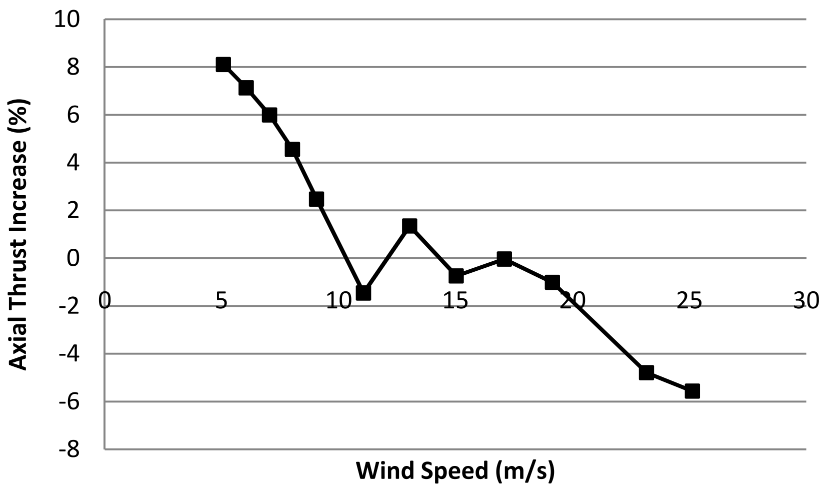

Figure 5.21: Percentage increase in axial thrust of the optimized winglet

From the figures above, it is clear that the increase in power is more than the increase in axial thrust. In fact the average percentage increase of power is 9% where the average percentage increase in axial thrust is 1.3 %. This is a good result which means that the addition of the optimized winglet to the geometry does not have a big impact on the structural characteristics, including loads, of the blade. a complete structural integrity analysis is performed in Chapter 6.

The winglets have an effect on the normal and tangential forces acting on the blade sections. As stated before, the tangential force represents the driving force while the normal force represents the axial thrust (loads) on the blades. Increasing the driving force leads to more power production. The normal and tangential force coefficients C_N and C_T are computed using Equations (3.4) and (3.5) and the results compared to the original blade are shown in Figures (5.22) and (5.23). The results are obtained for three different wind speeds along spanwise direction of the blade:

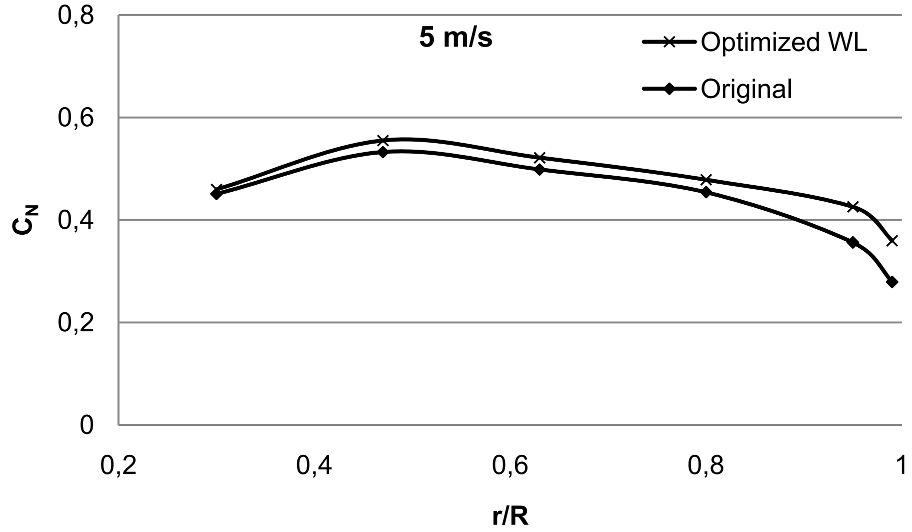

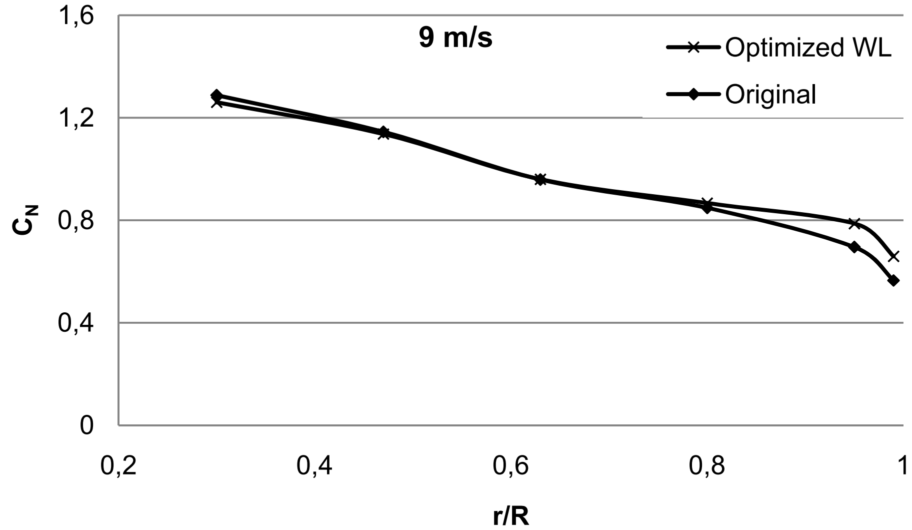

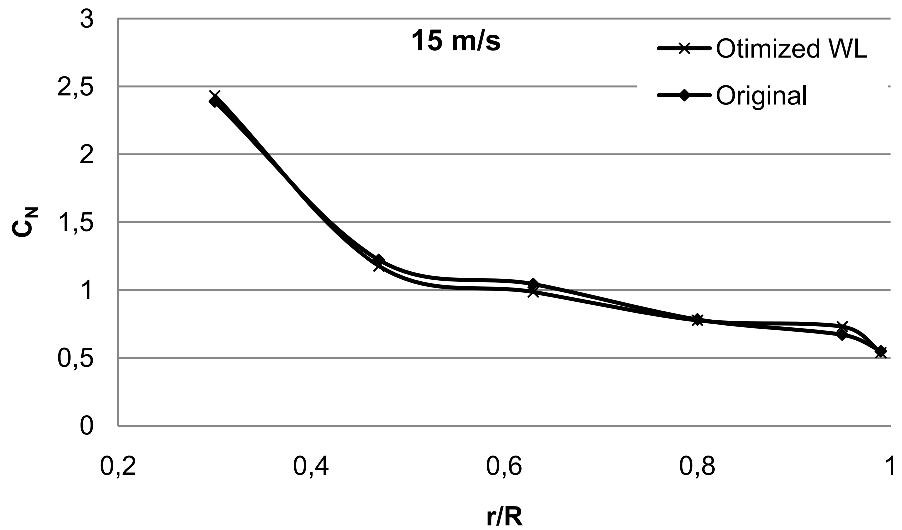

Figure 5.22: Comparison of original blade normal force coefficient with the optimized winglet one

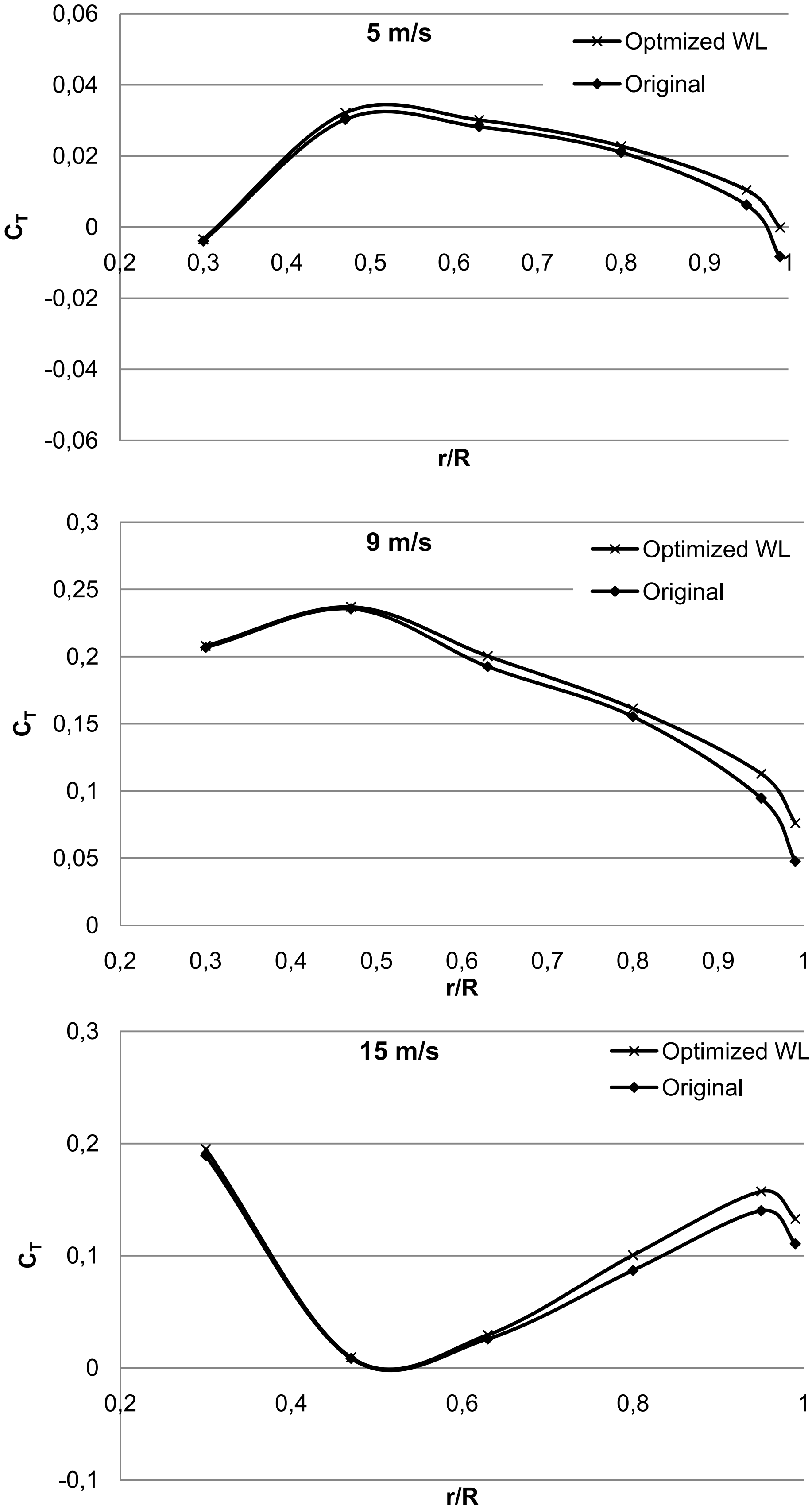

Figure 5.23: Comparison of original blade tangential force coefficient with the optimized winglet one

At 5 and 9m/s, Figure (5.22) shows that C_N of the optimized blade in the inboard region of the blade is almost same as C_N of the original blade. As one goes towards the tip, the C_N of the optimized blade becomes more and the percentage of increase over the original blade becomes maximum at 99% span. This shows the effect of the winglet on the tip region. Since the normal force gives an indication about the axial thrust, this result agrees with the one obtained in Figure (5.21) where the axial thrust of the optimized blade is more at 5 and 9m/s.

At 15m/s, C_N is less than for the optimized blade. Again this result agrees with the one of Figure (5.21) where the axial thrust at 5m/s decreases at 15m/s.

Figure (5.23) shows that the increase of C_T of the optimized blade over C_T of the original blade is more towards the tip region. This explains the increase in power at 5, 9 and 15m/s in Figure (5.19). As mentioned before, C_T represents for the driving force and its increase results in an increase in the torque and hence in the power.

The axial velocity streamlines comparison at the blade tip at wind speeds of 5 and 9 are shown in Figures (5.24) and (5.25).

Figures (5.24) and (5.25) show the effect of the winglet on the flow in the axial direction. In the original blade, a vortex tends to form at the suction side in the tip region of the blade and the flow slightly separates. However, with the optimized winglet, the flow is more attached and directed to the downstream without separation.

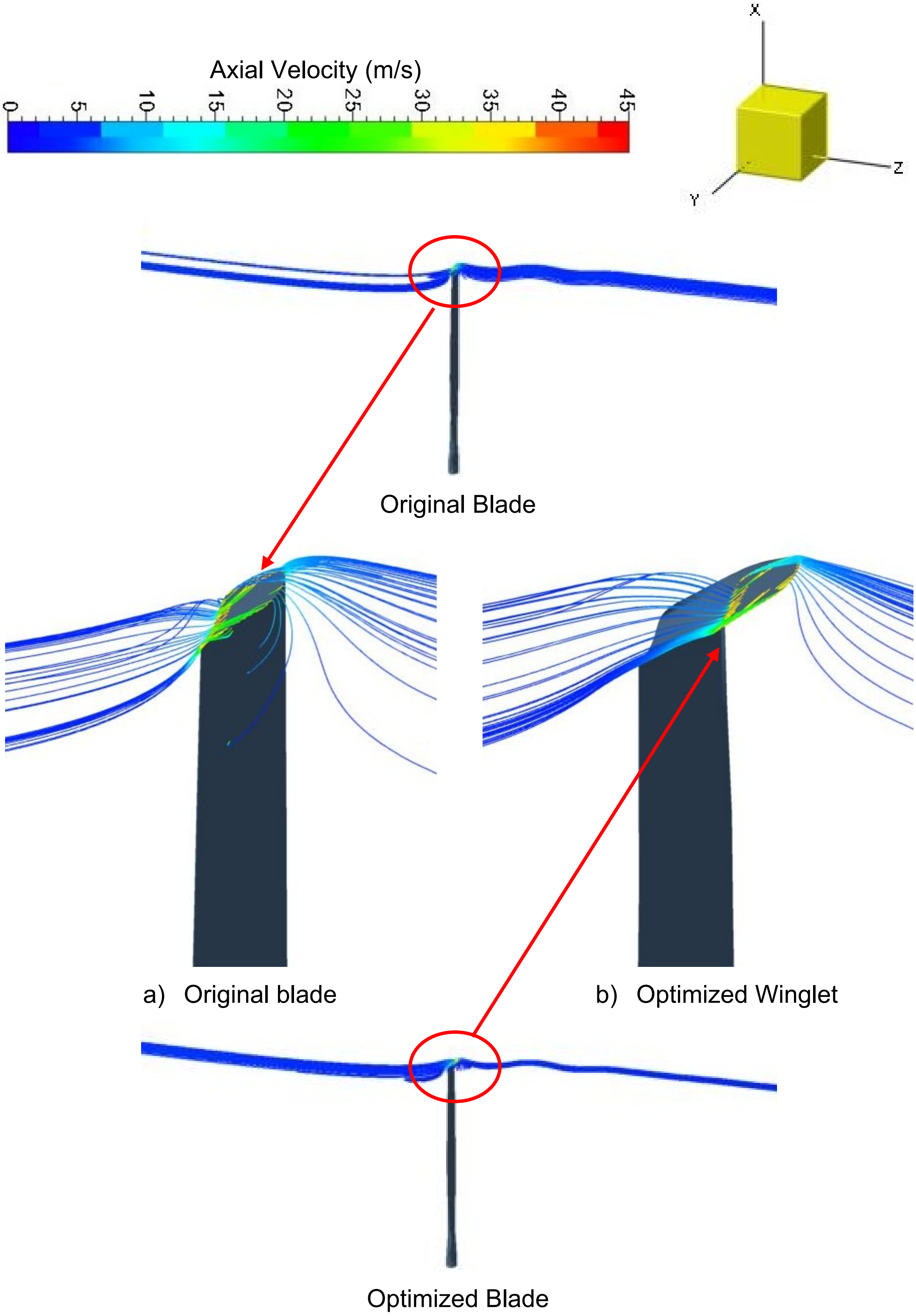

Figure 5.24: Comparison of axial velocity streamlines between original and optimized blades at 5m/s

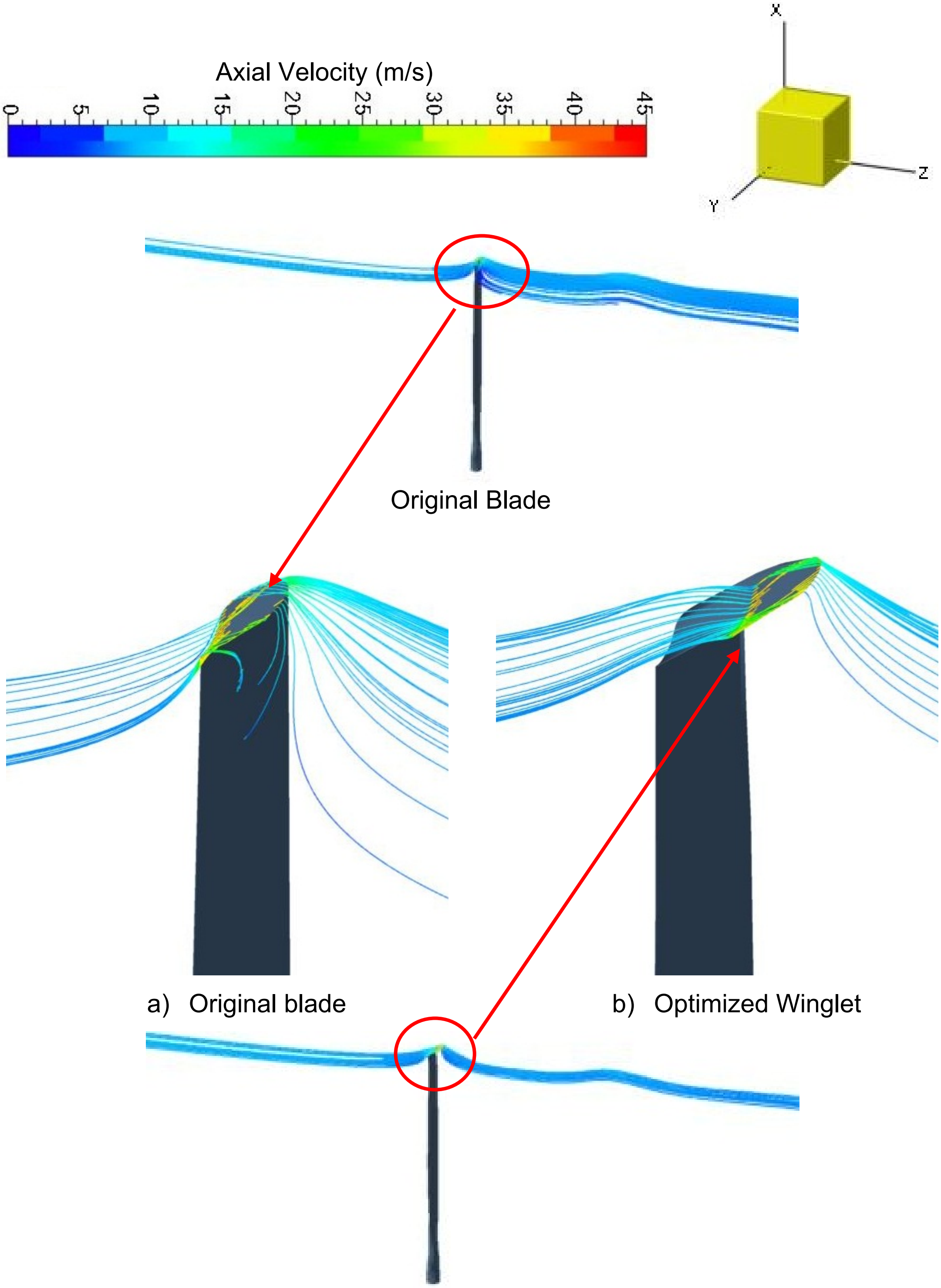

Figure 5.25: Comparison of axial velocity streamlines between original and optimized blades at 9m/s

To see the vorticities clearly, the relative velocity streamlines are plot as seen in Figures (5.26) and (5.27):

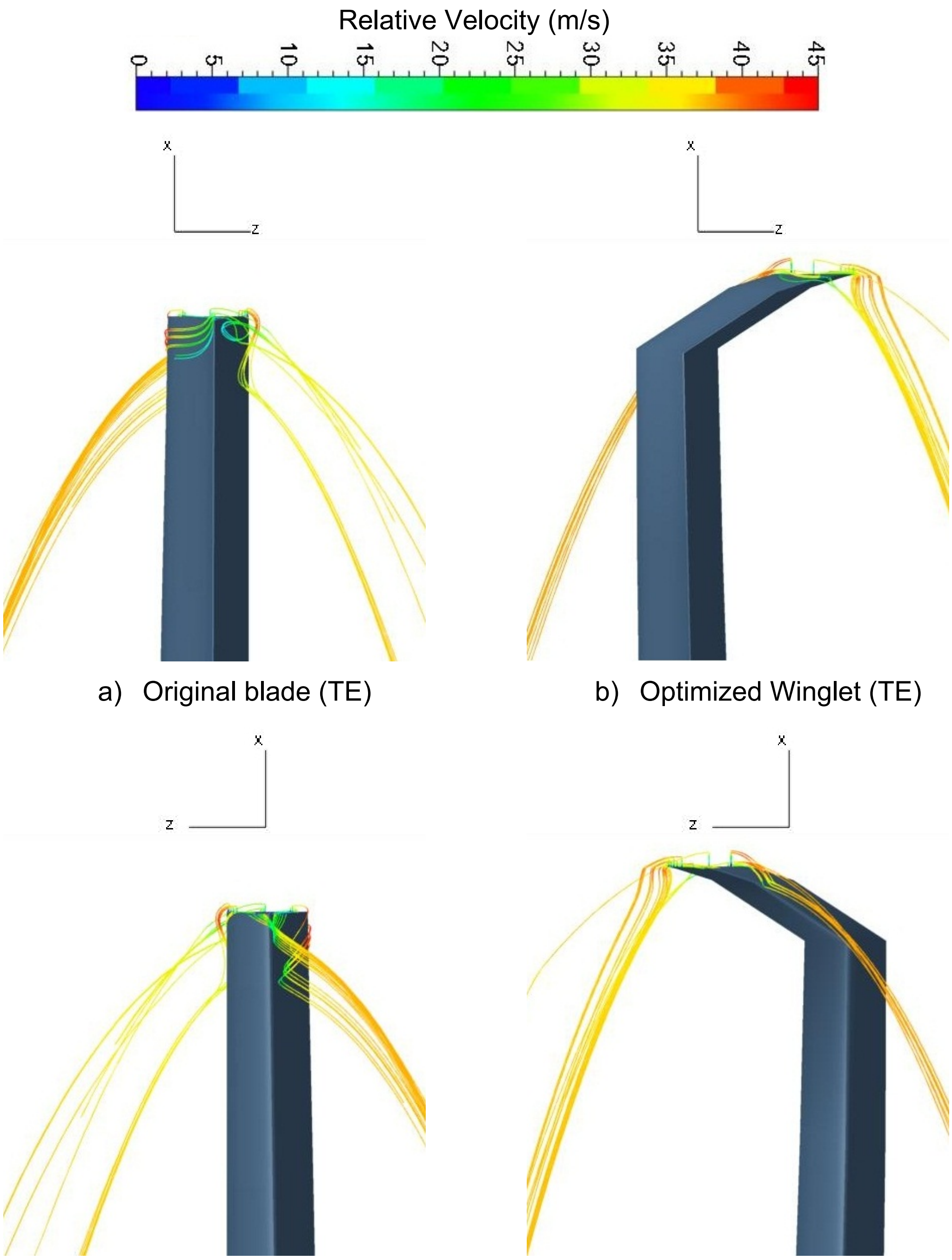

a) Original blade (TE) b) Optimized Winglet (TE)

c) Original blade (LE) d) Optimized Winglet (LE)

Figure 5.26: Comparison of relative velocity streamlines between original and optimized blades at 5 m/s

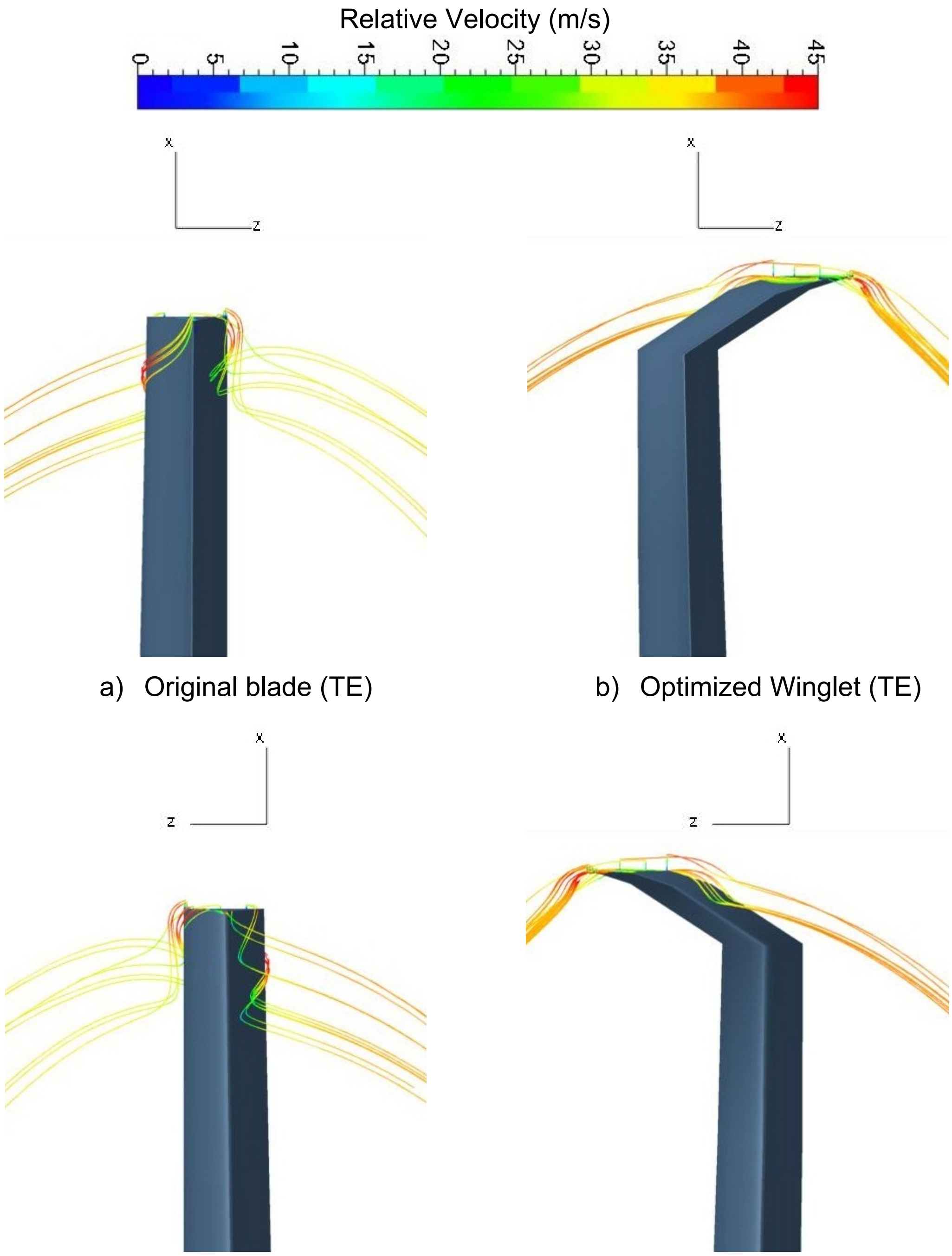

a) Original blade (TE)   b) Optimized Winglet (TE)

c) Original blade (LE)   d) Optimized Winglet (LE)

Figure 5.27: Comparison of relative velocity streamlines between original and optimized blades at 9 m/s

From Figures (5.26) and (5.27), one notices the vortex formation at the trailing edge of the original blade tip region. This vortex becomes less significant in the case of the optimized winglet and the flow becomes more attached. These results are in agreement with the increase of power due to the optimized winglet.

The axial velocity contours at 0.1 m behind the blade in the $x - y$ plane are plot for plot and compared form both cases as seen in Figures (5.28) and (5.29):

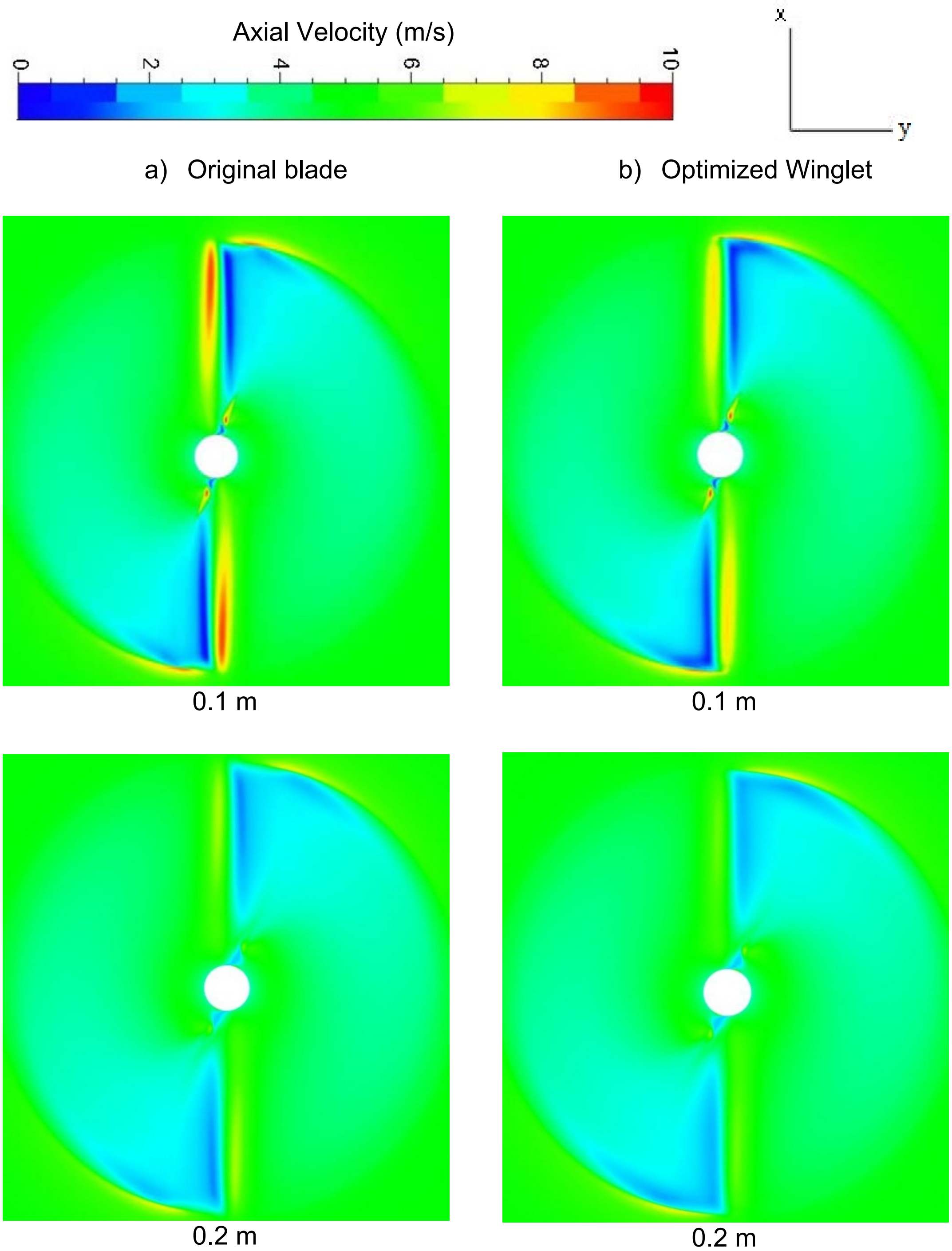

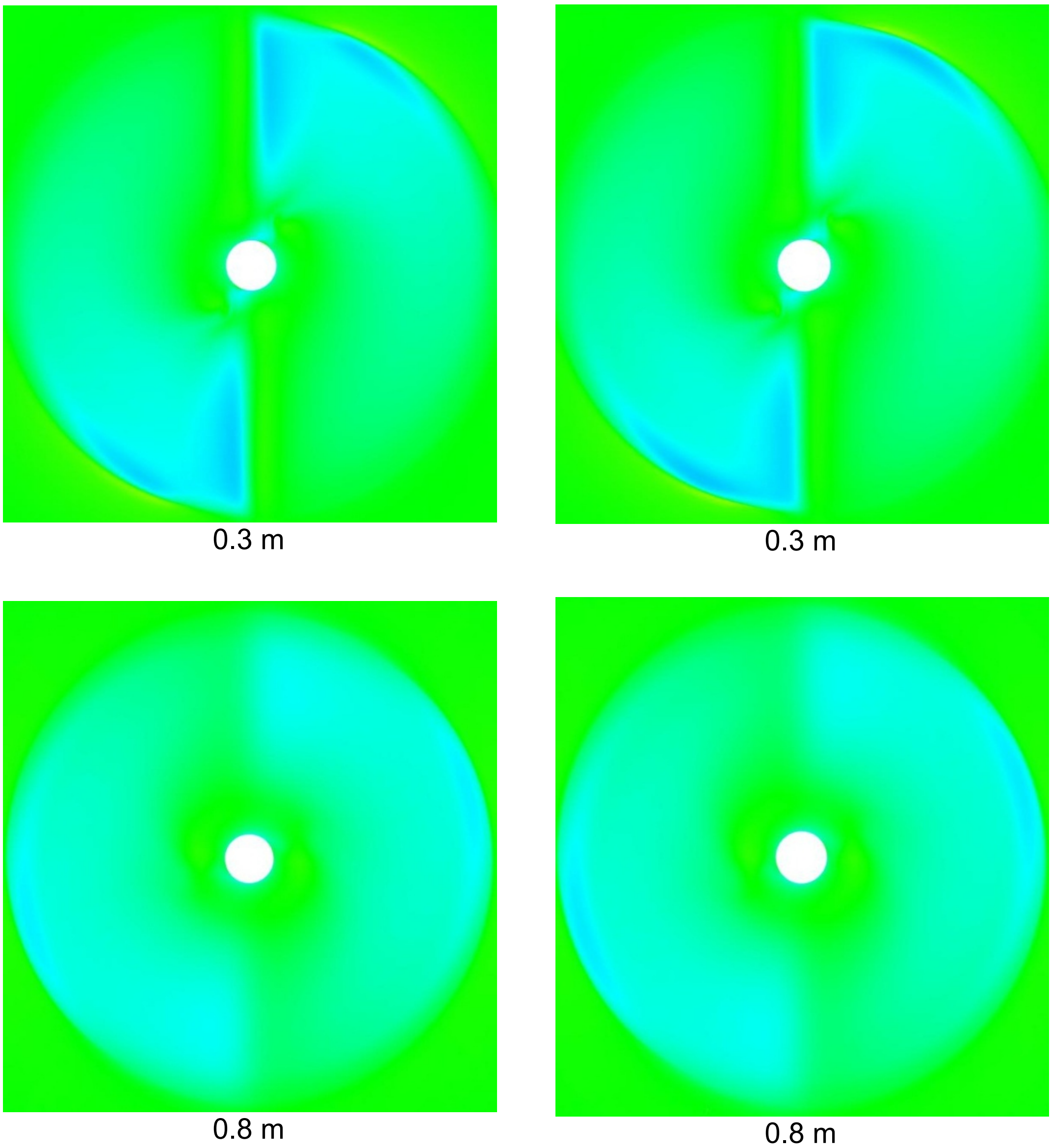

Figure 5.28: Comparison of axial velocity contours between original and optimized blades at different distances behind the blade in the x-y plane at 5 m/s

From Figure (5.28), at 0.1 m behind the blade, the flow around the optimized winglet is more attached towards the tip. This is also clear at 0.2 and 0.3 m. As one goes far behind the blade, the effect of the winglet decreases. So at 0.8 m, the flows around the original blade and optimized winglet-blade are same.

Similar results are observed in Figure (5.29) at 9m/s.

Another notice is that the velocity behind the blade is less in the case of the optimized winglet. And as the velocity behind the blade decreases, more power is captured by the blade. These notices explain the increase in the power due to the addition of the optimized winglet.

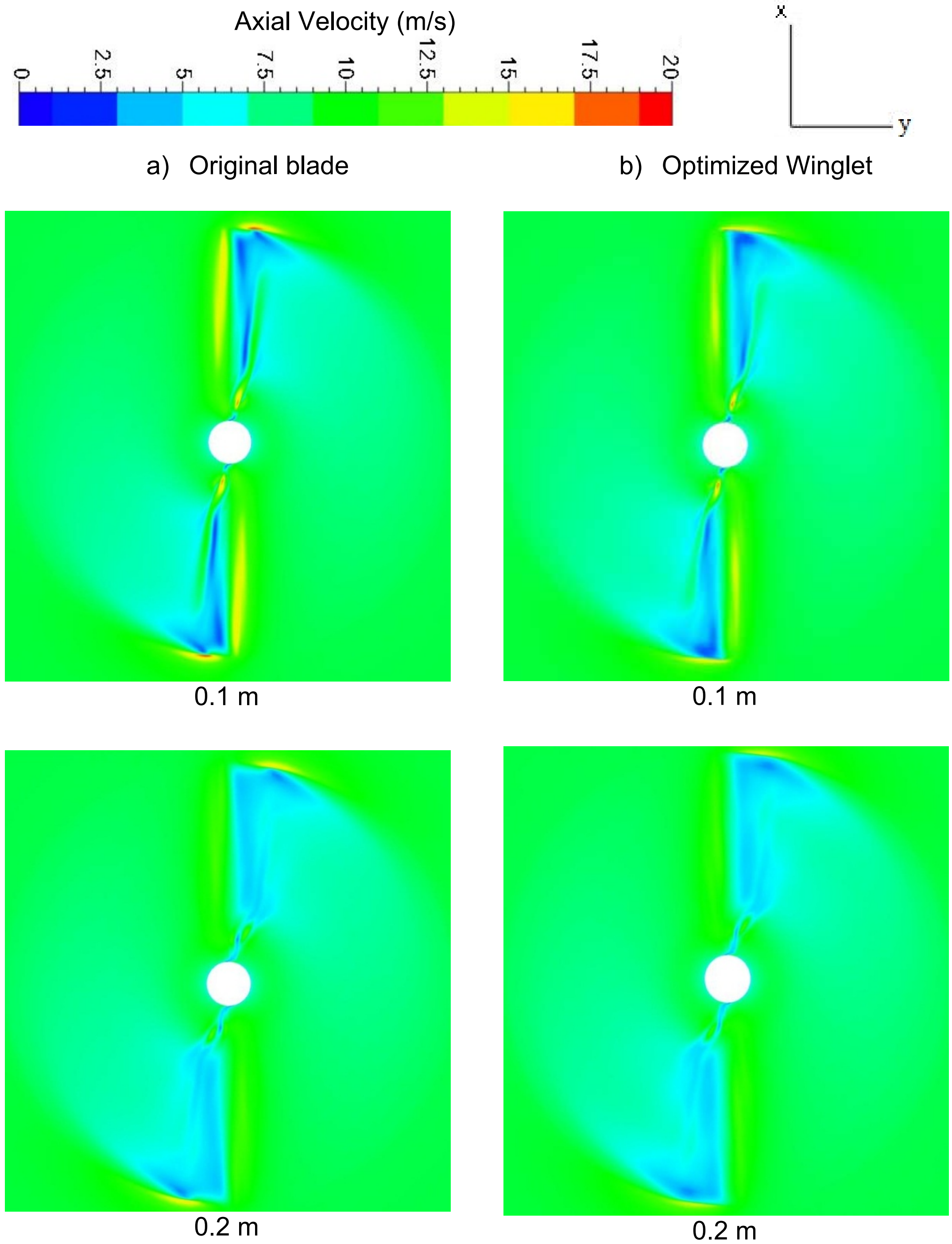
Axial Velocity (m/s)
0
2.5
5
7.5
10
12.5
15
17.5
20
x
y
a) Original blade
b) Optimized Winglet
0.1 m
0.1 m
0.2 m
0.2 m

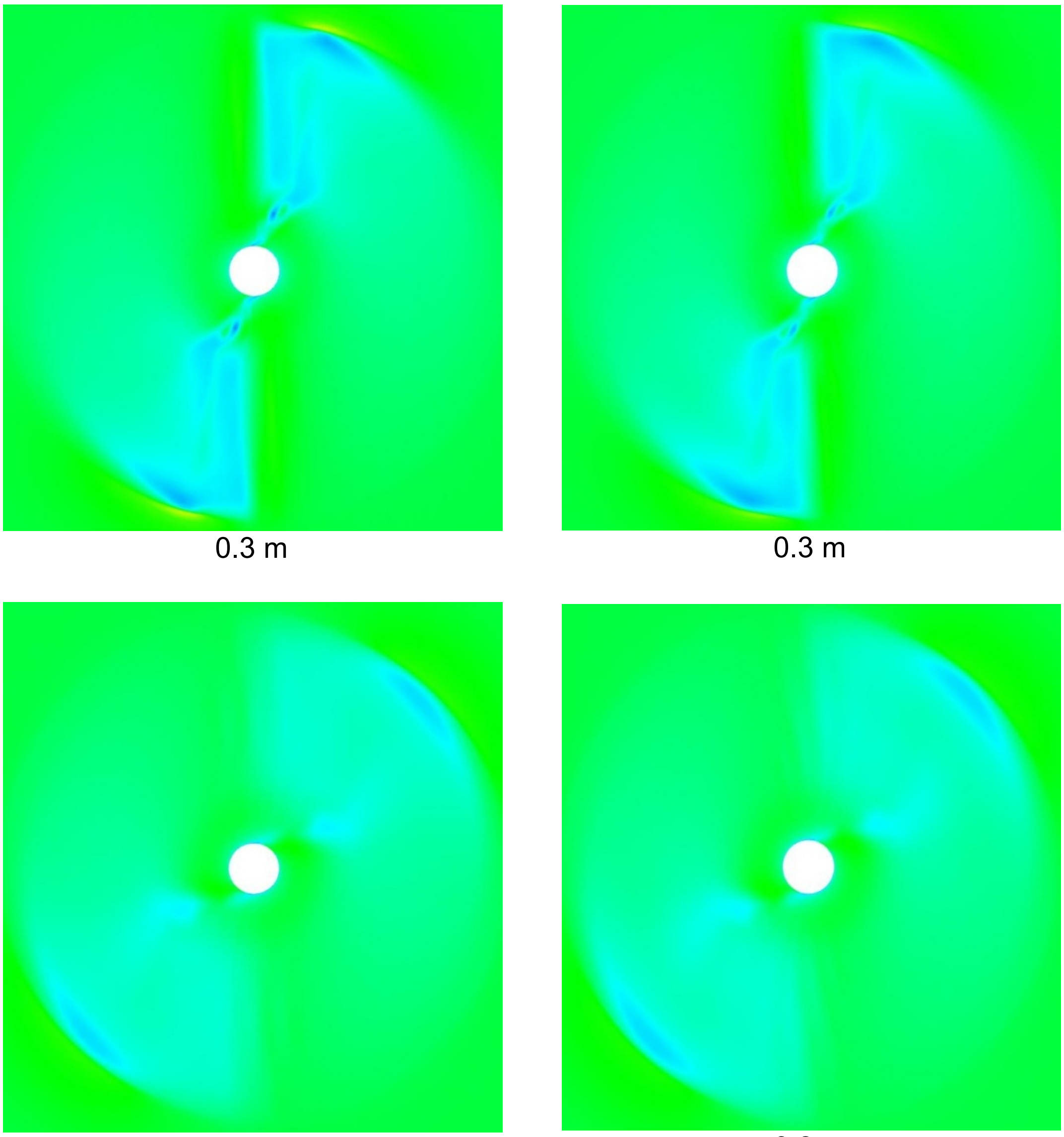

Figure 5.29: Comparison of axial velocity contours between original and optimized blades at different distances behind the blade in the x-y plane at 9 m/s

To see the effect of the winglet on the vorticity, the vorticity contours are plot at the TE of the blade in the tip region. From the results obtained in Figures (5.30), (5.31) and (5.32), it is noticed that the high vorticity at the tip of the original blade has been reduced I magnitude and shifted by the winglet.

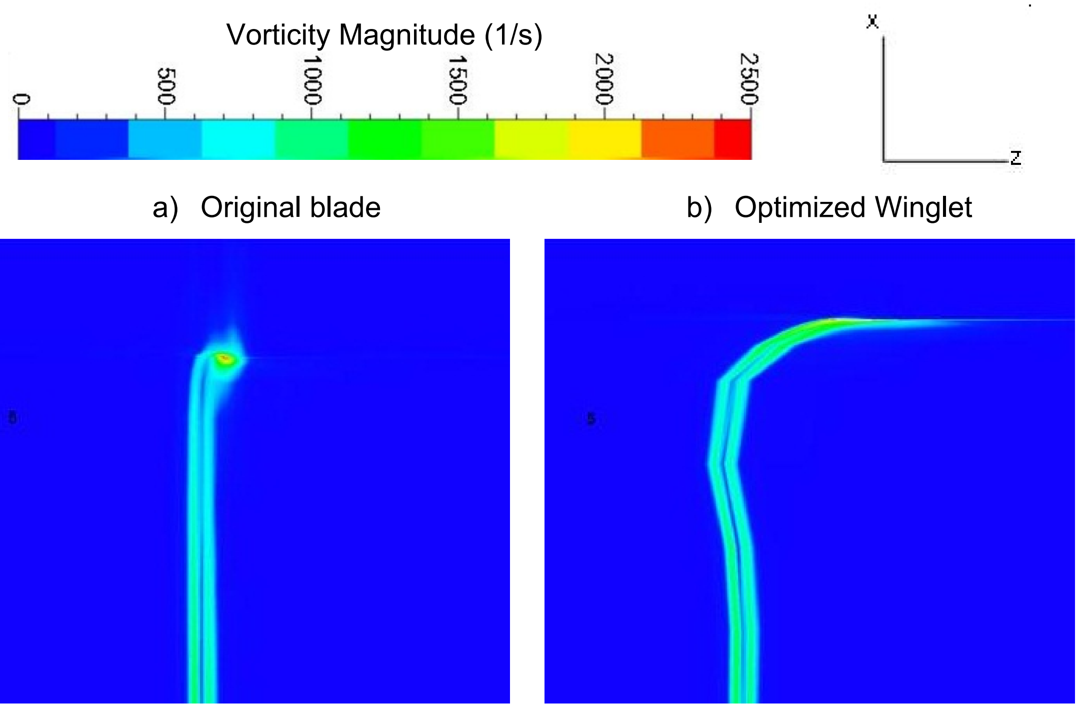

Figure 5.30: Comparison of vorticity contours between original and optimized blades at the TE in the x-z plane at 5 m/s

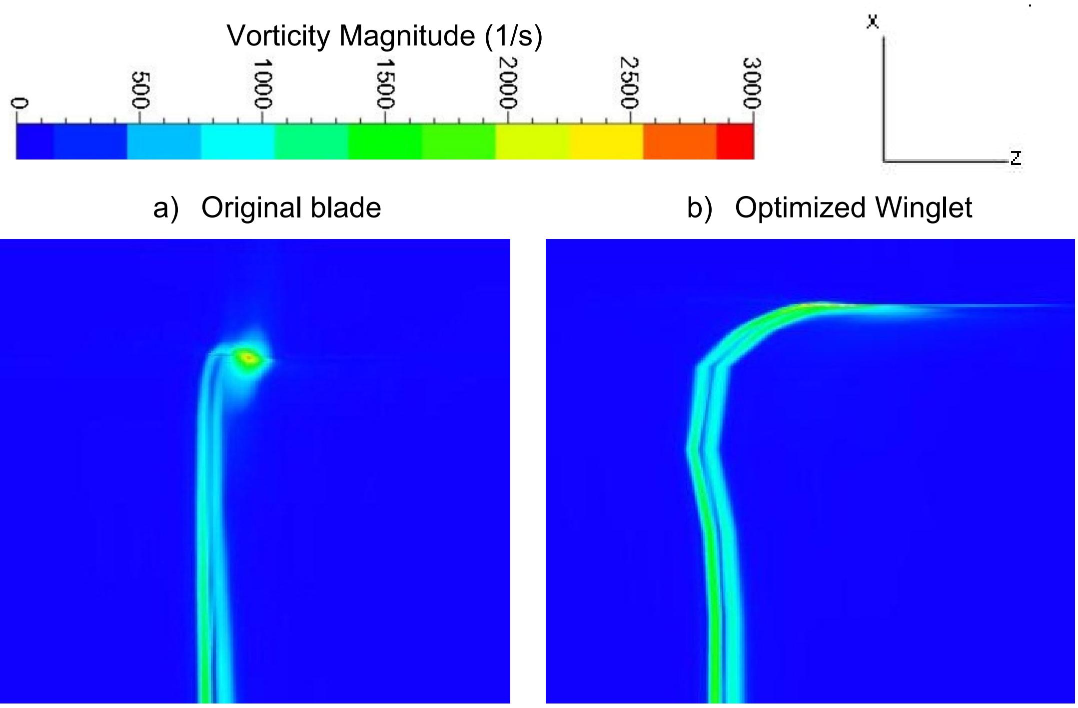

Figure 5.31: Comparison of vorticity contours between original and optimized blades at the TE in the x-z plane at 9 m/s

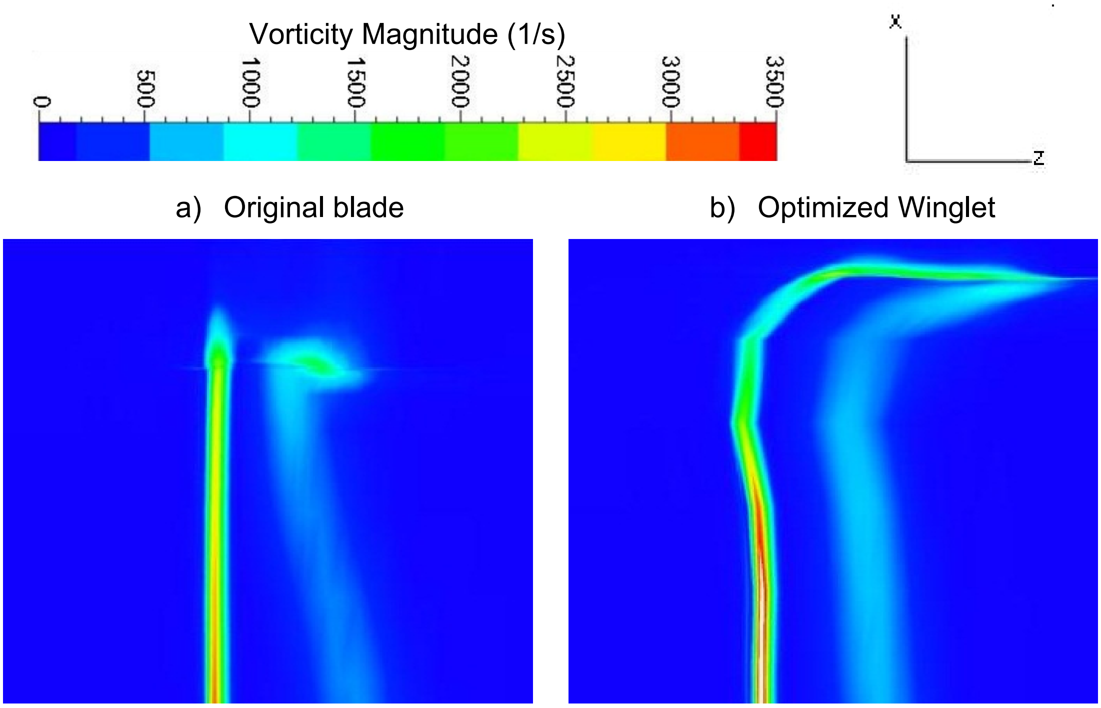

Figure 5.32: Comparison of vorticity contours between original and optimized blades at the TE in the x-z plane at 15 m/s

5.3 Blade Twist Design and Optimization

The twist optimization is a hard task as will be explained in this section. The twist mainly affects the stalling time (early or late stall) of the blade. For early stall, the blade generates more power at lower wind speeds. However this power decreases drastically as the wind speed increases. On the other hand, late stall results in less power at low speeds but high power at high speeds. To increase the power at wide range of wind speeds, extensive database generation and optimization should be done.

5.3.1 The Parametric Model

The parametric model consists of 10 sections from hub to tip. As explained in Sec. (4.2), the original blade consists of 19 sections. However, testing the twist for 19 sections is too cumbersome. For example, if the twist angle of each section is changed through 5 angles, then a database of $19^5 = 2{,}476{,}099$ samples will be necessary. So the number of sections has been decreased to 10 and the rest of the sections are obtained by interpolation.

The 3D view of the original and parametric models are shown in Figure (5.33):

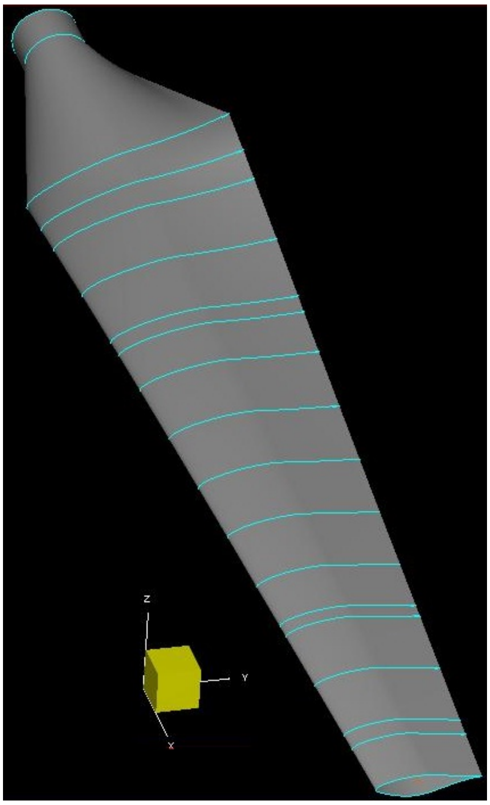

a) Original Blade

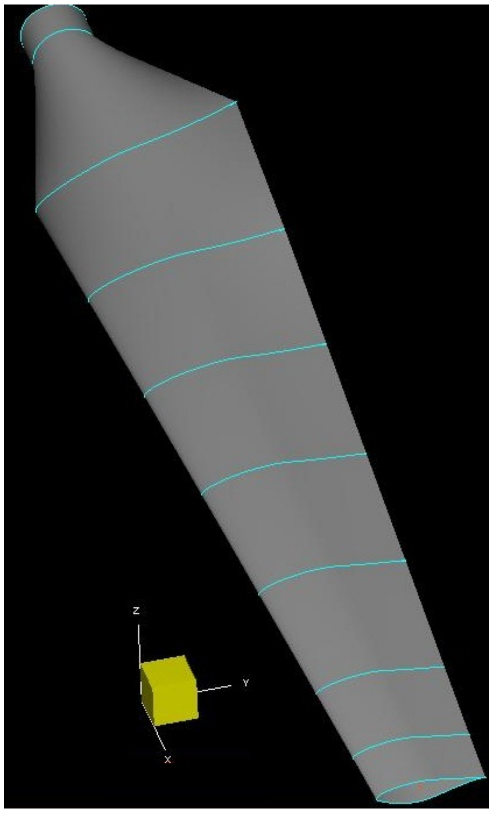

b) Model Blade

Figure 5.33: Original and model blades

5.3.2 Design Variables and Constraints

As stated before, the parametric model consists of 10 sections. The first two sections (towards the hub) are circular and their twist angle is set equal to the twist angle of the 3rd section. So the variable parameters are the twist angles of each of the remaining 8 sections of the blade.

The varying parameters are as follow:

- Twist angle of section 3: 17 angles (99, 100, …, 115)
- Twist angle of section 4: 5 angles (98, 99,…,102)
- Twist angle of section 5: 4 angles (96, 97,…,99)
- Twist angle of section 6: 4 angles (94, 95,…,97)
- Twist angle of section 7: 5 angles (90, 91,…,94)
- Twist angle of section 8: 5 angles (90, 91,…,94)
- Twist angle of section 9: 4 angles (90, 91,…,93)
- Twist angle of section 10: 4 angles (90, 91,…,93)

So the total number of varying parameters is 544000. However, as explained in Section (5.3.3), not all of the varying parameters are used in the database generation.

2D view for the section 4 at different twist angles is given in Fig. (5.34):

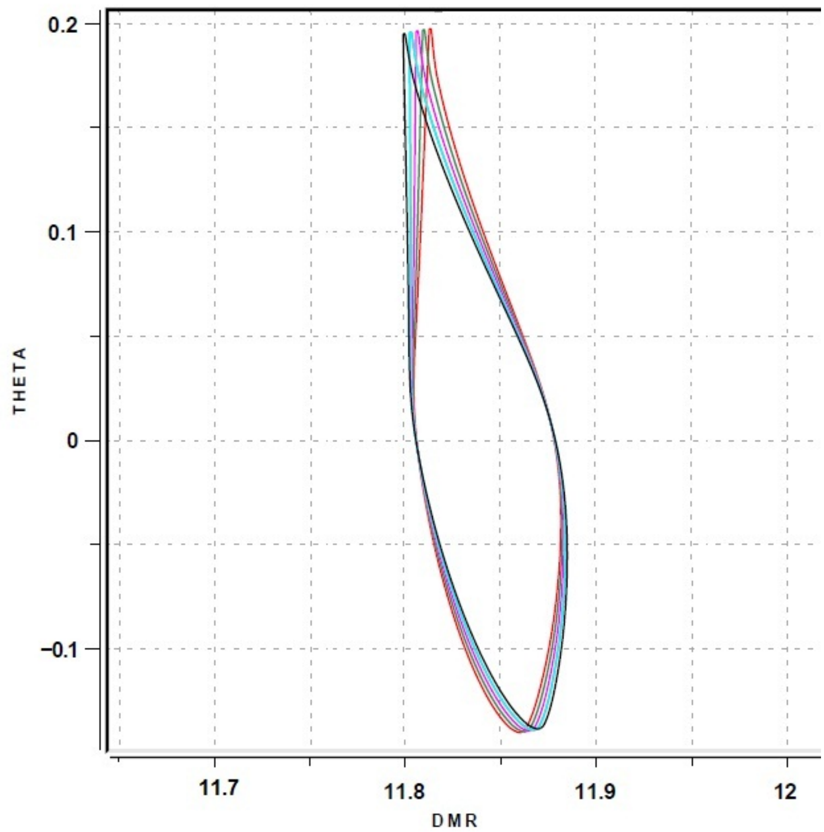

Figure 5.34: Range of twist variations of the blade

5.3.3 Database Generation

As mentioned before, the total number of varying parameters is 544000. This means that for three different wind speeds, a database of 544000×3 = 1632000 samples should be generated and all those samples should be used for optimization as input. However, the computer resources available are unable to accomplish this task. It needs years of continuous running to obtain such huge database with around 420000 Gb of needed free space. Instead, some of the varying parameters were kept constant while others are varying. This way gives an insight of the effect of the twist of the different sections on the power production. Around 300 samples were generated and to get faster optimization, only the best 90 samples were selected. The samples were tested for three different wind speeds; 5m/s, 9m/s and 19m/s.

From the results of the generated samples, it is very difficult to have a twist distribution which causes increase in power for wide range of operating wind speeds. It is easy to increase the power at a certain wind speed by optimizing the twist. However, this increase is at the expenses of a drastic decrease of power at a different wind speed.

5.3.4 Optimization Settings and Objective Function

To guarantee wide range of operating conditions, multipoint optimization is imposed. The optimization will carry out on three different wind speeds; 5m/s, 9m/s and 19m/s. To do so, the database is generated for each operating condition resulting in 270 samples (90 samples for each operating point). The design variables and their limits as well as the meshes are the same for each operating point. However, the CFD computations are different because the boundary conditions are different for the different wind speeds.

The objective of the optimization is to increase the torque. Hence increasing the power output. The same objective is imposed for each operating point.

The genetic algorithm is imposed as the optimization method. The settings of the GA which are used in this study are as follow:

- Population size = 50
- Reproduction cycles = 50
- Truncation rate = 20
- Elitism = 1

Where the above mentioned terms were defined in Section (5.1.4).

5.3.5 Optimization Results and CPU Cost

The convergence history of the optimization procedure is shown in Figure (5.35). One may notice that the error between the neural network predictions and the CFD results decreases and both of the curves converges after 29 iterations.

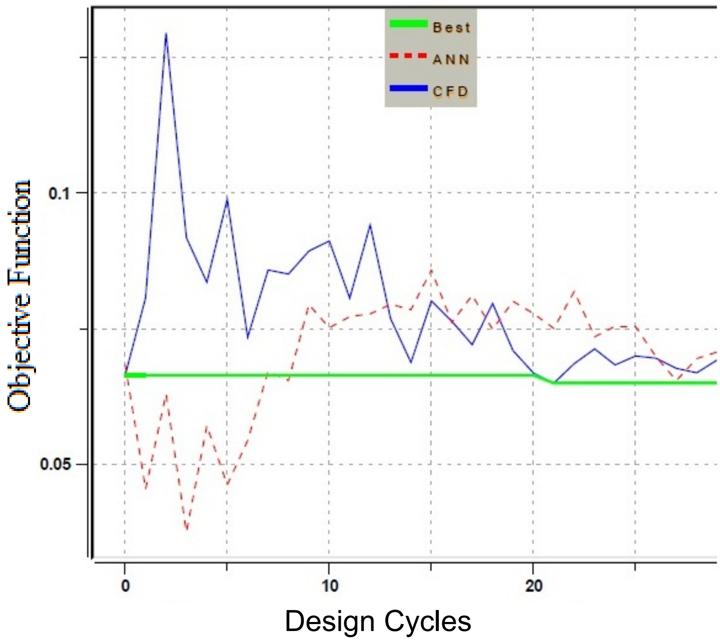

Figure 5.35: History of convergence of objective function

The optimized twist gave a slight increase in torque compared with initial geometry as shown in Table (5.3):

Table 5.3: Results of optimized twist

Operating Condition	Initial Torque (N.m)	Optimized Torque (N.m)	Percentage of increase (%)
5 m/s	290.3	302.1	4.0
9 m/s	1261.6	1299	3.0
19 m/s	887.8	913.6	3.0

As mentioned before, it is hard to obtain an optimum twist which satisfies wide range of operating conditions. This opens the door for finding the optimum angle for each wind speed. In other words, to change the stall regulated blade into pitch regulated blade which can capture the necessary wind to generate more power. However, in this case, not only the power is considered but the loads as well. The pitch regulated turbine is explained in Chapter 6.

The computations were done in parallel. 6 processors were used for the computations. The operating system is Windows Vista with Intel Core 2 Quad of 2.5GHz. The CPU cost of the different processes during the design is listed in Table (5.4):

Table 5.4: CPU cost of twist optimization

Process	CPU time (Intel 2.5 GHz)
CFD of initial geometry for three operating conditions.	3×2 H = 6 H
Database generation: 90 samples for each operating condition.	90 × 3 × 2 H = 540 H
Optimization: 29 iterations	29 × 3 × 2.2 H = 191.4 H
Total	737 H per processor

5.3.6 Results Final Optimized Twist

Here is a comparison between the optimized twist geometry and the original NREL VI blade. The computations were run for the wind speed range between 5 and 25 m/s.

The power curve comparison is shown in Figure (5.36):

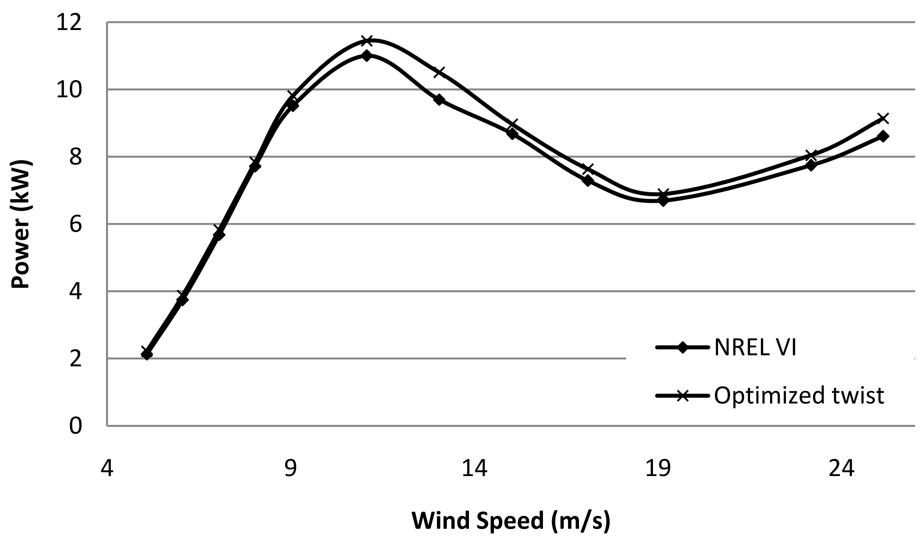

Figure 5.36: Comparison of power curve between NREL VI and optimized twist

Comparison of the axial thrust at different wind speeds is shown in Figure (5.37):

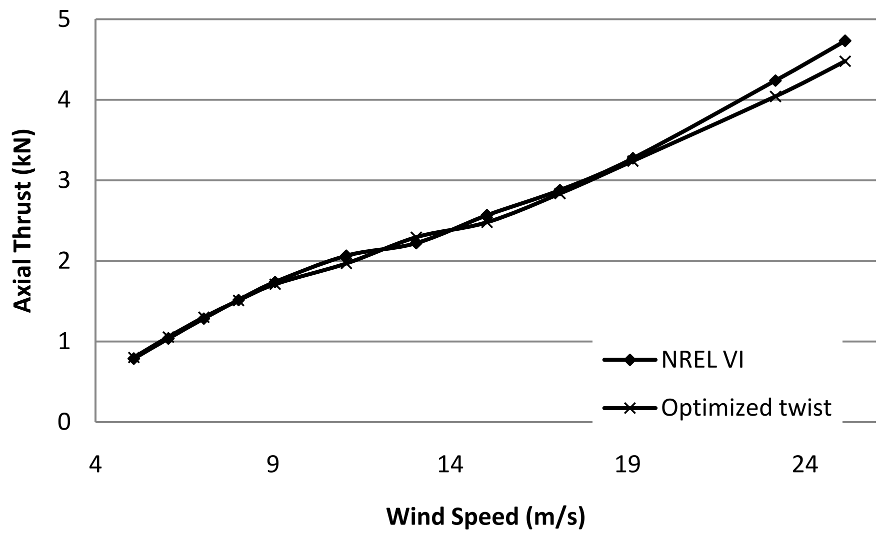

Figure 5.37: Comparison of axial thrust between NREL VI and optimized twist

From the two figures above, it is clear that the increase in power is more than the increase in axial thrust. In fact the average percentage increase of power is 4.0 % where the average percentage increase in axial thrust is -1.2 %. This is a good result which means that the optimized twist causes an increase in the power and a decrease in the axial thrust and loads. However, the increase in power is still very low (only 4%). This means that the twist angle distribution of the original blade is almost optimum. To increase the power to much higher levels, the pitch angle of the blade need to be optimized.

5.4 Blade Pitch Design

Due to the difficulty in designing a twist distribution which satisfies the objective function of increasing the power at different, low, mid and high, wind speeds, it seems to be more efficient of using pitch regulated blades than stall regulated ones. In this case, the power can be increased for each wind speed separately by setting the optimum pitch angle for each wind speed.

The parametric model is the same NREL VI blade without modification in the sections. The varying parameter is just the pitch angle of the blade. So generating a database for different pitch angles for each wind speed is enough to choose the best angle. The best angle is chosen according to the high power and low thrust.

5.4.1 Database Generation

A separate database is generated for each wind speed. Each database consists of different number of samples according to different pitch angles as shown in Table (5.5).

Table 5.5: Database of pitch design.

Wind Speed (m/s)	Range of pitch angle (deg.)	Number of samples
4	-4,-3,…,5,6	11
5	-4,-3,…,1,2	7
6	-6,-5,…,4,5	12
7	-6,-5,…,5,6	13
8	-4,-3,…,5,6	11
9	-4,-3,…,5,6	11
10	-1,0,…,4,5	7
11	-1,0,…,5,6	8
12	-1,0,…,5,6	8
13	-1,0,…,8,9	11
14	-1,0,…,8,9	11
15	-1,0,…,8,9	11
16	-1,0,…,8,9	11
17	-1,0,…,8,9	11
18	-1,0,…,8,9	11
19	-1,0,…,8,9	11
20	-1,0,…,8,9	11

5.4.2 Results

Changing the pitch angle has a great effect on the power and axial thrust of the wind turbine. The pitch angles were designed for a rated power of 12kW at a rated wind speed of 11m/s. At wind speeds higher than 11m/s, the pitch angle was changed to set the power constantly at 12kW.

The optimum pitch angles for the different wind speeds are shown in Figure (5.38):

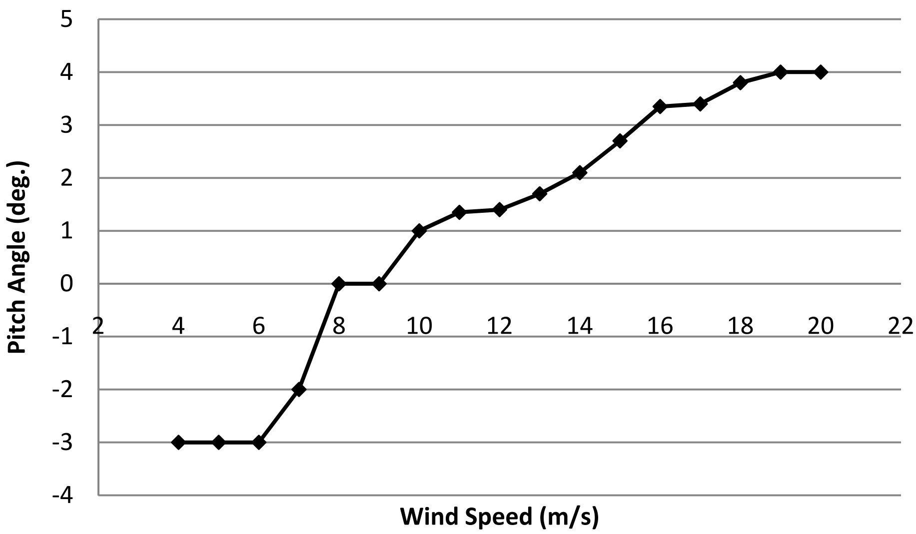

Figure 5.38: Optimum pitch angles

The pitch angles are added to the optimized twist distribution of each section of the blade. For example, at section 3 of the blade, the optimum twist angle is 112 deg and the optimum twist angle is -3 deg. So the real twist of the blade at section 3 is 109 deg.

A comparison between the NREL VI power curve and the computed power curve for the optimum pitch is shown in Figure (5.39):

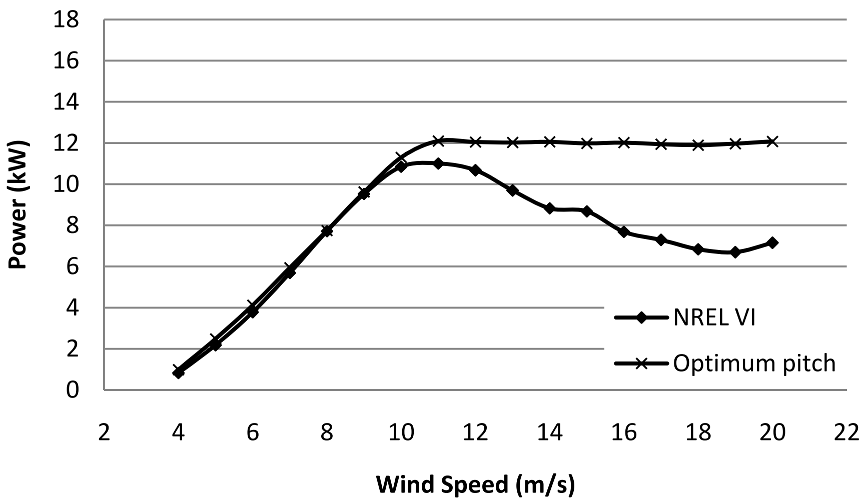

Figure 5.39: Comparison of power curve between NREL VI and optimum pitch

The optimum pitch has shown an average increase of about 8% in power for low wind speeds and an increase of about 30% in power for the whole wind speed range.

The results for the axial thrust are shown in Figure (5.40):

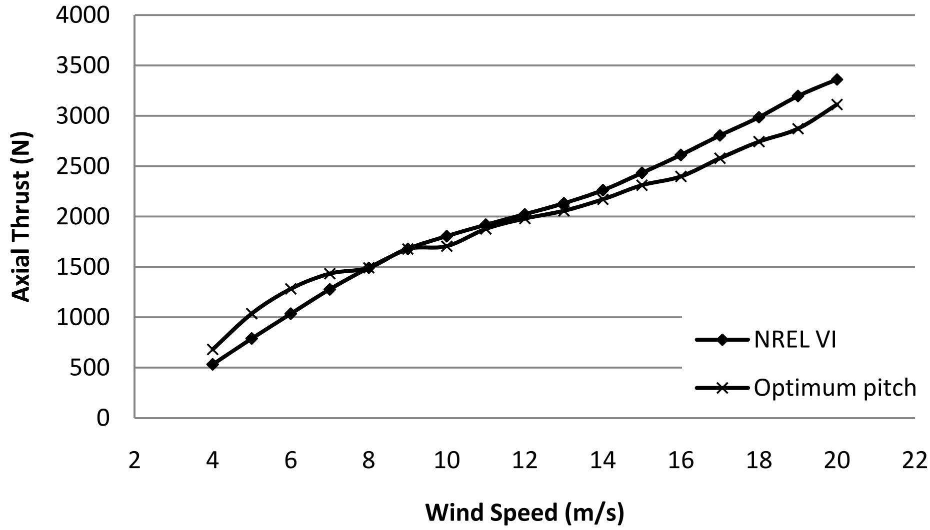

Figure 5.40: Comparison of axial thrust between NREL VI and optimum pitch

It is noticed that the axial thrust for the optimum pitch is higher than that of NREL VI up to 8m/s and after that it becomes less. At low wind speeds even though the axial thrust is higher, it still low in value and can be tolerated by the blades. At high wind speeds, the axial thrust becomes more important phenomenon from structure point of view. Large values of axial thrust may result in structural problems including the destruction of the blades. This is avoided in the optimum pitch angles as the axial thrust is less than that of NREL VI.

More results and CFD analysis are obtained in Section (5.5) for the final optimized blade where, optimum winglet, optimum twist distribution and optimum pitch angles are combined to produce the final design.

5.5 Final Design – Post-Processing

In this section, the optimized winglet, the optimized twist distribution and the optimum pitch angle for each speed are combined in one final blade.

The power curve comparison between the different designs is shown in Figure (5.41):

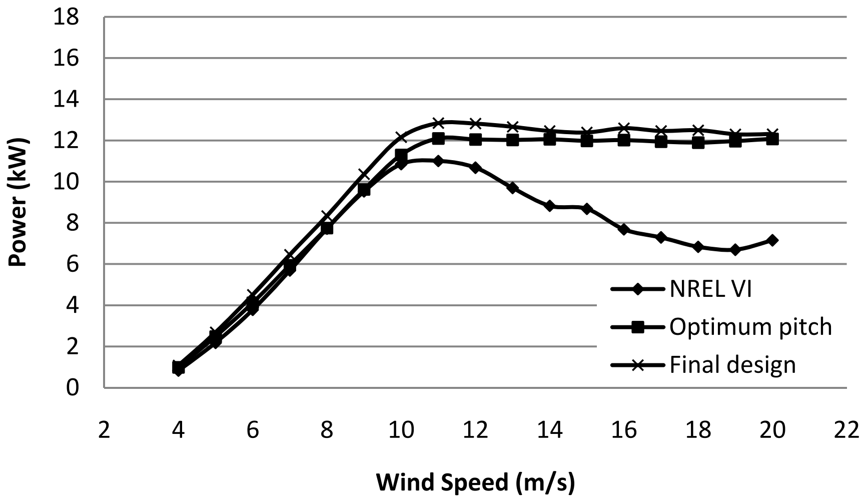

Figure 5.41: Comparison of power curve between NREL VI, optimum pitch and final design

It is clear that the rated power has been increased to 12.5kW. The percentage of increase in the power production compared to the original NREL VI is shown in Figure (5.42):

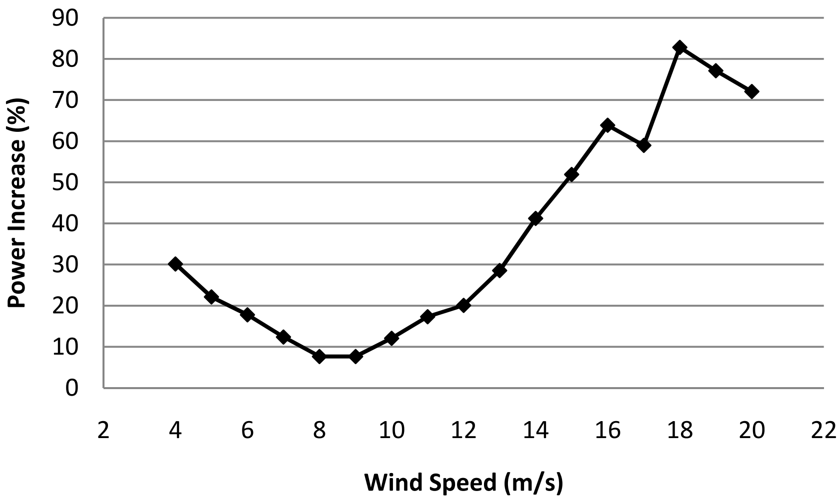

Figure 5.42: Percentage increase in power production of the final design

It is noticed that there is a large increase in power production due to the optimum winglet, twist and pitch. Even at low wind speeds, the increase is about 20%. The overall average increase in power is around 37%.

The results for the axial thrust are shown in Figure (5.43):

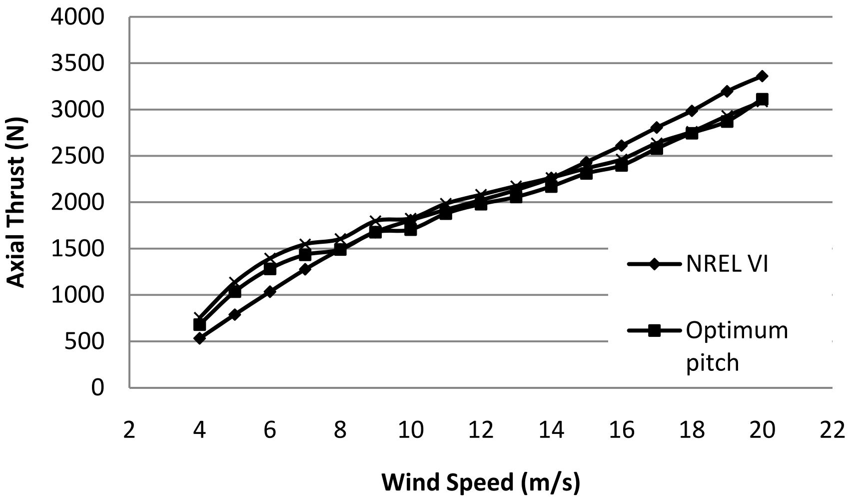

Figure 5.43: Comparison of axial thrust between NREL VI, optimum pitch and final design

The percentage of increase in the axial thrust compared to the original blade is shown in Figure (5.44):

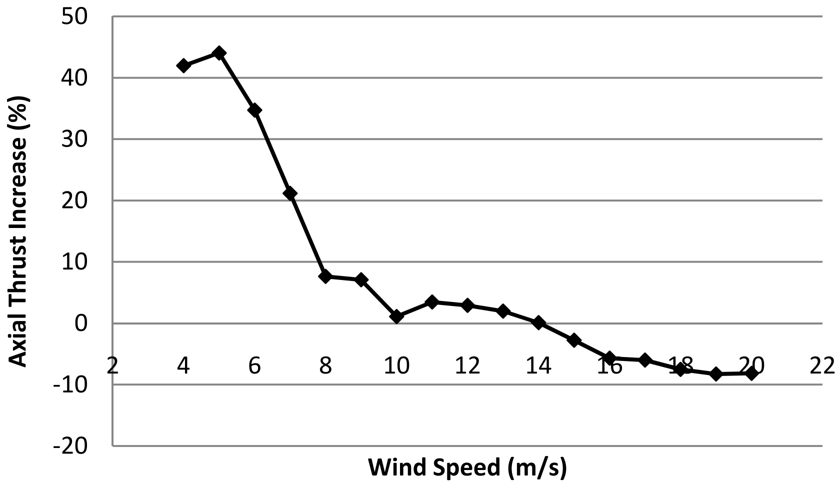

Figure 5.44: Percentage increase in axial thrust of the final design

Again, the increase in axial thrust is at low wind speeds but at high wind speeds, the axial thrust decreases. So the values of axial thrust at low wind speeds are still small and can be sustained by the blade.

To understand the increase in the power production, one needs to see the change in the aerodynamic forces acting on the blade, the pressure coefficient distribution and the formation of vorticies behind the blade. The normal and tangential force coefficients C_N and C_T are computed using Equations (3.4) and (3.5) and the results compared to the original blade are shown in Figures (5.45) and (5.46).

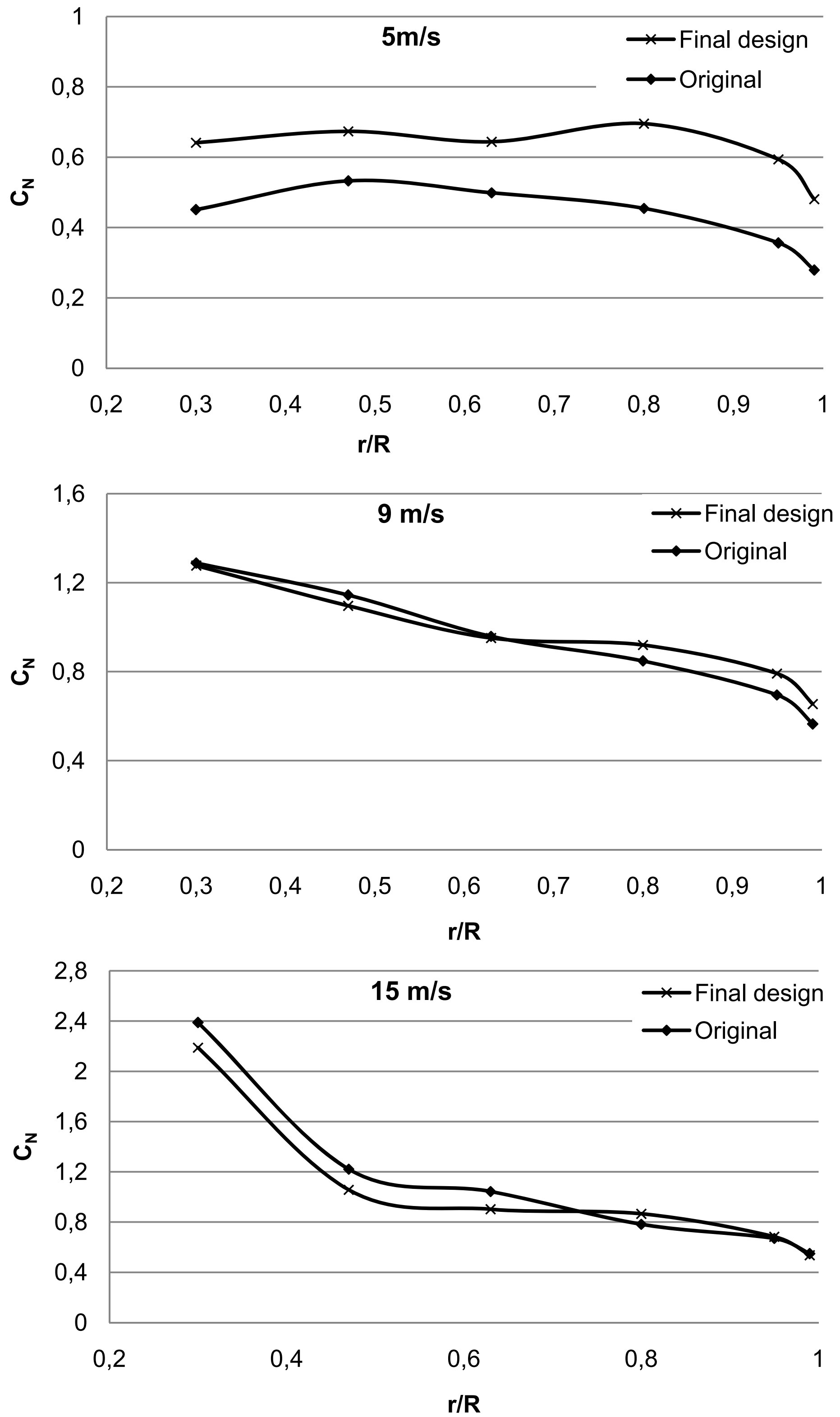

Figure 5.45: Comparison of original blade normal force coefficient with the final optimum blade

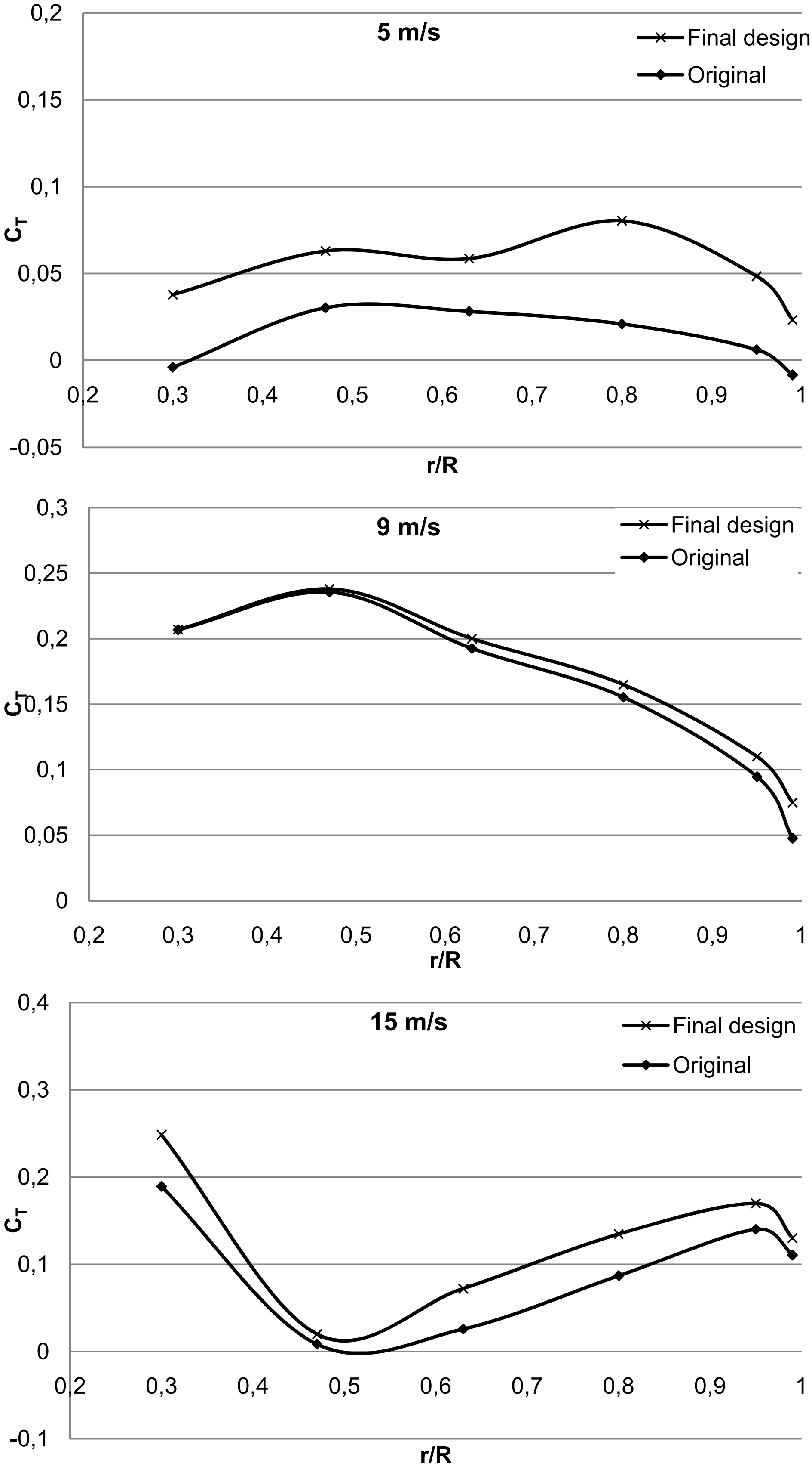

Figure 5.46: Comparison of original blade tangential force coefficient with the final optimum blade

At 5 m/s, Figure (5.45) shows that C_N of the optimized blade is about 50% higher than C_N of the original blade. This explains the large increase in axial thrust of the optimized blade at 5ms.

At 9m/s, it clear that the increase in C_N is small compared to the increase at 5m/s and 15 m/s. This is because the optimum pitch angle of the optimized blade is same as that of the original blade. So the increase in C_N is only due to optimum winglet and twist. Comparing Figure (5.45) with Figure (5.22) at 9 m/s, one notices that the trend of the curves is similar. As mentioned before, the optimum twist effect is not very significant on the axial thrust so the significant effect comes from the winglet and that is why the results in Figures (5.45) and (5.22) are similar.

At 15 m/s, the average C_N value of the optimized blade is about 4% less than C_N value of the original blade. This result agrees with the one in Figure (5.44) where the axial thrust has decreased at 15m/s.

Figure (5.46) shows that, at 5 and 15 m/s there is a significant increase in C_T values. This indicates that the driving force has increased which explains the increase in the power in Figure (5.42). Where at 9 m/s, the increase is less because the effect is only due to the winglet and twist as mentioned before.

The pressure coefficients at different spanwise locations for three wind speeds are obtained in Figures (5.47), (5.48) and (5.49):

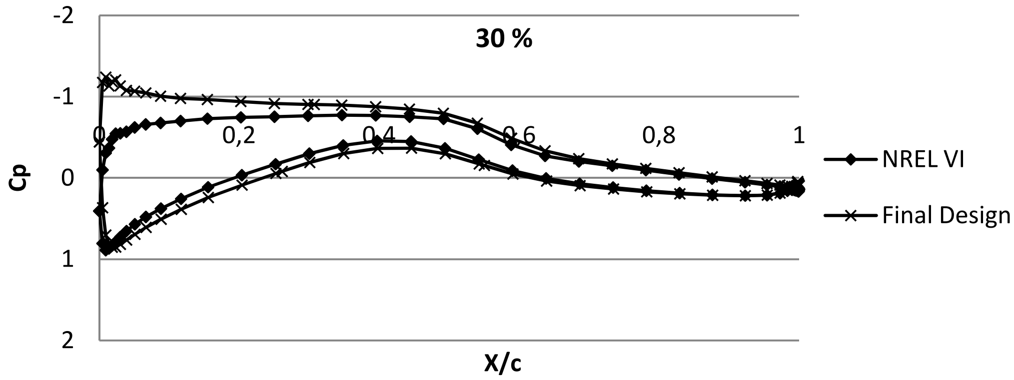
30 %
Cp
X/c
NREL VI
Final Design

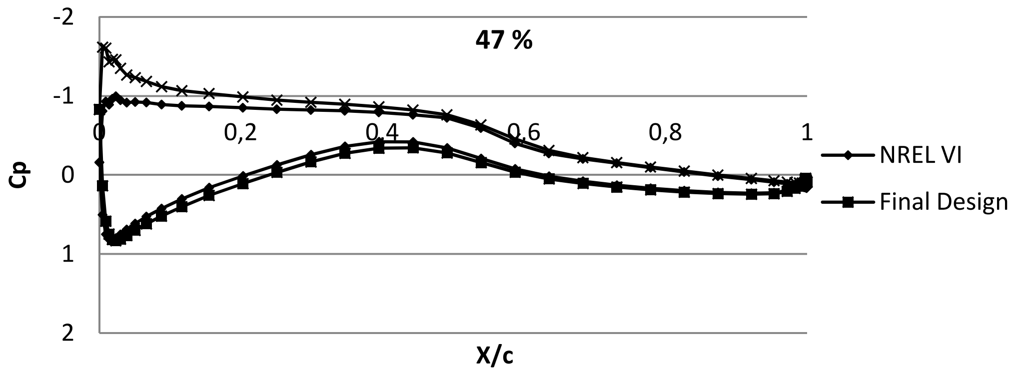
47 %
Cp
X/c
NREL VI
Final Design

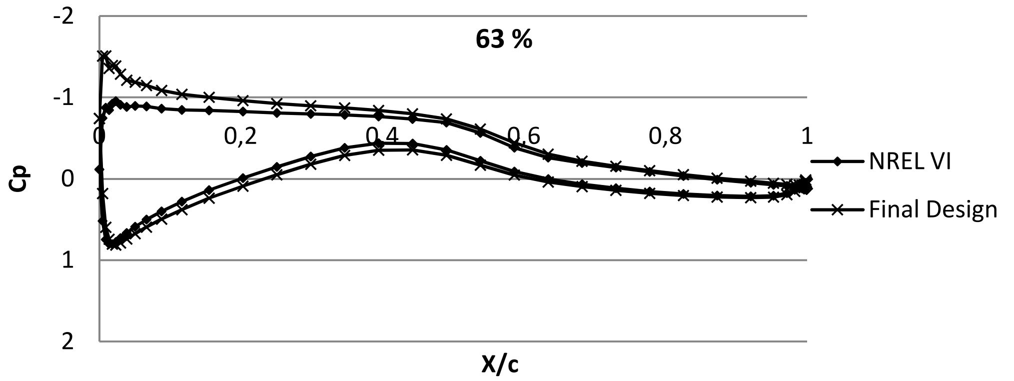
63 %
Cp
X/c
NREL VI
Final Design

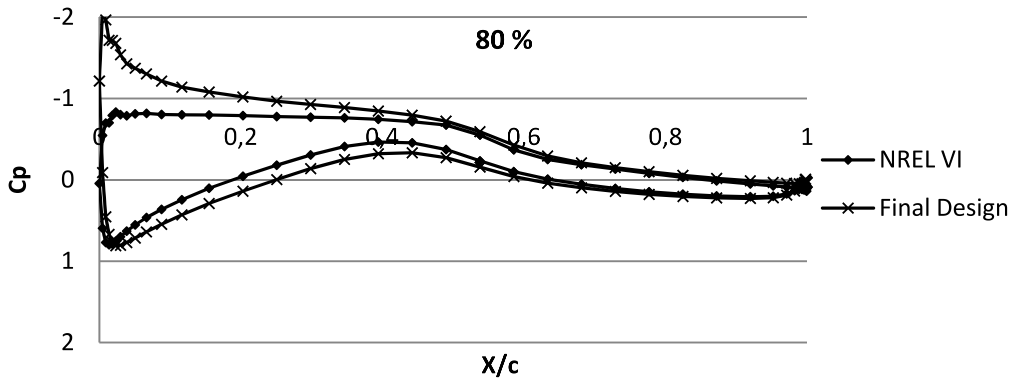
80 %
Cp
X/c
NREL VI
Final Design

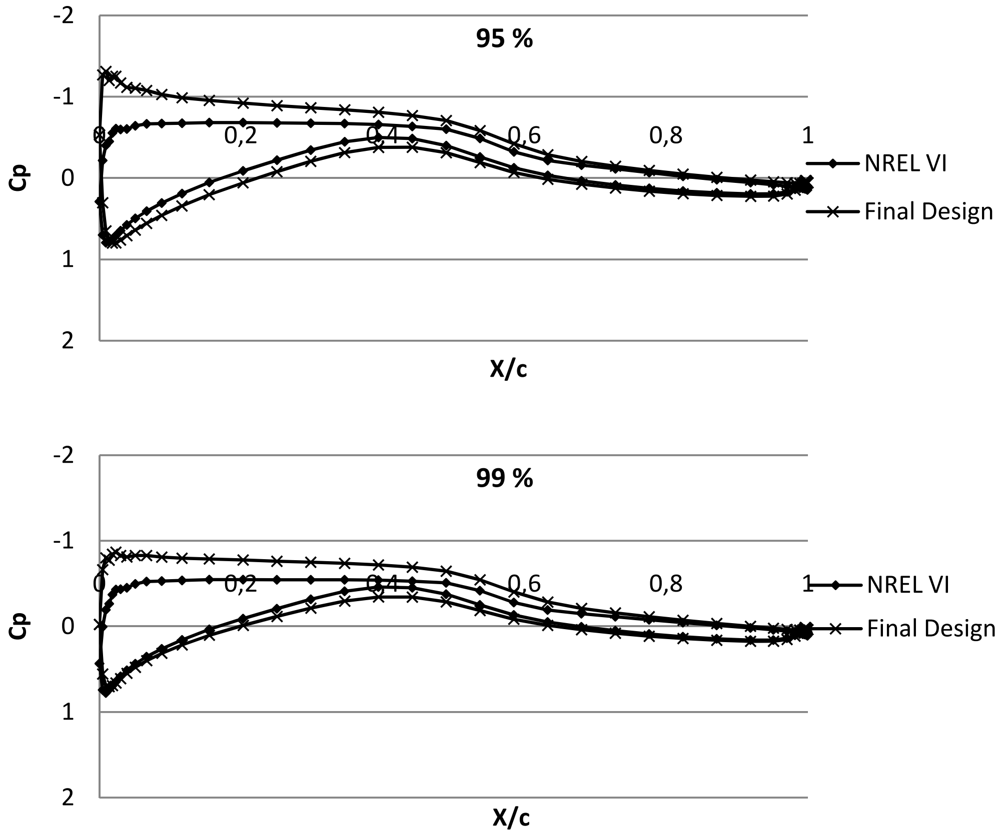

Figure 5.47: Cp distribution comparison between NREL VI and final design at 5m/s

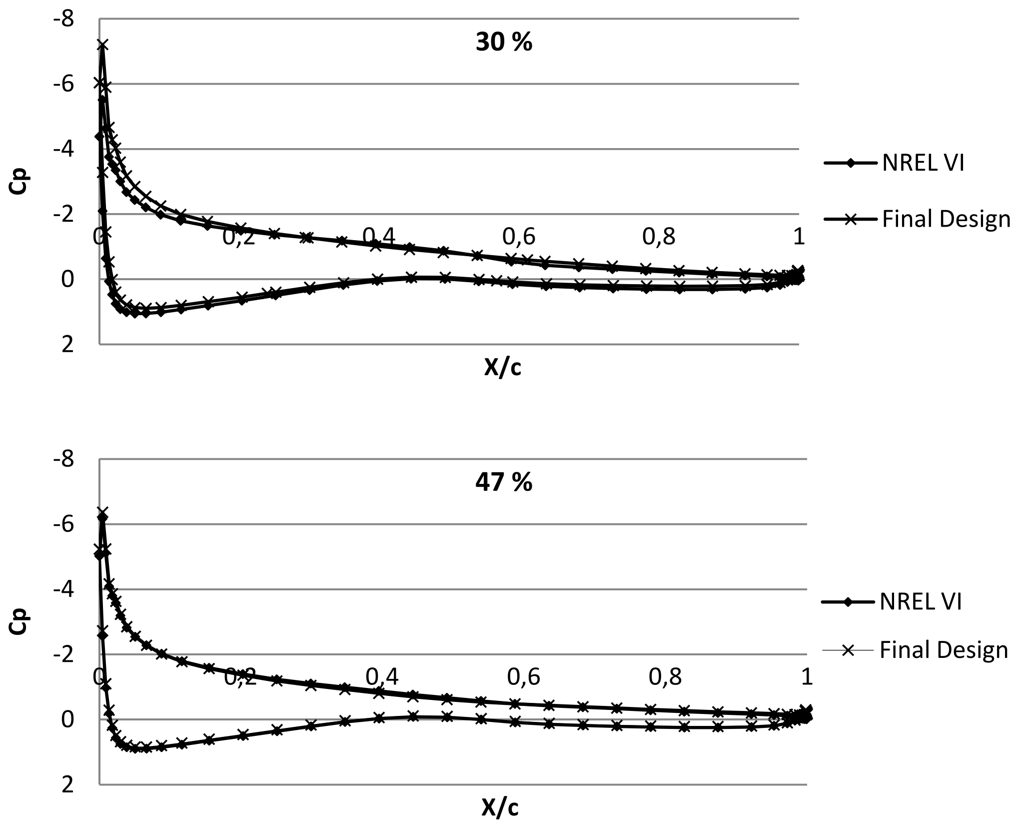

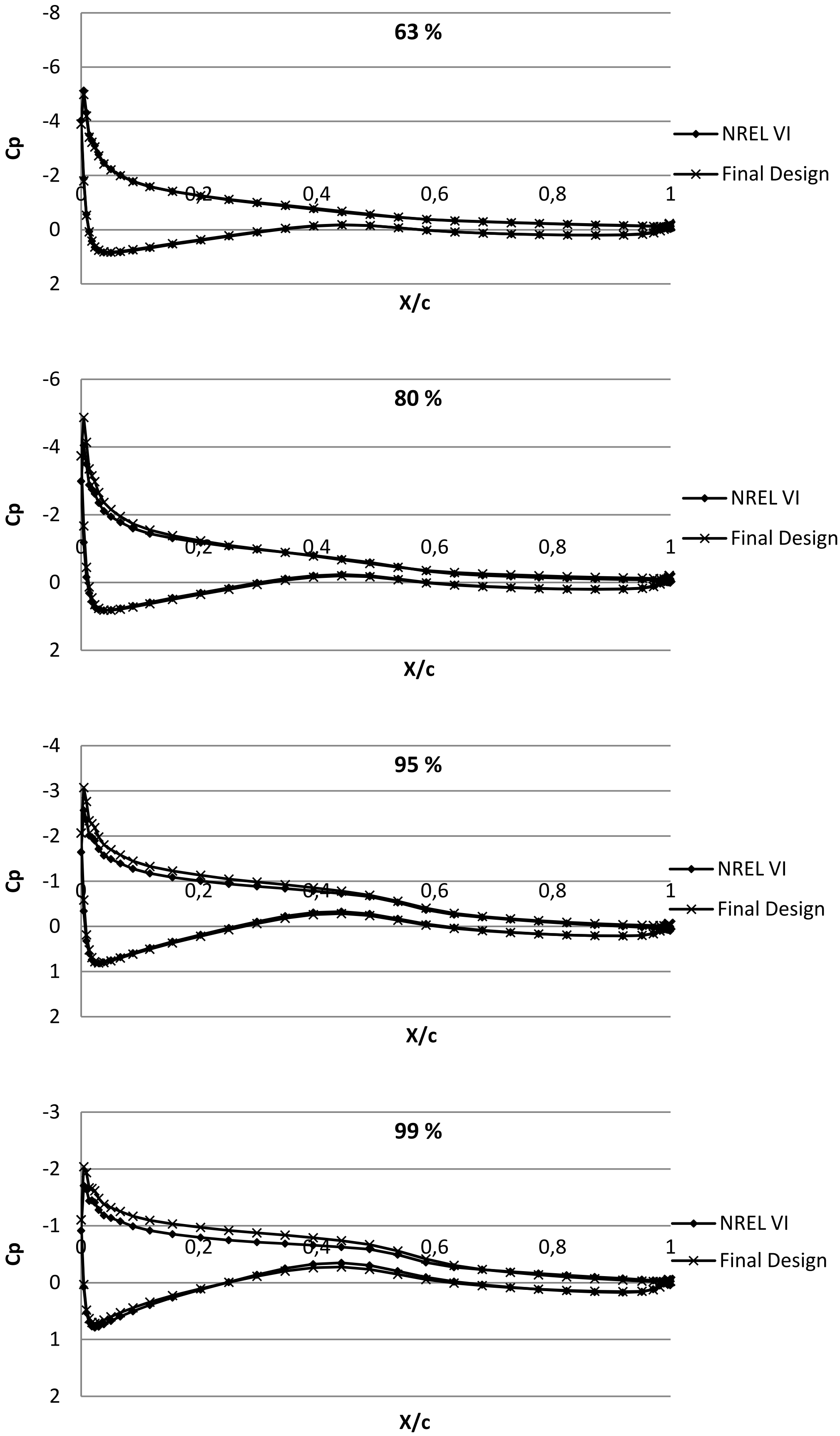

Figure 5.48: Cp distribution comparison between NREL VI and final design at 9m/s

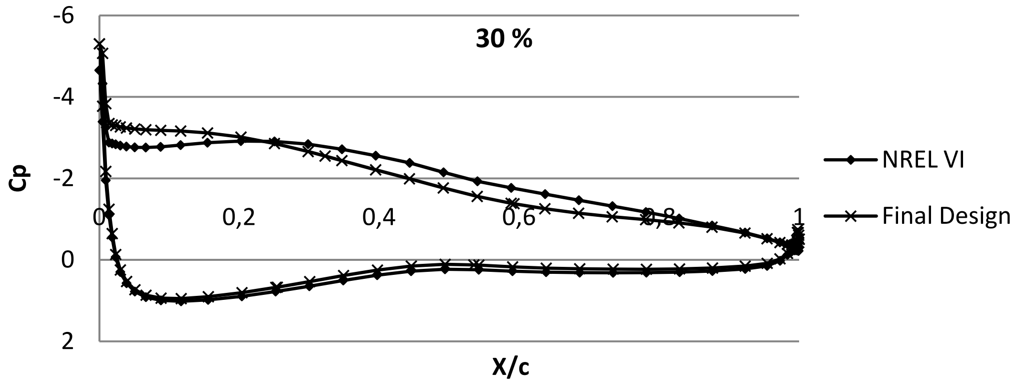
30 %
Cp
X/c
-6
-4
-2
0
2
0
0,2
0,4
0,6
0,8
1
NREL VI
Final Design

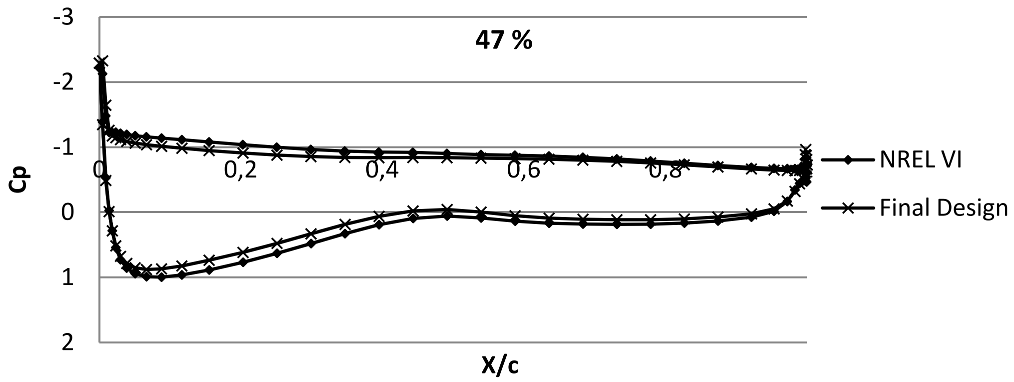
47 %
Cp
X/c
-3
-2
-1
0
1
2
0
0,2
0,4
0,6
0,8
NREL VI
Final Design

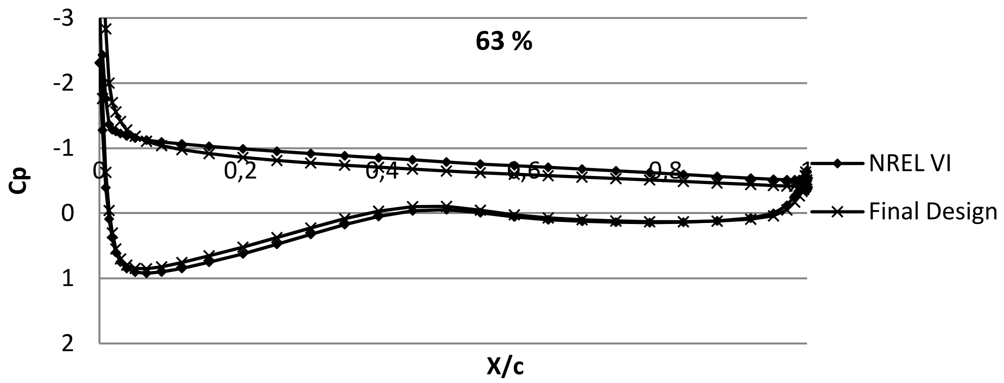
63 %
Cp
X/c
-3
-2
-1
0
1
2
0
0,2
0,4
0,6
0,8
NREL VI
Final Design

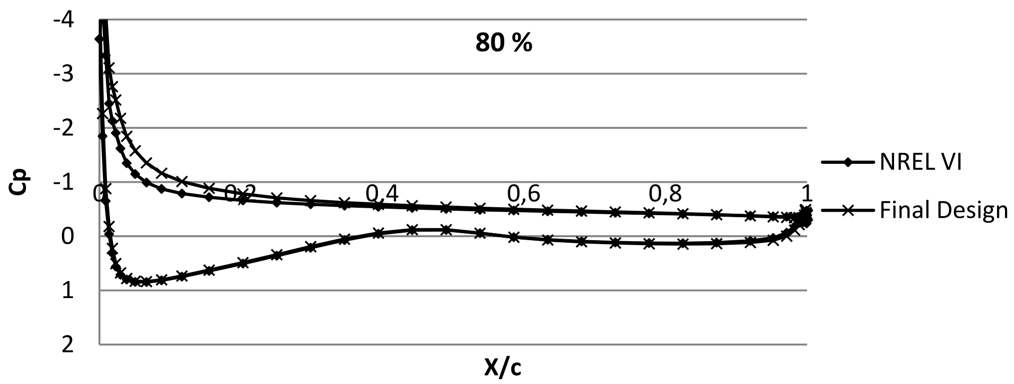
80 %
Cp
X/c
-4
-3
-2
-1
0
1
2
0
0,2
0,4
0,6
0,8
1
NREL VI
Final Design

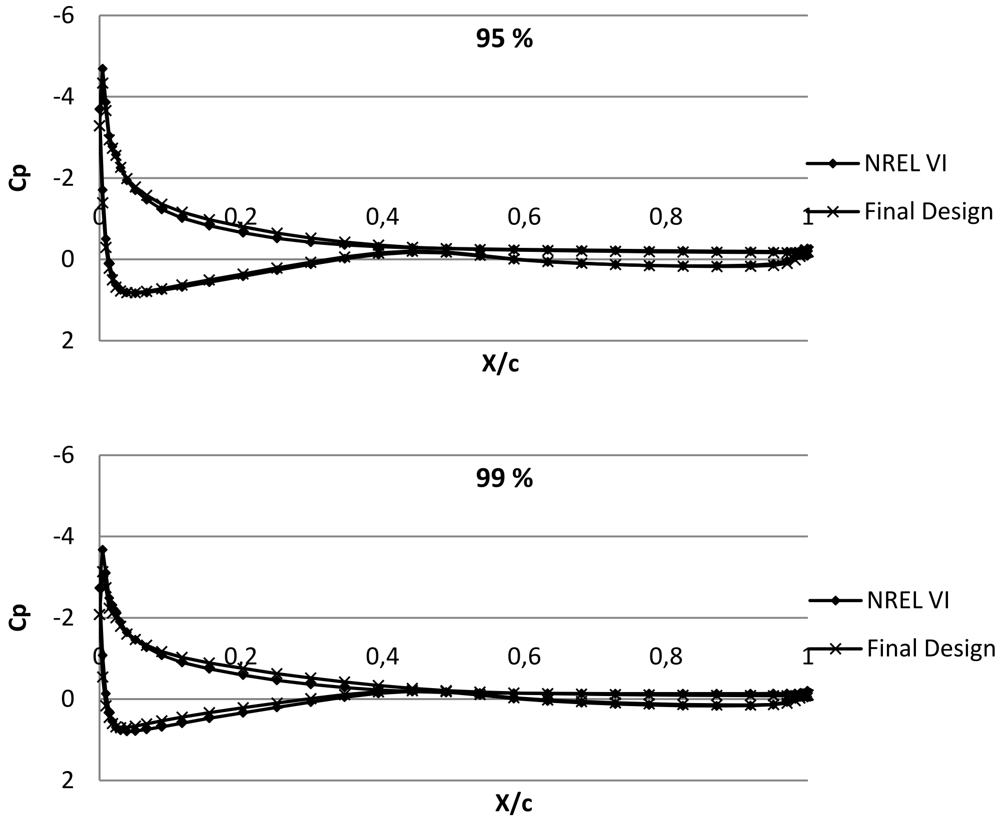

Figure 5.49: Cp distribution comparison between NREL VI and final design at 15m/s

At 5m/s, the pressure coefficient is different from the original blade. The pressure is less at the suction side while it is more at the pressure side resulting in more power.

At 9m/s, there is no clear difference between the pressure coefficient distribution of the optimized blade and the one of the original blade at the sections close to the root. Close to the tip region, sections 95% and 99%, the difference becomes clearer. At 9 m/s, the optimum pitch angle is the same as for the original blade. So the power difference comes from the optimized winglet whose effect is more towards the tip.

At 15 m/s there is change in the pressure distribution resulting in increase in the power.

The relative velocity streamlines are plotted at 13m/s and 15m/s as shown in Figures (5.50) and (5.51). The streamlines are not shown for pre-stall wind speeds (5 and 9m/s) because separation at pre-stall speeds is weak.

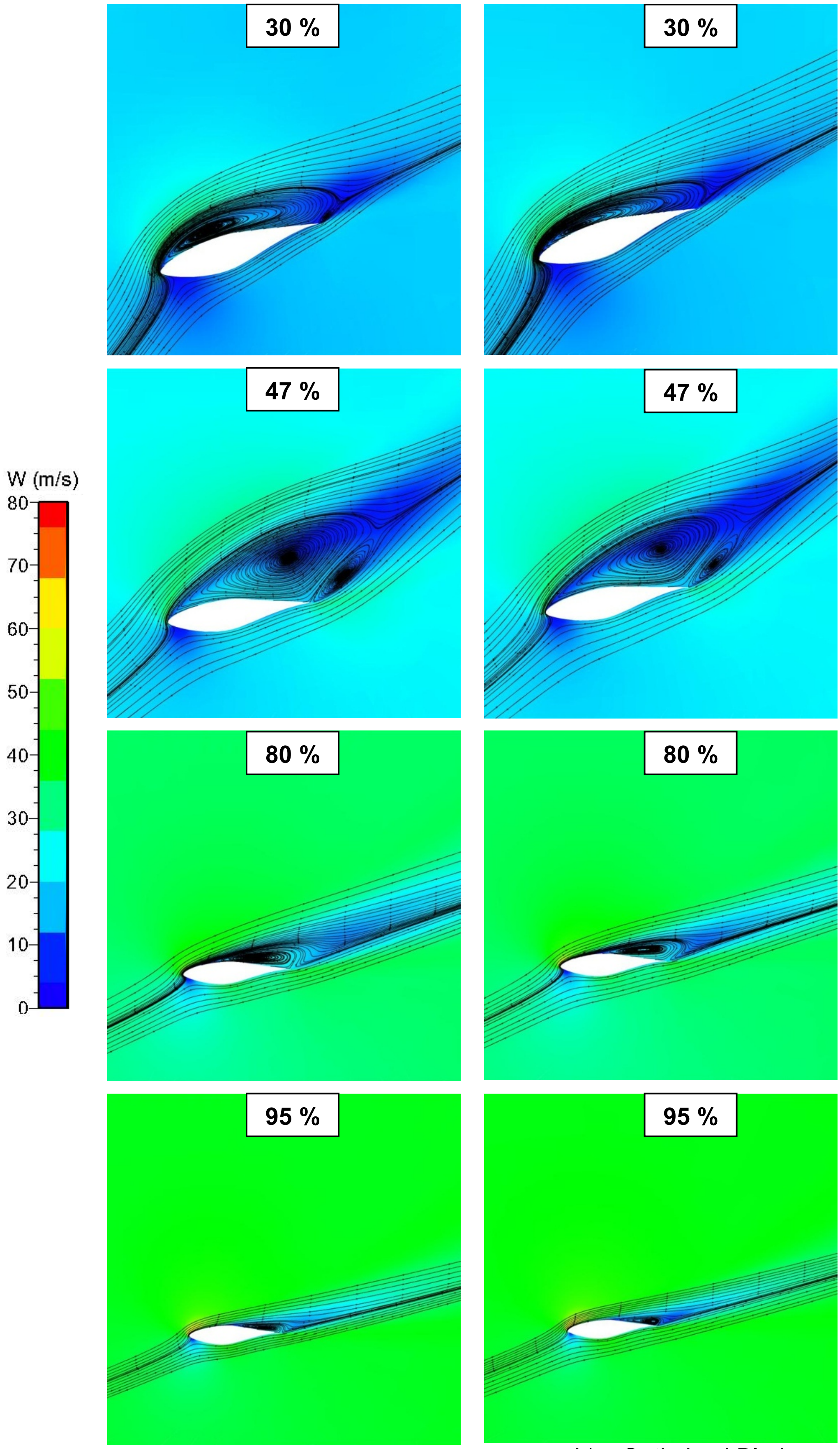

a) Original Blade b) Optimized Blade

Figure 5.50: Relative velocity contours with streamlines comparison at 13 m/s

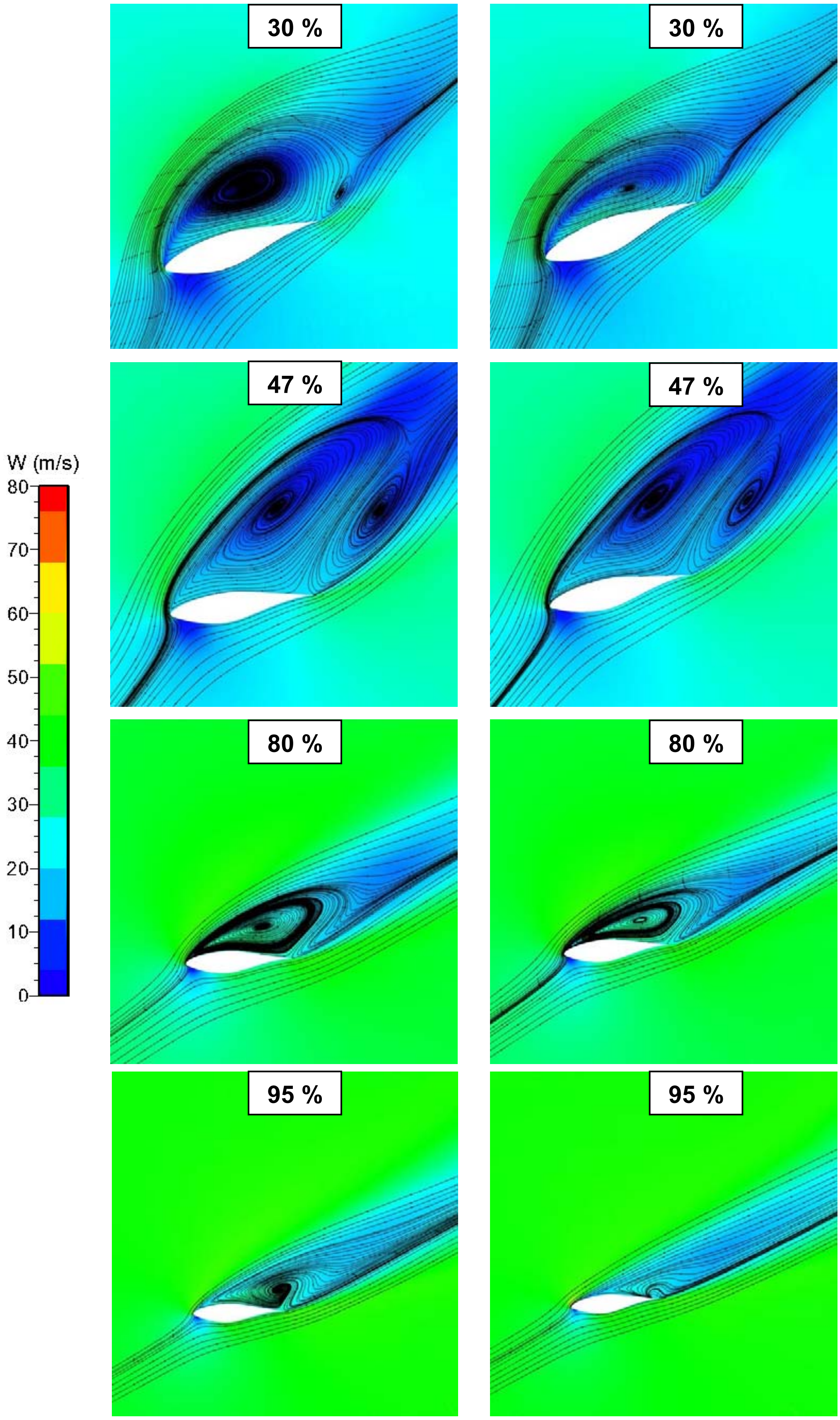

a) Original Blade b) Optimized Blade

Figure 5.51: Relative velocity contours with streamlines comparison at 15 m/s

At 13m/s, the vortex behind the optimized blade is less than that behind the original blade. This is also clear at 15m/s, where the vortex is closer to the blade. Towards the tip region, the effect of the optimum winglet appears. From Figure (5.51), at 95% a vortex was formed behind the original blade where it disappeared behind the optimized blade and the flow became more attached.

CHAPTER 6

CONCLUSIONS AND RECOMMENDATIONS

6.1 Concluding Remarks

The main purpose of this study is to aerodynamically design and optimize winglet, twist angle distribution and pitch angle for a wind turbine blade using CFD to produce more power. During the study many issues were considered and analyzed;

- Preconditioning
- NREL Phase II and VI for validation
- Turbulence models
- Different winglet, twist and pitch configurations

Based on the results of the optimization and the other issues, the following concluding remarks can be drawn;

- Since the Mach number of the airflow around the wind turbine blades is very small, preconditioning is necessary to overcome the lack of accuracy and the slow convergence of the compressible flow codes. A comparison between the solver without preconditioning, with Merkle preconditioner and with Hakimi preconditioner have been done and the results were compared with the measured pressure coefficient data for the NREL Phase VI. The results have showed the need for the preconditioner to obtain more accurate and faster solution. The most accurate solution was obtained by using the Merkle preconditioner. It is believed that the advantage of Merkle over Hakimi preconditioner in this study is the robustness of Merkle preconditioner at high aspect ratios. For wind turbines, due to the mesh in the far field, the aspect ratio might reach high values (e.g. 30000), and needs a very robust code to ensure good convergence with accurate results.

- Two test cases have been investigated to validate the RANS solver of Numeca Fine/Turbo. The test cases are NREL Phase II and VI. Different turbulence models were used in the validation. The $k-\varepsilon$ Launder – Sharma has shown superior results compared to the other models in both of the test cases. In fact it was expected that the SST $k-\omega$ would give better results since it takes the advantage of both the $k-\omega$ and $k-\varepsilon$ models. The results obtained in this study are in agreement with previous results in literature that the $k-\varepsilon$ model could predict the power more accurately than the SST $k-\omega$ model. To well assess this issues, different meshes with different y+ values should be tested and also more wind turbine test cases should be considered. However, the $k-\varepsilon$ Launder – Sharma has shown sufficient accuracy to be selected as the turbulence model for the further computations and also for the design and optimization. Comparing the computed spanwise pressure coefficient distribution by the RANS solver with the measured data, it is noticed that at pre-stalled wind speeds, the results are very close to the measured data except for small deviation at the LE which might be due to Kutta condition. As the wind speed increases above the stall value, the deviation becomes bigger especially in the suction side of the blade where vortices are formed. The vortices are stonger towards the root and the deviation between the computed data and measured data is more towards the root. Since the $k-\varepsilon$ Launder – Sharma model is a low Reynolds number model, it is not capable of accurately capture the flow at stall especially when there is a great separation. As one goes towards the tip of the blade, even at post-stall wind speeds, the separation becomes less and the accuracy of the solver becomes more.

- Before starting the design process and in order to decrease the number of design variables to decrease the CPU cost of the computations, a pre-deign study has been made. Different winglet configurations have been analyzed and the results for the power production were compared with the results of the original blade. Among the different configurations, it was noticed that adding a winglet to the wind turbine blade and making it pointing towards the suction side of the blade results in more power production. That configuration was used for the winglet design and optimization. Also the effect of twist and pitch on the power production was investigated and the results have showed the big effect of pitch and twist on power production.

The results also have showed that it is difficult to have one pitch angle which causes an increase in power for wide range of wind speeds. The increase in power at certain wind speed for a certain pitch angle is usually at the expense of the power at different wind speeds.

- The Genetic algorithm together with the artificial neural network were used in the optimization of the winglet. The design variables were the cant and twist angles and the objective function was the power output. To ensure validity of the design for wide range of operating conditions, multipoint optimization was carried out to maximize the power at wind speeds of 5, 7 and 9 m/s. The CPU time was 968 hours. The optimized winglet has shown an increase in power of about 9.5%. Both the power and the loads (represented by the axial thrust) have increased. However the increase in power is much more than the increase in the axial thrust means that such increase in the axial thrust has no significant effect on the structural properties of the blade. Results for the aerodynamic forces (normal and tangential force coefficients) were obtained. These results have shown that both of the forces increase especially in the tip region which shows the effect of the winglet. Other results showed how the winglet affects the flow by making it more attached at the tip resulting in more power production. So the addition of winglet increases to the wind turbine blade increases the power output of the turbine and optimizing the winglet results in even more power. The 9.5% increase in power is relatively good increase. Talking about big wind turbines of 2MW rated power, then such turbine produces about 6,132,000 kWh in a wind farm of 35% capacity factor. Such amount of energy makes about 204400 EUR. So any 9.5% increase in energy amount means an increase of about 20000 EUR per year which is usually the cost of maintenance of a wind turbine per year.

- The twist design and optimization was also conducted by GA and ANN. The variable parameters were the twist angles at 8 sections of the blade resulting in 300 samples for the database and 90 samples for the optimization. And the objective functions were the power output at three different wind speeds The results for the optimized twist have shown no significant increase in power meaning that the original blade has already an optimum twist distribution.

- To obtain better power production at every wind speed, the best way is to change the pitch angle for every wind speed. In other words, to change the blade from stall regulated into pitch regulated. A database was generated which included many samples for wind speeds between 5 and 20 m/s resulting in total of 176 samples. The optimum pitch angle was selected according to maximum power and tolerable thrust. However, at high wind speeds (higher than stall) the power keeps increasing. To prevent so, the pitch angles at post-stall wind speeds were chosen such that the power does not exceed the rated value (12 kW). By pitch regulating the power at low wind speeds increased by about 20% and it increased by about 30% for the whole speed range. Another factor that should be considered is the increase in axial thrust. The axial thrust has considerably increased at low wind speeds but it decreased at mid and high wind speeds. The increase in value at low wind speeds is still small and can be tolerated by the blade. There would have been structural problems if such increase occurred at high wind speeds.

- Finally, the optimum winglet, the optimum twist and the optimum pitch angle for each wind speed were combined to yield the final design. The results of the final design have shown a large increase in power production compared to the original blade. The average of power increase was about 37%.

6.2 Recommendations and Future Work

Recommendations for future work include:

- Grid sensitivity analysis for different turbulence models and different wind turbine blades. Different grids with different y+ values should be tested to decide on the best turbulence model for wind turbine simulations.
- For the winglet optimization, more design variables are to be considered such as different airfoils.
- For the twist optimization again different airfoils are to be included in the design variables.

REFERENCES

[1] König, F.v., *"Wind Energy in Practical Use"*, Munichi Udo Pfriemer Verlag, 1978.

[2] Fröde, E. u. F., *"Windmills"*, Cologne, Du Mont Buchverlag, 1981

[3] Erich Hau, *"Wind Turbines"*, 2nd Edition, Springer, 2006.

[4] Notebaart, J. C. *"Windmills",* Den Haag, Mouton-Verlag, 1972

[5] Park, J. *"The Wind Power Book",* Chesire Books, Pal0 Alto, CA, 1981.

[6] Eldridge, F. R. *"Wind Machines",* 2nd Edition, Van Nostrand Reinhold, New York, 1980.

[7] nglis, D. R. *"Windpower and Other Energy", Optiom* University of Michigan Press, Ann Arbor, MI, 1978.

[8] Freris, L. L. *"Wind Energy Conversion Systems",* Prentice Hall, New York, 1990.

[9] Dodge, D. M, *"Illustrated History of Wind Power Development"*, http://telosnet.com/wind, last visited 15-December-2011

[10] Ackerrnann, T. And Soder, L. *"Wind Energy Technology and Current Status"*: A Review Renewable and Sustainable Energy Reviews, 4,315-374, 2000.

[11] Eggleston, D. M., Stoddard, F. S. *"Wind Turbine Engineering Design",* Van Nostrand Reinhold, New York, 1987.

[12] Golding, E. W. *"The Generation of Electricity by Wind Power",* E. & F. N. Spon. London, 1977.

[13] Johnson, G. L. *"Wind Energy Systems",* Prentice Hall, Englewood Cliffs, NJ, 1985.

[14] Spera, D. A. *"Wind Turbine Technology: Fundamental Concepts of Wind Turbine Engineering".* ASME Press, New York, 1994.

[15] Hanison. R., Hau, E., Snel, H. **"***Large Wind Turbines: Design and Economics",* Wiley, Chichester, 2000.

[16] Ancona, D. F.*"Power Generation, Wind Ocean', in Wilk's Encycopedia of Architecture: Design, Engineering and Construction"*, Volume 4, John Wiley & Sons, Ltd/Inc., New York, pp. 32–39, 1989.

[17] Gipe, P., *“Wind Energy Comes of Age”*, John Wiley & Sons, Ltd/Inc., New York, 1995.

[18] Heymann, M. *“Die Geschichte der Windenergienutzung 1890–1990 (The History of Wind Energy Utilisation 1890–1990)”*, Campus, Frankfurt are Main, 1995.

[19] Hills, R. L. *“Power From Wind – A History of Windmill Technology”*, Cambridge University Press, Cambridge, 1994.

[20] Kealey, E. J. *“Harvesting the Air: Windmill Pioneers in Twelfth-century England”*, University of California Press, Berkeley, CA, 1987.

[21] Koeppl, G. W. *“Putnam’s Power from the Wind”*, 2nd edition, Van Norstrand Reinhold Company, New York, 1982.

[22] Righter, R. *“Wind Energy in America: A History”*, University of Oklahoma Press, USA, 1996.

[23] Shepherd, D. G. *“Historical Development of the Windmill”*, DOE/NASA-5266-2, US Department of Energy, Washington, DC, 1990.

[24] Shepherd, D. G. *“Historical Development of the Windmill’, in Wind Turbine Technology”*, SAME Press, New York, 1994.

[25] Heidelberg, D. and Kroemer, J. *“Vertikalachsen-Rotor mit integriertem Magnetgenerator”, (Vertical axis rotor with integrated magnetic generator),* BremTec:Windenergie ’90, Bremen 1990

[26] Pedersen, M.B. and Nielsen, P. *“Description of the two Danish 630 kW Wind Turbines Nibe A and Nibe B. Kopenhagen”*, 3. BHRA International Symposium onWind Energy Systems 26–29 Aug., 1980

[27] Tangler, J. L., Smith, B. and Jager, D., *“SERI Advanced Wind Turbine Blades”*, NREL/TP-257-4492, Golden, CO, 1992.

[28] Eppler, R., “*Airfoil Design and Data”*, Springer-Verlag, New York, 562pp, 1990.

[29] Selig, M. S., Donovan, J. F. and Fraser, D. B. “*Airfoils at Low Speeds”,* Soartech 8, Virginia Beach, VA, H. A. Stokely, 1989.

[30] Glauert, H. *“An Aerodynamic Theory of the Airscrew” ,ARC R&M* 786, January 1922.

[31] Hansen, A. C. and Butterfield, C. P., *"Aerodynamics of Horizontal-Axis Wind Turbines", Annual Review of Fluid Mechanics.* Volume 25, pp. 115-149, 1993.

[32] Laino, D. and Butterfield, C. P., *"Using YAWDYN to Model Turbines with Aerodynamic Control Systems",* ASME Wind Energy Conference, New Orleans, 1994.

[33] Hansen, A.C. and Laino, D.J., *"User's Guide to the Wind Turbine Dynamics Computer Programs YawDyn and AeroDyn for ADAMS",* 1999 Available for download from: http://wind.nrel.gov/designcodes/simulators/yawdyn/ (accessed July, 2008).

[34] Leishman, J. G. and Beddoes, T. S., *"A semi-Empirical Model for Dynamic Stall", Journal of the American Helicopter Society*, Volume 34, pp. 3-17, 1989.

[35] Marshall L. Buhl Jr., *"The NWTC Design-Codes Suite: An Overview", NRELNWTC*, January 2005.

[36] Özlem Ceyhan, *"Aerodynamic Design And Optimization Of Horizontal Axis Wind Turbines By Usıng BEM Theory And Genetic Algorithm"*, MSc Thesis, Middle East Technical University, September 2008.

[37] Gerber, Tangler, Duque, and Kocurek, *"Peak and Post-Peak Aerodynamics from Phase VI NASA Ames Wind Turbine Data", Journal of Solar EnergyEngineering*, Volume 127, Issue 2, pp. 192-199, May 2005.

[38] Earl P. N. Duque, Wayne Johnson, C. P. vanDam, *"Numerical Predictions of Wind Trubine Power and Aerodynamic Loads for the NREL Phase II Combined Experiment Rotor",* Proceedings of the 1999 ASME Wind Energy Symposium, Reno, NV, Jan. 1999.

[39] Earl P. N. Duque, C. P. van Dam, and Shannon C. Hughes, *"Navier-Stokes Simulations of The NREL Combined Experiment Phase II Rotor"*, AIAA paper 99-0037, January 1999.

[40] Kocurek, D., *"Lifting Surface Performance Analysis for Horizontal Axis Wind Turbines",* NREL Subcontract Report, SERI/STR-217-3163, Golden, CO, 316 pp., 1987

[41] [6] Gupta, S., and Leishman, J. G., 2005. *"Comparison of momentum and vortex methods for the aerodynamic analysis of wind turbines"*. In Proceedings of the 24th ASME Wind Energy Symposium, Reno, NV, Jan. 10-13.

[42] Sorensen, N. N., and Michelsen, J. A., *"Aerodynamic predictions for the Unsteady Aerodynamics Experiment Phase II rotor at the National Renewable Energy Laboratory",* AIAA paper 2000-0037, 2000

[43] Gupta, A., *"Prediction of aerodynamic forces on wind turbine blades using computational fluid dynamics"*, Master Thesis, Applied Science in Industrial Systems Engineering, University of Regina, 2007.

[44] Nilay Sezer-Uzol, “*Unsteady Flow Simulations Around Complex Geometries Using Stationery or Rotating Unstructured Grids*”, PhD Thesis, The Pennsylvania State University, 2006.

[45] Guanpeng Xu, *“Computational Studies of Horizontal Axis Wind Turbines”*, PhD thesis, Georgia Institute of Technology, May 2001

[46] Sarun Benjanirat, *“Computational studies of horizontal axis wind turbines in high wind speed condition using advanced turbulence models”*, PhD thesis, Georgia Institute of Technology, December 2007

[47] Imamura, H., Hasegawa, Y., and Kikuyama, K., *“Numerical Analysis of the Horizontal Axis Wind Turbine with Winglets”*, JSME International Journal, Series B vol. 41 nr. 1, JSME Tokyo Japan pp 170-176, February 1998.

[48] Johansen, J. and Sørensen, N.N., *“Numerical Analysis of Winglets on Wind Turbine Blades using CFD”*, EWEC 2007 Conference proceedings, Madrid, Spain, 2007.

[49] Johansen, J. and Sørensen, N.N, *“Aerodynamic Investigation of Winglets on Wind Turbine Blades Using CFD”*, Risø-R-1543(EN), February 2006.

[50] Maughmer, M.D, *“The Design of Winglets for High-Performance Sailplanes”*, AIAA 2001-2406, AIAA Applied Aerodynamics Conference, 19th, Anaheim, CA, June 11-14, 2001.

[51] Chattot, J.J., *“Effects of Blade Tip Modifications on Wind Turbine Performance using Vortex Model”*, *Computers & Fluids,* Vol. 38, pp. 1405-1410, 2009.

[52] Simms D.A., Robinson M.C., Hand M.M., Fingerish L.J*., “A Comparison of Baseline Aerodynamic Performance of Optimally-Twisted Versus Non-Twisted Blades”*, 15th ASME Wind Energy Symposium, 1996.

[53] LIU Xiong, CHEN Yan, YE Zhiquan, *“Optimization model for rotor blades of horizontal axis wind turbines*”, Research Article, Higher Education Press and Springer-Verlag, 2007.

[54] J.G. Schepers et. all, “*Final report of IEA AnnexXIV: Field Rotor Aerodynamics”,* ECN-C--97-027, May 1997.

[55] D.A. Simms, M.M. Hand, L.J. Fingersh, and D.W. Jager, “*Unsteady Aerodynamics Experiment Phases II–IV Test Configurations and Available Data Campaigns”,* NREL/TP-500-25950, July 1999.

[56] Hand, M., Simms, D., Fingersh, L., Jager, D., Cotrell, J., Schreck, S., and Larwood, S., *“Unsteady Aerodynamics Experiment Phase VI: Wind Tunnel Test Configurations and Available Data Campaigns”,* NREL/TP 500-29955, 2001.

[57] Giguere, P., and Selig, M. S., *“Design of a Tapared and Twisted Blade for the NREL Combined Experiment Rotor”*, NREL/SR-500-26173, April 1999.

[58] F. Stoddard, V. Nelson, K. Starcher, B. Andrews, *“Determination of Elastic Twist in Horizontal Axis Wind Turbines (HAWTs)”*, Subcontract Report, NREL/SR-500-12087, June 2006.

[59] Dayton A. Griffin, *“WindPACT Turbine Design Scaling Studies Technical Area 1.Composite Blades for 80- to 120-Meter Rotor”*, NREL/SR-500-29492, April 2001.

[60] Ta’asan S., *“Trends in Aerodynamics Design Optimization: A Mathematical Viewpoint”*, AIAA Paper 95-1731, June 1995.

[61] Blaize M., Knight D., and Rasheed K., *“Automated Optimal-Design of 2-Dimensional Supersonic Missile Inlets”*, Journal of Propulsion and Power, Vol. 14, No. 6, 890-898, 1998.

[62] Vanderplaats G.N., *“Numerical Optimization Techniques for Engineering Design”*, McGraw-Hill, 1984.

[63] Misegades K.P., *“Optimization of Multi-element Airfoils”*, VKI PR 1980-5, 1980.

[64] Van Laarhoven P.J.M., Aarts E.H.L., *“Simulated Annealing: Theory and Applications”,* Kluwer Academic Publishers, 1987.

[65] Aly S., Marconi F., Ogot M., Pelz R., Siclari M., *“Stochastic Optimization Applied To CFD Shape Design”*, AIAA-95-1647-CP, pp. 11-20, 1995.

[66] Tekinalp O., Karslı G., *“A new Multiobjective Simulated Annealing Algorithm”*, Journal of Global Optimization, 2006.

[67] Goldberg, D. E., “*Genetic Algorithms in Search, Optimization, and Machine Learning”*, Addison-Wesley, 2-6, 1989.

[68] Holt G, Bassler S., “Preliminary Design of Axial Compressors Using Artificial Intelligence and Numerical Optimization Techniques”, ASME Paper 91-GT-334, 1991.

[69] Özhan Öksüz, “Multiploid Genetic Algorithms For Multi-Objective Turbine Blade Aerodynamic Optimization”, PhD Thesis, Middle East Technical University, December 2007.

[70] De Falco I., *“An Introduction to Evolutionary Algorithms and Their Application to Aerofoil Design Problem*”, VKI LS 1997-05, 1997.

[71] Quagliarella D., “*Genetic Algorithm Applications in Computational Fluid Dynamics”*, Genetic Algorithms in Engineering And Computational Science, pp. 417-442, John Wiley & Sons, 1995.

[72] Periaux J., Sefrioui, M, Stoufflet B., *"Robust Genetic Algorithms for Optimization Problems in Aerodynamic Design*", Genetic Algorithms in Engineering And Computational Science, pp. 371-396, John Wiley & Sons, 1995.

[73] Trigg M.A, Tubby G.R., Sheard A. G., *"Automatic Genetic Optimization Approach to 2D Blade Profile Design For Steam Turbines*", Journal of Turbomachinery, pp. 11-17, 1999.

[74] O. Oksuz, I.S. Akmandor, M. S. Kavsaoglu, *"Aerodynamic Optimization of Turbomachinery Cascades Using Euler/Boundary Layer Coupled Genetic Algorithms"*, Journal of Propulsion and Power, Vol.18, No.3, May-June 2002, pp.652-657.

[75] Poloni C., *"Hybrid GA for multi-objective aerodynamic shape optimization"*, Genetic Algorithms in Engineering And Computational Science, pp. 397-415, John Wiley & Sons, 1995.

[76] K. Chiba, S. Obayashi, K. Nakahashi, *"Design Exploration of Aerodynamic Wing Shape for Reusable Launch Vehicle Flyback Booster"*, Journal of Aircraft, Vol.43, No. 3, pp. 832-836, 2006.

[77] Charles Hirch, *"Numerical Computation of Internal and External Flows"*, John Wiley & Sons Ltd., Vol.2, 1991.

[78] Stephen B. Pope, *"Turbulent Flows"*, Cambridge University Press, 2000.

[79] T. Cebeci, J. P. Shao, F. Kafyeke, E. Laurendeau, *"Computational Fluid Dynamics for Engineers"*, Horizon Publishing, Springer, 2005.

[80] David C. Wilcox, *"Turbulence Modeling for CFD"*, DCW Industries, Inc., 1993.

[81] C. J. Chen, S. Y. Jaw, *"Fundamentals of Turbulence Modeling"*, Taylor and Francis, 1998.

[82] Spalart P.R., Allmaras S.R., *"A One-Equation Turbulence Model for Aerodynamic Flows"*, AIAA 92-0439, AIAA 30th Aerospace Sciences Meeting and Exhibit, Reno, NV, Jan 6-9, 1992.

[83] Klaus A. Hoffmann, Steve T. Chiang, *"Computational Fluid Dynamics"*, Volume III, Engineering Education System, Wichita, Kansas, 4th Edition, 2000.

[84] Launder, B.E. and Sharma, B.I.,*" Application of the Energy Dissipation Model of Turbulence to the Calculation of Flow Near a Spinning Disc"*, Letters in Heat and Mass Transfer, Vol. 1, No. 2, pp. 131-138, 1974.

[85] Yang, Z. and Shih, T.H., *"New Time Scale Based k-□ Model for Near-Wall Turbulence"*, AIAA Journal, Vol. 31, No.7, pp. 1191 – 1198, 1993.

[86] Menter, F.R., *“Two-Equation Eddy-Viscosity Turbulence Models for Engineering Applications”*, AIAA Journal, Vol. 32, No. 8, pp. 269-289, 1994.

[87] Durbin P.A., “*Near-wall turbulence closure modeling without damping function”*, Theor. Comput. Fluid Dynamics, Vol. 3, No. 1, pp 1-13, 1991.

[88] Durbin, P., *“Separated flow computations with the* $k - \epsilon - \overline{v^2}$ *model”*, AIAA Journal, 33, 659-664, 1995.

[89] Launder B.E. and Spalding D.B., *“The numerical computation of turbulent flow”*, Comput. Methods App. Mech. Eng., vol. 3, pp. 269-289, 1974.

[90] Wilcox D., *“Reassessment of the scale-determining equation for advanced turbulence models”*, AIAA Journal, vol.26, pp.1299-1310, 1988.

[91] Wilcox D., *"Turbulence model for CFD*", tech. rep., DCW Industries, Inc., 5354 Palm Drive, La Canada, Calif, 1993

[92] Lien F.S. and Kalitzin G., “*Computations of transonic flow with the v2-f turbulence model”*, International Journal of Heat and Fluid Flow 22, 53-61, 2001.

[93] Abu-Ghannam B J, Shaw R, 1980, *"Natural Transition of Boundary Layers – the Effects of Turbulence, Pressure Gradient and Flow History"*, J. Mech. Engg. Sci., 22(5):213-228.

[94] Hakimi N., *"Preconditioning methods for time dependent Navier-Stokes equations"*, PhD Thesis, Dept of Fluid Mechanics, Vrije Universiteit Brussel, 1997.

[95] Numeca CFD Fine/Turbo Theory Manual, April 2010.

[96] Choi, D., Merkle, C. L., *“The Application of Preconditioning in Viscous Flows”*, Journal of Computational Physics Vol. 105, pp. 207-223, 1993.

[97] E. F. Toro, *“Riemann Solvers ad Numerical Methods for Fluid Dynamics”*, Springer, 2nd Edition, 1999.

[98] http://www.cfd-online.com/Wiki/Sutherland_law, Last Visited 13-August-2010.

[99] ECN site: www.ecn.nl, lasted visited 21-May-2009.

[100] Sommers, D. M., *“Design and Experimental Results for the S809 Airfoil”*, Airfoils, Inc., State College, PA, 1989.

[101] Walter P. Wolfe, Stuart S. Ochs, *"CFD Calculations of S809 Aerodynamic Characteristics"*, AIAA Paper 97-0973, 1997.

[102] Numeca CFD AutoGrid user manual, March 2010.

[103] Earl P.N. Duque et. all, *"Numerical Predictions of Wind Turbine Power and Aerodynamic Loads for the NREL Phase II Combined Experiment Rotor",* AIAA-2000-0038, 2000.

[104] Numeca CFD AutoBlade user manual, October 2007.

[105] Bardina, J. E., Huang, P. G. and Coakley, T.J., *"Turbulence Modeling Validation, Testing, and Development,"* NASA Technical Momorandum 110446, April 1997

[106] Thomas, F., "*Fundamentals of Sailplane Design"*, Translated by Judah Milgram, College Park Press, MD, 1999.

[107] Falk, T.J. and Matteson, F. H., *"Sailplane Aerodynamics",* American Soaring Handbook, Soaring Society of America, 1971.

[108] Whitcomb, R.T., "*A Design Approach and Selected Wind-Tunnel Result at High Subsonic Speed for Wing-Tip Mounted Winglets*", NASA TN D-8260, July 1976.

[109] Mac Gaunaa and Jeppe Johansen, *"Determination of the Maximum Aerodynamic Efficiency of Wind Turbine Rotors with Winglets"*, Journal of Physics: Conference Series 75 (2007) 012006, 2007.

[110] Final Report IEA Wind Annex XX: HAWT Aerodynamics and models from Wind Tunnel Measurements, NREL/TP-500-43508, December 2008.

[111] Krose, B, VanderSmagt, P., (1996), *"An Introduction to Neural Networks"*, 8th Edition, University of Amsterdam, Amsterdam.

[112] Numeca CFD Fine/Design 3D v3 user manual, October 2007.

[113] Demeulenaere, A. et al, *"Design And Optimization Of An Industrial Pump: Application Of Genetic Algorithms And Neural Network*", *2005 ASME Fluids Engineering Division Summer Meeting & Exhibition,* FEDSM2005-77487, June 19-23 2005, Houston, Texas

CURRICULUM VITAE

PERSONAL INFORMATION

Surname, Name: Elfarra, Monier Ali
Nationality: Palestinian
Date and Place of Birth: 27 November 1977, Gaza Strip – Palestine
Marital Status: Married with a son
Phone: +90 541 205 11 92
email: monier@ae.metu.edu.tr

EDUCATION

MS	METU Aerospace Engineering, 2005
BS	METU Aeronautical Engineering, 2000
High School	Khan-Younis High School for Boys

WORK EXPERIENCE

2007-Present	PARS Makina, R&D Engineer
2005-2007	*Pakistan* Embassy International Study Group, Physics Teacher
2002-2003	Orient Pearl - Saudi Arabia, Site Engineer

LANGUAGES

Arabic (Native), English (Fluent), Turkish (Fluent), Hebrew (Basic)

PUBLICATIONS

- Elfarra M. A, Akmandor I. S., Uzol N.S, “Investigation And Optimization Of Winglets For HAWT Rotor Blades”, To appear on the ETC 9, Istanbul 2011.

- Elfarra M. A, Uzol N.S., Akmandor İ.S., *“Investigations On Tip Tilting For HAWT Rotor Blades”*, 10th International Conference on Clean Energy (ICCE-2010) Famagusta, N. Cyprus, September 2010.

- Ersin Şekerci, Monier Elfarra, and Can Albasan, “*Rüzgar Türbini Tahmini Yıllık Enerji Üretim Hesaplama Yönetmeleri ve Araziye Uygun Rüzgar Türbini Seçimi*”, Rüges 2009

- Sinan Akmandor, Monier Elfarra, Ersin Şekerci and Can Albasan, "*Türkiye'de Rüzgar Enerjisi Güç Tahmini Ve Yerli Türbin Üretimi*", ICCI 2009, İstanbul

- Monier El-farra, Ali Akturk, and I. Sinan Akmandor, "*Two Dimensional Finite Volume and Finite Difference Weighted Essentially Non-Oscillatory Euler Schemes*", Kayseri VI. Havacilik Sempozyumu 2006.

- Monier El-farra, Ali Akturk, and I. Sinan Akmandor, "*Two Dimensional Finite volume Weighted Essentially Non-Oscillatory Euler Scheme*", 3rd Ankara International Aerospace Conference , AIAC 2005 – 047.

- Ali Akturk, Monier El-farra, and I. Sinan Akmandor, "*Two Dimensional Finite volume Weighted Essentially Non-Oscillatory scheme using different flux computations*", 3rd Ankara International Aerospace Conference, AIAC 2005-097.

HOBBIES

Gym, Swimming, Computers, Old Arabic poems, History